Performance Enhancement of PowerWindow, a Linear Cascade Wind Turbine, for Application in Urban Environments

Seyed AmirHosein Jafari

A thesis submitted to fulfil the requirements of the degree of

Doctor of Philosophy

Centre for Infrastructure Engineering (CIE)

WESTERN SYDNEY
UNIVERSITY

December 2019

ABSTRACT

Linear Cascade Wind Turbines (LCWTs) are new generation wind turbines. Unlike conventional horizontal and vertical axis wind turbines (HAWTs and VAWTs) where the blades have rotational movement around the rotor axis, LCWTs have two sets of blades in a linear cascade configuration. One of the major advantages of this configuration is that the two sets of blades moves translationally in directions opposite to each other and perpendicular to the approaching wind direction. The recently developed PowerWindow, which is a special type of LCWT, has flexibility for different applications because of its modular design. Furthermore, PowerWindow's capability of generating power in low wind velocity conditions makes it an effective and safe wind turbine for the application in urban environments. However, the coefficient of performance of the first generation PowerWindow is noticeably lower than the existing commercialised HAWTs and VAWTs. Moreover, similar to other wind turbines, the application of PowerWindow in urban environment is constrained by poor wind conditions such as low and/or intermittent wind velocity and continuously variable wind directions.

The first study of this research project develops an efficient analytical model based on blade element momentum (BEM) theory to investigate the aerodynamics of PowerWindow,. This analytical model elucidates some fundamental flow characteristics of PowerWindow, such as the axial induction factor and local instantaneous angle of attack along the blades. The model also quantifies the effects of the blade pitch angle, linear speed ratio, and the solidity on the angle of attack, axial induction factor and power generation of PowerWindow. The validity and accuracy of the analytical model is verified through Computational Fluid Dynamic (CFD) simulations. The results indicate that by doubling the solidity or increasing the blade design angle, the PowerWindow's coefficient of performance increases significantly. The analytical model enables the researchers to efficiently find the design parameters of PowerWindow and its power generation for various wind conditions.

Suitable locations for installing PowerWindow on the ground are limited. The second study of this research project investigates elevated and ducted installation configurations for the device. In the elevated configuration, PowerWindow is installed on a tower or between two tall buildings. In a ducted configuration, it is installed inside a ducted area, such as a through-building opening. Aerodynamic performances of the elevated and ducted PowerWindow are investigated using computational fluid dynamics simulations and compared with each other. The effects of solidity on the flow mechanism and power generation are quantified. It was found that the ducted PowerWindow's coefficient of performance is higher than the elevated one and increasing solidity of the ducted configuration creates a greater increase in the power generation compared to the elevated one. This study also investigates the effect of solidity on the pressure gradient across PowerWindow and recommends an efficient solidity for the both elevated and ducted configurations.

To enhance the power generation capacity and operation probability of PowerWindow, the third study of this research project proposes the attachment of stator vanes to PowerWindow to improve the flow direction in the device. By controlling the angle of attack, the stator vanes increase the acting force and in the same time decrease the undesirable force on the PowerWindow blades. An analytical model, using BEM theory, was developed and verified using CFD simulations for analysing the new configuration, which is referred to as stator-augmented PowerWindow thereafter. This study shows that the stator vanes are able to minimise/neutralise the undesirable axial force on PowerWindow, so that the thrust coefficient becomes negligible in the stator-augmented model. In addition, by increasing the acting lift force on the blades, the stator-augmentation will simultaneously enhance the coefficient of performance. Unlike in the original PowerWindow, the rotation direction of the stator-augmented PowerWindow remains the same regardless of the wind direction, as a result, the power generation capacity of the device will be increased significantly.

The fourth study of this research project investigates the power generation capacity of a stator-augmented PowerWindow installed in the through-building openings of a tall building. By employing a new equivalent momentum sink method, the flow characteristics of the ducted flow (including pressure, velocity, and turbulence intensity) in the presence of a wind turbine are predicted for different wind directions. This study shows that a properly designed layout can maintain the velocity in the through-building openings and enhances the power generation for a much wider range of wind directions compared with the free-stream wind turbine installed at the same elevation. The power generations of a stator-augmented PowerWindow and a conventional HAWT (Ampair 300), installed in the same through-building openings are compared with each other. The results show that the power generation of the ducted stator-augmented PowerWindow is similar to that of the ducted HAWT in certain wind directions. However, it can also effectively generate power at wind directions under which the ducted HAWT is unable to operate. This advantage of building integrated stator-augmented PowerWindow significantly increases the annual power generation.

ACKNOWLEDGEMENTS

I would like to express my deepest gratitude to my supervisors: Professor Kenny Kwok, Professor Farzad Safaei, Associate Professor Buyung Kosasih, Associate Professor Ming Zhao and Professor Bijan Samali. I wish to thank; Kenny Kwok for extending my insight and knowledge and pushing my boundaries; Farzad Safaei for supporting me both academically and personally; Buyung Kosasih for providing scholarly support whenever I needed; Ming Zhao for his devotional supervision during the last two years of my study; and Bijan Samali for his spiritual and financial support during my whole PhD time.

I would like to extend my gratitude to the Centre for Infrastructure Engineering (CIE) at the Western Sydney University for giving me the opportunity and the fund to explore my area of interest and to present my findings in distinguished journals and conferences.

I would like to thank my companion friends in Wollongong who never allowed me to feel alone even thousands of kilometres from home. I would like to extend my special gratitude to my dear friend and colleague Sina Hassanli not only for his companionship during my PhD time, but also for the invaluable, and thought-provoking conversations we had beyond this research.

And I would like to extend my warmest gratitude to my family for their unconditional love and support and putting up with me being tired and irritable often during my PhD. They have always been the main source of energy and the reason for me to continue even in difficulties.

STATEMENT OF AUTHENTICATION

All the analytical and numerical analyses, which aim to improve the configuration and application of PowerWindow, conducted and reported in this PhD thesis are original except as acknowledged in the text. I hereby declare that I have not submitted this material, either in full or in part, for a degree at this or any other institution.

Seyed A Jafari
02/12/2019

ANTHOLOGY OF DISSEMINATION

The present thesis is prepared based on publications. The following three published articles and one accepted article (in production) are included in the thesis:

Published articles:

1. **Jafari SAH**, Kwok KCS, Safaei F, Kosasih B, Zhao M, Aerodynamic Analysis of a Linear Cascade Wind Turbine. *Journal of Wind Energy*. 2018; 21 (11): 1141-1154. https://doi.org/10.1002/we.2219.

2. **Jafari SAH**, Kwok KCS, Safaei F, Kosasih B, Zhao M, The effects of installation configuration and solidity on the power generation of a linear cascade wind turbine. *Journal of Wind Engineering and Industrial Aerodynamics*. 2018; 180: 122-135. https://doi.org/10.1016/j.jweia.2018.07.015.

3. **Jafari SAH**, Kwok KCS, Safaei F, Kosasih B, Zhao M, Aerodynamic Analysis of a Stator-augmented Linear Cascade Wind Turbine. *Journal of Wind Energy*. 2019; in press.

4. **Jafari SAH**, Hassanli S, Kwok KCS, Safaei F, Kosasih B, Zhao M, Building Integration of stator-augmented PowerWindow, a Linear Cascade Wind Turbine. *Journal of Energy Science & Engineering*. 2019; 00: 1- 18. https://doi.org/10.1002/ese3.300.

The journal articles have been published under my name, SAH (Seyed AmirHosein) Jafari, and I was the first author. I conducted all the numerical model development, calculations, and post-processing of data under the supervision of the co-authors.

The following conference papers are also prepared and presented based on the studies undertaken during this research project. These studies have served one of the main purposes of the project which is building integration of stator-augmented PowerWindow. However, these papers are not included in the thesis:

1. Hassanli S, **Jafari SAH**, Kwok KCS, Flow enhancement in tall buildings for wind energy generation, *8th International Colloquium on Bluff Body Aerodynamics and Applications*. 2016: Boston, United States.

2. **Jafari SAH**, Kwok KCS, Hassanli S, Integration of wind turbines in tall buildings for wind power generation, *8th International Colloquium on Bluff Body Aerodynamics and Applications*. 2016: Boston, United States.

3. **Jafari SAH**, Hassanli S, and Kwok KCS, Performance analysis of a small wind turbine mounted inside a tall building, *18th Australasian Wind Engineering Society Workshop*. 2016: Adelaide, Australia.

4. **Jafari SAH**, Hassanli S, Eftekharian E, Kwok KCS, Effect of Incident Wind Angle on Power Generation of Building Integrated Wind Turbines, *9th Asia-Pacific Conferences on Wind Engineering*, 2017: Auckland, Newzealand.

5. Hassanli S, **Jafari SAH**, Eftekharian E, Kwok KCS, Performance Assessment of Cascaded Wind Turbines Inside Through-building Openings, *9th Asia-Pacific Conferences on Wind Engineering*, 2017: Auckland, Newzealand.

TABLE OF CONTENT

LIST OF TABLES

LIST OF FIGURES

NOMENCLATURE

a_f	Axial induction factor(dimensionless)
A	Air swept area (m^2)
B	Airfoil plan area (m^2)
C_D	Drag coefficient (dimensionless)
C_L	Lift coefficient (dimensionless)
C_P	Coefficient of performance (dimensionless)
C_{sp}	Surface Pressure Coefficient (dimensionless)
C_T	Trust Coefficient (dimensionless)
F_D	Drag force (N)
F_L	Lift force (N)
F_v	Vertical aerodynamic force on LAWT blades (N)
H	Building height (m)
ṁ	Mass flow rate (kg/s)
N	Number of blades in one side of PowerWindow
P	Power (Watt)
P	Pressure (Pa)
R_P	Power generation ratio (dimensionless)
R_V	Velocity ratio (dimensionless)
TKE	Turbulence kinetic energy (m^2/s^2)
U_{10}	Free-stream velocity at 10 m above sea level (m/s)
$U_{3/4H}$	Free-stream velocity at 3/4H (m/s)
U_{ref}	Free-stream velocity at H (m/s)
V	Air velocity in horizontal direction (ms^{-1})
α	Angle of attack (°)
β	Effective angle (°)

θ_b	Blade pitch angle (°)
θ_v	Vane pitch angle (°)
ε	Affected flow ratio (dimensionless)
σ	Solidity (dimensionless)
μ	Air viscosity (m^2/s)
ρ	Air density (kg m^{-3})
λ	Blade speed ratio (dimensionless)
τ	Aerodynamic torque on HAWT rotor (N.m)
ϕ	Incident wind angle (°)
ω	Rotational speed of HAWT rotor (rad/s)

CHAPTER 1. INTRODUCTION

1.1. Significance and aim of research project

Urban environments have many attractions and difficulties when it comes to the development of wind energy harvesting systems. Critical issues of using these systems in urban environments include noise, aesthetics, integration into architectural systems, and efficient use of the available wind resource [1, 2]. Wind in urban areas tend to be more turbulent and multi-directional. The presence of buildings increases the turbulence of the wind and also deflects the direction of the wind from a horizontal free stream [3]. Aesthetics is also a concern as many people find conventional wind turbines unattractive. There are also environmental concerns, such as the consideration of bird safety [2, 4]. Conventional horizontal and vertical axis wind turbines cannot easily be integrated with architectural designs due to their configuration and accommodation requirements [5, 6]. These systems need to be properly integrated with the architecture of urban environments.

This research project aims to enhance the performance and application of a new wind turbine referred to as PowerWindow. PowerWindow is a type of Linear Cascade Wind Turbine (LCWT) that has recently been developed based on a modular approach and is flexible for integration with the architecture of urban environments [7]. Furthermore, PowerWindow is capable of generating power in low wind velocity conditions with very low operation speed, which makes it an effective and safe wind turbine for application in urban environments. Hence PowerWindow is potentially an alternative to the conventional wind turbines for the application in urban environments.

1.2. Methodology of the research project

Two approaches/methods are applied in this study for performance analysis and the improvement of PowerWindow. These approaches are:

(i) Numerical modelling using computational fluid dynamic (CFD) simulations.
(ii) Analytical modelling using the blade element momentum (BEM) theory.

1.2.1. CFD simulation

CFD is a numerical calculation method for analysis and prediction of flow characteristics such as velocity, pressure, and turbulence [8]. Three-dimensional (3D) Direct Numerical Simulation (DNS) based on the Navier‑Stokes equations is theoretically realistic, but it require extremely and very often unaffordable long calculation time [9]. CFD simulations can model turbine blades and estimate the complex turbulent flows adjacent to blades and in the wake region created at both the near and far

downstream[10]. CFD simulation is very useful, particularly when a rotor is subjected to complex flow conditions with high turbulence level and variable flow directions. If a significant part of the blades are operating in a stall condition, it is impossible to rely on pre-determined lift coefficients achieved by wind tunnel experimental tests [11]. Some very accurate and realistic CFD methods are available for representation turbine wakes, which need very long calculation times, so they are not usually used for turbine performance evaluation [12].

The major advantage of CFD simulations compared to experimental prototyping is that they need less time and are not as costly. Moreover, the CFD simulations can give a further insight into flow mechanism passing through the wind turbines [13], if the CFD model is validated using experimental data. CFD simulations also have some advantages compared to some simplified methods such as the BEM model. CFD simulations have successfully been used for performance analysis of large-scale wind turbines [14, 15], and wake effects on turbines downstream [16]. CFD simulations are also able to predict VAWT performance more accurately than a BEM model [17]. However, BEM models are more time and cost-efficient than CFD simulations.

1.2.2. BEM theory

The BEM method is a mathematical method for the fluid dynamics analysis and performance evaluation of wind turbines [18]. The BEM aerodynamic analysis concept based on Glauert's airscrew theory [19] has been used extensively for the analysis of propellers and was initially used in the helicopter industry [20]. Its application was later extended to assess the performance of wind turbines [21]. BEM was recently used for analysing HAWTs [22-25] and VAWTs [26, 27], by using tabulated airfoil data. It has also been successfully applied to tidal turbines [28-30].

The BEM method needs two-dimensional (2D) airfoil data in addition to the cord length and twist angle information along the spanwise direction to find the optimum shape for a blade. The limitation of BEM is that once the wind turbine blade optimisation is achieved at one operating condition with specific relative tip speed ratio and angle of attack, that design may no longer be optimal for other TSR and angles of attack [31, 32]. Two assumptions are made in the BEM theory: (i) there is no aerodynamic interaction between the blade elements; and (ii) the forces on the blades are determined solely by the lift and drag characteristics of the airfoil shape of the blades [33]. Since the BEM model is directly based on the data of two dimensional (2D) airfoils, empirical corrections is necessary to account for three-dimensional (3D) effects, such as tip losses, rotational flow, and dynamic stall [33]. One correction method is including the total energy loss (due to the tip and hub) factor to improve the accuracy of BEM calculation. Prandtl [34] and Byand [35] developed BEM tip loss correction models. A modified BEM method has also been developed based on calibration using actuator disc simulations [36].

The predictions obtained by a well calibrated BEM method is reliable and requires much less computational time compared to CFD simulations [26]. By comparing the results of CFD simulations and BEM methods for small scale propellers, Carroll and Marcum [37] showed that the BEM method predicts the thrust with acceptable accuracy when a propeller has weak separation and the blade has a high aspect ratio with little or no cord variation. However, in cases where flow separation occurs in large regions, or the aspect ratio of the blades is low, or the cord varies significantly, the accuracy of BEM reduces. Moreover, one fundamental limitation of the BEM method compared to the CFD simulation is that it cannot analyse the rotor impact on the surrounding flow [38]. Therefore, a combination of the BEM method and CFD simulations have been used in recent studies [8, 29, 38-41]. Because PowerWindow comprises uniform blades with large aspect ratio (see Figure A1 in Appendix A1), and the flow separation is not allowed under the operation condition, the BEM is expected to be an efficient and valid method for aerodynamics analysis and power estimation. This research project will use both CFD and BEM to obtain more accurate and reliable results of power generation of PowerWindow.

1.3. Objectives of the research project

This research project aims to increase the power generation performance of PowerWindow in urban environments. The research objectives are:

1) To understand the power generation mechanism of PowerWindow using both BEM theory and CFD simulations.

2) To improve the power generation of PowerWindow in building integration configuration of the device using reliable blade element momentum (BEM) theory computational fluid dynamic (CFD) simulations.

3) To improve the power generation performance and operation probability of PowerWindow using stator-augmented configuration employing reliable BEM theory CFD simulations.

4) To investigate the power generation performance and operation probability of the improved version of PowerWindow when integrated in a tall building and comparing it with that of a conventional HAWT.

1.4. Thesis content

Chapter 1. Introduction: describes the significance, aims and contributions of the research project.

Chapter 2. Wind Turbine Technologies and Urban Applications: describes the conventional and the new wind turbine technologies (including LCWTs), as well as their performance and application in urban areas.

Chapter 3. Aerodynamic Analysis of a Linear Cascade Wind Turbine: an analytical model is developed to investigate the aerodynamics and the power generation of PowerWindow. Based on blade element momentum (BEM) theory, this analytical model elucidates some flow characteristics of PowerWindow (such as axial induction factor and local instantaneous angle of attack along the blades) and provides an understanding of the effects of design characteristics on the power generation of PowerWindow when operating in an elevated position. The validity and accuracy of the analytical model is verified by Computational Fluid Dynamic (CFD) simulations.

Chapter 4. The Effect of Installation Configuration and Solidity on Power Generation of a Linear Cascade Wind Turbine: analytical and computational fluid dynamic models for PowerWindow are developed to investigate the power generation of the current prototype operating in two different installation positions: elevated and ducted. Aerodynamic performances of the elevated and ducted PowerWindow using computational fluid dynamic simulations are compared with each other. This study also investigates the effect of an important design characteristic (solidity) on the power generation of PowerWindow operating at each installation configuration.

Chapter 5. Aerodynamic Analysis of a Stator-augmented Linear Cascade Wind Turbine: stator vanes are attached to the PowerWindow to control the angle of attack and improve the flow direction in the device. An analytical model using blade element momentum theory is developed for the new configuration, referred to as stator-augmented PowerWindow. The analytical model is verified by computational fluid dynamics simulations. This study proved the effectiveness of the stator vanes on improving the efficiency of PowerWindow.

Chapter 6. Building Integration of Stator-augmented Linear Cascade Wind Turbine: investigates the power generation capacity of a stator-augmented PowerWindow installed in the through-building openings of a tall building. By employing a new approach, referred to as the equivalent momentum sink method, the flow characteristics of the ducted flow, including pressure, velocity, and turbulence intensity is predicted when subjected to different wind directions in the presence of a wind turbine. This study also compares the annual power generation probability of stator-augmented PowerWindow with a conventional horizontal axis wind turbine, Ampair 300, installed in the same through-building openings.

Chapter 7. Conclusion: presents the achievements and the future perspectives of the stator-augmented LCWT designed and developed in this research project.

1.5. Publications

The following journal articles are published based on the studies undertaken in this thesis:

1. Aerodynamic Analysis of a Linear Cascade Wind Turbine, **Jafari SAH**, Kwok KCS, Safaei F, Kosasih B, Zhao M, *Journal of Wind Energy*, 2018; 21 (11): 1141-1154 (https://doi.org/10.1002/we.2219).

2. The effects of installation configuration and solidity on the power generation of a linear cascade wind turbine, **Jafari SAH**, Kwok KCS, Safaei F, Kosasih B, Zhao M, *Journal of Wind Engineering and Industrial Aerodynamics*, 2018; 180: 122-135 (https://doi.org/10.1016/j.jweia.2018.07.015).

3. Aerodynamic Analysis of a Stator-augmented Linear Cascade Wind Turbine, **Jafari SAH**, Kwok KCS, Safaei F, Kosasih B, Zhao M, *Journal of Wind Energy*, 2019. 22 (8): p. 1148-1163 (https://doi.org/10.1002/we.2346).

4. Building Integration of stator-augmented PowerWindow, a Linear Cascade Wind Turbine, **Jafari SAH**, Hassanli S, Kwok KCS, Safaei F, Kosasih B, Zhao M, *Journal of Energy Science & Engineering*, 2019; 00: 1-18 (https://doi.org/10.1002/ese3.300).

CHAPTER 2. WIND TURBINE TECHNOLOGY, PERFORMANCE AND URBAN APPLICATION

2.1. Developments in wind turbine technology

The estimated onshore wind energy is $20{,}000\times10^9$–$50{,}000\times10^9$ kWh/year worldwide [41]. Global electricity generation from renewable and non-renewable sources in 1980-2050 is shown in Figure 2.1. (a). The curve for the years 1980-2010 provides historic data for the electricity generated in that period. The curve for the years 2010-2035 is based on the forecast of the United States Energy Information Administration [4]. Global electricity generation using wind power in 1990-2015 is shown in Figure 2.1. (b) [4].

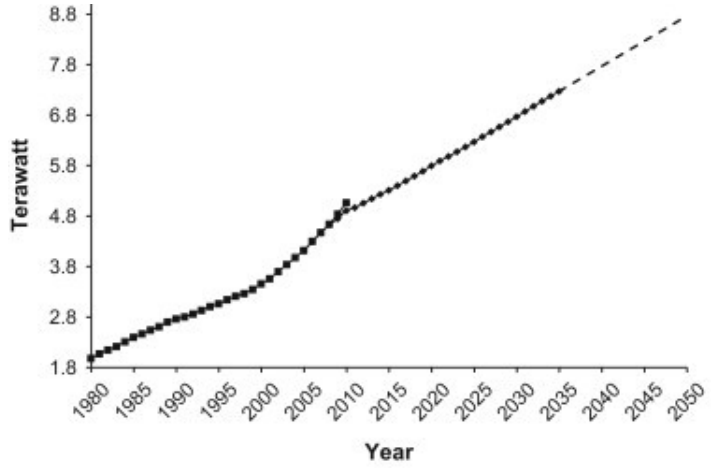

(a)

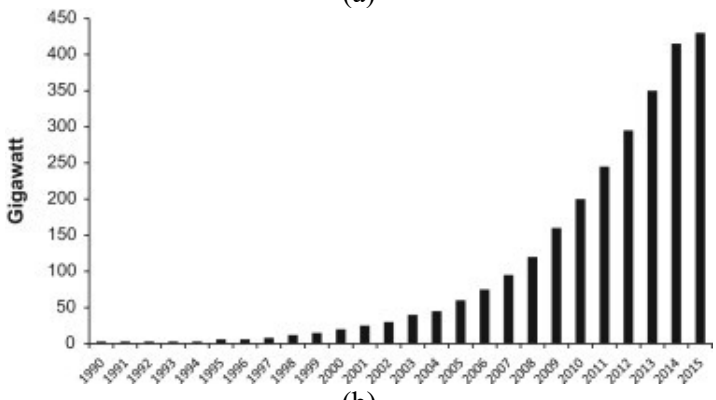

(b)

Figure 2-1: (a) Global electricity generation in 1980-2050 and (b) wind power contribution in 1990-2015 [41].

Before 1990, global wind turbines' power generation capacity was typically less than 100 kW. This capacity increased to 500 kW by 1990, and to 750 to 1000 in the following few years. By 2000 and 2005, the turbine power generation capacity reached 2500 and 3500 kW, respectively [41]. The largest wind turbine in the world is currently Vestas V164 [42] with 187 m height and 9.5MW power

rating (introduced in 2011), followed by Enercon E126 [43] with 126 m height and 7.5MW power rating (introduced in 2007). Figure 2.2 shows the relative size of Vestas V164 to Buying 747 (aeroplane) and some other conventional wind turbines.

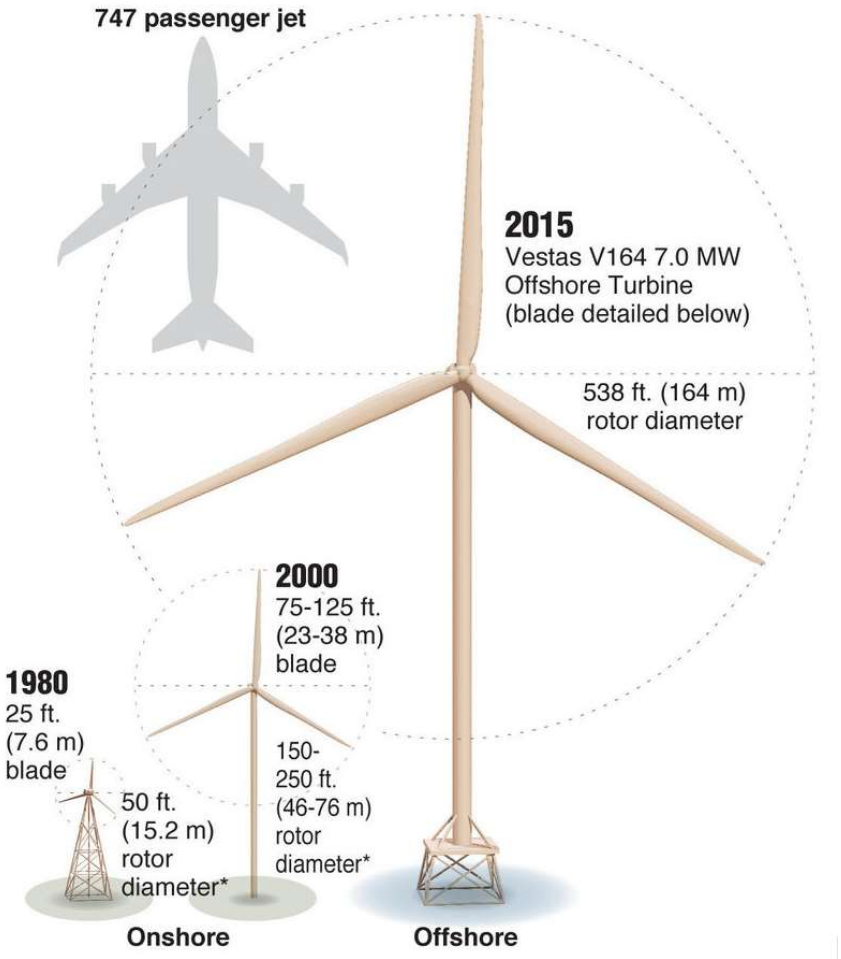

Figure 2-2: The relative size of Vestas V164 to Buying 747 (aeroplane) and some other conventional wind turbines [44].

2.1.1. Conventional Wind Turbine Technologies

2.1.1.1. Horizontal Axis Wind Turbine (HAWT)

In a HAWT, the main rotor shaft is arranged on a horizontal axis. The maximum coefficient of performance of a modern HAWT has been reported between 45% to 50% [45]. Because the rotor is not able to capture the wind energy from all direction, a HAWT should be pointed to the wind direction. Hence a special mechanism is required to turn the rotor to the wind direction. HAWTs are very sensitive to their blade surface roughness and profile design [27]. Large scales HAWTs normally have three blades and an 'active yaw system' which adjusts the orientation of the HAWT rotor towards the direction of the wind. An active yaw system includes a wind sensor which can sense the

wind direction, and a servo motor which creates a torque to rotate the rotor and generator above the stationary tower [25]. There are limitations on how closely HAWTs can be placed next to each other. This is because the rotary model creates a rotation of air flow in its vicinity and wake, due to tip vortices and rotational torque imparted on the air flow. The interference from these turbulent flows reduces the efficiency of adjacent wind turbines at close distances. A number of large HAWTs installed in a wind farm are shown in Figure 2.3 (a), with due consideration of interface effects.

(a) (b)

Figure 2-3: (a) Number of three-bladed HAWTs used in a wind farm, (b) a counter rotating HAWT [46].

Small HAWTs with 2-5 blades are usually integrated with the buildings or vehicles. In small scale HAWTs, the yaw system consists of a tail wing which creates a regulator moment to turn the wind turbine rotor towards the wind direction, as shown in Figure 2.4 (a-e). This yaw system is also known as a 'passive yaw system'.

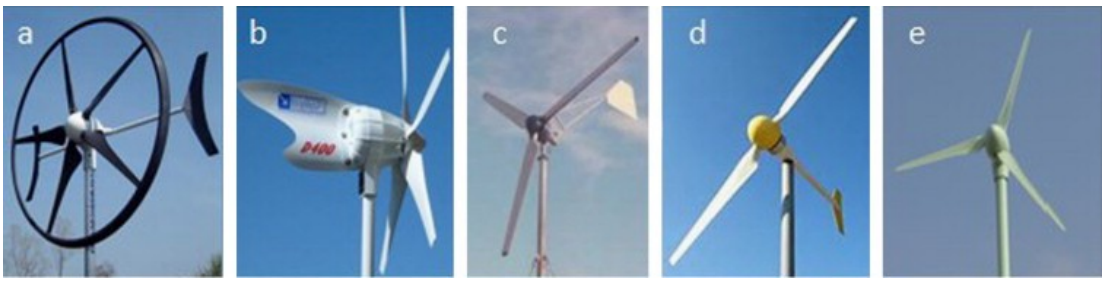

Figure 2-4: Examples of small HAWTs. (a) Swift wind turbine, (b) Eclectic wind turbines, (c) Fortis Montana wind turbine, (d) Scirocco wind turbines, (e) Tulipo wind turbine [47].

2.1.1.2. Vertical Axis Wind Turbine (VAWT)

In a VAWT the main rotor shaft is arranged along a vertical axis. The primary advantage of VAWTs compared to HAWTs is that there is no yaw mechanism required, which significantly simplifies their design and configurations [27]. Therefore, the VAWTs are more applicable than the HAWTs in multi-directional wind areas, such as urban areas. VAWTs are also less noisy compared to HAWTs, which make them preferable to HAWTs for urban area applications. However, the VAWTs

have some notable constraints compared to the HAWTs. Their tip speed ratio is basically lower than the HAWTs and are unable to self-start [48]. VAWTs are effectively applied to high-rise buildings in cities where wind speed exceeds 14 m/s [49]. Generally, VAWT designs can be categorised into three groups: (a) Savonius VAWT, (b) Curved-blade Darrieus VAWT, and (c) Straight-blade Darrieus or H-rotor VAWT, which are shown in Figures 2.5 (a), (b) and (c), respectively. Similar to the HAWTs, Darrieus (Curved-blade and Straight-blade/H-rotor) VAWTs are lift-type wind turbines which typically have a maximum coefficient of performance from 30% to 45%. Savonius VAWTs are the only drag-type wind turbines, and their coefficient of performance does not exceed 25%, according to most investigators [27]. Savonius VAWT is more suitable for low wind speeds conditions. The greatest advantage of a Savonius rotor compared to the lift-type VAWTs is its self-start ability [50]. Savonius VAWTs also have other advantages such as having low cost, simple construction, insensitivity to the wind direction, low angular velocity and low noise in operation [51].

(a) (b) (c)

Figure 2-5: (a) Savonius VAWT, (b) Curved-blade Darrieus VAWT, and (c) Straight-blade Darrieus or H-rotor VAWT [46].

Darrieus VAWTs have the highest coefficient of performance in contrast to the other models, but they have common weaknesses, such as low starting torque and a weak configuration structure [49]. The Eole is one of the largest Darrieus VAWT, with a 96 m height and a maximum power of 3.8 MW [45]. Darrieus VAWTs are basically lift-type wind turbines with a number of (usually) aerofoil-shaped blades attached to a vertical shaft. Gupta and Biswas [52] studied the application of twisted blades in Darrieus VAWT rotor at the trailing edge. The coefficient of performance of the Darrieus VAWT is superior to that of the Savonius VAWT [53].

In straight-blade or H-rotor VAWTs, drag/stall effect created by the front blade constrains the speed and the other blade(s) can propel the entire rotor. As a result, the straight-blade/H-rotor Darrieus VAWT is self-regulating and can achieve its optimal rotational speed in a short time after its cut-in wind speed in all wind velocities [45]. Although the Darrieus VAWTs are generally known to

have lower coefficient of performance than the HAWTs, Mertens et al. [54] have reported that their efficiency of performance could exceed HAWT if it is located on a rooftop. Figure 2.6 (a-d) shows different types of Darrieus wind turbines.

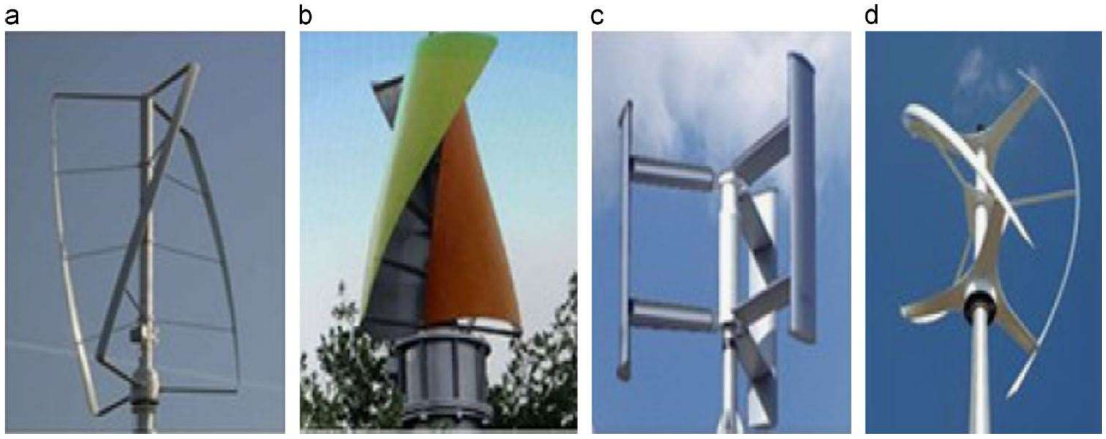

Figure 2-6: Different types of Darrieus wind turbines. (a) Turby turbine, (b) WindSide Turbine, (c) Ropatec turbine, and (d) Gorlov helical turbine [47].

Wang et al. [55] designed a novel Darrieus VAWT that has blades that can be deformed automatically into a desired geometry and thus achieve a better aerodynamic performance. The results indicated that compared to conventional turbines with the same solidity, the maximum percentage increase in power coefficient that the low solidity turbine with three deformable blades can achieve is approximately 14.56%. When the solidity is high and the turbine operates at a low tip speed ratio of less than the optimum value, the maximum power coefficient increase for the turbines with two and four deformable blades are 7.51% and 8.07%, respectively.

2.1.2. New Wind Turbine Technologies

2.1.2.1. Axial-mode Linear Wind Turbine (ALWT)

ALWT [56] is a non-rotating wind turbine with a plurality of self-supporting airfoil kites for capturing useful power. The system comprises of multiple airfoil kites (50) in tandem attached to a pivotal control housing (32) by control lines (58L and 58R) and support lines (60L and 60R), as show in figure 2.7. Control lines 58L and 58R can change length with respect to the length of support lines 60L and 60R to control the airfoil kites' 50 angle-of-attack, pitch angle, direction of flight, and flight speed. The length of control lines 58L and 58R are controlled from ground station 30 by a movable pulley system in control housing 32 to adjust the airfoil's direction to follow a specific flight path 140. Control lines 58R and 58L and support lines 60R and 60L are also wound on a power shaft and pulley system in control housing 32. As the airfoil kites are propelled by the wind at a very-high speed, the airfoils generate a powerful axial force. The control lines 58L and 58R and support lines 60L and 60R are then reeled-out under this axial tension causing the power shaft and pulley system in control

housing 32 to turn a generator to generate electricity. After airfoil kites 50 have finished their reel-out power stroke 140 a, the airfoil's pitch angle is made negative so they can be reeled-in by their control and support lines using a minimum of force along path 140 b. Once the airfoils have been rewound to the proper distance, the airfoils are again angled for a high-speed operation to generate powerful axial force and reeled-out along 140 c to provide another power stroke. The airfoil kites are then reeled-in again along path 140 d and the entire process repeats starting with power stroke 140 a. Since the force to rewind the airfoils is much less than the force generated during reel-out, there is net power generated.

ALWT represents a new approach for wind energy harvesting. Expensive components of the linear turbine remain on the ground and protected; only the airfoils are exposed, with all heavy components of the system placed on the ground. This allows buoyant airfoils to be used. Also, because of the very low canter of gravity for the system, it can easily be placed at sea with the addition of a few control systems to compensate for the added rocking motion of the platform due to waves.

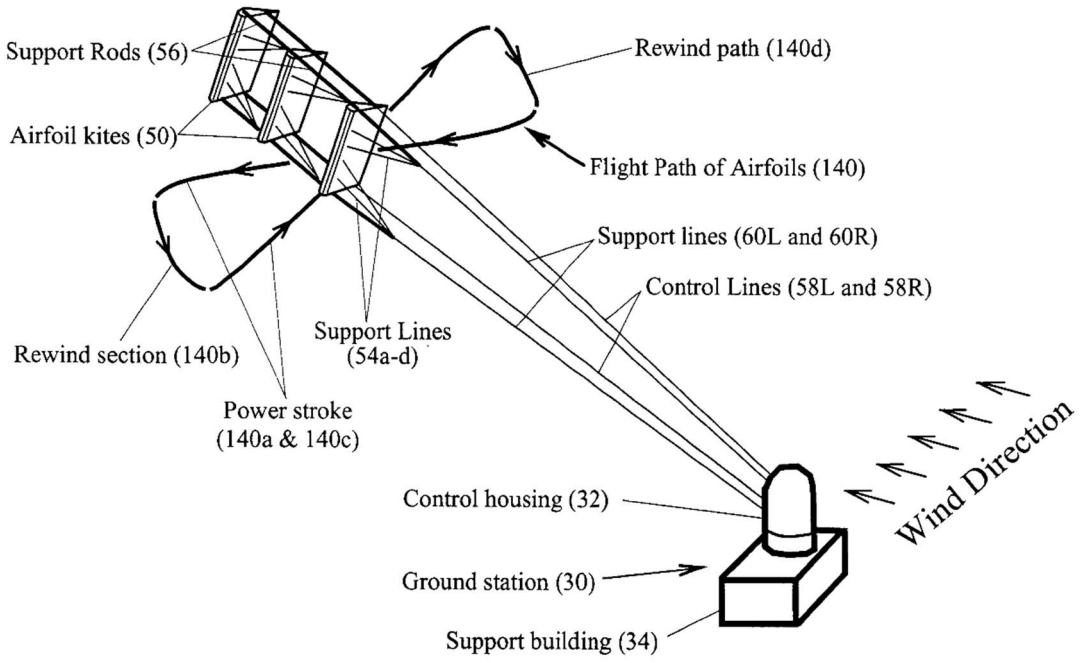

Figure 2-7: Sketch of ALWT.

2.1.2.2. Linear Cascade Wind Turbine (LCWT) – PowerWindow

LCWTs are a new generation of wind turbines with two series of blades in a linear cascade configuration which translationally move in opposite directions to each other but are both perpendicular to the incoming wind direction, as shown in 2.8. The power generation of LCWTs is due to the translational movement of the blades. However, LCWTs have two rotating parts at both

ends of the frame of which one, or both, of them is/are directly/indirectly connected to the electricity generator.

Variable-geometry oval-trajectory (VGOT) Darrieus turbine might be the first developed LCWT. Ponta et al. [57] studied the application of large scale Darrieus VAWTs and presented a new design which was a variable-geometry oval-trajectory (VGOT) Darrieus turbine. Figure 2.8 shows the blades move on rail tracks located in an elevated position, instead of rotating around a single rotor shaft. The blades are mounted on wheels which are coupled with electrical power generators. This design reportedly uses multi-directional power absorption capability of VAWT but operates with a high coefficient of performance (nearly 57% in the optimum design configurations) and resolve the low starting torque problems [58, 59].

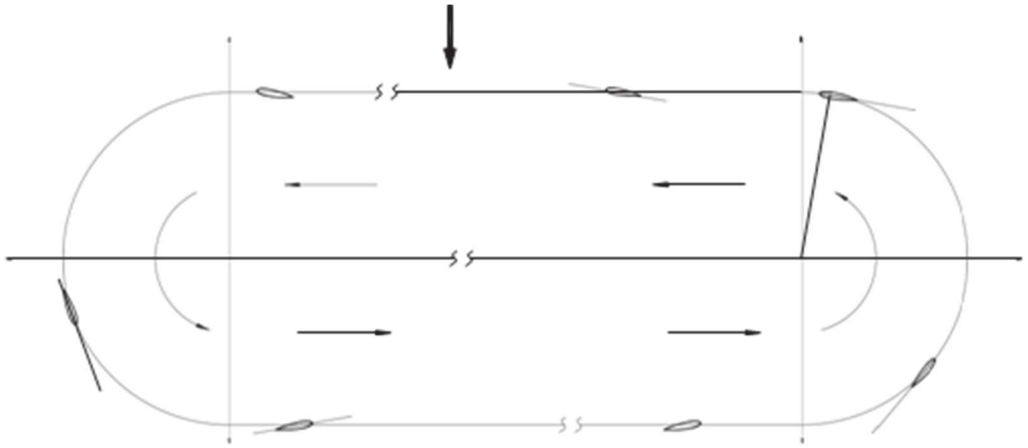

Figure 2-8: VGOT Darrieus turbine configuration [57].

As can be seen in Figure 2.9, the VGOT Darrieus blades are attached to a wagon which can follow a non-circular trajectory. Increasing the ratio of the transit perpendicular area to the total incoming wind area may result in increasing the wind energy conversion and optimising the efficiency of the entire plant. The VGOT Darrieus blades generate higher power output when tracking along the perpendicular line to the approach wind direction, but they consume power instead of generate power when tracking along the line parallel to the approach wind direction. The VGOT Darrieus configuration allows the swept area to be increased, by increasing the height of the trajectory line and/or widening the blades. On the other hand, the inflow direction remains constant along these straight tracks, which also results in the system's aerodynamic and structural stability, while in the traditional Darrieus VAWTs the blades are subjected to a variable inflow in both magnitude and direction over the blades.

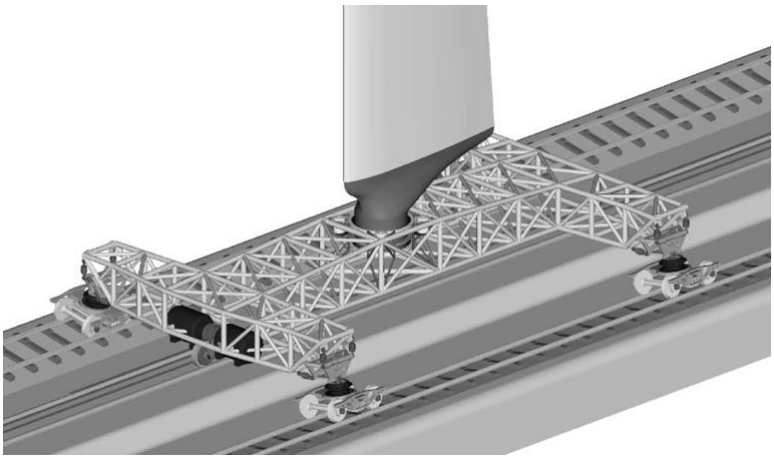

Figure 2-9: VGOT Darrieus blades are attached to a wagon following a non-circular trajectory [57].

PowerWindow is another design among the LCWTs which is capable of operating in relatively low wind velocities and hence, may particularly be suitable for urban environments [60]. Figure 2.10 (a) shows a sketch of the PowerWindow prototype. A PowerWindow module is composed of a light frame that could be mounted on a support tower or structural frame. A couple of rotating disks connected with a shaft are mounted at the top and bottom of the side frame, and the generator is attached to the bottom shaft. There are two chains running over these disks and several blades of appropriate profile are attached to the chain.

As the belt goes around, the blades 'flip over,' changing side and orientation to adjust their angle of attack as they move from one plane to another, as shown in Figure 2.10. The adjustment is done by observing that the force of gravity acts at the centre of mass, while the lift force acts at the centre of pressure which for most profiles is closer to the leading edge of the blade. In PowerWindow, the blade is attached to the belt at a point which is in front of the centre of mass but behind the centre of pressure in the upwind state. In the current prototype, the point of attachment is at approximately a third of the cord length [7]. The blade is free to rotate within a certain degree around the point of attachment and the angular rotation is constrained by a simple pin-and-groove mechanism, shown in Figure 2.10 (b), which in the current prototype limits the angles of attack to ±16°.

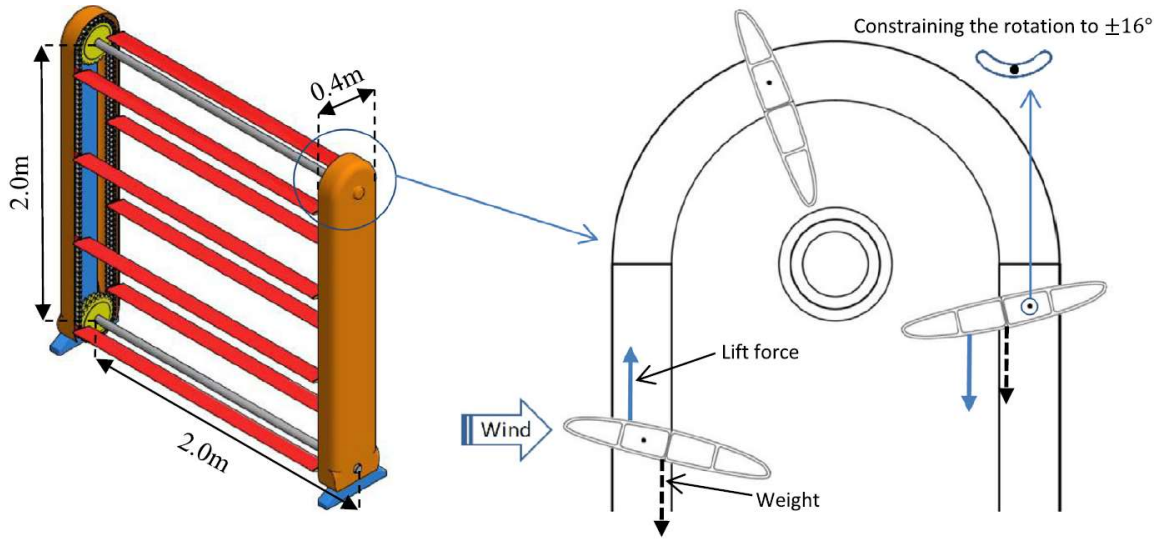

(a) (b)

Figure 2-10: (a) Sketch of the PowerWindow prototype, (b) blades changing their side and orientation at the top of PowerWindow [7].

The angle of attack is also automatically adjusted as the blade changes orientation at the top and bottom of the module. An active yaw system is needed for a PowerWindow. However, due to front-rear symmetry, the yaw motion to orient the PowerWindow towards the wind is only required to be within the 180° range. For large towers, it is envisaged that the yaw motion could also be applied to individual rows of modules, or a subset thereof, rather than the whole plant (see Figure 2.11).

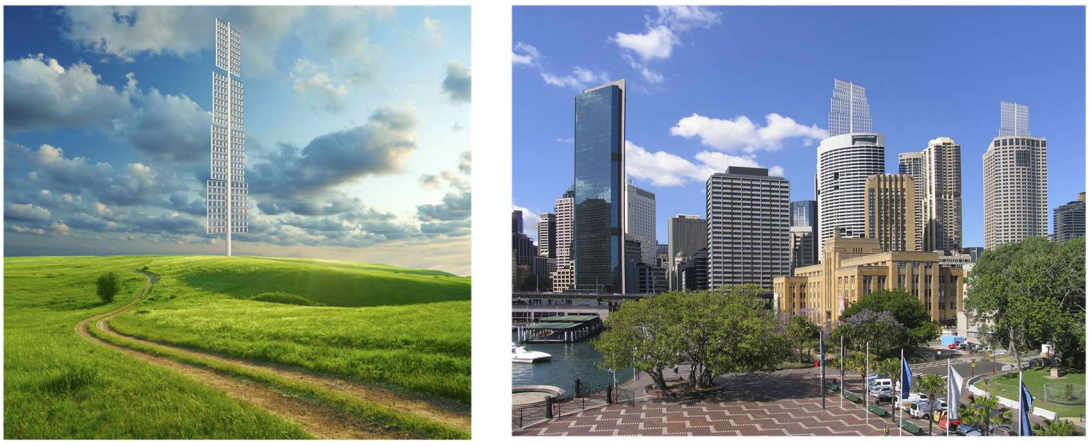

Figure 2-11: An artist's impression of installations of PowerWindow modules on a tower or on top of buildings [7].

2.2. Performance of the wind turbines

There are well-established limitations on the maximum efficiency of wind turbines. The most important limitation is the Betz's limit. Betz's law computes the maximum energy which can be captured from the wind energy in free stream, regardless of the wind turbine design. Betz's law

applies mass and momentum conservation principles of the flow stream passing through an ideal disk including the rotor, namely the "actuator disk" which extracts the maximum energy from the wind stream. Betz's law shows that no wind power generator can capture more than 59.3% of the wind kinetic energy [40].

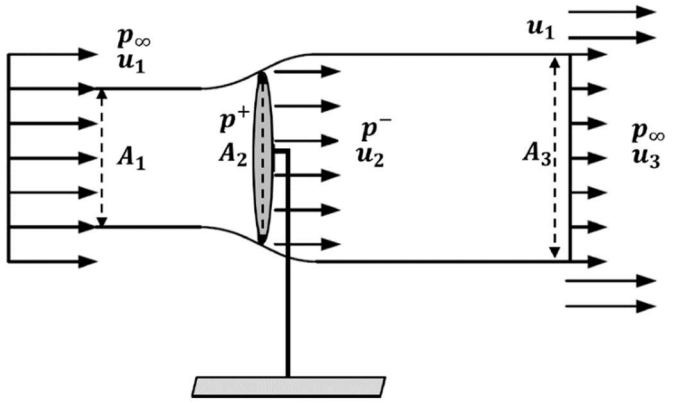

Figure 2-12: Stream-tube at the up-stream and down-stream of the actuator disc.

Considering an air stream-tube entering the actuator disc shown in Figure 2.12, the wind speed at the upstream of stream-tube equals tou_1 and its cross-sectional area equals to A_1. As the actuator disc captures greater kinetic energy from the wind, its exit velocity decelerates. By assuming air as an incompressible flow with low speed ($u \leq 0.3\,Ma$), the cross-sectional area of the stream-tube expands, instead of compressing the flow in the stream-tube, and this decelerates its velocity. The cross-sectional area of the stream-tube increases toA_2 in this section. The wind static pressure also drops from P^+ to P^- when passing the actuator disk. As a result, the downstream flow continues the expansion till the static pressure of the flow reaches atmospheric pressure, P_∞. This increases the cross-sectional area of the stream-tube far from the actuator disk from A_2 to A_3, where wind velocity is decelerated to u_3.

Assuming constant mass flow rate ṁ through the stream-tube, using continuity equation:

$$\dot{m} = \rho A_1 u_1 = \rho A_2 u_2 = \rho A_3 u_3 \tag{2-1}$$

Equation 2.6 gives the total wind power available in the wind flow when its speed is $u_1$and passing through the cross-sectional area A_2 at the actuator disk section.

$$P_{max} = \tfrac{1}{2}\dot{m}_2 {u_1}^2 = \tfrac{1}{2}(\rho A_2 u_2){u_1}^2 = \tfrac{1}{2}\rho A_2 {u_1}^3 \tag{2-2}$$

This is the maximum wind power available in the wind flow.

Equation 2.7 gives the power extracted by the wind turbine:

$$P_{ext} = \tfrac{1}{2}\dot{m}{u_1}^2 - \tfrac{1}{2}\dot{m}{u_3}^2 = \tfrac{1}{2}\rho A_2 u_2({u_1}^2 - {u_3}^2) \quad (2\text{-}3)$$

Also, using Bernoulli's equation, it can be written as:

$$\tfrac{1}{2}\rho {u_1}^2 + P_\infty = \tfrac{1}{2}\rho {u_2}^2 + P^+ \quad (2\text{-}4)$$

$$\tfrac{1}{2}\rho {u_2}^2 + P^- = \tfrac{1}{2}\rho {u_3}^2 + P_\infty \quad (2\text{-}5)$$

From equations 2.8 and 2.9, it can be derived that:

$$P^+ - P^- = \tfrac{1}{2}\rho {u_1}^2 - \tfrac{1}{2}\rho {u_3}^2 \quad (2\text{-}6)$$

The total axial thrust exerted by the turbine over the wind flow equals to the change rate in the momentum of the flow.

$$(P^+ - P^-)A_2 = \dot{m}(u_1 - u_3) \quad (2\text{-}7)$$

$$\text{Or } (P^+ - P^-)A_2 = \rho A_2 u_2(u_1 - u_3) \quad (2\text{-}8)$$

From equations 2.7 and 2.8:

$$\rho A_2 u_2(u_1 - u_3) = A_2(\tfrac{1}{2}\rho {u_1}^2 - \tfrac{1}{2}\rho {u_3}^2) \quad (2\text{-}9)$$

This implies $u_2 = \frac{1}{2}(u_1 + u_3)$

The coefficient of performance (C_P) of a wind turbine is defined as the ratio of the extracted power over the total available power, as shown in equation 2.14:

$$C_P = \frac{P_{ext}}{P_{max}} = \frac{\frac{1}{2}\rho A_2 u_2({u_1}^2 - {u_3}^2)}{\frac{1}{2}\rho A_2 {u_1}^3} \quad (2\text{-}10)$$

Therefore C_P can be written as shown in equation 2.15 and 2.16:

$$C_P = \frac{\frac{1}{4}\rho A_2(u_1+u_3)({u_1}^2 - {u_3}^2)}{\frac{1}{2}\rho A_2 {u_1}^3} \quad (2\text{-}11)$$

$$C_P = \frac{1}{2}(1 + \frac{u_3}{u_1})(1 - \frac{{u_3}^2}{{u_1}^2}) \quad (2\text{-}12)$$

If $y = \frac{u_3}{u_1}$

$$C_P = \frac{1}{2}(1 + y)(1 - y^2) \quad (2\text{-}13)$$

The maximum coefficient of performance occurs when $\frac{dC_P}{dy} = 0$, hence:

$$\frac{dC_P}{dy} = \frac{1}{2}(1+y)(1-3y) = 0 \qquad (2\text{-}14)$$

Since $y = \frac{u_3}{u_1} \neq -1, y = \frac{1}{3}$. This gives maximum value of coefficient of performance: $C_{P,max} = C_P\left(y = \frac{1}{3}\right) = \frac{16}{27}$.

In Practical, wind turbines operate below, or well below the Betz Limit. This suggests that for maximum power extraction, a wind turbine should be operated around its optimal wind tip ratio. Modern HAWT rotors consist of two or three thin blades and are designated as low solidity rotors. This implies a low fraction of the area swept by the rotors being solid. This configuration results in an optimum match to the frequency requirements of modern electricity generators and also minimises the size and weight of the gearbox or transmission required, as well as increases efficiency. The relationship between C_P and the tip speed ratio is shown for different types of wind turbines in Figure 2.13. It can be noticed that, as expected, the power coefficient reaches a maximum at different positions for different turbine designs.

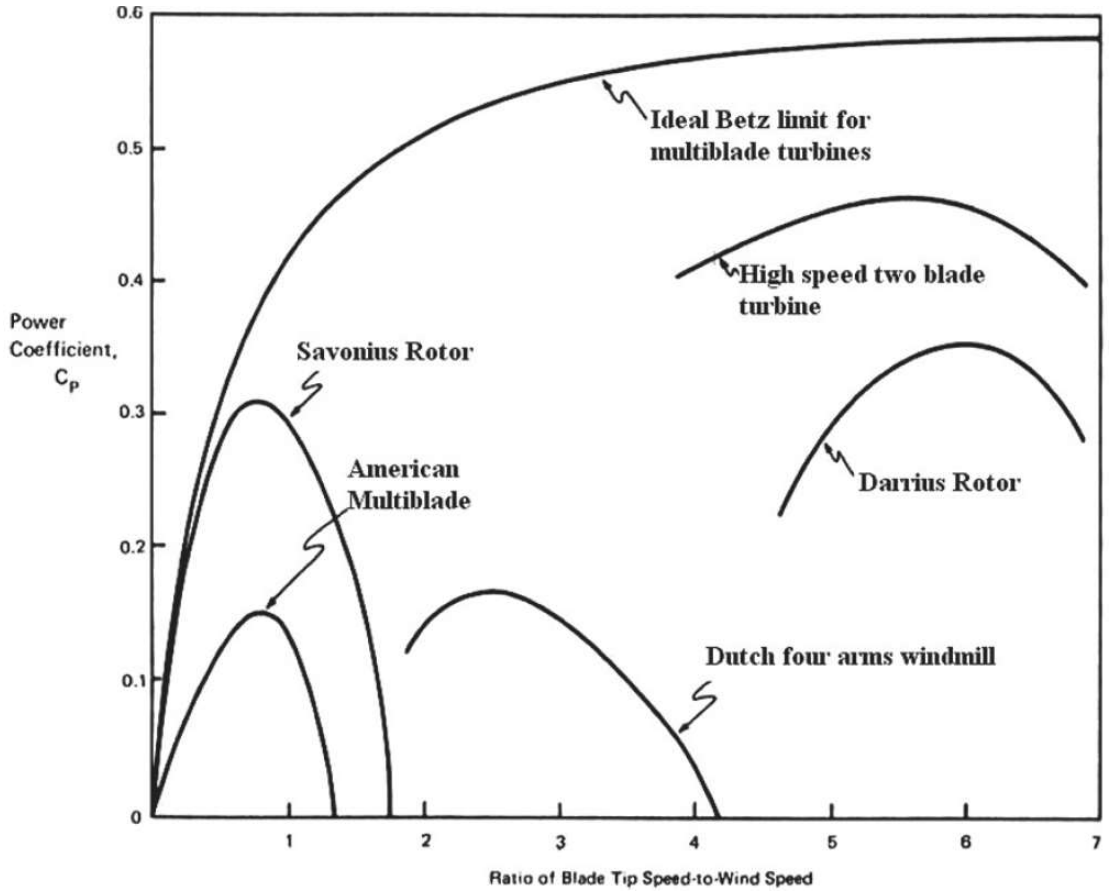

Figure 2-13: C_P as a function of the tip speed ratio for different wind turbines.

2.3. Urban application of wind turbines

Renewable energy generation in urban environments has received increased attention over recent years due to the advantage of exploitation proximity with the point of use. Interests in the design and development of small-scale wind turbines for integration with urban buildings has increased dramatically worldwide during the last few decades [61-63]. The focus has been on power generation from wind in urban built environments, and this idea is underpinned by the benefits of having power generated at the point of use. Despite this significant benefit, there are technological, economic and social hurdles which undermine wind turbine installations in urban built environments [64] including (i) lack of suitable area for medium to large size wind turbines; (ii) noise pollution generated mainly from medium to large-sized wind turbines operating in high wind velocity conditions; and (iii) relatively low power output and unreliable performance due to unfavorable urban wind conditions such as low wind energy content (low wind velocity), continuously variable wind directions, high turbulence level and strong gust occurrences.

Billinton and Guung [65] showed that the site wind condition (speed and direction) has a significant impact on the reliability and performance of a wind turbine. Therefore, new large wind turbines commonly use an active yaw mechanism to orient the wind turbine rotor to the wind direction. Minimising the yaw angle maximises the power output and minimises the non-symmetrical loads. However, the effect of yaw is less significant in high wind speeds compared to low-to-medium speeds, because the wind direction is generally less variable at high wind speeds compared to low-to-medium speeds [65]. The characteristics of urban wind and proposed exploitation have been researched and reported in the literature. The results generally show that urban winds have a strong multi-directional component that requires detailed analysis to assess wind turbine behaviour and performance [66].

Toja-Silva et al. [66] reported that horizontal-axis wind turbines perform better in flat-terrain applications, whereas in high-density building environments, the superiority of vertical-axis wind turbines is demonstrated. Dayan [3] showed that although the 'roughness' of the terrain in urban environments can mean a reduced and more turbulent wind flow compared to open spaces, urban wind speeds increase the further you are from the ground. Hence, mounting turbines at high points on top of buildings may provide an ideal opportunity for onsite wind power generation, as illustrated in Figures 2.15 (a) and (b). Walker [67] presented a review of literature regarding urban wind speeds for the installation of building-mounted wind turbines. It was reported that the wind resource “seen” by a building-mounted wind turbine is affected by positioning (height above roof ridge and position relative to the prevailing wind direction), high urban terrain roughness, and wind shadow caused by adjacent buildings, as shown in Figure 1.15 (b).

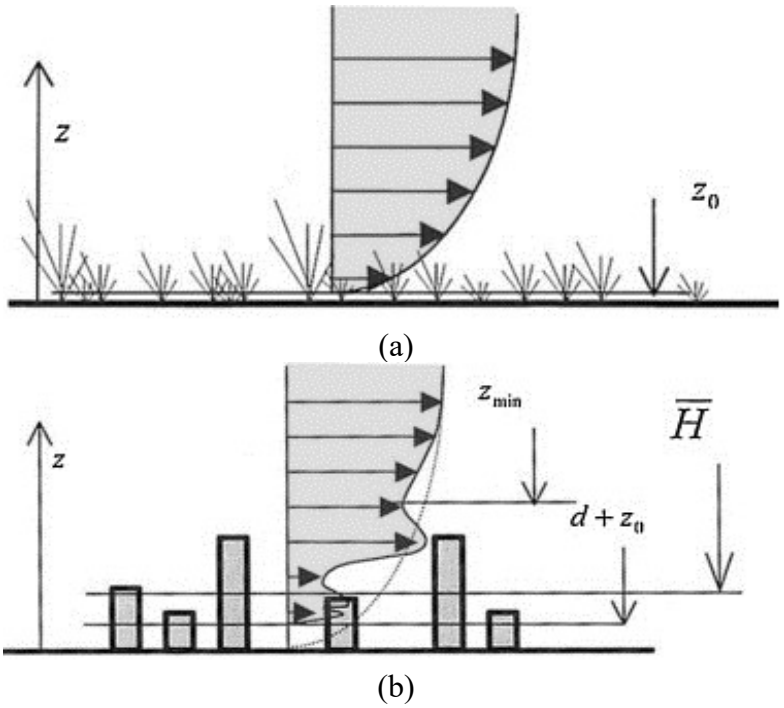

Figure 2-14: Diagrammatic approximations of wind velocity profiles in (a) open field and (b) urban settings [68].

Many investigations [47, 68] have been done on advances in integration of small wind turbines on urban buildings. Most of the research studies in this field have focused on roof-mounted wind turbines. Duffy [1] has investigated different mounting positions for small wind turbines on existing structures. Leto et al. [64] presented a numerical study of wind flow characteristics in three suburban landscapes characterised by houses with different roof profiles and showed wind flow characteristics are strongly dependent on the profile of the roofs. Figure 2.16 shows examples of roof-mounted HAWT and VAWT, and a HAWT installed in an urban highway. Grant et al. [69] reported that a roof-mounted ducted wind turbine, which uses pressure differentials created by wind flow around a building, is available as an alternative to more conventional approaches. The integration of wind turbine systems to the skin/facade of buildings is also a new concept. One approach suggested by Park, Jung [70] was to incorporate smalls scale wind turbines into an external ventilated façade. In this approach, guide vanes are able to effectively collect the incoming wind and increase wind speed to a sufficient level to be used by small scale wind turbines. The results showed that the proposed system could produce 24KWh, which is about 6.3% of the daily electricity usage of a target building.

(a) (b) (c)

Figure 2-15: (a) a rooftop HAWT [68], (b) a rooftop VAWT (windterra Eco 1200) [68], and (c) HAWT installed in urban highway [47].

Wang et al. [71, 72] investigated the aerodynamic design of a small urban wind turbine, which reportedly boosted wind speed and power output by a factor of 1.5 and 2.2, respectively, compared with the bare wind turbine of the same swept area. Their results also indicated that power captured improved, particularly at locations where the average wind speed was lower and wind was more turbulent. Grant et al. [69] considered the urban wind power potential and used a roof-mounted ducted wind turbine to utilise the pressure difference generated by wind flow around a building, and concluded that ducted turbines in the most promising applications could exceed the Betz limit. Therefore, a number of studies undertaken in this research project have investigated the application and power generation performance of PowerWindow when installed in a through-building opening, where a ducted space is embedded throughout a building.

CHAPTER 3. AERODYNAMIC ANALYSIS OF A LINEAR CASCADE WIND TURBINE

A reprint of this study entitled 'Aerodynamic Analysis of a Linear Cascade Wind Turbine', Jafari SAH, Kwok KCS, Safaei F, Kosasih B, Zhao M, published by the Journal of Wind Energy, 2018; 21 (11): 1141-1154 (https://doi.org/10.1002/we.2219) is appended in Appendix B1.

The work presented in this chapter is an extension of the research conducted and presented in MPhil thesis by Jafari SAH, 'Performance Analysis of PowerWindow: a Linear Wind Generator', 2014, University of Wollongong (UOW). Therefore, there are some overlaps between the original material presented in both studies which are presented in Appendix A. This chapter is identifying the most effective design parameters of PowerWindow and evaluating their influence on its power generation performance using an analytical model developed in the MPhil research [46]. It should be noted that the analytical model is developed based on the numerical model of the prototype published in 'Power generation analysis of PowerWindow, a linear wind generator, using computational fluid dynamic simulations', Jafari SAH, Safaei F, Kosasih B, Kwok KCS, the Journal of Wind Engineering and Industrial Aerodynamics, 2015; 147: 226–23 (https://doi.org/10.1016/j.jweia.2015.10.006).

3.1. Introduction

The general configuration and aerodynamic mechanism of PowerWindow are presented in Appendix A: **A.1. Introduction**. The Coefficient of Performance (C_P) is below 15%, which is still relatively low compared to horizontal and vertical axis wind turbines (HAWTs and VAWTs) [46]. Here, C_P refers to the ratio of the power captured by the generator to the entire wind energy passing through its swept area, as shown in Equation 3.1:

$$C_P = \frac{P_{captured}}{P_{wind}} = \frac{P_{captured}}{1/2(\rho A \ {V_{wind}}^3)} \tag{3-1}$$

where ρ is the air density, A is the wind turbine swept area and V_{wind} is the wind speed.

The aerodynamic performance of PowerWindow, when mounted on the ground (in *grounded* position), has previously been investigated [7]. This study investigates the aerodynamic performance of PowerWindow at some distance elevated from the ground (referred to as elevated PowerWindow thereafter). Understanding the effect of the design parameters of elevated PowerWindow on the flow characteristics and power generation mechanism is valuable because i) this configuration is the most common mounting configuration compared to grounded, wall-mounted or ducted configurations and ii) any improvement in the aerodynamic performance of the elevated installation can be applied to any other mounting configuration.

Time efficient and cost-effective approach for improving the aerodynamic design of any wind turbine is exploiting analytical models. Studies on wind turbines have proved that Blade Element Momentum (BEM) theory is an effective tool for developing analytical models for wind turbines [18, 21, 37-39, 74]. Analytical modelling, in combination with CFD simulations [29, 37, 38, 75, 76] and experimental verification [8, 77-79], is arguably the most efficient approach to evaluate the power generation of a wind turbine and identify aerodynamic design improvement.

This study reports the application of analytical BEM of the elevated PowerWindow to: (i) calculate the power generation and investigate the contribution of the front and the rear blades toward the power generation; (ii) investigate the flow characteristics such as axial induction factor (a_f) and angle of attack (α) of the front and rear blades; and (iii) identify the potential effect of some design parameters of PowerWindow which can enhance its power generation performance.

3.2. Modified blade element momentum model

The fundamental BEM theory for aerodynamic analysis is Glauert's airscrew theory [19], which was initially developed for propellers analysis, particularly within the helicopter industry [20]. The BEM theory has recently been used in the analysis of HAWT [22-25], and VAWT [26] using

tabulated airfoillift and drag data. This study has used an analytical model for PowerWindow based on the BEM theory.

BEM theory combines momentum theory and blade element theory. The theory assumes that: (i) the aerodynamic interactions between the blades are negligible and (ii) the resultant force on each blade is calculated only based on the lift and drag characteristics of 2D airfoil [25]. Based on the classical momentum theory, the maximum C_P of a wind turbine with a single ideal rotor with no energy loss cannot exceed 0.59, which is known as Betz limit. In practice, the peak value of C_P curve of conventional horizontal axis wind turbines with a single rotor ranges between 0.4 - 0.5 due to losses such as viscous loss, three-dimensional loss, and transmission loss [80]. In PowerWindow, because rotational movement of the blades does not exist, it is expected that: three-dimensional loss should be much weaker compared to VAWT and HAWT, and viscous loss may be more significant because of the cascade configuration of the blades. Hence, to consider the dominance of the viscous loss and other characteristic changes due to the cascade configuration of the PowerWindow, the BEM theory was modified by replacing the lift and drag coefficient (C_L and C_D) of the isolated blade being replaced with the C_L and C_D of the cascade configuration. C_L and C_D present the ratio of the lift and drag generated by a single blade to the dynamic pressure of the approach wind. The aerodynamic of the cascade and the BEM model developed for PowerWindow based on the C_L and C_D of the cascade are presented in Appendix A: **A.2.1. Aerodynamics of cascade** and **A.2.2. Application of the modified BEM model for PowerWindow** [46].

3.3. Computational fluid dynamic model

A two-dimensional (2D) CFD model of the elevated PwerWindow has been developed by Jafari (2014) [46] for verification of the analytical (modified BEM). The turbulence model, mesh and boundary conditions selected/generated are presented in Appendix A3: **A.3.1. Turbulence model** and **A.3.2. Mesh and boundary conditions**. It has been shown that three-dimensional (3D) CFD simulations are quite realistic, but are also computationally expensive [9]. Because PowerWindow does not have a complex 3D geometry, CFD simulations in Jafari (2014) have been conducted based on 2D modeling. However, the three-dimensionality due to the end effects still exists, and both the BEM and 2D CFD models will be re-evaluated with 3D CFD simulations later in Chapter 4.

3.4. Results and discussion

3.4.1. Sensitivity analysis of the coefficient of performance to blade design angle

The blades of conventional (HAWT and VAWT) wind turbines are directly attached to rotors. PowerWindow blades are attached to two chains that allow them to deviate from the fixed θ_0 slightly.

Consequently, the aerodynamic performance of PowerWindow is dependent on the deviation of θ_0. Therefore, the sensitivity of C_P to θ_0 was investigated using the BEM model and validated by the CFD simulations and presented in Appendix **A.4.**

3.4.2. Effect of blade design angle on the coefficient of performance

The results in the previous section indicate that the aerodynamic performance of PowerWindow is also a function of θ_0. Therefore, the modified BEM model is used to calculate a_f (induction factor) and C_P for different θ_0. Figure 3.1 and 3.2 show a_f and C_P against λ when $\theta_0 = 6°,12°,18°$ and $24°$ at $\sigma = 0.428$. While the focus of in this part of study is the effect of θ_0, a constant $\varepsilon = 0.5$ has been considered for all models. Further investigation is needed to identify the accurate ε.

Figure 3.1 and 3.2 show that θ_0 has a significant effect on a_f and consequently C_P as expected from the sensitivity analysis. Figure 3.1 shows a_f increases with λ to an optimum point where further increasing λ results in a decrease in a_f. The reason is that α decreases with the decrease of λ (see Equation (A 19) and (A 29)). The C_P is a function of a_f and increasing a_f up to $1/3$ results in increase of C_P. a_f and α are mutually dependent (Equation A 19 and A 29 as a result, C_P is also dependent on α and in any configuration the maximum C_P is achievable in an optimum α. α is a function of θ_0 and λ itself. Increasing θ_0 has shifted the optimum λ (the operation point) to higher values to keep the optimum α. The overall effect is increasing a_f and C_P (Equations A 19, A 20, A 24 and A 25). As the results show, increasing θ_0 of prototype by $8°$ (from $16°$ to $24°$) has increased C_P by almost 100% (from 0.075 to 0.15).

There should be a limit on increasing θ_0 which is reasonably dependent on the velocity of the approach wind. The stall is strongly possible for a low λ where $24° < \theta_0$. However, as shown in Figure 3.2, increasing σ may result in postponing stall condition at higher θ_0. On the other hand, the axial load exerted on PowerWindow will also increase by increasing θ_0 and σ, which is not desirable, and an optimum configuration will be further investigated in Chapter 6.

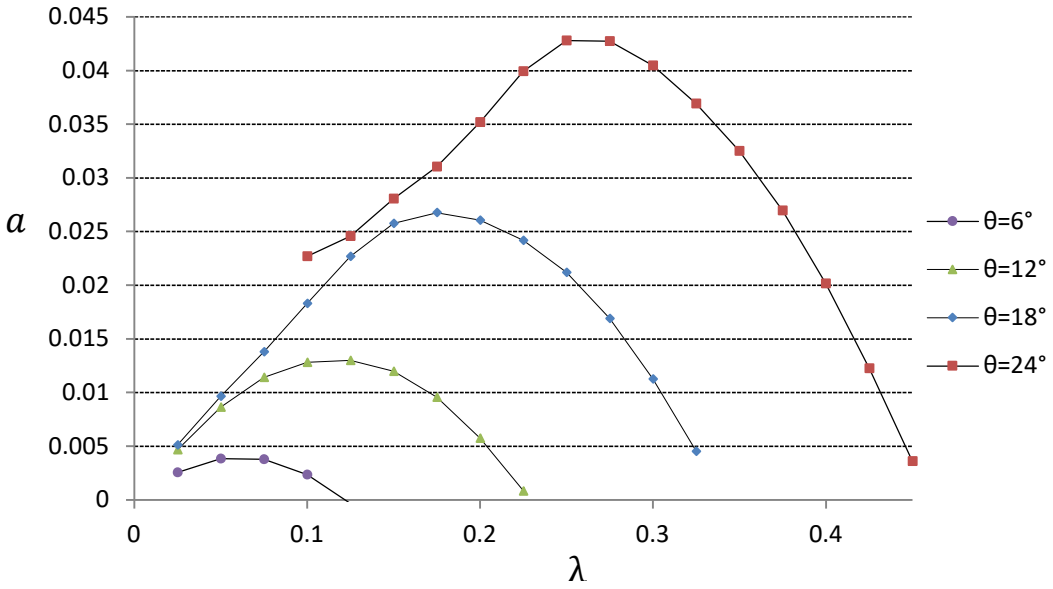

Figure 3-1: a_f of the elevated PowerWindow against λ at $\theta_0 = 6°,12°,18°$ and 24°when$\sigma = 0.428$ and assuming $\varepsilon = 0.5$.

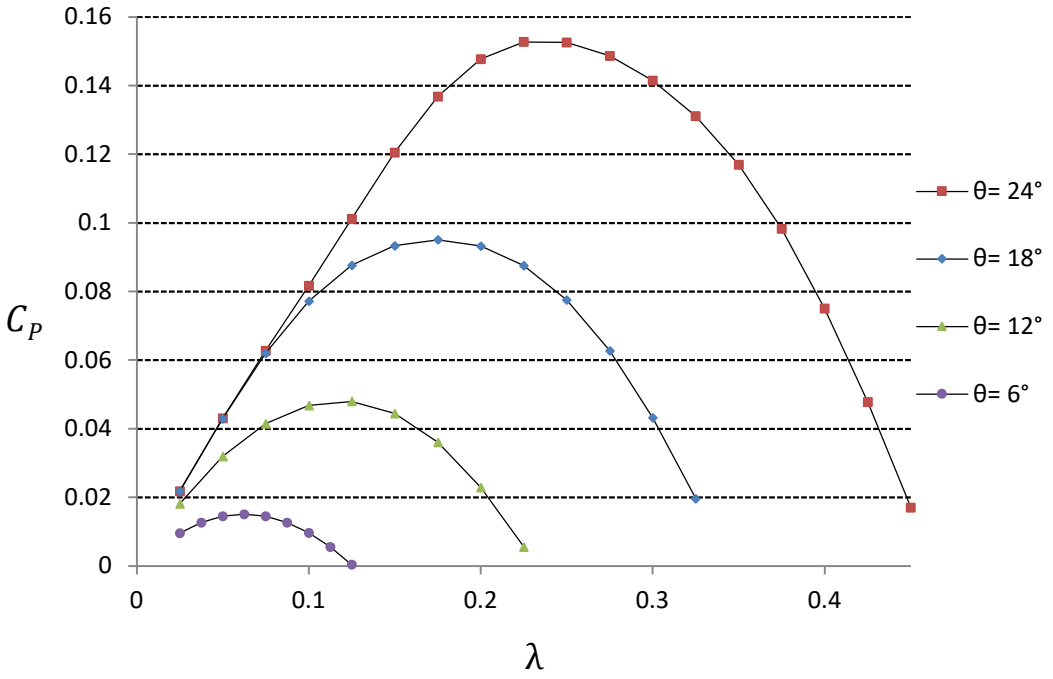

Figure 3-2: C_P of the elevated PowerWindow against λ at $\theta_0 = 6°,12°,18°$ and 24° when$\sigma = 0.428$ and assuming $\varepsilon = 0.5$.

3.4.3. Effect of solidity on coefficient of performance

Another parameter of PowerWindow, σ is also investigated in this study. An investigation has been conducted using the modified BEM model to estimate C_P of the elevated PowerWindow at high σ

values. The C_L and C_D of the linear cascade configurations at two high σ values are calculated using CFD simulations. Figure 3.3 compares C_P of the elevated PowerWindow versus λ for $\theta_0 = 16°$ and $\sigma = 0.428$ (based on the prototype configuration), 0.857 and 1.714. As observed in Figure 3.3, with the configuration of $\sigma = 0.428$, the front blades can significantly redirect the flow. Therefore, at this stage a reasonable range has been considered for ε in the BEM model: $0.5 < \varepsilon < 1.0$, and the analytical results have been undertaken for both values so that the accurate answer would ideally be between these two results.

The optimum λ is expected to become lower by increasing σ [48, 87], while Figure 3.3 does not show any particular change in optimum λ by increasing σ. The reason is that with the current configuration the optimum λ is primarily limited by θ_0 rather than σ.

Figure 3.3 also shows that increasing σ from 0.428 to 0.857 has greatly enhanced C_P, but the enhancement is very negligible when σ increases from 0.857 to 1.714. The reason can be investigated in Figure A 3 (a). It is shown that at higher σ, for the same α, C_L is lower, resulting in reduction of the vertical force exerted on each blade. However, increasing σ also results in increasing the projection area and eventually the total force exerted on all the blades. Hence, there would always be an optimum σ for each θ_0 where the maximum C_P would be achieved.

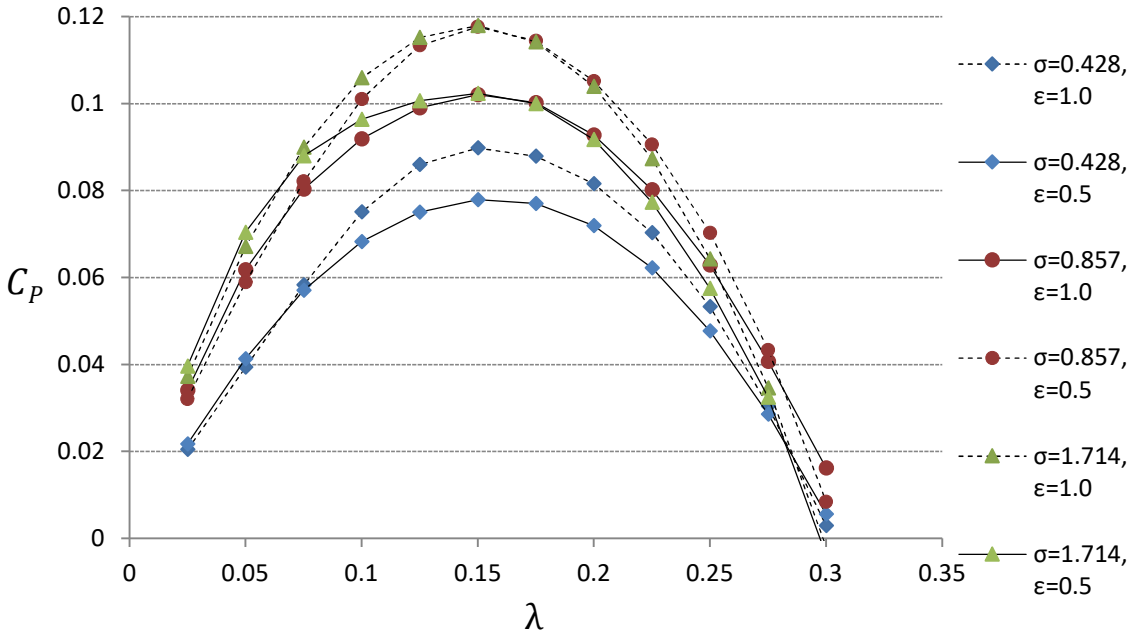

Figure 3-3: C_P of the elevatedPowerWindow against λ when $\theta_0 = 16°$ (and $\varepsilon = 0.5$) when $\sigma = 0.428$ (and $\varepsilon = 0.75$), 0.857 and 1.714 (and $\varepsilon = 1.0$).

3.4. Conclusion

A modified BEM model was used to predict the coefficient of performance (C_P). Investigations on the aerodynamic mechanism of the elevated PowerWindow show that the front blades increase the angle of attack (α) on the rear blades and consequently the total power generation is increased. The effects of the Solidity (σ) and blade design angle (θ_0) on the performance of the elevated PowerWindow were also investigated. It was found that increasing θ_0 enhances the power generation. $C_P$was increased from 0.075 to 0.15 by increasing θ_0 from 16° to 24°. However, increasing θ_0 beyond an optimum point causes stall that results in a degradation of C_P. Similarly, increasing σ from 0.428 to 0.857 enhances C_P from 0.08 to 0.12. Moreover, it was shown that increasing σ postpones stall condition and allowing θ_0 to be increased to above 24° to achieve a more power generation. The BEM model has shown the aerodynamic performance of PowerWindow can be significantly improved by optimizing σ and θ_0.

CHAPTER 4. THE EFFECT OF INSTALLATION CONFIGURATION AND SOLIDITY ON POWER GENERATION OF A LINEAR CASCADE WIND TURBINE

A reprint of this study entitles 'The effects of installation configuration and solidity on the power generation of a linear cascade wind turbine', Jafari SAH, Kwok KCS, Safaei F, Kosasih B, Zhao M, published by the Journal of Wind Engineering and Industrial Aerodynamics, 2018; 180: 122-135 (https://doi.org/10.1016/j.jweia.2018.07.015) is appended in Appendix B2.

4.1. Introduction

Due to the growing public awareness of the rising level of greenhouse gas emissions, significant efforts have been made to develop renewable energy technologies that can be applied in suburban and urban environments worldwide during the past decades. Building-integrated wind turbines are potential low-cost renewable energy devices that could be adopted in suburban and urban environments [64]. Small scale wind turbines integrated with urban buildings have attracted increasing interest because of their advantage of being installed and generate power at the point of use [61, 62]. Therefore, it is expected that more and more buildings with integrated wind turbines will be constructed in the future, driven by the concept of sustainability [88]. Efforts have also been made to overcome the hurdles that restrain the installation of wind turbines in urban built environments such as: (i) lack of suitable space for medium-large size wind turbines; (ii) noise pollution in high wind velocity conditions; and (iii) relatively low power output and unreliable performance due to unfavorable urban wind conditions including low wind velocity, continuously changing wind directions and high turbulence level [54, 61, 89].

PowerWindow, as a Linear Cascade Wind Turbine (LCWT) is capable of generating electricity at very low blade speed ratios (λ) [7]. Operating at low λ is an advantage for both remote and grid-tied turbines and controlling the blade speed is necessary for two reasons. First, it is desirable that blade speed remain proportional to the wind velocity (U) over a large range of U to maintain maximum power generation at the optimal λ. The process to achieve the optimal λ is called Maximum Power Point Tracking (MPPT) [90]. The second reason of controlling blade speed is the safety at high wind speeds. In the event that the controller loses power, the turbine must be protected aerodynamically and/or mechanically [91]. Furthermore, PowerWindow is designed to operate efficiently even at very low λ, making it a safe option in urban environments.

PowerWindow is modular design and can easily fit into any designated area in a building. A PowerWindow module (Shown in Figure 4.1) is composed of a light frame that could be mounted on the support tower or structural frame. A couple of rotating disks connected together with a shaft are mounted at the top and bottom of one side of the frame. The generator is connected to the bottom shaft. Two chains are running over the two disks and blades of appropriate aerofoil profile are attached to the chain. If the wind blows in the horizontal direction in Figure 4.1, the blades that facing the wind are referred to as ‘front’ blades and the ones behind are referred to as ‘rear’ blades. Unlike those of conventional wind turbines, horizontal axis wind turbine (HAWT) or vertical axis wind turbine (VAWT), the front and rear blades of the LCWT move in opposite directions that are perpendicular to the approach wind velocity, instead of around rotor axis. Since the LCWT does not

create a trailing swirl as the conventional wind turbines do, it allows another unit behind it to operate efficiently.

Investigations have proved that the installation of small wind turbines on urban buildings has great potential to generate energy efficiently [3]. In addition to simplicity in construction and low cost of materials, which have been a major driving factor in the decision-making process, wind characteristics must be considered in order to achieve maximum and energy efficiency. Wind characteristics in urban environment and in close proximity of common types of wind turbines currently being used in urban environment have been investigated in some studies. VAWTs have been preferred for small scale power production in urban environment as they possess the required design factors and overcome the disadvantages of urban wind flows, including low and turbulent wind speed, constraints of installation space, strict vibration and noise limitation, among others [47].

Studies have shown that the performance of urban wind turbines strongly depends on the installation location. For example, HAWT has better performance in flat-terrain applications, whereas, in high-density building environments, VAWT is superior [66]. An investigation on the power production of two small-size commercial wind turbines: a HAWT and a VAWT, with same rated power installed in the same area has shown that the overall energy production of the HAWT is higher than that of the VAWT [92]. But, the effects of gusts wind speed and direction fluctuations on HAWT is stronger than VAWT, and VAWT was also proved to be operational at high wind velocities [92]. Although the roughness of the terrain in urban environments can reduce the velocity and increase the turbulence of the flow compared to open spaces, it is reported that mounting turbines at high elevations on buildings may provide a perfect opportunity for onsite wind power harvesting [3]. By investigating the wind flow over the buildings based on local meteorological data and local building characteristics, it is reported that the amplification of wind speed between a group of buildings and at the top part of buildings can the wind power density by 3–8 times [68]. The investigations of the possibility of using double skin façade for wind energy harvesting purposes showed that the free-stream wind speed and wind power density can be amplified up to a maximum of 1.8 and 4.2 times, respectively, inside the corridors of the double skin façade [93-95].

Due to the limitation of the grounded installation of PowerWindow in urban areas, this study investigates two alternative installation configurations: *elevated* and *ducted* configurations for PowerWindow. In the elevated configuration, PowerWindow installed on top of a tall building is referred to as on top of building-mounted and PowerWindow between two tall buildings is referred to as between two building-mounted position [68]. In the ducted configuration the PowerWindow installed inside a ducted area such as a through-building opening is referred to as building-integrated position [2]. Based on the inlet and outlet design of the duct and the approaching wind direction, the ducted flow may have a higher speed than the free stream at the same elevation.

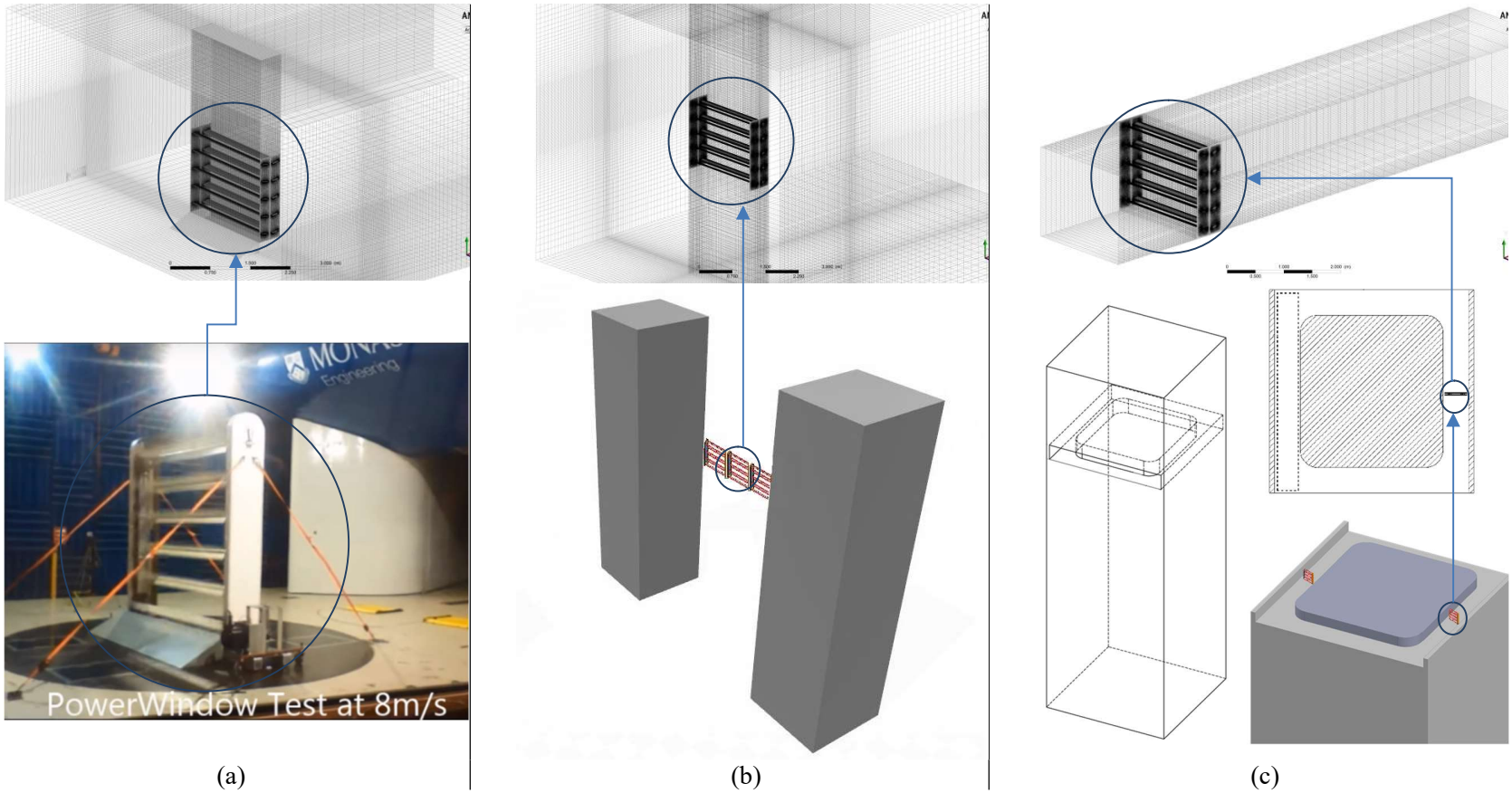

(a) (b) (c)

Figure 4-1: PowerWindow installed in the (a) grounded (in wind tunnel), (b) elevated (between two buildings) and (c) ducted (in a through-building opening) configurations.

Figure 4.1 (a-c) show PowerWindow installed in the (a) grounded (in wind tunnel), (b) elevated (between two buildings), and (c) ducted (in a through-building opening) configurations. The first scope of this study is to estimate the power generation performance of the proposed configurations and compare them with each other.

The power generation performance of any wind turbine is dependent on different design parameters. Airfoil shape, solidity, pitch angle, and rotating speed are the most important parameters which have been investigated in recent studies. Mohamed et al. [50] investigated the optimal blade shape of a modified Savonius turbine and obtained an about 40% increase in the power output coefficient. Lee e al. [80] investigated the effects of pitch angle and rotating speed on the aerodynamic performance of a counter-rotating wind turbine. Mohamed [48] investigated the performance of a H-rotor Darrieus turbine with new airfoil shapes and obtained an about 27% increase in the power output coefficient. In another study, Mohamed [87] investigated the effects of solidity on a small H-rotor Darrieus turbines and reported that optimizing solidity can significantly improve the performance of the wind turbine. He also reported that the rotating speed of the turbine under the operating condition strongly depends on solidity.

Among the mentioned design parameters, solidity influences the required pressure gradient (ΔP) across a wind turbine the most. In PowerWindow, solidity, σ, presents the ratio of the total area of the blades projected to the approaching wind direction to the total area of the wind turbine that the wind passes through:

$$\sigma = NB/A \tag{4-1}$$

where N, B and A represents the number of the blades, projected area of the blades and the projected area of PowerWindow, respectively.

High σ demands high ΔP across the wind turbine, which may or may not be realistically available in some installation configurations. Studies have also shown increasing σ results in decrease of the operating speed ratio (λ) of the turbine [48, 87]. λ, known as blade speed ratio in the LCWTs, is the ratio of the blade's speed to the approach wind velocity:

$$\lambda = \frac{V_{blade}}{U_{wind}} \tag{4-2}$$

Another investigation on the effect of the blade pitch angle (θ_b) on the power generation performance of PowerWindow showed that the angle of attack (α) of the wind is strongly dependent on λ [96]. The second scope of this study is to investigate the effect of σ on the power generation performance of PowerWindow in both the elevated and ducted installation configurations.

4.2. Model geometry and CFD setup

4.2.1. Experimental setup

Figure 4.2 (a) shows the PowerWindow prototype mounted directly on the floor in Monash University wind tunnel with a $12\text{m(Length)} \times 9\text{m(Width)} \times 5\text{m(Height)}$ test section. Figure 4.2 (b) shows the dimensions of the prototype ($2\text{m} \times 2\text{m} \times 0.4\text{m}$). The prototype has 12 blades (resulting in $\sigma = 0.428$), and each blade has a 2m span length, 150 mm cord length, and 23 mm thickness (Figure 4.3). The reason for using a mid-cord symmetrical blade is to enable power to be generated by both the front and rear blades. A standard airfoil could result in a strong aerodynamic vertical force when the blades were located at the front but, this would locate the trailing edge of the blades toward the wind at the rear side and dramatically decrease the aerodynamic vertical force on them. θ_b was set to $16°$ in the experimental test. In the experimental test on the prototype, the inlet wind velocity was set to $8\ \text{m/s}$ with a turbulence intensity of 5%, which results in a Reynolds number of 7.1×10^4, based the length of the cord. A torque sensor was attached to the lower shaft to measure the power output. Variable electrical load and associated power electronics were also developed to measure the electrical power output produced by the generator (after accounting for the losses in the gearbox and generator). Unfortunately, the torque sensor showed some instability in its readings during the test. Therefore, only the electrical power output has been considered. The records showed a maximum electrical power output of 140 W from the prototype's generator. The detailed wind tunnel setup has been further explained in [7].

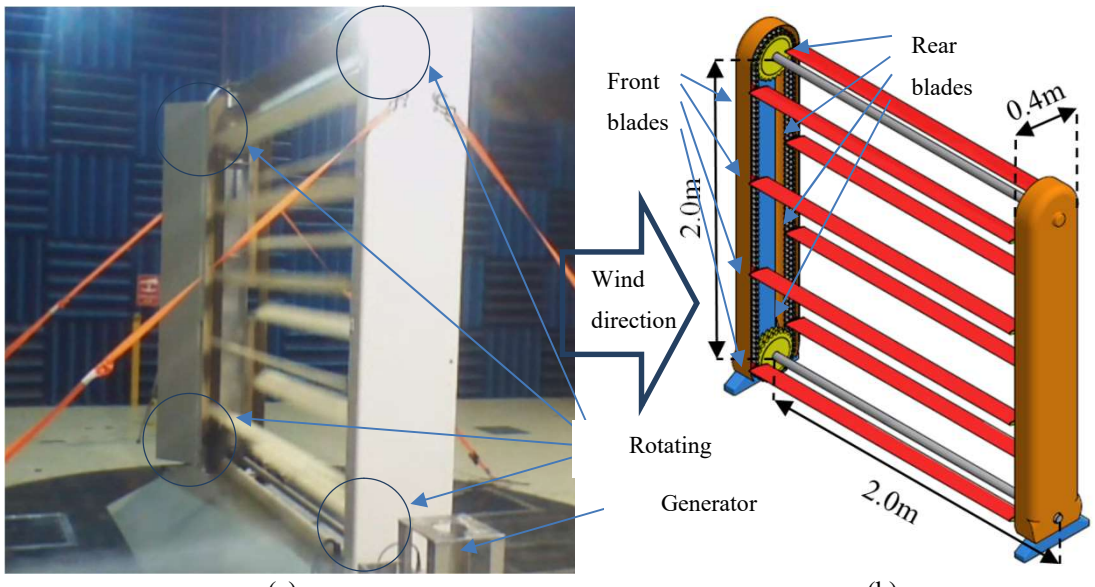

Figure 4-2: (a) PowerWindow prototype in the wind tunnel (grounded position), (b) Sketch of the PowerWindow prototype showing its dimensions

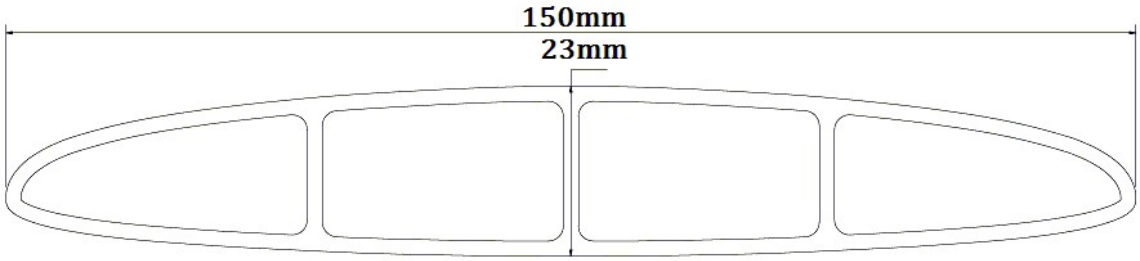

Figure 4-3: Cross section view of PowerWindow blade showing cord C and thickness T.

4.2.2. Numerical setup

4.2.2.1. Transition – turbulence model

In CFD simulations based the Reynolds-averaged Navier–Stokes (RANS), selecting an appropriate turbulence model is important to ensure the accuracy of flow separation prediction on every wind turbine blade. The shear stress transport (SST) k-ω models have been validated extensively for simulating 2D flow separation [83]. Menter [85] reported that flow over the rotor blades can be subject to a significant region of laminar-turbulence transition, which can affect the separation behavior of the boundary layer on the blade surface. Therefore, transition SST 4 eqn $k-\omega$ maybe a more suitable model to be used in case of separation. Based on flow over a flat plate [97], Reynold number of 7.1×10^4 in the wind tunnel test is within the laminar-turbulent transition region. However, transition SST 4 eqn model needs more (almost twice) calculation time than SST 2 eqn model so, the accuracy level of these two models is investigated and compared.

The numerical results indicated that SST 2 eqn model predicts the vertical aerodynamic force on PowerWindow blades 3-5% higher than SST eqn model. Figure 4.4 (a) and (b) show velocity vectors and turbulent kinetic energy (TKE) contours around the middle blades of PowerWindow simulated by SST 2 eqn and SST 4 eqn model, respectively. The separation region is indicated within a blue circle near the trailing edge of the front and rear blades. The comparison shows that both models have predicted very similar locations for flow separation over the front and rear blades while, SST 4 eqn model has predicted higher TKE levels around the blades and separation region compared to SST 2 eqn model. As the TKE level is higher, energy loss is greater, and power generation is lower. For more accuracy and minimizing the error in critical circumstances, this study uses SST 4eq $k-\omega$ model in ANSYS-Fluent 16.1 for the simulations.

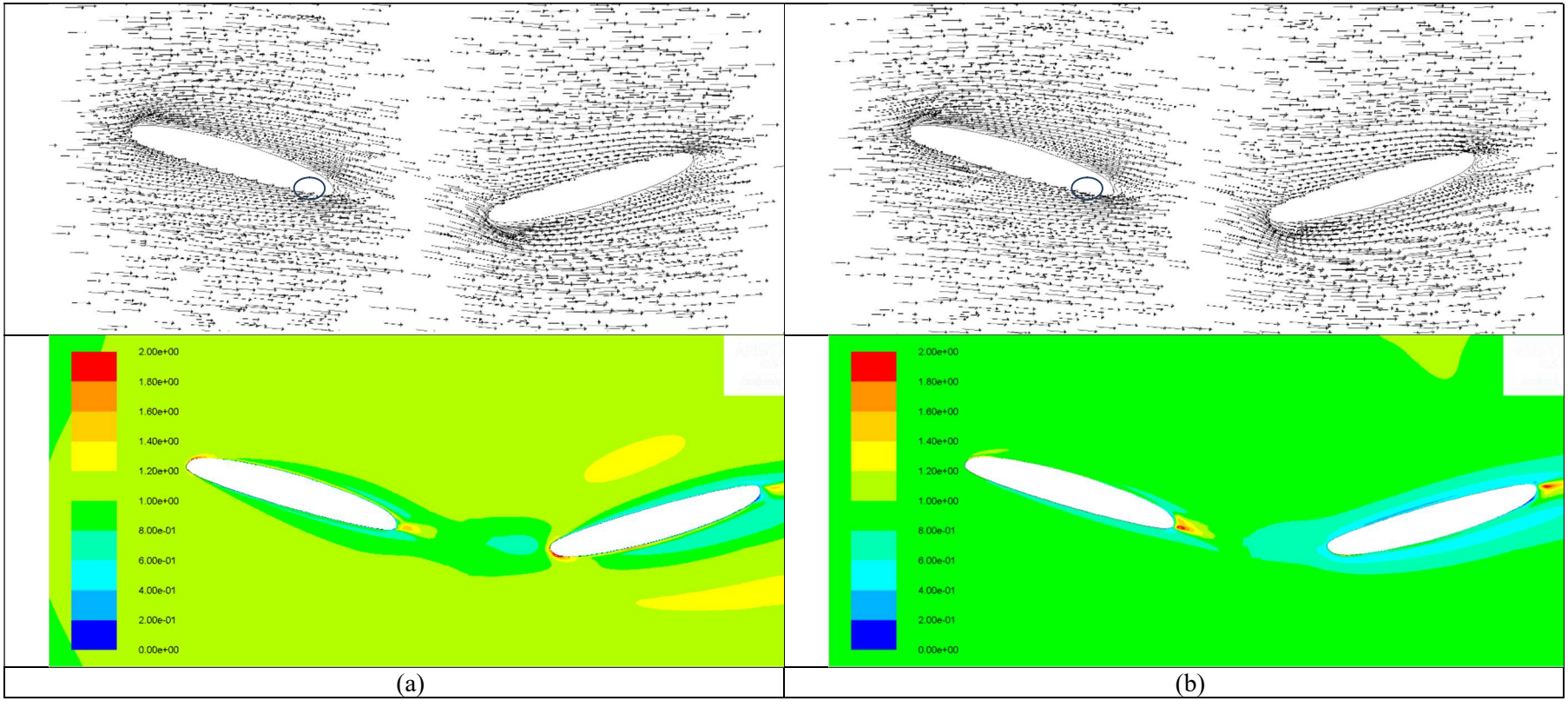

Figure 4-4: Velocity vectors and TKE ($^{m^2}/_{s^2}$) contours around PowerWindow blades by (a) SST 2 eqn and (b) SST 4 eqn model.

SST 4 eqn model is a modified SST k − ω RANS turbulence model by the addition of two other transport equations for γ (the intermittency) and the transition onset criteria. The transport equation for γ is defined as

$$\frac{\partial(\rho\gamma)}{\partial t}+\frac{\partial(\rho U_j\gamma)}{\partial x_j}=P_{\gamma 1}-E_{\gamma 1}+P_{\gamma 2}-E_{\gamma 2}+\frac{\partial}{\partial x_j}\left[\left(\mu+\frac{\mu_t}{\sigma_y}\right)\frac{\partial\gamma}{\partial x_j}\right] \tag{4-3}$$

where x is length (m), t is time (s), ρ is air density (kg m^{-3}), U is velocity of air (m s^{-1}), P is pressure (Pa) and μ is molecular viscosity (Pa·s) and the second transport equation for the transport of the transition momentum thickness Reynolds number, $\widetilde{\mathrm{Re}}_{\theta e}$ (local transition onset momentum thickness Reynolds number) is

$$\frac{\partial(\rho\widetilde{\mathrm{Re}}_{\theta t})}{\partial t}+\frac{\partial(\rho U_j\widetilde{\mathrm{Re}}_{\theta t})}{\partial x_j}=P_{\theta t}+\frac{\partial}{\partial x_j}\left[\sigma_{\theta t}(\mu+\mu_t)\frac{\partial\widetilde{\mathrm{Re}}_{\theta t}}{\partial x_j}\right] \tag{4-4}$$

These equations are coupled with the SST turbulence model

$$\frac{\partial}{\partial t}(\rho k)+\frac{\partial}{\partial x_j}(\rho u_j k)=\widetilde{P}_k-\widetilde{D}_k+\frac{\partial}{\partial x_j}\left[(\mu+\sigma_k\mu_t)\frac{\partial k}{\partial x_j}\right] \tag{4-5}$$

$$\frac{\partial}{\partial t}(\rho\omega)+\frac{\partial}{\partial x_j}(\rho u_j\omega)=\alpha\frac{P_k}{\nu_t}-D_\omega+C\,d_\omega+\frac{\partial}{\partial x_j}\left[(\mu+\sigma_k\mu_t)\frac{\partial\omega}{\partial x_j}\right] \tag{4-6}$$

$$P_k=\gamma_{eff}\,P_k \tag{4-7}$$

$$\widetilde{D}_k=\min[\max(\gamma_{eff},0.1),1.0]\,D_k \tag{4-8}$$

P_k and D_k are the turbulent kinetic energy (TKE) production and destruction terms in the original SST turbulence model and γ_{eff} is the effective intermittency calculated by the additional two equations. Menter [85] expressed that this approach has two main advantages. The first is that it improves the robustness of the model because the intermittency does not enter directly into the momentum equations. The second advantage is that it allows the model to predict the effects of high freestream turbulence levels on buffeted laminar boundary layers. The reason is that for large free stream eddy viscosities, the small values of intermittency in the boundary layer do not cancel out the local eddy viscosity.

4.2.2.2. Mesh and boundary conditions

In CFD simulations, high mesh quality is primarily achievable by using a fine structured mesh. But, a fully structured mesh usually needs numerous elements which are computationally expensive. In order to achieve a balance between solution accuracy and calculation time, a combination of

structured and unstructured mesh is used in this study. This technique reduces the number of elements while having a high-quality mesh around the body [13]. Therefore, as previously investigated in the mesh independence study on the CFD model the PowerWindow prototype [98], 200 structured rectangular elements (1.5mm length of each cell along the cord-wise) with y^+ below 2.0 are generated adjacent to the blade surface while this structured region is connected to the surrounding structured region via unstructured triangular elements with maximum skewness of 0.17, as shown in Figure 4.5 (b). The structured coarser mesh is generated around the hybrid region in both the ducted and elevated model, as shown in Figure 4.5 (a). The 3D model contains 3,698,740 elements in the wind tunnel model, 3,103,560 elements in the ducted model and 4,078,320 elements in the elevated model. In the elevated model, assuming the PowerWindow frame as a solid blocking area (with 100% porosity which is overestimated) would result in 11% blockage effect. In the both models, distance of the device from inlet and outlet are 2m and 8m respectively.

The frame of the hybrid region containing the front and rear blades is selected as multiple reference frame (MRF) which can move vertically within the domain. The reason for selecting the MRF model was that unlike the rotating geometries, in PowerWindow, the frame containing the blades will not remain inside the domain by time transition. Therefore, MRF as a steady-state model that is capable of solving moving reference frame equations has been used in the study. In MRF, flow in each moving cell zone is solved using the moving reference frame equations. If the zone is stationary, the stationary equations are used. At the interfaces between cell zones, a local reference frame transformation is performed to enable flow variables in one zone to be used to calculate fluxes at the boundary of the adjacent zone.

Moving mesh has not been used in this study, as it needs periodic boundary condition that would change the continuity equations around the blades. If continuity equation is not satisfied, some air could flow in and out from the top and bottom of the blades, resulting in significant change in the flow direction. In the MRF (front and rear) moving zones, 50 cells have been generated span-wise along the blade's surface which has resulted in $45 < y+ < 115$ over the inner and outer side of the frame's surfaces. It should be noted that on both sides of the blades, there are a pair of interfaces laid on each other with a structured mash over the outer surface (facing the stationary zone) and unstructured mesh over the inner surface (facing the moving zone).

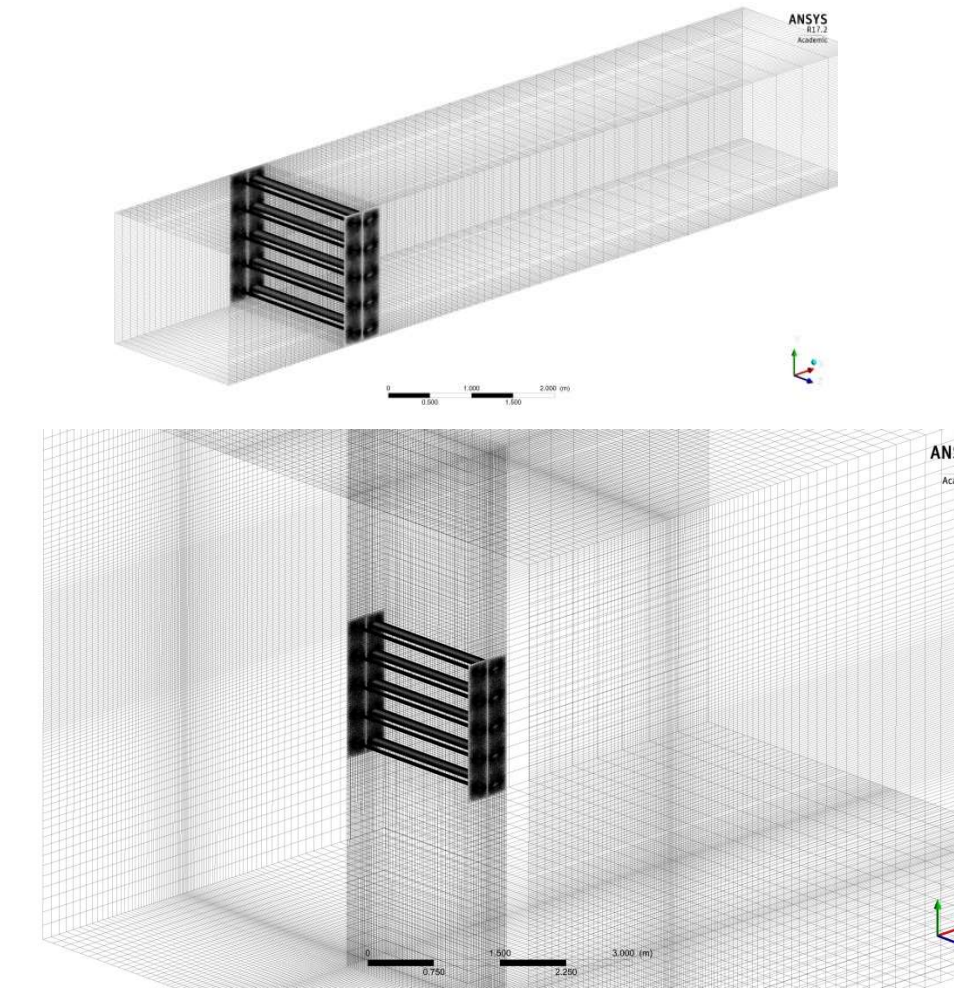

(a)

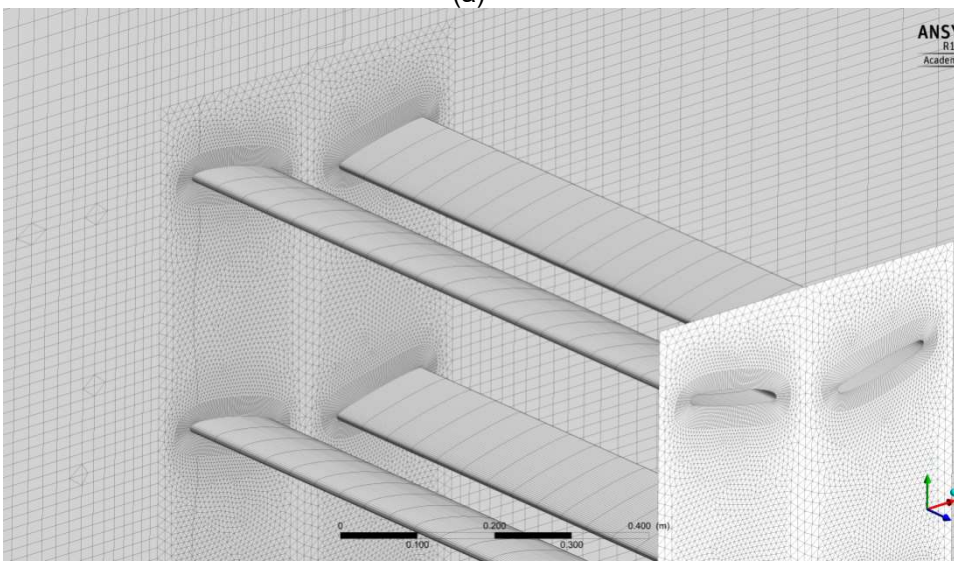

(b)

Figure 4-5: (a) Structured coarse mesh generated around the unstructured region. (b) Structured-unstructured hybrid mesh around the blades including fine structured rectangular elements adjacent to the blade surface.

The boundaries of the blades are set to a moving wall with zero velocity relative to their adjacent cells. As a result, their vertical velocity would be equal to the MRF surrounding cells. The inlet boundary condition has a uniform velocity of $8\ \mathrm{m/s}$ and the outlet boundary of the domain is set to atmospheric pressure. Turbulence intensity of 5% and turbulence viscosity ratio of 10 is set for inlet, while outflow was selected for outlet boundary conditions. In the elevated configuration, a realistic wind profile strongly depends on the elevation from the ground and topology of the area. In the ducted configuration, the wind profile at upstream of PowerWindow strongly depends on the distance of the device from the duct inlet and also the entry design. Therefore, a uniform wind profile is considered at the inlet of the models in this study. The standard pressure correction method and a first-order upwind scheme are used. The top and bottom boundaries of the domain are selected as a stationary wall. Gambit [86] is used as the mesh generation tool in this study. The CFD simulations are at prototype scale, thus avoiding the need to accommodate any scaling dictated by similarity criteria.

4.3. Validation of the CFD model

Due to the lack of experimental data of the proposed installation configurations (elevated and ducted configurations) for PowerWindow, the experimental data of the wind tunnel configuration is used to validate the CFD model. The accuracy of the CFD model is investigated by comparing the power generation predicted by the CFD model with that recorded in the experimental test. CFD model of the grounded PowerWindow has been created with $\sigma = 0.428$ and $\theta_b = 16°$ (similar to the prototype). The CFD model has been tested in four different poses, shown in Figure 4.6 (a), to investigate the effect of position of the front blades relative to the rear ones on their aerodynamic force and power generations. In each pose L_0 shows the elevation of the front blade relative to its adjacent rear blade. L_0/C ratio is $2/3$, $1/3$,0 and $-1/3$ respectively in poses a, b, c and d while the cord length of each blade is $1C = 5\mathrm{cm}$. The vertical and horizontal forces exerted on the front and rear blades are found through simulations.

The coefficient of performance (C_P) is selected to measure the power generation efficiency of PowerWindow prototype and the CFD models. C_P is the ratio of the power captured by the wind energy device to the entire wind energy passing through its swept area. The total power captured by the CFD model, ignoring the power generated by the single top and bottom blades, can be calculated via multiplying the total vertical force exerted on both front and rear blade by their velocity. C_P is calculated by dividing this power by the total wind power passing the swept area of the model.

$$C_P = \frac{P_{measured}}{P_{wind}} = \frac{\sum_1^n (Lift_{front} \times U\lambda) + \sum_1^n (Lift_{rear} \times U\lambda)}{1/2(\rho U^3)} = \frac{Lift_{total} \times U\lambda}{\frac{1}{2}\rho U^3 A} \tag{4-9}$$

Unlike in the HAWTs and some VAWTs, in a LCWT such as PowerWindow, λ does not depend on the distance of a particular part of blade to the rotating centre but, is constant along the blades and can be measured by multiplying the angular velocity of the gear by its radius:

$$V_{blade} = \omega_{gear} \times r_{gear} \tag{4-10}$$

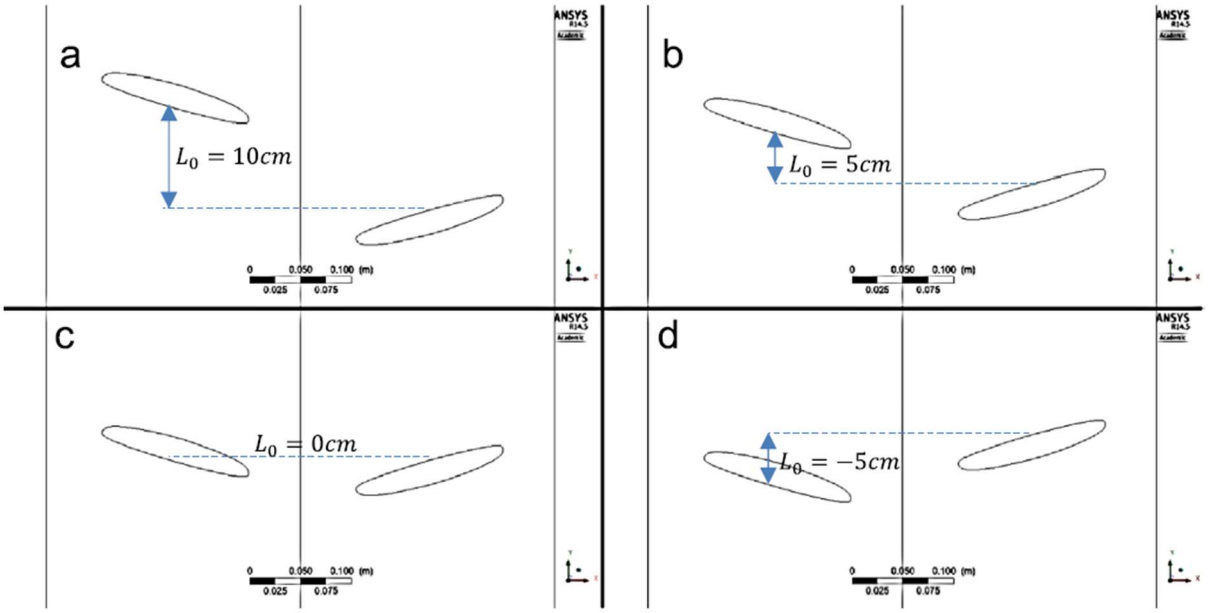

(a)

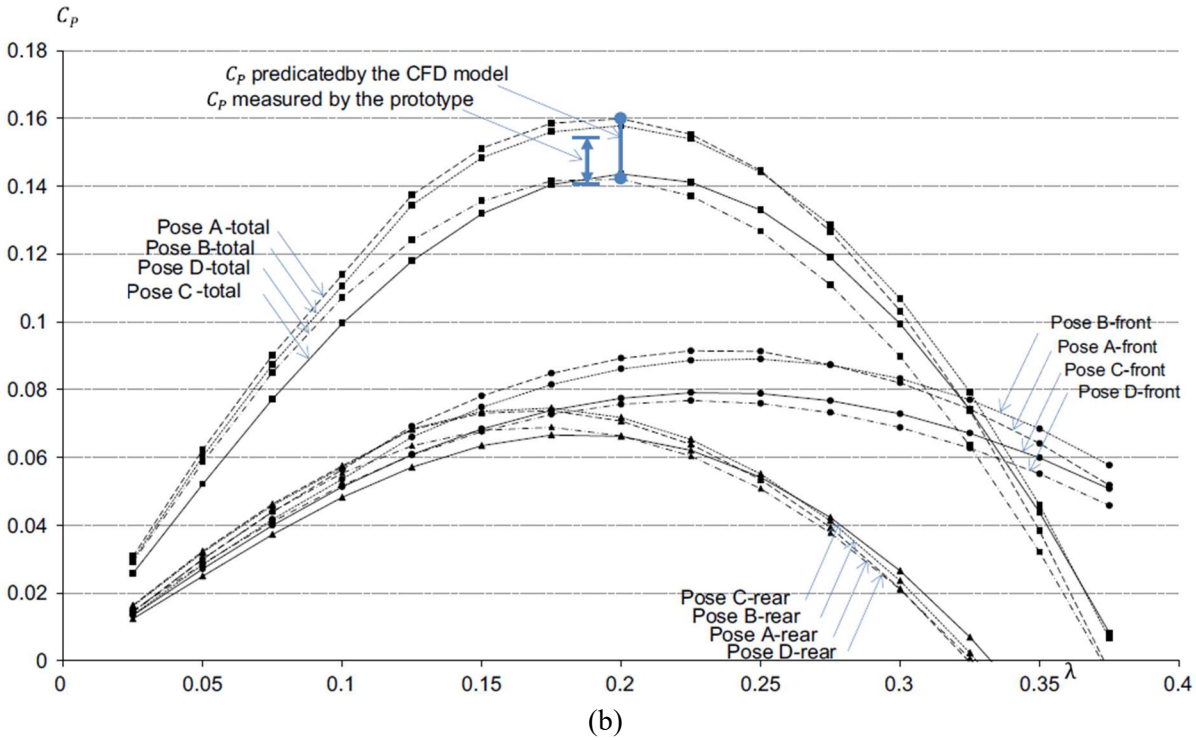

(b)

Figure 4-6: (a) Front and rear blades of the PowerWindow CFD model in poses (a) when $^{L_0}/_{C} = 2/3$, (b) when $^{L_0}/_{C} = 1/3$, (c) when $^{L_0}/_{C} = 0$ and (d) when $^{L_0}/_{C} = -1/3$ (C = 15cm). (b) C_P of the PowerWindow prototype recorded in the experimental test and predicted by the CFD simulations against λ.

Figure 4.6 (b) shows the C_P achieved by the front, rear and the total blades of the CFD model versus λ. The arrow between the horizontal solid lines shows the C_P achieved by the prototype in the experimental test. The curved lines show the C_P predicted by the CFD model in different values of λ. The operating condition of the CFD model is λ at which the maximum C_P is achieved ($\lambda = 0.2$). It can be seen that the prototype C_P in the experimental test has validated the CFD results. Operating conditions predicted by the CFD model is indicated by a blue solid line within two circles which shows $0.14 < C_P < 0.16$ at $\lambda = 0.2$. Operating recorded in the wind tunnel test is indicated by a blue arrow within to blue lines indicating shows $0.14 < C_P < 0.155$ at $\lambda = 0.1875$. The generated results show a close agreement between the experimental test and the CFD simulations, which verifies the validity of the CFD model. The verification has been further reported in [7].

4.4. Results and discussion

4.4.1. Effect of installation configuration on power generation

This study investigates elevated and ducted installation configurations and their effect on the power generation. PowerWindow is a modular LCWT, and the aerodynamic performance of a multiple unit can be different from a single unit. An illustration of the pressure distribution on the prototype blades using the 3D model is presented in Figure 4.7. This figure shows that the pressure difference between the high- and low-pressure sides of the bottom blades is greater than that of the top blades, which is mainly due to the ramp installed at the bottom inlet in the wind tunnel. The ramp accelerates the flow toward the bottom blades and increases velocity magnitude there, resulting in higher dynamic pressure and consequently the stagnation pressure (on the higher-pressure side of the blades). The vertical velocity also increases as the wind passes over the ramp. The increase in the vertical velocity results in a higher α and consequently, the pressure created on the bottom blades. Therefore, such a difference in the pressure distribution over the top and bottom blades is not expected to be observed in the elevated and ducted configuration, where there are no ramps.

Figure 4.7 also shows that the pressure distribution over the blades changes along the span so that the pressure difference across the sides of a blade at the middle is greater than that near the ends of the blade. The dissimilarity between the pressure distributions on the middle and both sides of the blades is because the flow near the sides can easily bypass the frame instead of passing through it. As a result, the axial velocity decelerates near the blades, and reduces the pressure difference between the high- and low-pressure sides of the blades near the sides. However, the pressure distribution along the span of the elevated and ducted PowerWindow blades are not exactly the same. Figure 4.8 shows the pressure distribution along the span of the middle blades in the elevated and ducted PowerWindow. Evidently in both configurations, the pressure difference between the high- and low-pressure sides of a blade at the middle is greater than that near the ends of the blade. This difference is negligible in the

elevated model but is more significant in the ducted one. In the elevated PowerWindow, the flow can easily bypass the frame instead of passing through it. As a result, the axial velocity slightly decelerates near the blades and reduces the pressure difference between the high- and low-pressure sides of the blades near there. In the ducted configuration, the ends of the blade span are located in the boundary layers of the duct where the velocity decreases and becomes zero on the wall. Therefore, there is less/no velocity gradient along the blades, which results in less/no pressure gradient. This study illustrates and compares flow characteristics around the PowerWindow blades, at the mid-span in the elevated and ducted configurations.

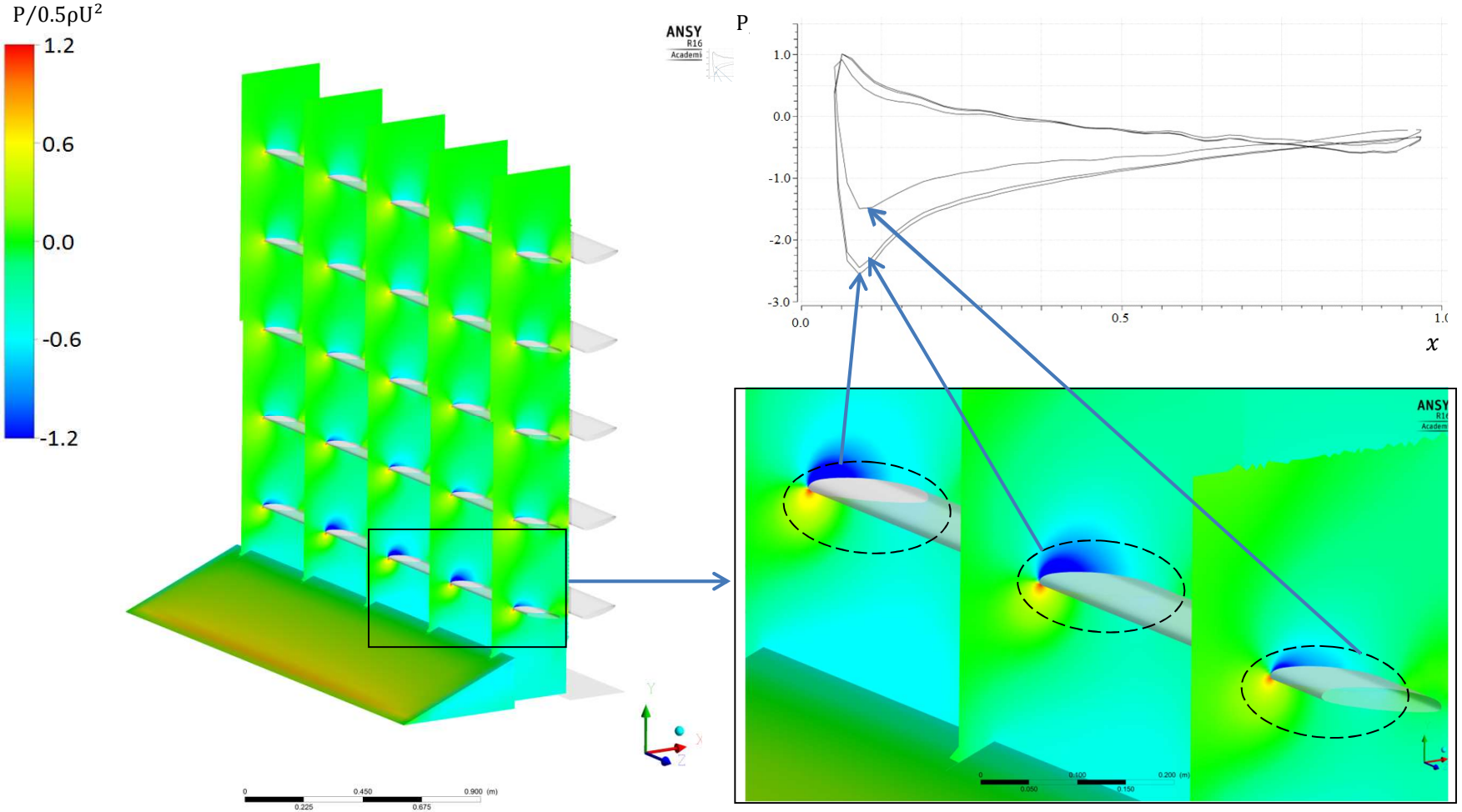

Figure 4-7: Pressure distribution around the blades of the PowerWindow prototype (in wind tunnel configuration) at different sections along the span.

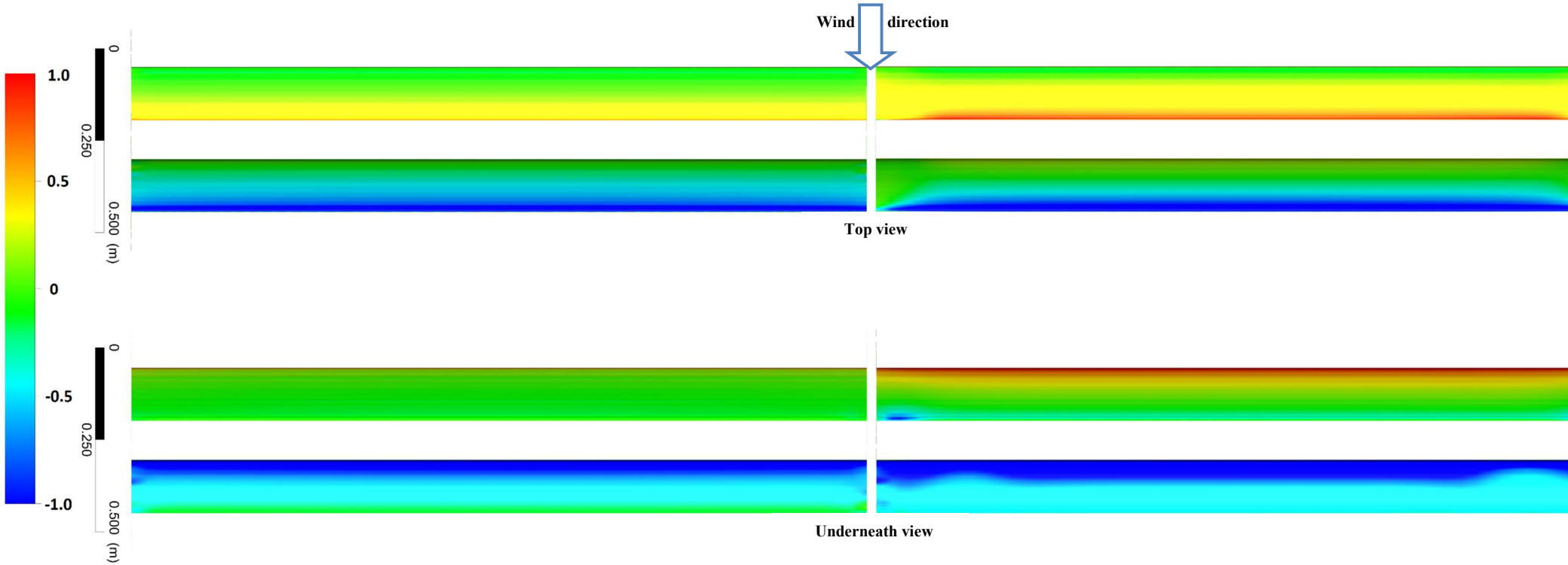

(a) (b)

Figure 4-8: Pressure distribution along the span of a blade in (a) elevated and (b) ducted PowerWindow (middle blades) from top view and underneath view when operating at λ=0.15.

Figure 4.9 shows velocity contours around the PowerWindow blades at the mid-span when PowerWindow is installed in the (a) elevated, and (b) ducted configurations at $\lambda = 0.15$. It can be seen that the free stream velocity has slightly decreased below $8\mathrm{m/s}$ at upstream of the front blades in the elevated configuration while the stream velocity has increased to up to $9\mathrm{m/s}$ between the front and rear blades of the ducted configuration. The mean velocity between the front and rear blades of the elevated model has been measured $7.2\mathrm{m/s}$ while it has remained $8\mathrm{m/s}$ between the front and rear blades of the ducted model. The reason is the absence of the bypass flow in the ducted configuration which forces the flow to pass through PowerWindow. Higher velocity creates a lower α at the same λ on the blades of the ducted configuration. Therefore, λ at the operating condition increases in this configuration to optimize α.

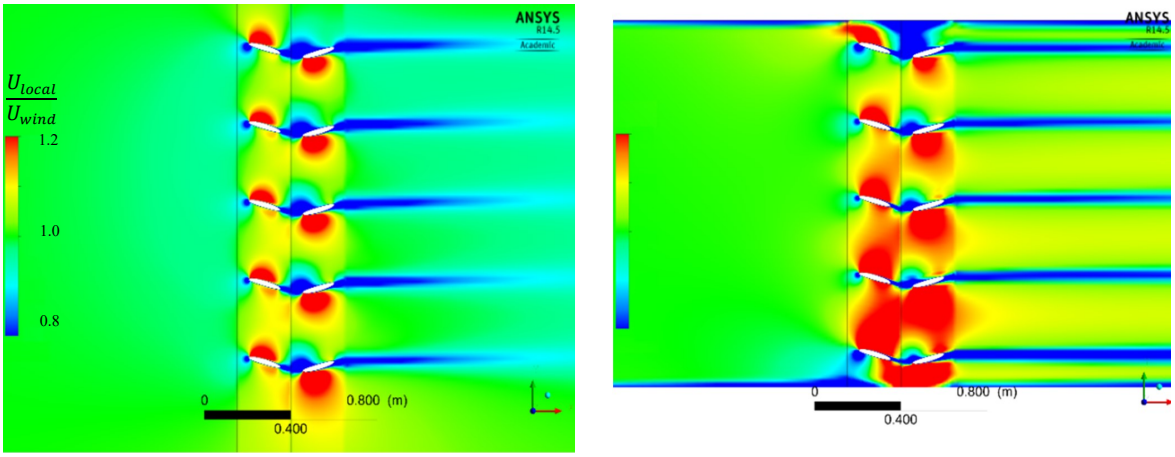

(a) (b)

Figure 4-9: Velocity contours around the PowerWindow blades at the mid-span when installed in the (a) elevated, and (b) ducted configurations at $\lambda = 0.15$.

The higher velocity also creates greater pressure gradient between the higher and lower pressure sides of the ducted PowerWindow blades, resulting in a higher vertical force on them and evidently higher power generation. Figure 4.10 shows pressure contours around the PowerWindow blades and streamlines around the middle blades at the mid- span when installed in the (a) elevated, and (b) ducted configurations and operating at λ=0.15. This figure proves that the pressure gradient around the blades is higher in the ducted configuration and shows that the ducted configuration demands a higher pressure gradient between the upstream and downstream sides of the PowerWindow (ΔP), which may not be available in the duct particularly at higher σ. Comparison of the streamlines between the elevated and ducted configuration shows that the lower pressure side of the rear blades of the elevated PowerWindow is mainly located in the separation area, while the separation has been postponed to the trailing edge in the ducted PowerWindow and flow is mainly attached to the blade's

surface. This results in a major difference between the pressure distributions over the blade surface of the elevated and ducted PowerWindow.

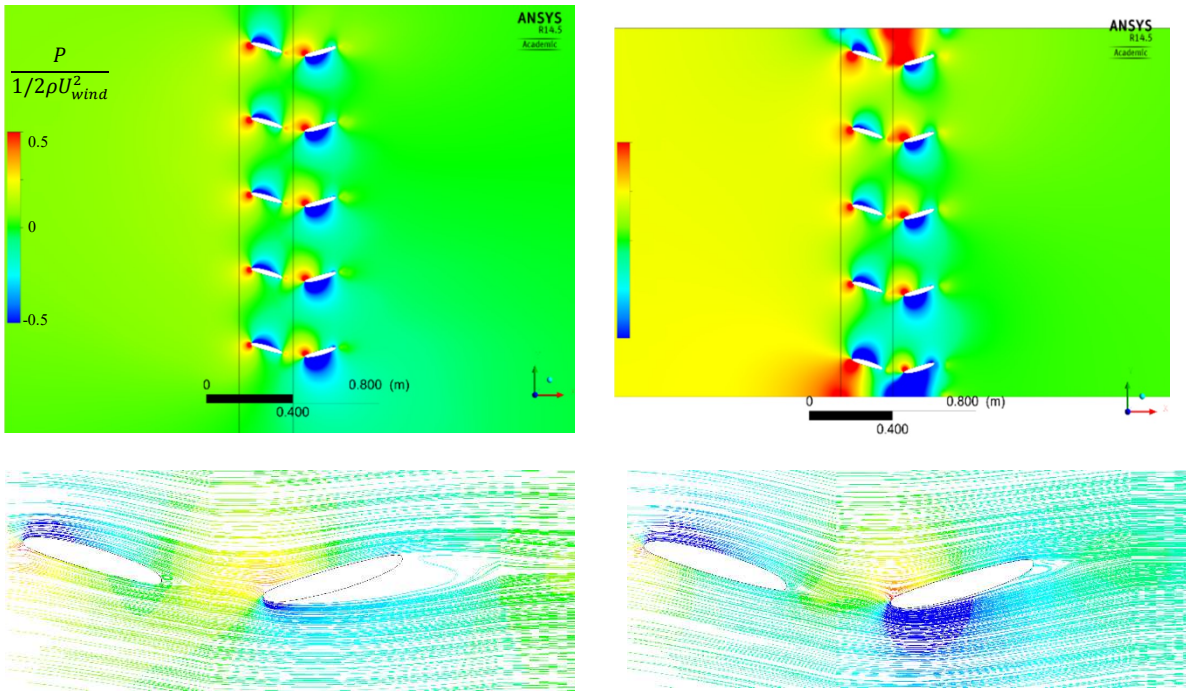

Figure 4-10: Pressure contours around the PowerWindow blades and streamlines around the middle blades at the mid- span when installed in the (a) elevated, and (b) ducted configurations and operating at $\lambda = 0.15$.

For a more accurate comparison, the distribution of surface pressure coefficient ($C_{SP} = P/0.5\rho U^2$) along the cord-length of the front and rear blades of the elevated (blue color) and ducted (red color) PowerWindow are presented in Figure 4.10. This figure shows that in both configurations, the pressure difference between the high- and low-pressure sides of the rear blades is greater than the front ones. As a result, they are expected to have a greater contribution to the total power generation. The reason is that the front blades accelerate the downward flow and increase α over the rear blades and higher α results in higher ΔP between the high- and low-pressure sides of the rear blades. As shown in Figure 4.9, the higher α creates flow separation over a major part of the rear blades of the elevated PowerWindow, while the separation area has been diminished to a very smaller part in the ducted PowerWindow. Nevertheless, Figure 4.11 shows a slight difference between C_{SP} along the cord-length of the rear blades of the elevated and ducted PowerWindow. The only major difference is around the trailing edge of the rear blades.

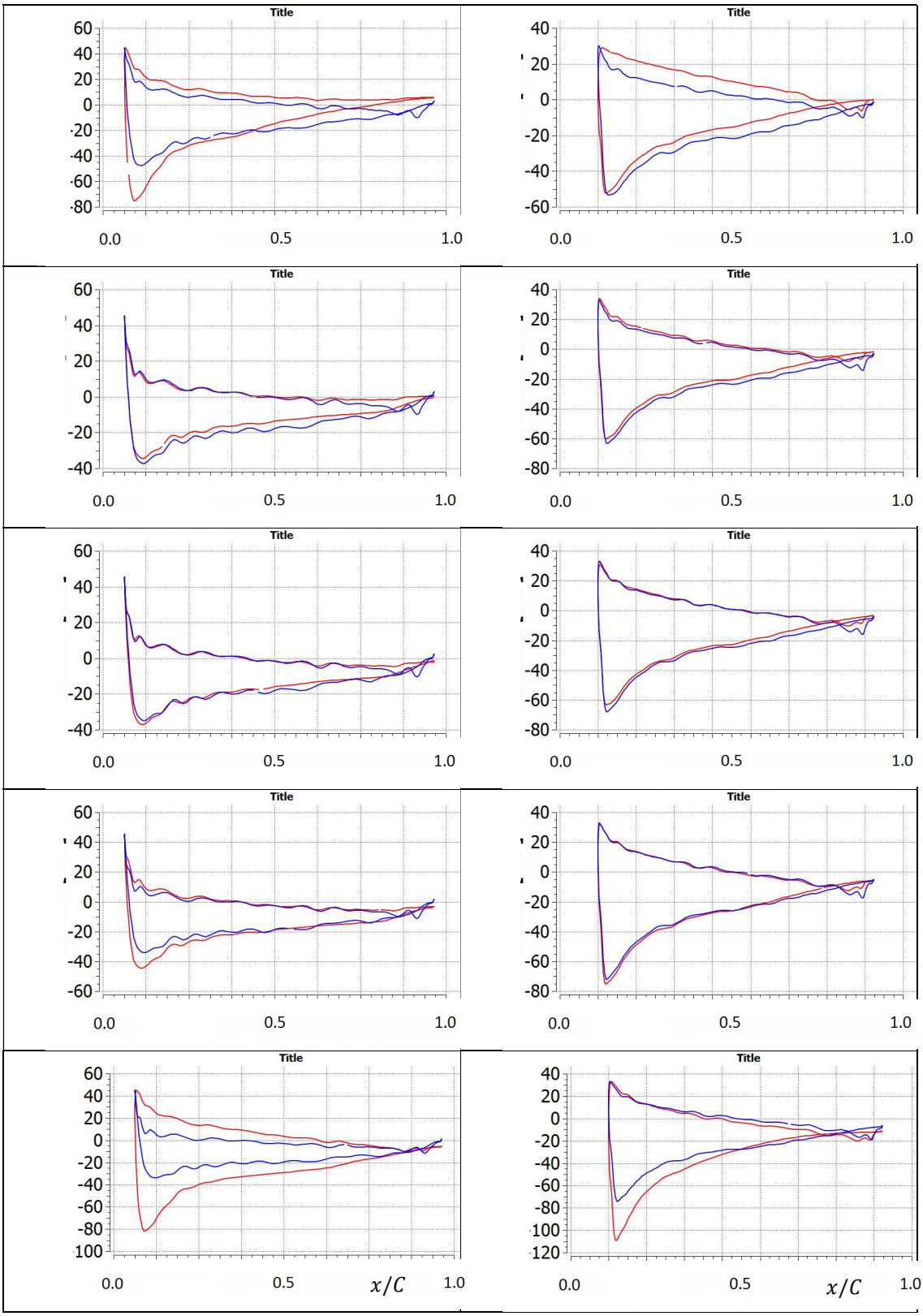

Figure 4-11: Pressure distribution along the cord-length of the front (left) and rear (right) blades of the elevated (blue curves) and ducted (red curves) PowerWindowat $\lambda = 0.15$.

It can be seen that on the trailing edges of the elevated configuration, high- and low-pressure lines have crossed each other, which creates a reverse force and decreases the total vertical force on them. As a result, the total vertical force on the blades of the ducted configuration and its power generation at the same λ is expected to be greater than the elevated one. The reason behind this phenomenon lies in the flow separation from the blade's surface. Separation begins as the flow passes along the cord-length of the pressure side of the blades and reaches the trailing edge. In the elevated configuration, the flow is less confined and can more freely separate from the blade's surface while in the ducted configuration, the flow is relatively confined and is forced to pass over the blade's surface.

Figure 4.12 shows the comparison between CFD results of C_P of the elevated, ducted and prototype (wind tunnel configuration) PowerWindow configuration. The C_P achieved for the elevated PowerWindow by 3D simulations in this study agrees with the 2D simulations and BEM results undertaken in the previous study [96]. As expected from the pressure distribution on the blades, the ducted configuration with $C_P = 0.12$ has 50% higher power generation than the elevated one with $C_P = 0.08$. However, the wind tunnel configuration with $C_P = 0.14$ has the highest performance. It can also be seen that in the ducted and elevated configurations, the rear blades have $30 - 50\%$ greater contribution to the total power generation compared to the front blades while in the wind tunnel configuration, the front blades have a greater contribution in the total power generation. The higher performance of the wind tunnel configuration in power generation, particularly for the front blades, is due to the ramp installed at the bottom inlet which accelerates the flow upward and increases α over the front blades there.

Figure 4.12 also shows that the operating λ in the ducted configuration with $\lambda = 0.2$ is higher than in the elevated one with $\lambda = 0.15$. The reason is that the maximum vertical force exerted on the blades depends on α and the optimum αover the blades of the elevated configuration is higher than the optimum α in the elevated one due to the flow separation and higher α can be achieved in lower λ.

Comparing Figures 4.6 and 4.12 shows that C_P of both the elevated and ducted configurations are still lower than the C_P of the wind tunnel configuration when all the models are exposed to an identical 8m/s approach wind velocity which is mainly due to the ramp effect in the wind tunnel configuration. However, some amplification factors will be applied to the approach wind velocity for the elevated and ducted configurations which may results in greater power generation in them.

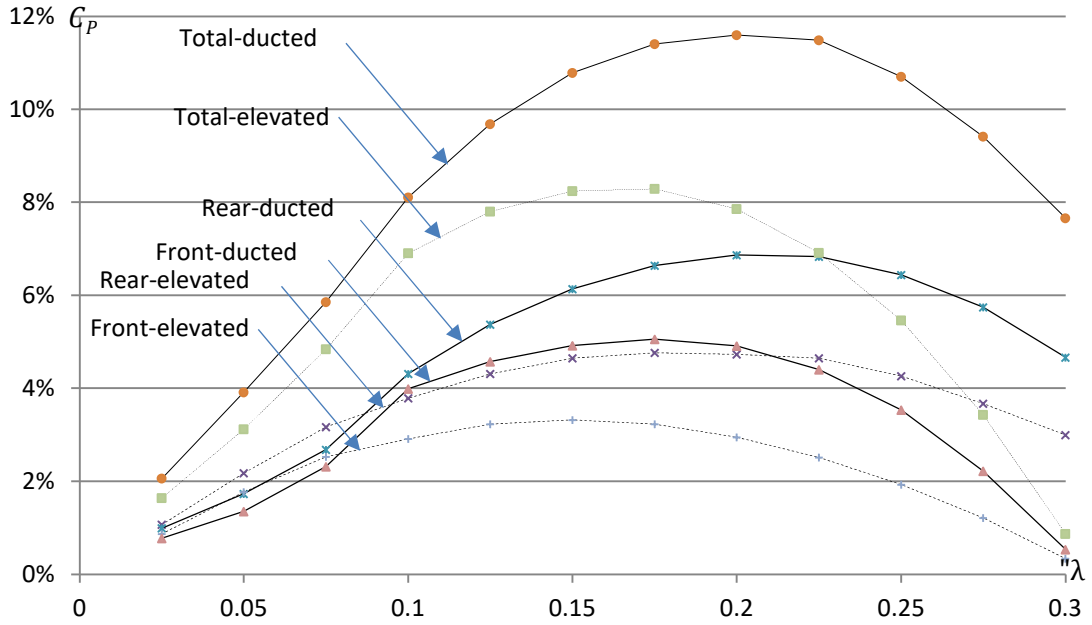

Figure 4-12: C_P of PowerWindow in elevated and ducted configurations against λ.

The passages between the two buildings can be treated as a potential location for wind energy harvesting. A study on the Venturi effect of two perpendicular buildings by Blocken, Moonen [99] showed that wind speed amplification factors for converging passages at ground level are greater than the upper levels. The reason is that wind flow bypasses over the buildings rather than being forced to pass through the buildings. In another study by Blocken, Stathopoulos [100] for the same model, it was found that the wind speed amplification factors in diverging directions are most often larger than converging directions. The study was extended by Li, Luo [101], who investigated the wind amplification factor with the building orientation varying from 0° to 180°. Lu and Ip [102], investigated the flow characteristics between two identical neighbour buildings with dimensions of $25\text{m} \times 25\text{m} \times 70\text{m}$ and distances of $10, 15, 20\text{m}$ from each other. It was concluded that the wind speed increases by a factor of 2 from the inlet wind speed of about $7.5\ \text{m/s}$.

In the ducted configuration, PowerWindow is installed inside a ducted area such as a through-building opening. Based on the inlet and outlet design of the duct and the approach wind direction, the ducted flow may have a higher speed than the free stream at the same elevation. To achieve greater performance, through-building openings can be embedded toward the dominant wind direction. Li et al. [2] provided a performance assessment of four wind turbines installed in four through-building openings in a tall building, Pearl River Tower, conducting a 1:150 scale wind tunnel test and reported that the wind speeds in the tunnels could be intensified by an average factor of 1.90.

4.4.2. Effect of solidity on power generation

As previously mentioned, σ is one of the most influential design parameters on power generation of every wind turbine including PowerWindow. The C_L and C_D values of an airfoil cascade configuration are different from an isolated one and strongly depends on σ. Due to the higher surface area, cascade configuration increases drag. Meanwhile, by restraining the flow, it postpones stall. Studies have shown that C_D increases with an increase in the roughness height. A sufficient increase in the roughness height does eliminate the operating condition of the cascade blades, which reduces the value of the stall angle [81]. Simple domains containing one airfoil blade with periodic boundaries at the top and bottom were generated for this part of the study. $C_L$andC_D of the linear cascade configuration have been extracted for some selected higher σ values: $\sigma = 0.857 \text{ and } 1.714$. Similar to the prototype test condition, in all simulations, the inlet wind velocity was set to $8\ \mathrm{m}/s$, and the Reynolds and the Mach numbers are $7.1 \times 10^4$and 2.33×10^{-2}, respectively, based on the cord length the airfoil and room temperature (300K).

Figures 4.13 (a) and (b) show C_L and C_D extracted for the isolated airfoil and the linear cascade configuration with $\sigma = 0.428,\ 0.857 \text{ and } 1.714$ against a range of α:$-14° < \alpha < 36°$. Polynomial curves have been fitted to the undertaken results for C_L and C_D in the prototype condition: $\sigma = 0.428$. This function facilitates the calculation of the lift and drag forces in the BEM model by making them dependent on α. As can be seen in Figure 4.13 (a) the maximum C_L of cascade airfoils is lower than the maximum C_L of the isolated airfoil. In addition, as σ increases, the maximum C_L decreases and shifts to higher α (postpones stall). Therefore, the cut-in speed (the minimum wind speed that the wind can overcome inertia and start moving the blades without the help of the generator) of PowerWindow is expected to be lower with higher σ.

As previously reported, in elevated and ducted configurations the flow redirection by the front blades enhances the vertical force created on the rear blades and thus, their contribution in the total power. The influence of the front blades on the flow direction when meeting the rear blades (β_2) depends on σ of the cascade. Higher σ results in more intense flow redirection and higher α_2 on the rear blades. The flow redirection also depends on λ, because the higher momentum that the air gives to the blades the more it will be redirected to the opposite of the blades moving direction. Therefore, β needs to be investigated against both σ and λ.

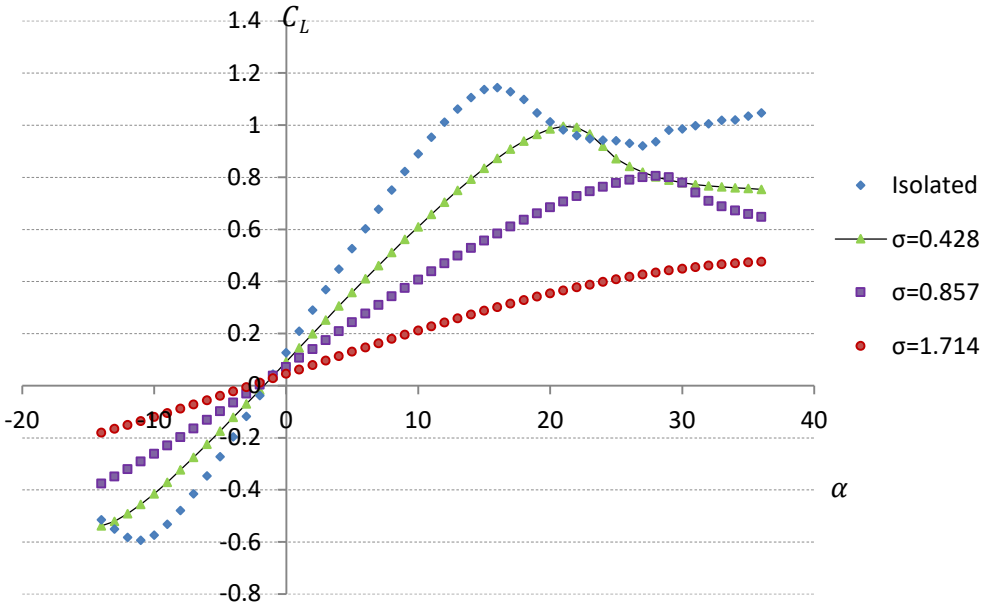

(a)

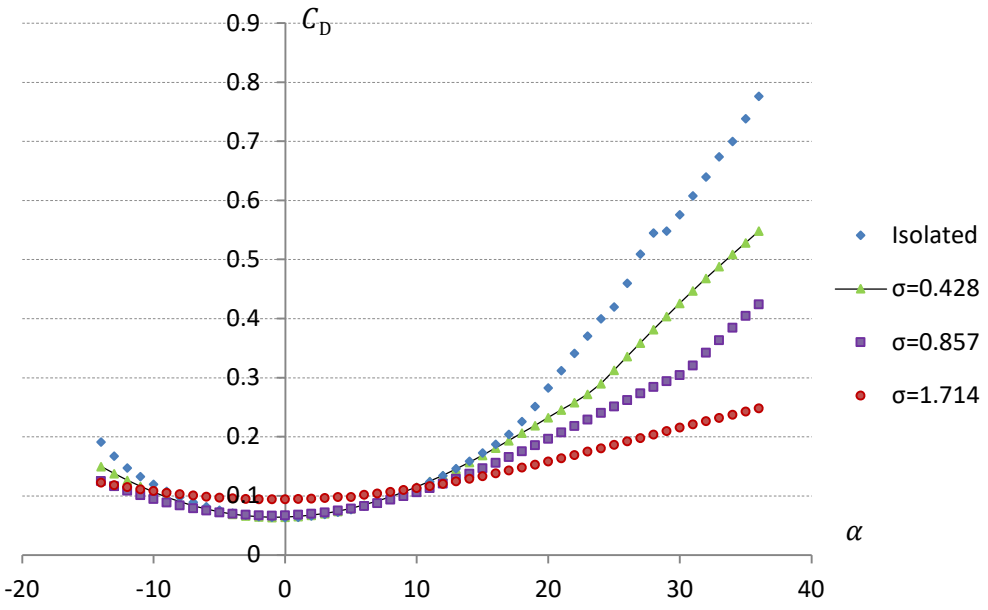

(b)

Figure 4-13: (a) C_L and (b) C_D of the PowerWindow isolated and linear cascade configurations with $\sigma = 0.428, 0.857$ and 1.714 against α.

Figure 4.14 (a-c) shows streamlines when flow passes through linear cascade configuration of PowerWindow blades (at the mid-section) with $\sigma =$ (a) 0.428, (b) 0.857 and, (c) 1.714 against a range of λ $(0.025 < \lambda < 0.25)$. In the prototype $\sigma = 0.428$ and $\sigma = 0.857$ and $\sigma = 1.714$ are selected by doubling the number of the cascade blades. As can be seen in the figure, β increases by increasing both σ and λ. However, it can be seen that increasing σ diminishes the effect of λ on β so

that, in $\sigma = 0.428$, β increases from 11° to 16° by increasing λ from 0.025 to 0.25 while in $\sigma = 1.714$, β increases only from 21° to 22° by a similar increase in λ.

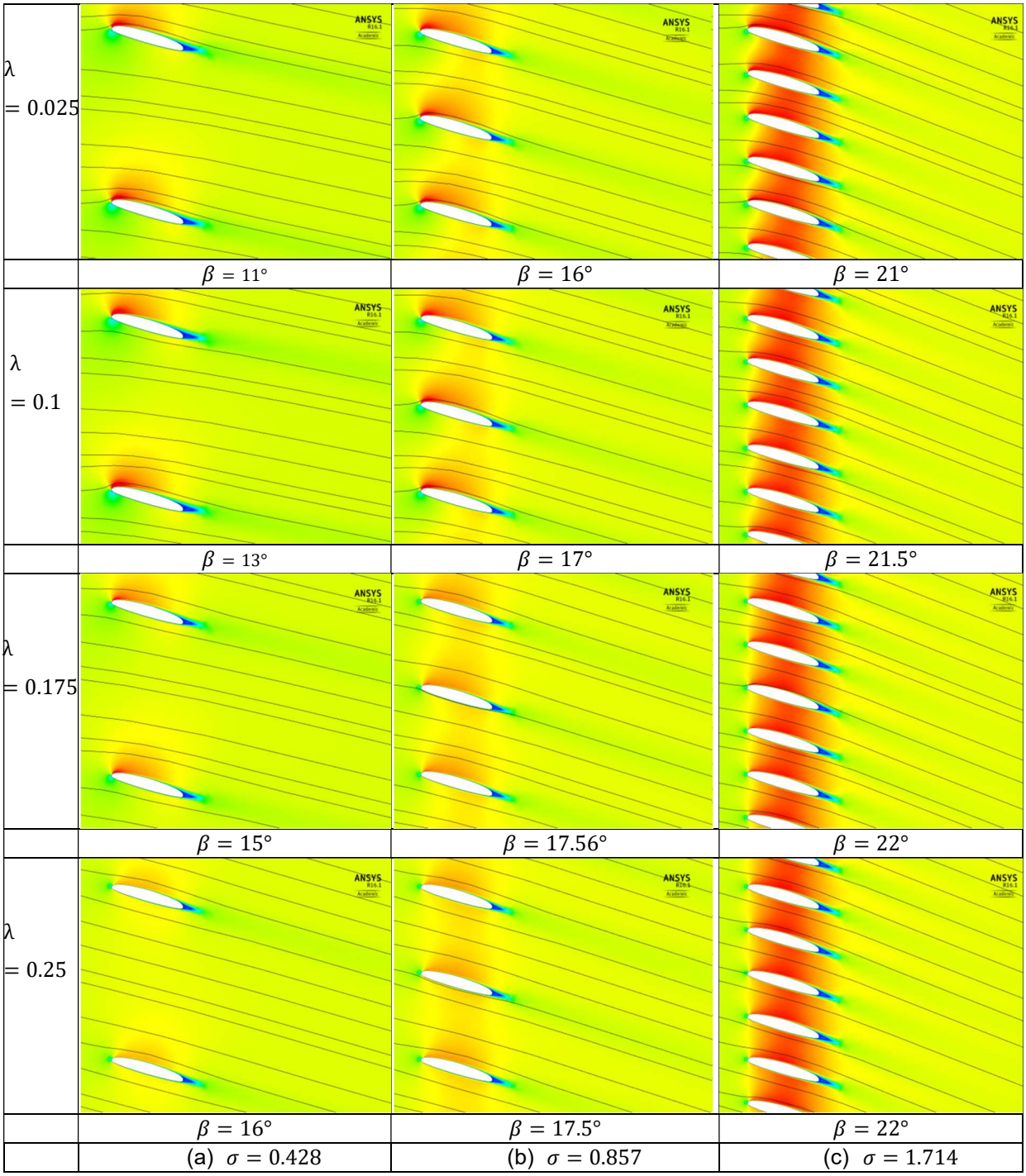

Figure 4-14: Flow streamlines when passing through linear cascade configuration of PowerWindow blades with $\sigma = 0.428$, $\theta_b = 16°$, (b) 0.857 and, (c) 1.714 when $0.025 < \lambda < 0.25$.

Based on these results, Figure 4.15 shows the relationships between β and λ at different values of solidity, $\sigma = 0.428$, 0.857 and 1.714. The governed relations between the β and λ at each σ helps to calculate the angle of attack over the rear blades, α_2, and derive a more accurate analytical model. α_2 can be calculated using Equation 4.11 [96]:

$$\tan \alpha_2 = \tan(\theta_b + \beta) - \left(2\lambda/\left(1 - a_f\right)\right) \quad (4\text{-}11)$$

where, a_f is the reduction ratio in velocity to the approach wind velocity. Power generation of the rear blades can be calculated using Equation 4.12 [96]:

$$Power = \sum_1^N \left(\frac{\rho B}{2}\right) V_{rel}{}^2 \left[C_L \cos(\theta_b - \alpha_2) - C_D \sin(\theta_b - \alpha_2)\right](V_{wind}\lambda) \quad (4\text{-}12)$$

Equation 4.11 shows how α_2 increases by increasing β and Equation 4.12 shows how increasing α_2 to an optimum point increases power generation by the rear blades. Using the relationships between β and λ at each σ helps to calculate the power generation of the rear blades with different configurations in further studies.

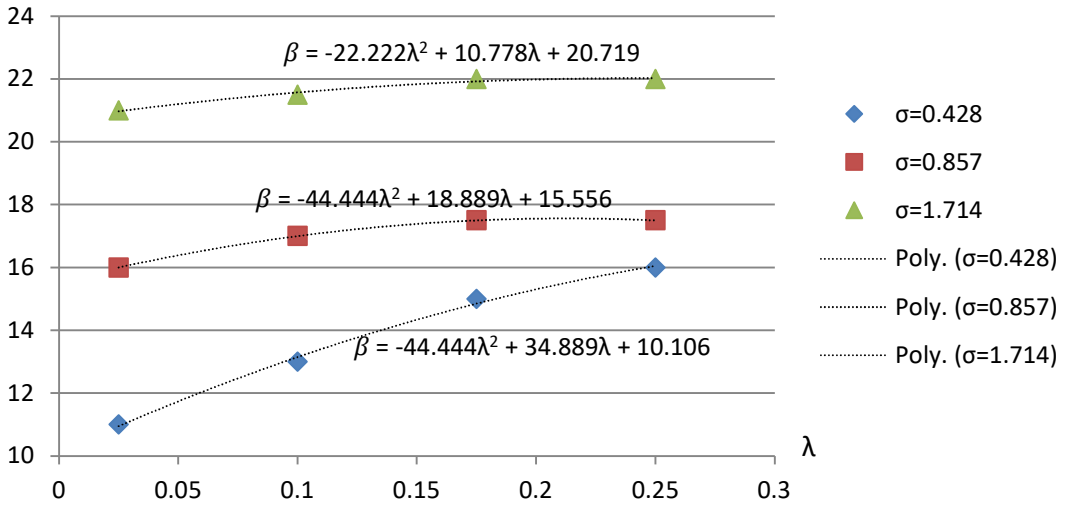

Figure 4-15: Relation between the redirection angle of the flow and λ at with$\sigma = 0.428,\ 0.857$ and 1.714when $\theta_b = 16°$.

Among the design parameters, σ is the most influential on the required ΔP across a wind turbine. Increasing σ results in higher vertical force by increasing the projected area of the cascade while, higher σdemands a greater ΔP across PowerWindow which may not be available/achievable everywhere. Using CFD simulations, C_P of the elevated and ducted PowerWindow with different σs has been calculated. The maximum C_P at the operating λ has been identified for each configuration and presented against σ in Figure 4.16. This figure shows that C_P of the elevated PowerWindow increases by 50% by doubling σ (at $\sigma = 0.857$) while further increase in σ is less effective. In the

ducted configuration $C_P$steadily increases by increasingσ. The results show that increasing σ from 0.428 to 0.857 makes a significant enhancement (≈ 55%) in C_P , increasing σ from 0.428 to 1.284 enhances C_P by 90%, and increasing σ from 0.428 to 1.714 enhances C_P by 145%. The reason is that the flow cannot bypass PowerWindow and is forced to pass through the unit. However, higherσ demands grater pressure gradient which may result in lower ducted flow velocity. Therefore, appropriate ΔP needs to be investigated before increasing σ.

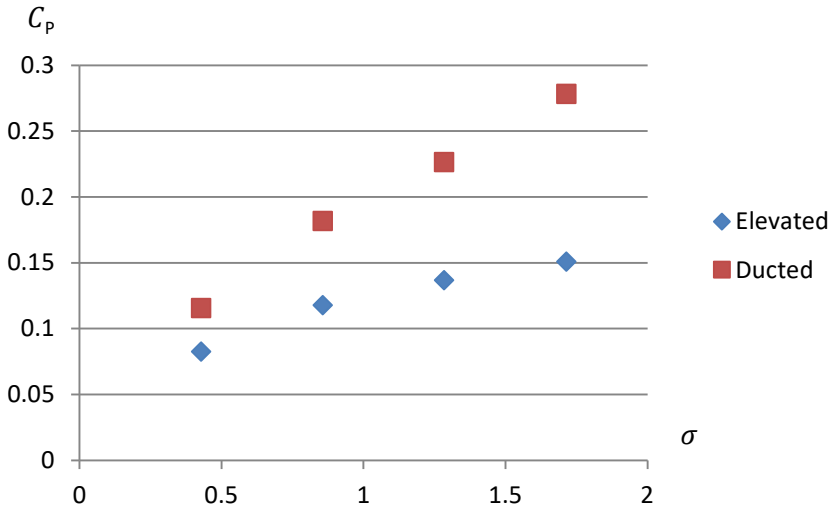

Figure 4-16: C_P of the elevated and ducted PowerWindow with different σs.

For investigating the optimum ΔP, maximum power generation of the ducted turbine can be calculated. The required ΔP for the maximum power generation would be considered as the optimum ΔP. Ignoring every energy loss at the inlet, due to the wall friction and by the device itself, and assuming atmospheric pressure at the leeward face of the building, the entire reduction in the momentum of the air entering the duct will be captured by the ducted turbine. Considering uas reduced velocity of the approach wind at the inlet of the through-building opening, and uniform cross-section area along the through-building opening (from the inlet to the outlet), ideal power generation of a ducted turbine can be calculated as below:

$$P = 0.5\rho u(U^2 - u^2)A \tag{4-13}$$

Derivation of the power generation equation for the ducted turbine gives the optimum u at which, the maximum power generation will be achieved:

$$\frac{dP}{du} = 0 \rightarrow u = \frac{\sqrt{3}}{3}U \tag{4-14}$$

The maximum C_P of the ducted turbine can be calculated using the optimum u as below:

$$P_{max}: u = \frac{\sqrt{3}}{3}U \rightarrow C_{P\,max} = \frac{2\sqrt{3}}{9} \tag{4-15}$$

Assuming atmospheric pressure at the leeward face of the building, where the other outlet of the duct is located, the optimum ΔP to the dynamic pressure of the approach wind can be calculated accordingly:

$$(\Delta P/0.5\rho U^2)_{opt} =$$
$$(P_{inlet} - P_{outlet})/0.5\rho U^2 = (0.5\rho U^2 - 0.5\rho u^2)/0.5\rho U^2 = 2/3 \cong 0.66 \quad (4\text{-}16)$$

The ΔP demanded between the inlet and outlet of the CFD model of the ducted PowerWindow at each σ is measured and compared with the dynamic pressure of the approach wind in Table 1.

Table 4-1: The ration of ΔP to the dynamic pressure of the approach wind at different σ.

σ	$\Delta P/0.5\rho U^2$
0.428	0.2
0.857	0.33
1.284	0.4
1.714	0.5

Table 4.1 shows that the ratio of ΔP to the dynamic pressure of the approach wind at higher selected σs is still below the optimum value (0.66 as calculated in Equation 16). Therefore, increasing σ by 300% can ideally increase C_P of the ducted PowerWindow. For any σ if the ΔP to the dynamic pressure of the approach wind exceeds 0.66, wind velocity reduction drops such that decreases the power generation even if C_P increases. However, in a through-building opening with inlet and outlet larger than the cross-section area of the duct, u increases due to continuity. In such a case, the optimum u/U ratio and consequently the optimum ratio of ΔP to the dynamic pressure of the approach wind will change, and the optimum σ needs to be investigated for each through-building opening accordingly.

4.5. Conclusion

A 3D CFD model of PowerWindow was developed and validated with the experimental data from the wind tunnel test of the prototype. Elevated and ducted installation configurations of PowerWindow are analyzed. In elevated configuration PowerWindow is installed on top of a tall building. In the ducted configuration it is installed inside a ducted area such as a through-building opening. Aerodynamic performances of the elevated and ducted PowerWindow were investigated and compared using computational fluid dynamic simulations. The numerical results indicated that with the current design parameters, the elevated and ducted configurations have respectively 8% and 12% coefficient of performance, and in both configurations the front blades alter the flow direction and further enhance the power generation of the rear ones. The effect of solidity was also investigated

on the flow mechanism and power generation of elevated and ducted PowerWindow. It was shown that the solidity of the front blades has a significant effect on the flow direction approaching the rear ones which increases their contribution in power generation. It was also shown that increasing solidity results in a greater coefficient of performance in both configurations. However, the optimum solidity of the ducted configuration depends on the inlet and outlet design of the through-building opening at needs to be investigated for each design.

CHAPTER 5. AERODYNAMIC ANALYSIS OF A STATOR_AUGMENTED LINEAR CASCADE WIND TURBINE

A reprint of this study entitled 'Aerodynamic Analysis of a Stator-augmented Linear Cascade Wind Turbine', Jafari SAH, Kwok KCS, Safaei F, Kosasih B, Zhao M, published by the Journal of Wind Energy, 2019. 22(8): p. 1148-1163 (https://doi.org/10.1002/we.2346) is appended in Appendix B3.

5. 1. Introduction

Linear Cascade Wind Turbines (LCWTs) are a new generation of wind turbines. Unlike the conventional horizontal axis wind turbine (HAWT) and vertical axis wind turbines (VAWT), the blades of LCWTs do not rotate around the rotor axis but move translationally in a direction perpendicular to the approach wind direction. PowerWindow, shown in Figure 5.1 (a), is a compact modular LCWT which can easily fit into any designated area in a building. It is also capable of generating electricity even when the ratio of blade speed to wind speed (referred to as the blade speed ratio, λ) is quite low. Therefore, it can be a safe option for application in built environments.

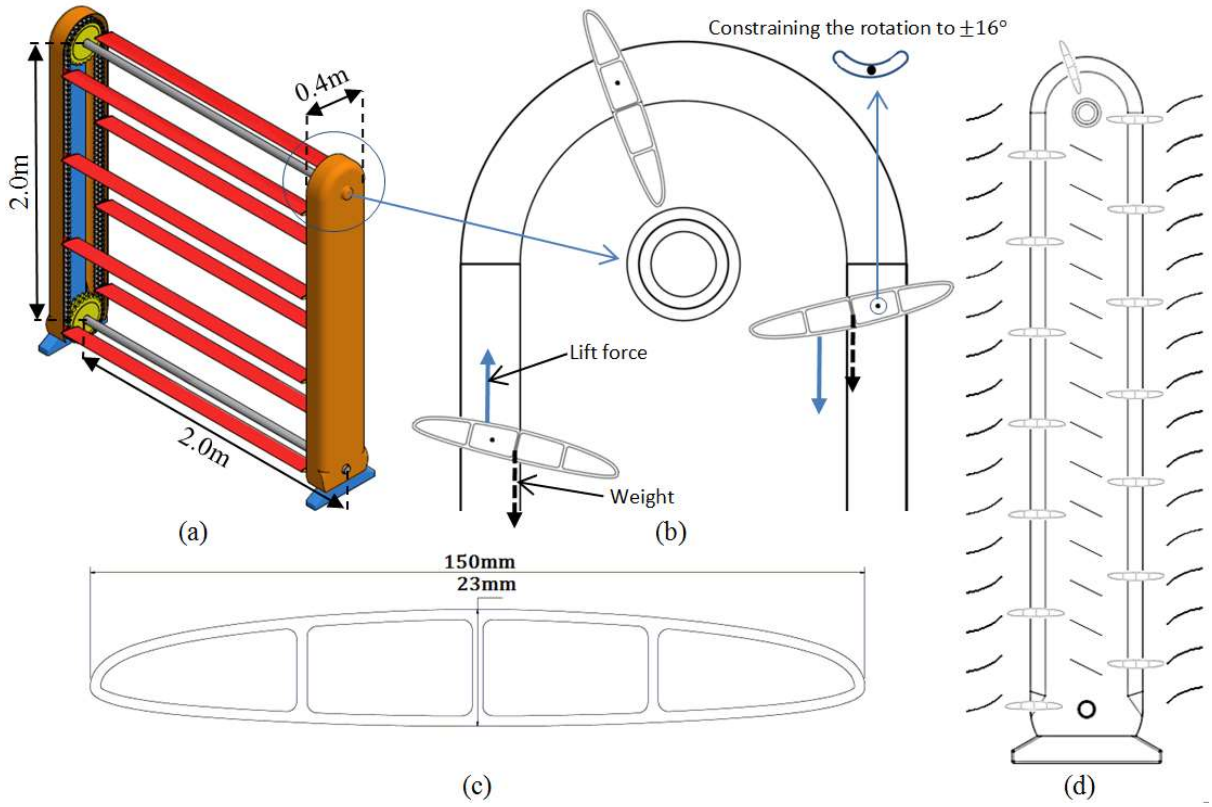

Figure 5-1: (a) Sketch of the PowerWindow prototype, (b) Blades changing their side and orientation at the top of PowerWindow, (c)Cross section view of the airfoil blades, and (d) Sketch of the stator-augmented PowerWindow (from side view).

The power generation mechanism of PowerWindow is similar to Variable-Geometry Oval-Trajectory (VGOT) Darrieus turbine [57-59], which is a modified version of a straight-blade Darrieus or H-rotor Vertical Axis Wind Turbine (VAWT) [27]. Similar to VGOT, PowerWindow has an adjustable blade pitch angle (θ_b), which enables optimizing the angle of attack (α) when exposed to different approach wind velocities. Here, θ_b refers to the angle between the cord length of the blades and the horizontal direction. Therefore, α equals θ_b if the blades are stationary and is smaller than θ_b as the blades move. Note that the pitch angle in HAWTs and VAWTs may vary along the span of the blade, while in PowerWindow θ_b is constant spanwise. When $\theta_b \neq 0$, it is required that the angle

flips to $-\theta_b$when the blades roll over. A passive mechanism for this purpose has been designed for PowerWindow, as described in Section 5.2.

The power generation performance of a wind turbine is dependent on different design parameters such as airfoil shape, solidity, pitch angle and rotating speed. Mohamed [48] investigated the performance of a H-rotor Darrieus wind turbine using 20 different airfoil shapes and increased the power output coefficient by 27%. Mohamed [87] also investigated the impacts of solidity on the performance of a small H-rotor Darrieus turbines and found that the rotational speed of the rotor decreases by increasing the solidity. Lee et al. [80] investigated effects of the pitch angle and rotating speed on aerodynamic performance of a counter-rotating wind turbine and showed that the rotational speeds of the wind turbine rotors are strongly dependent on their pitch angles, while both the parameters (pitch angle and rotating speed) significantly affect the aerodynamic performance of the turbine.

In our previous work [103], we examined the effect of solidity on the performance of PowerWindow. The aim of this paper is to explore the optimization of the angle of attack. It can be observed that the optimum α is dependent on the wind speed. Therefore, one approach would be to adjust the pitch angle θ_b for different approach wind velocities. It is conceivable to design an *active* pitch angle control mechanism for this purpose. However, this addition has a number of drawbacks. Firstly, it increases the complexity (and cost) of the mechanism of attachment between the blades and the belt/chain. Secondly, controlling the drag force is not easy and may result in undesirable load on the system.In the wind tunnel test on the prototype model [7], θ_b could be altered manually. The results presented in [5] are for $\theta_b = 16°$. But increasing $\theta_b$would also increase the axial load (aerodynamic force along the wind direction) on PowerWindow [104].

This study aims to develop an alternative approach to optimize α and enhance power generation performance of PowerWindow. Instead of optimizing θ_b for the turbine blades, stator vanes are attached to the device, and the vane pitch angle (θ_v) is used to control the flow direction toward the blades in order to create a desirable α. This approach has been widely used in gas turbines. As shown in Figure 5.2, in gas turbines, stationary vanes, also known as stator are located between the rotors and redirect the flow. When fluid passes through a stator, the velocity of fluid increases due to its special shape and a part of enthalpy gets converted into kinetic energy [105, 106]. The angle of the stator vanes can be adjusted to redirect the flow and create the optimum α over the rotor blades based on the flow velocity. The black vectors show the absolute velocity of the flow and blue ones show the relative velocity of the flow to the rotor blades.

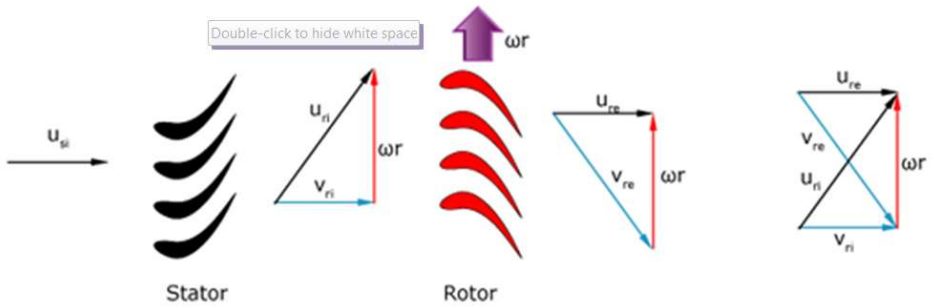

Figure 5-2: Absolute (black vectors) and relative (blue vectors) velocity of the flow to the rotor blades.

This study proposes to use stator vanes to improve the flow direction in PowerWindow. This new configuration (with stator vanes attached to the original PowerWindow) is referred to as *stator-augmented PowerWindow*. It is demonstrated that by attaching stator vanes and adjusting their angle, it is possible to increase the acting force (vertical load) while at the same time having the ability to decrease/control the undesirable force (axial load) on PowerWindow. The complexity of the device is also significantly reduced because neither the active mechanism for adjusting the blades' pitch angle in response variations of wind speed nor the passive mechanism for flipping the pitch angle in each rotation is needed. This is because the pitch angle will be set at a fixed value of $\theta_b = 0$. Another advantage of using stator vanes to control the angle of attack is that the direction of rotation of PowerWindow will remain the same regardless of the wind direction. In the original PowerWindow, when the wind direction is reversed, the turbine will also rotate in the opposite direction. The stator-augmented design, therefore, will be particularly useful for fixed in-building installations.

The effect of stator augmentation has been investigated on the coefficient of performance (C_P) and the thrust coefficient (C_T) of the stator-augmented PowerWindow. C_P refers to the ratio of the power captured by the generator to the entire wind energy passing through its swept area and C_T shows the ratio of the force exerted on a turbine rotor to the dynamic pressure of the approach flow:

$$C_P = \frac{P_{captured}}{1/2\rho A V^3} \tag{5-1}$$

$$C_T = \frac{F_x}{1/2\rho A V^2} \tag{5-2}$$

when ρ is the density of the flow, A is swept area.

In this study, Blade Element Momentum (BEM) theory has been selected for analysing the power generation of the stator-augmented PowerWindow, as this approach has shown to be very effective for the design and optimization of HAWTs [23, 107, 108] and VAWTs [26]. In addition, we have developed a similar model for the original PowerWindow (without the stator vanes) in our previous research [96], hence, comparative studies can be conducted on C_P and C_T of both configurations. A

Computational Fluid Dynamic (CFD) model of the stator-augmented PowerWindow has also been developed to verify the analytical results by simulation.

5. 2. Description of the original and stator-augmented PowerWindow

A sketch of the original PowerWindow is shown in Figure 5.1 (a). In PowerWindow, the approach wind exerts lift force on the blades pushing the front blades upward and the rear ones downward, causing the belt to roll. As the belt goes around, the blades change side and orientation. The blades are attached to the belt in a way that they can rotate about the support point with $\pm\theta_b$ as shown in Figure 5.1 (b). The blade's angular rotation is constrained by a simple pin-and-groove mechanism, which limits θ_b to some upper bound value for the pitch angle.

PowerWindow blades have a symmetrical shape, as shown in Figure 5.1 (c). In the original PowerWindow, the point of attachment is at about a third of the cord length, which is forward of the centre of mass but behind the centre of pressure in the upwind state. When a blade is at the front (upwind plane), the force of gravity acting on the centre of mass and the lift force acting at the centre of pressure make the blade rotate in the clockwise direction. When a blade is at the rear (downwind plane), both the gravity and the pressure force make the blade rotate in the anticlockwise direction.

In PowerWindow, the lift forces acting on the front and the rear blades oppose each other. Therefore, the original PowerWindow is designed such that blades 'flip over' to $-\theta_b$ in each rotation. While as shown in Figure 5.1 (d), in the stator-augmented PowerWindow, $\theta_b = 0$ and using the stator vanes θ_v adjusts α over the front and rear blades. The point of attachment should also be in the middle of the blades. The stator vanes' pitch angle θ_v creates an upward lift on the front and a downward lift on the rear blades, whether the approach wind comes from front or back. This mechanism allows the stator-augmented PowerWindow to operate effectively in the clockwise direction with respect to bidirectional approach wind. θ_v for the front and rear vanes needs to be identical but it can be different for the middle vanes. As a simple preliminary configuration for the analysis and evaluation of this paper, the stator vanes have been selected to have the same length and distance from each other as the cord length of the blades, and θ_v is selected for every vane. The middle vanes are simple flat vanes but the front and rear vanes are designed with a curved shape to minimize flow separation from their surface. Further details are discussed later in the computational fluid dynamic model.

5. 3. Blade element momentum model

The basic aerodynamic analysis of the BEM theory is based on Glauert's airscrew theory [19], which was initially developed for the analysis of propellers, particularly within the helicopter

industry [20]. This theory has recently been used in the analysis of HAWT [22-25], and VAWT [26] using tabulated airfoil lift and drag coefficients (C_L and C_D). For most of the well-known airfoils, the recorded databases of C_L and C_D is available for a limited range of angle of attack (α), Reynolds and Mach numbers. However, it has been reported that the C_L and C_D values are usually higher than those which are typically experienced by wind turbine blades during the operation [26].

5.3.1. Aerodynamic of the PowerWindow blade and cascade configuration

In this study, $k-\omega$ shear stress transport (SST) turbulence model was used in the CFD simulations to calculate the lift and drag coefficient ($C_L$and C_D) values of airfoil blades. The BEM theory was modified by replacing C_L and $C_D$of the isolated blade by the C_L and C_D of the cascade configuration, which takes into account the viscous loss and effects of other characteristic changes due to the cascade configuration of the PowerWindow. C_L and C_D are presented below:

$$C_L = \frac{Lift}{\frac{1}{2}\rho BV^2} \tag{5-3}$$

$$C_D = \frac{Drag}{\frac{1}{2}\rho BV^2} \tag{5-4}$$

Where, ρ is air density, B is airfoil plan area and V is the air velocity.

In PowerWindow, solidity (σ) is the ratio of the total surface area of the windward side of the (front/rear) blades to the total area of PowerWindow exposed to the approach wind:

$$\sigma = NB/A \tag{5-5}$$

Where N, B and A represent the number of the blades, area of each blade and area of PowerWindow respectively.

The C_L and C_D of the linear cascade (a series of airfoils located in a line parallel to each other)configuration are calculated for the original PowerWindow, where $\sigma = 0.428$, and also for some higher σ values: $\sigma = 0.857$ and 1.714, to demonstrate the influence of σ on the aerodynamic performance of PowerWindow. In all simulations, the inlet wind velocity was set to $8\ ms^{-1}$, which is achievable in appropriate places in urban environments. The Reynolds and the Mach number based on cord length the airfoil and room temperature (300K) are $7.1 \times 10^4$and 2.33×10^{-2}, respectively. Figures 5.3 (a) and (b) show the numerical results of $C_L$and C_D for an isolated airfoil and one of the airfoil in linear cascade configuration with $\sigma = 0.428,\ 0.857$ and 1.714against a range of α:$-14° < \alpha < 36°$. Polynomial curves have been fitted to the C_L and C_D values at $\sigma = 0.428$ to present their relation with α.

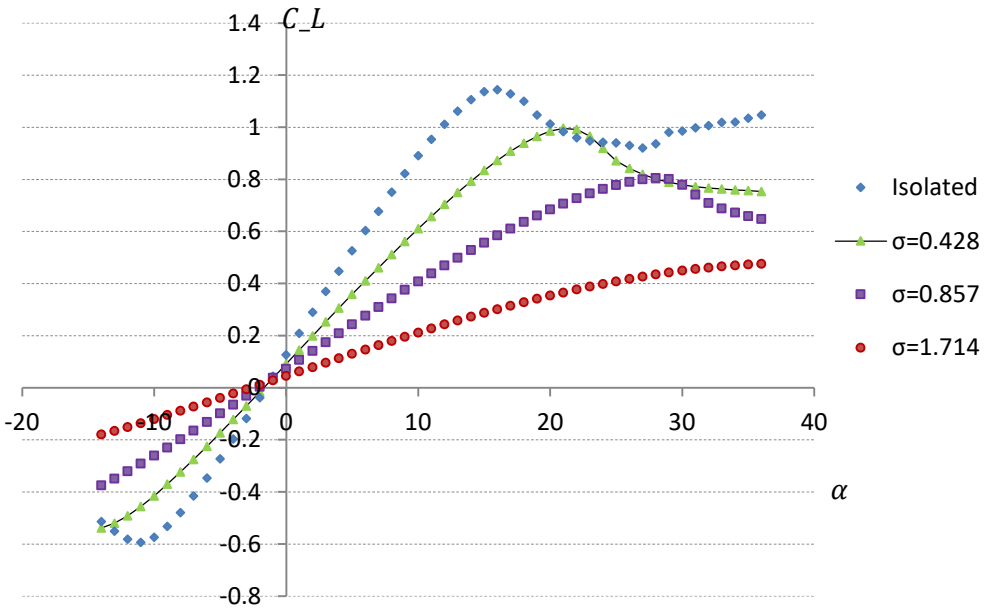

(a)

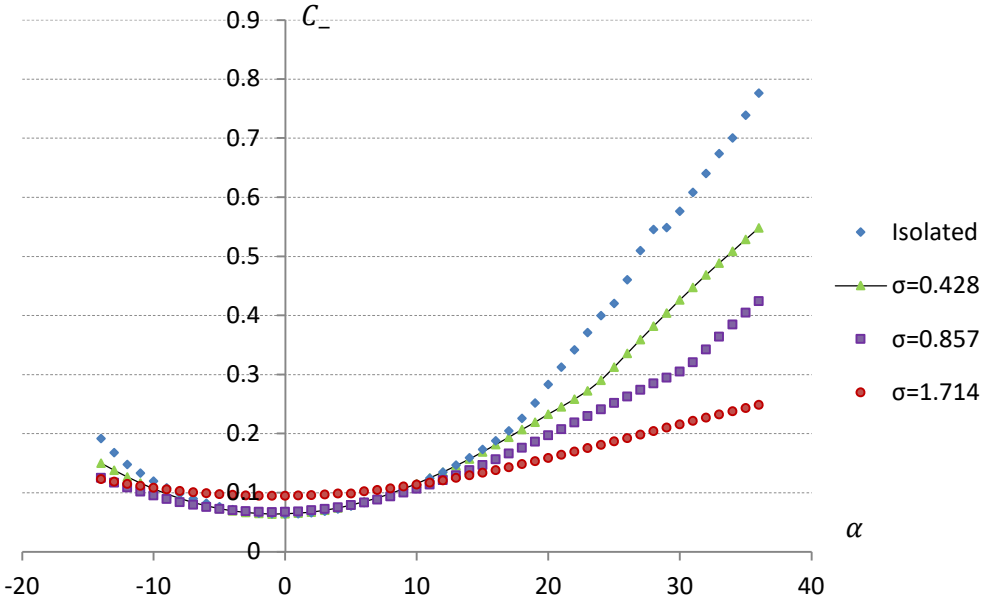

(b)

Figure 5-3: (a) C_L and (b) C_D of the PowerWindow isolated and linear cascade configurationswith $\sigma = 0.428, 0.857$ and1.714 against α. For $\sigma = 0.428$:$C_L = 3.93 \times 10^{-15}\alpha^{11} - 4.35 \times 10^{-13}3\alpha^{10} + 1.47 \times 10^{-11}\alpha^{9} - 2.55 \times 10^{-11}\alpha^{8} - 6.89 \times 10^{-9}\alpha^{7} + 7.05 \times 10^{-8}\alpha^{6} + 9.76 \times 10^{-7}\alpha^{5} - 1.14 \times 10^{-5}\alpha^{4} - 8.05 \times 10^{-5}\alpha^{3} + 5.68 \times 10^{-4}\alpha^{2} + 5.48 \times 10^{-2}\alpha + 8.73 \times 10^{-2}andC_D = -3.02 \times 10^{-9}\alpha^{5} + 1.86 \times 10^{-7}\alpha^{4} - 4.39 \times 10^{-6}\alpha^{3} + 4.07 \times 10^{-4}\alpha^{2} + 9.43 \times 10^{-4}\,\alpha + 6.63 \times 10^{-2}$.

5.3.1. Momentum analysis of stator-augmented PowerWindow

An analytical model of the original PowerWindow has been developed using BEM theory in a previous study [96]. This study develops a BEM model to analyze the power generation mechanism of a stator-augmented PowerWindow and compare that with the original PowerWindow. Figure 5.4

(a) and (b) show a flow stream tube around the original and stator-augmented PowerWindow. In the stator-augmented PowerWindow, vanes are attached to the front, middle and rear of the blades. Blades are attached horizontally to the chains and the stator vanes create a desirable α on them.

The flow stream in and around PowerWindow is divided into 5 main zones and flow characteristics of the approach wind is assumed to be changing while proceeding from one zone to the next one. The upstream flow far from PowerWindow is before Boundary 0. Boundaries 1 and 2 are the leading edge and the trailing edge of the front blades of PowerWindow. Boundaries 3 and 4 are the leading edge and trailing edge of the rear blades of PowerWindow. In Figure 5.4 (b), boundaries 1_s and 4_s are added to indicate the flow at upstream of the front stator vanes and downstream of the rear stator vanes respectively. Beyond Boundary 5 is the downstream flow far from PowerWindow. The velocity and pressure at each boundary $i = 1 \; or \; 2$ is denoted by V_i and P_i respectively.

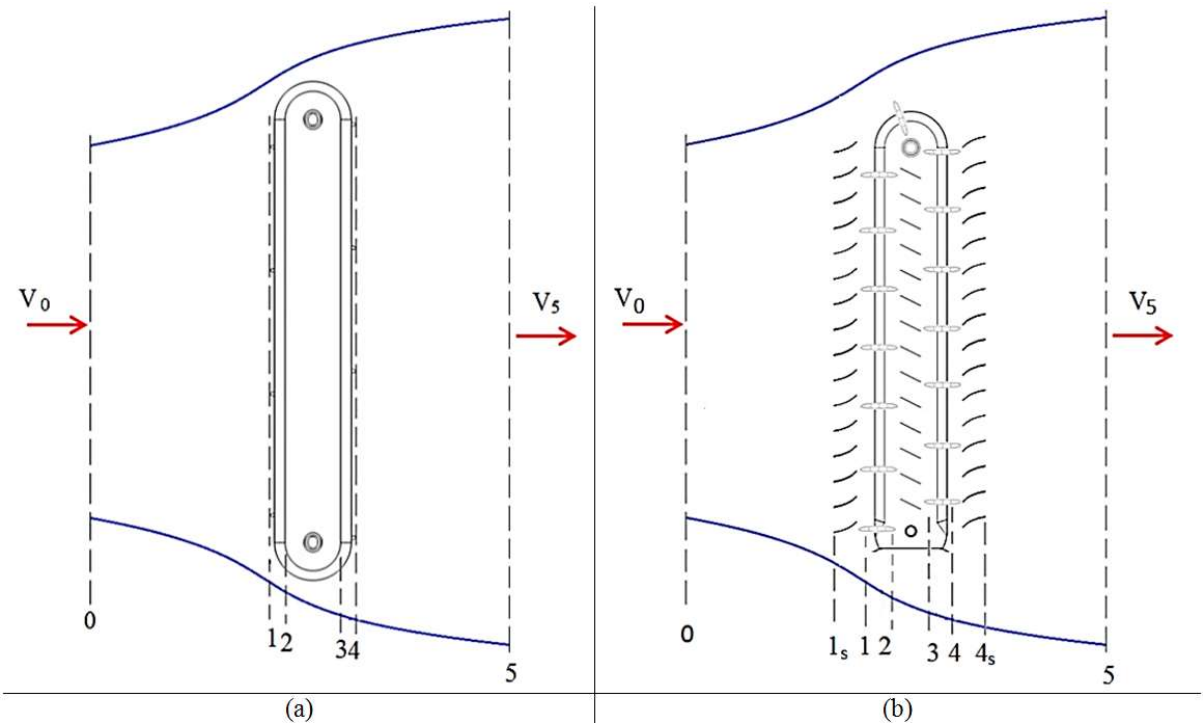

Figure 5-4: Flow stream passing through the (a)original and (b) stator-augmented PowerWindow from far upstream to far downstream.

Prior to entering PowerWindow between 0 and 1, flow expands and its velocity reduces from $V_{0,x}$ to $V_{1,x}$ and air pressure increases fromp_0 to p_1 (note that $p_0 = \; p_{atm}$). By passing across the front and rear blades (and vanes) pressure of the flow drops from $p_{\,1}$ to $p_2 (\, p_{\,2} < p_1)$ and p_3 to $\; p_4 (\, p_{\,4} < p_3)$. Within the space between the front and rear blades, the flow does not expand, so it is reasonable to assume that $V_{2,x} = V_{3,x}$. Therefore, due to the close vicinity of the stator vanes and PowerWindow blades it can be assumed that: $V_{1,x} \equiv V_{1s,x} \equiv V_{2,x} \equiv V_{3,x} \equiv V_{4,x} \equiv V_{4s,x}$. However, in the original PowerWindow: $\; p_2 = p_3$,while in the stator-augmented PowerWindow pressure drops when passing

across the middle vanes and: $p_3 < p_2$. Therefore, in the stator-augmented PowerWindow: $p_{4s} < p_4 < p_3 < p_2 < p_1 < p_{1s}$. Finally, in the second expansion air velocity reduces from $V_{4,x}$ to $V_{5,x}$ and its pressure increases from p_4 to p_5 ($p_5 = p_{atm}$).

An axial induction factor (a_f) is defined as the ratio of decrease in velocity to the approach velocity:

$$a_f = \frac{V_0 - V_1}{V_0} = \frac{V_4 - V_5}{V_0} \tag{5-6}$$

It should be noted that a unified a_f is considered for the entire blade system since the gap between the front and rear blades is not large enough for wind to recover its velocity/pressure.When $p_3 = p_2$ and $V_{1,x} = V_{2,x} = V_{3,x} = V_{4,x}$, the power extracted by the front and rear blades can be calculated by the following equations:

$$P_{front} = V_{1,x}A(p_1 - p_2) = V_{0,x}A(1 - a_f)(p_1 - p_2) \tag{5-7}$$

$$P_{front} = V_{1,x}A(p_3 - p_4) = V_{0,x}A(1 - a_f)(p_3 - p_4) \tag{5-8}$$

The pressure drop created by the stator vanes depends on the length of the vanes, their distance from each other, and the velocity of the approach wind. However, assuming inviscid flow and ignoring the pressure drop, the total wind power captured by the device can be calculated using the following equation:

$$P_{total} = V_{average}A(p_1 - p_4) \tag{5-9}$$

where A is to the frontal area of PowerWindow.

As a_f assumes equal air velocity reduction at upstream and downstream of PowerWindow, V_5 can be calculated based on V_1 as follows:

$$V_{5,x} = V_{0,x}(1 - 2a_f) \tag{5-10}$$

$V_{average}$ can be calculated as below:

$$V_{average} = \frac{V_{0,x} + V_{5,x}}{2} = \frac{V_{0,x} + V_{0,x}(1 - 2a_f)}{2} = V_{0,x}(1 - a_f) \tag{5-11}$$

$P_1 - P_4$ can be presented based on the velocities:

$$P_1 - P_4 = \frac{1}{2}\rho {V_{0,x}}^2 - \frac{1}{2}\rho {V_{5,x}}^2 = \frac{1}{2}\rho {V_{0,x}}^2\left(1 - (1 - 2a_f)^2\right) = \frac{1}{2}\rho {V_{0,x}}^2\left(1 - (1 - 4a_f + 4{a_f}^2)\right) = \frac{1}{2}\rho {V_{0,x}}^2(4a_f - 4{a_f}^2) = \frac{1}{2}\rho {V_{0,x}}^2 4a_f(1 - a_f) \tag{5-12}$$

Combining Equations 5.9, 5.11 and 5.12 and considering $P_0 = P_5 = P_{atm}$ and $V_{0,x}$=V_{wind}, P_{total} can be calculated as follows:

$$P_{PW,total} = \frac{1}{2}\rho A V_{wind}^3 4a_f\left(1 - a_f\right)^2 \quad (5\text{-}13)$$

The effect of the tangential (vertical) momentum and the induction factor (a'_f) is assumed to be negligible on power generation of PowerWindow because the front and rear blades are chained together and the inlet flow simultaneously moves the front blades up and the rear ones down with the same velocity.

5.3.2. Blade element analysis of stator-augmented PowerWindow

Blade element theory divides a blade into small elements so that the forces on each of these small elements can be individually calculated. These forces are then integrated along the entire blade and over one rotor revolution in order to obtain the forces produced by the entire propeller or rotor [82]. Figure 5.5 (a) and (b) show the aerodynamic forces on the blades of the original and stator-augmented PowerWindow, respectively. The horizontal (F_x) and vertical (F_y) forces can be calculated along the entire the span of the front and rear blades by the following equations:

$$F_x = F_{L_x} - F_{D_x} = (F_L \sin\alpha - F_D \cos\alpha) \quad (5\text{-}14)$$

$$F_y = F_{L_y} + F_{D_y} = (F_L \cos\alpha + F_D \sin\alpha) \quad (5\text{-}15)$$

Table 5.1 presents and compares F_x and F_y on the blades of the original and stator-augmented PowerWindow, and the contribution of the lift (F_L) and drag (F_D) in creating those aerodynamic forces. It can be observed that in the original PowerWindow $F_{L_x}$and F_{D_x}strengthen each other and F_{L_y} and F_{D_y} oppose each other, while in the stator-augmented PowerWindow, F_{L_x} and F_{D_x} are opposing each other and $F_{L_y}$and F_{D_y} are strengthening each other. The opposite act of F_{L_x} and F_{D_x}in the stator-augmented PowerWindow enables us to control, reduce and even neutralize the undesirable axial load as discussed later.

Table 5-1: Aerodynamic forces and α created on blades of the original and stator-augmented PowerWindow.

	Original	Stator-augmented
$F_{L_x} =$	$1/2\,\rho B {V_{rel}}^2 C_L \sin\beta$	$1/2\,\rho B {V_{rel}}^2 C_L \sin\alpha$
$F_{D_x} =$	$1/2\,\rho B {V_{rel}}^2 C_D \cos\beta$	$1/2\,\rho B {V_{rel}}^2 C_D \cos\alpha$
$F_{L_y} =$	$1/2\,\rho B {V_{rel}}^2 C_L \cos\beta$	$1/2\,\rho B {V_{rel}}^2 C_L \cos\alpha$
$F_{D_y} =$	$1/2\,\rho B {V_{rel}}^2 C_D \sin\beta$	$1/2\,\rho B {V_{rel}}^2 C_D \sin\alpha$
$F_x =$	$F_{L_x} + F_{D_x}$	$F_{L_x} - F_{D_x}$
$F_y =$	$F_{L_y} - F_{D_y}$	$F_{L_y} + F_{D_y}$
$\alpha =$	$\theta_b - \beta$	$\theta_v - \beta$

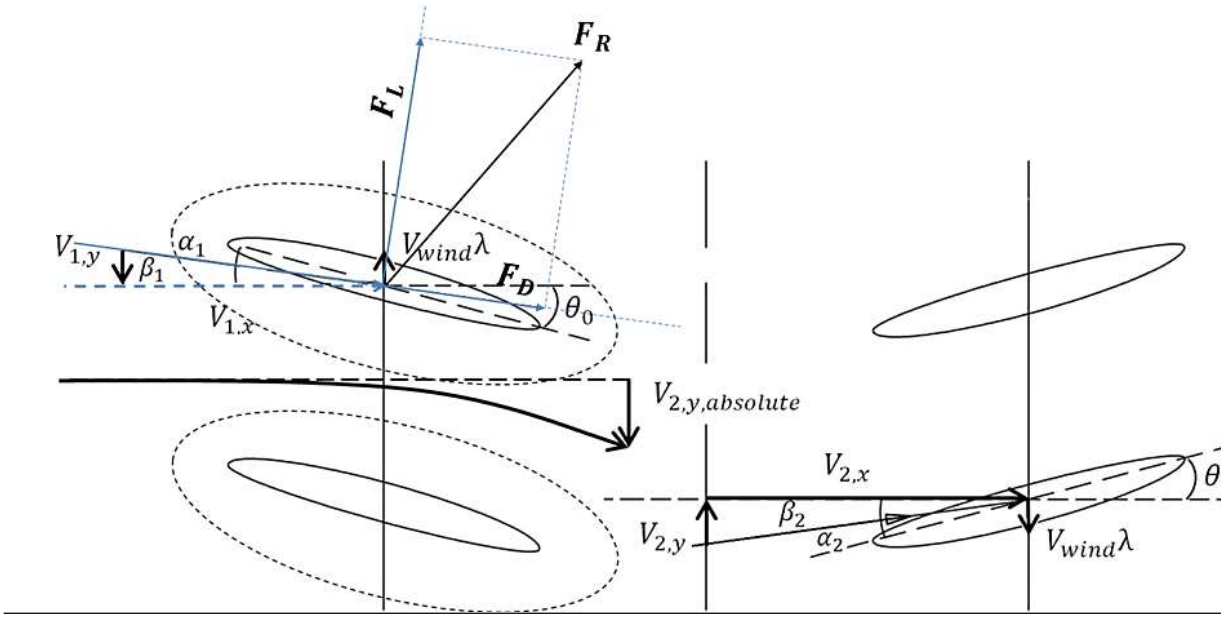

(a)

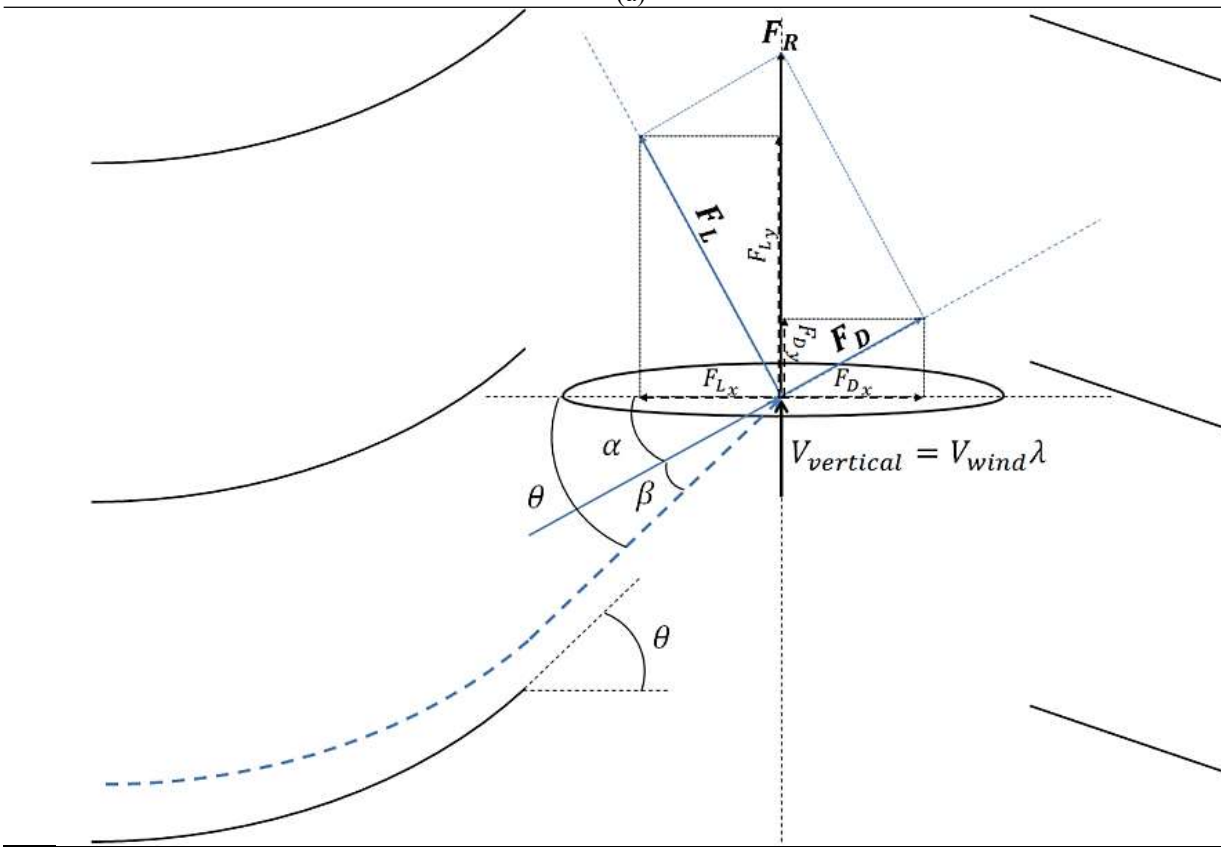

(b)

Figure 5-5: Aerodynamic forces created on the blades of the: (a) original and (b) stator-augmented PowerWindow.

The airfoil plan area is shown by B. Wind relative velocity shown by V_{rel}, can be calculated as discussed later. Effective angle (β), which is created by the perpendicular speed of the PowerWindow blades to the approach wind, as shown in Figure 4 (b), is equal to the difference between θ_v and α ($\beta = \theta_v - \alpha$), and α is obtained as described below.

Power generation by each of the front and rear blades can be calculated by multiplying the vertical force exerted on the blade (F_{yi}) by their linear speed. The total power of PowerWindow is the sum of the power generated by all the blades. As explained before, λ is the ratio of the blade's speed to the approach wind velocity:

$$\lambda = \frac{V_{blade}}{V_{wind}} \tag{5-16}$$

Power generation of a stator-augmented PowerWindow can be calculated by multiplying F_y by the linear speed of the blades ($V_{blade} = V_{wind}\lambda$) as below:

$$P_{total} = \sum_1^N \left(\frac{\rho B}{2}\right) {V_{rel}}^2 \left[C_L \cos\alpha + C_D \sin\alpha\right](V_{wind}\lambda) \tag{5-17}$$

Where V_{rel} refers to the wind relative velocity magnitude when approaching the PowerWindow blades and can be calculated using the equations below:

$${V_{rel}}^2 = {V_x}^2 + {V_y}^2 \tag{5-18}$$

$$V_x = V_{wind}\left(1 - a_f\right) \tag{5-19}$$

$$V_y = V_x \tan\alpha - \lambda V_{wind} = V_{wind}\left(\left(1 - a_f\right)\tan\alpha - \lambda\right) \tag{5-20}$$

The angle of attack α over the front and rear blades ($i = 1{,}2$) can be calculated using the equation below:

$$\beta = \tan^{-1}\left(\lambda/\left(1 - a_f\right)\right) \tag{5-21}$$

$$\alpha_i = \alpha_{v,i} - \beta \tag{5-22}$$

When $\theta_{v,i}$ is the leading angle of the stator vanes (angle of the flow from the horizontal axis which the stator vanes have created).The value of $\theta_{v,i}$ should be the same for the front and rear stator vanes ($\theta_{v,1} = \theta_{v,3}$) but it can be different for the middle one ($\theta_{v,2}$).

According to Equation 5.15, power generation by the front blades of the stator-augmented PowerWindow can be calculated as follows:

$$P_{front} = N\left(\frac{\rho B}{2}\right)\lambda \mathrm{V_{wind}}^3\left(\left(1-a_f\right)^2+\left(\left(1-a_f\right)\tan\theta_{v,1}-\lambda\right)^2\right)\left[C_{L_{\alpha 1}}\cos\left(\theta_{v,1}-\tan^{-1}\left(\lambda/\left(1-a_f\right)\right)\right)+C_{D_{\alpha 1}}\sin\left(\theta_{v,1}-\tan^{-1}\left(\lambda/(1-a_f)\right)\right)\right] \quad (5\text{-}23)$$

As explained in the previous study[104], the direction of the flow approaching the rear blades is affected by the front blades, and β_2 and α_2 may not be equal to β_1 and α_1, even if: $\theta_{v,1} = \theta_{v,2} = \theta_{v,3}$.Using the affected flow ratio (ε) investigated in another study[103], β_2 and α_2 can be calculated as follow:

$$\beta_2 = \tan^{-1}\left((1+\varepsilon)\lambda/\left(1-a_f\right)\right) \quad (5\text{-}24)$$

$$\alpha_2 = \alpha_{v,2} - \tan^{-1}\left((1+\varepsilon)\lambda/\left(1-a_f\right)\right) \quad (5\text{-}25)$$

Using β_2 in equation 5.25, power generation by the rear blades of the stator-augmented PowerWindow can be calculated as follows:

$$P_{rear} = \left(\frac{\rho B}{2}\right)\lambda \mathrm{V_{wind}}^3\left(\left(1-a_f\right)^2+\left(\left(1-a_f\right)\tan\theta_{v,2}-(1+\varepsilon)\lambda\right)^2\right)\left[C_{L_{\alpha 2}}\cos\left(\theta_{v,2}-\tan^{-1}\left((1+\varepsilon)\lambda/\left(1-a_f\right)\right)\right)+C_{D_{\alpha 2}}\sin\left(\theta_{v,2}-\tan^{-1}\left((1+\varepsilon)\lambda/\left(1-a_f\right)\right)\right)\right] \quad (5\text{-}26)$$

5.3.3. Blade element momentum analysis of stator-augmented PowerWindow

Equating the total power generation (Equation 5.13) from momentum theory with the total power generation of the front and rear blades (Equations 5.23 and 5.26) determines a_f and then the power generation of the front and rear blades of the stator-augmented PowerWindow as follows:

$$\tfrac{1}{2}\rho A \mathrm{V_{wind}}^3 4a_f\left(1-a_f\right)^2 = N\left(\frac{\rho B}{2}\right)\lambda \mathrm{V_{wind}}^3\left[\left(\left(1-a_f\right)^2+\left(\left(1-a_f\right)\tan\theta_{v,1}-\lambda\right)^2\right)\left[C_{L_{\alpha 1}}\cos\left(\theta_{v,1}-\tan^{-1}\left(\frac{\lambda}{(1-a_f)}\right)\right)+C_{D_{\alpha 1}}\sin\left(\theta_{v,1}-\tan^{-1}\left(\frac{\lambda}{(1-a_f)}\right)\right)\right]+\left(\left(1-a_f\right)^2+\left(\left(1-a_f\right)\tan\theta_{v,2}-(1+\varepsilon)\lambda\right)^2\right)\left[C_{L_{\alpha 2}}\cos\left(\theta_{v,2}-\tan^{-1}\left(\lambda/\left(1-a_f\right)\right)\right)+C_{D_{\alpha 2}}\sin\left(\theta_{v,2}-\tan^{-1}\left(\lambda/\left(1-a_f\right)\right)\right)\right]\right] \quad (5\text{-}27)$$

Table 5.2 compares β_i and α_i of the original and stator-augmented PowerWindow and power generation by their front and rear blades.

Adjusting the orientation of the stator vanes can change the contribution of the lift (F_L) and drag (F_D) on the resultant force (F_R) over the blades and significantly increase C_P and decrease C_T of PowerWindow. Using stator vanes may be an effective approach for creating the optimum resultant force on the PowerWindow blades. An ideal F_R on the PowerWindow blades has no horizontal

component and is purely vertical. In the stator-augmented PowerWindow a zero C_T will be achieved when F_{L_x}andF_{D_x} neutralize each other ($F_x = F_{D_x} \rightarrow F_{R_x} = 0$) which needs the following condition:

$$F_L \sin\alpha = F_D \cos\alpha \rightarrow \frac{\sin}{\cos\alpha} = \frac{F_D}{F_L} = \tan\alpha \tag{5-28}$$

According to Table 5.1, θ_i which results in $F_x = 0$ hence $C_T = 0$ can be calculated as follows:

$$\tan\alpha = \frac{C_D}{C_L} \rightarrow \tan\left(\theta_{v,i} - \tan^{-1}\left(\lambda/(1-a_f)\right)\right) = \frac{C_D\left[\theta_{v,i} - \tan^{-1}\left(\lambda/(1-a_f)\right)\right]}{C_L\left[\theta_{v,i} - \tan^{-1}\left(\lambda/(1-a_f)\right)\right]} \tag{5-29}$$

$$\theta_{v,i} - \tan^{-1}\frac{C_D\left[\theta_{v,i} - \tan^{-1}\left(\lambda/(1-a_f)\right)\right]}{C_L\left[\theta_{v,i} - \tan^{-1}\left(\lambda/(1-a_f)\right)\right]} = \tan^{-1}\left(\lambda/(1-a_f)\right) \tag{5-30}$$

Table 5-2: Aerodynamic parameters and power generation of the original and stator-augmented PowerWindow

	Original	Stator-augmented
$\beta_1 =$	$tan^{-1}\left(\lambda/(1-a_f)\right)$	$\tan^{-1}\left(\lambda/(1-a_f)\right)$
$\alpha_1 =$	$\theta_b - \beta_1$	$\theta_{v,1} - \beta_1$
$\beta_2 =$	$tan^{-1}\left(\frac{\left((\varepsilon+1)\lambda - \varepsilon(1-a_f)tan\theta_b\right)}{(1-a_f)}\right)$	$\tan^{-1}\left((1+\varepsilon)\lambda/(1-a_f)\right)$
$\alpha_2 =$	$\theta_b - \beta_2$	$\theta_{v,2} - \beta_2$
$P_{front} =$	$N\left(\frac{\rho B}{2}\right)V_{wind}{}^3\,\lambda\left((1-a_f)^2 + \lambda^2\right)\left[C_{L_{\alpha1}}cos\left(tan^{-1}\left(\frac{\lambda}{(1-a_f)}\right)\right) - C_{D_{\alpha1}}sin\left(tan^{-1}\left(\frac{\lambda}{(1-a_f)}\right)\right)\right]$	$N\left(\frac{\rho B}{2}\right)\lambda \mathrm{V}_{\mathrm{wind}}{}^3\left((1-a_f)^2 + \left((1-a_f)\tan\theta_{v,1} - \lambda\right)^2\right)\left[C_{L_{\alpha1}}\cos\left(\theta_{v,1} - \tan^{-1}\left(\lambda/(1-a_f)\right)\right) + C_{D_{\alpha1}}\sin\left(\theta_{v,1} - \tan^{-1}\left(\lambda/(1-a_f)\right)\right)\right]$
$P_{rear} =$	$N\left(\frac{\rho B}{2}\right)V_{wind}{}^3\,\lambda\left((1-a_f)^2 + \left((\varepsilon+1)\lambda - \varepsilon(1-a_f)tan\theta_b\right)^2\right)\left[C_{L_{\alpha2}}cos\left(tan^{-1}\left(\frac{\left((\varepsilon+1)\lambda - \varepsilon(1-a_f)tan\theta_b\right)}{(1-a_f)}\right)\right) - C_{D_{\alpha2}}sin\left(tan^{-1}\left(\frac{\left((\varepsilon+1)\lambda - \varepsilon(1-a_f)tan\theta_b\right)}{(1-a_f)}\right)\right)\right]$	$N\left(\frac{\rho B}{2}\right)\lambda \mathrm{V}_{\mathrm{wind}}{}^3\left((1-a_f)^2 + \left((1-a_f)\tan\theta_{v,2} - (1+\varepsilon)\lambda\right)^2\right)\left[C_{L_{\alpha2}}\cos\left(\theta_{v,2} - \tan^{-1}\left((1+\varepsilon)\lambda/(1-a_f)\right)\right) + C_{D_{\alpha2}}\sin\left(\theta_{v,2} - \tan^{-1}\left((1+\varepsilon)\lambda/(1-a_f)\right)\right)\right]$

In the conventional wind turbines and the original PowerWindow model, increasing C_P is always associated with increasing C_T, while in the stator-augmented PowerWindow, C_P can be increased while decreasing C_T, which is highly desirable. Utilising the developed BEM model and developing an active control system for adjusting the stator vanes direction, the optimum $\theta_{v,i}$ for the stator vanes

can be calculated and adjusted, which based on the approach wind velocity maximizes C_P and minimizes C_T for the stator-augmented PowerWindow. Moreover, as discussed earlier, another advantage of the stator –augmented model is that the direction of rotation of the turbine remains the same regardless of the direction of the approach wind.

5.4. Computational fluid dynamic model

5.4.1. Transition – turbulence model

In CFD simulations, the accuracy of flow separation prediction on every blade is significantly dependent on selecting an appropriate viscous model. The shear stress transport (SST) models have been validated extensively for separating 2D flows with Reynolds-averaged Navier–Stokes (RANS) models [83]. Menter [85] suggests that flow over the rotor blades can be subject to a significant region of laminar-turbulence transition and because the transition process can affect the separation behavior of the boundary layer on the blade surface v2-f (transition SST) model is the best model in case of separation. Based on flow over a flat plate [97], Reynold number of 7.1×10^4 is calculated on the PowerWindow blades in the wind tunnel test, which indicates that blades are located in a laminar-turbulent transition region. Therefore, the v2-f model seems to be the most accurate model for these simulations.

The v2-f model is a modified SST k-ω RANS turbulence model by the addition of two other transport equations for γ (the intermittency) and the transition onset criteria [85]. Menter [85] expressed that this approach has two main advantages. The first is that it improves the robustness of the model because the intermittency does not enter directly into the momentum equations. The second advantage is that it allows the model to predict the effects of high freestream turbulence levels on buffeted laminar boundary layers. The reason is that for large free stream eddy viscosities, the small values of intermittency in the boundary layer do not cancel out the local eddy viscosity.

5.4.2. Mesh and boundary conditions

In this study, stator vanes at the front and rear of PowerWindow are designed with a curved shape (24° circle arc) to minimize flow separation from their surface. As a simple preliminary configuration, the stator vanes have been selected to have the same length and distance from each other as the cord length of the blades (150mm). The $2m \times 2m \times 0.8m$ stator-augmented PowerWindow was located in a $6m \times 8m \times 14m$ domain having $3m$ distance from the inlet and $10m$ from the outlet.

In CFD simulations, higher mesh quality is primarily achievable by using finer structured mesh. But, a fully structured mesh usually needs numerous elements which is computationally expensive. In order to achieve a balance between solution accuracy and calculation time, a combination of structured and unstructured mesh is used in this study. This technique helps to decrease the number of elements while having a high-quality mesh around the body [13]. Therefore, as previously investigated in the mesh independence study for the CFD model of the PowerWindow prototype [98], 200 structured rectangular elements (1.5mm length of each cell along the cord-wise direction), with y^+ below 1.0, are generated adjacent to the blade surface. This structured region, as shown in Figure 6 (c), is connected to the surrounding structured region via unstructured triangular elements with a maximum skewness of 0.17, as shown in Figure 6 (b). The 3D model contains 4,078,320 elements in the original model and 5,128,740 elements in the stator-augmented model. In both cases y^+ is below 300 over all the walls.

The frame of the hybrid region containing the front and rear blades is selected as multiple reference frame (MRF) which can move vertically within the domain. The boundaries of the blades are set to a moving wall with zero velocity relative to their adjacent cells. As a result, their vertical velocity would be equal to the MRF surrounding cells. The inlet boundary condition has a constant free stream velocity of $8m.s^{-1}$ and the outlet boundary of the domain is set to atmospheric pressure. Turbulence intensity of 5% and turbulence viscosity ratio (the ratio of turbulent to laminar viscosity) of 10 is set for inlet, and outflow boundary condition was set for the outlet. The magnitude of the inlet velocity and turbulent intensity were selected to be consistent with the wind tunnel condition where the first experimental test was undertaken (on the original PowerWindow Prototype). The standard pressure correction method and a first-order upwind scheme are used. The top and bottom boundaries of the domain are selected as a stationary wall. Gambit [86] is used as the mesh generation tool in this study. The CFD simulations are at the prototype scale, thus avoiding the need to accommodate any scaling dictated by similarity criteria.

It should be noted that λ cannot be determined automatically, it needs to be manually increased. The value of λ that results in the maximum power generation gives the ideal operating λ.

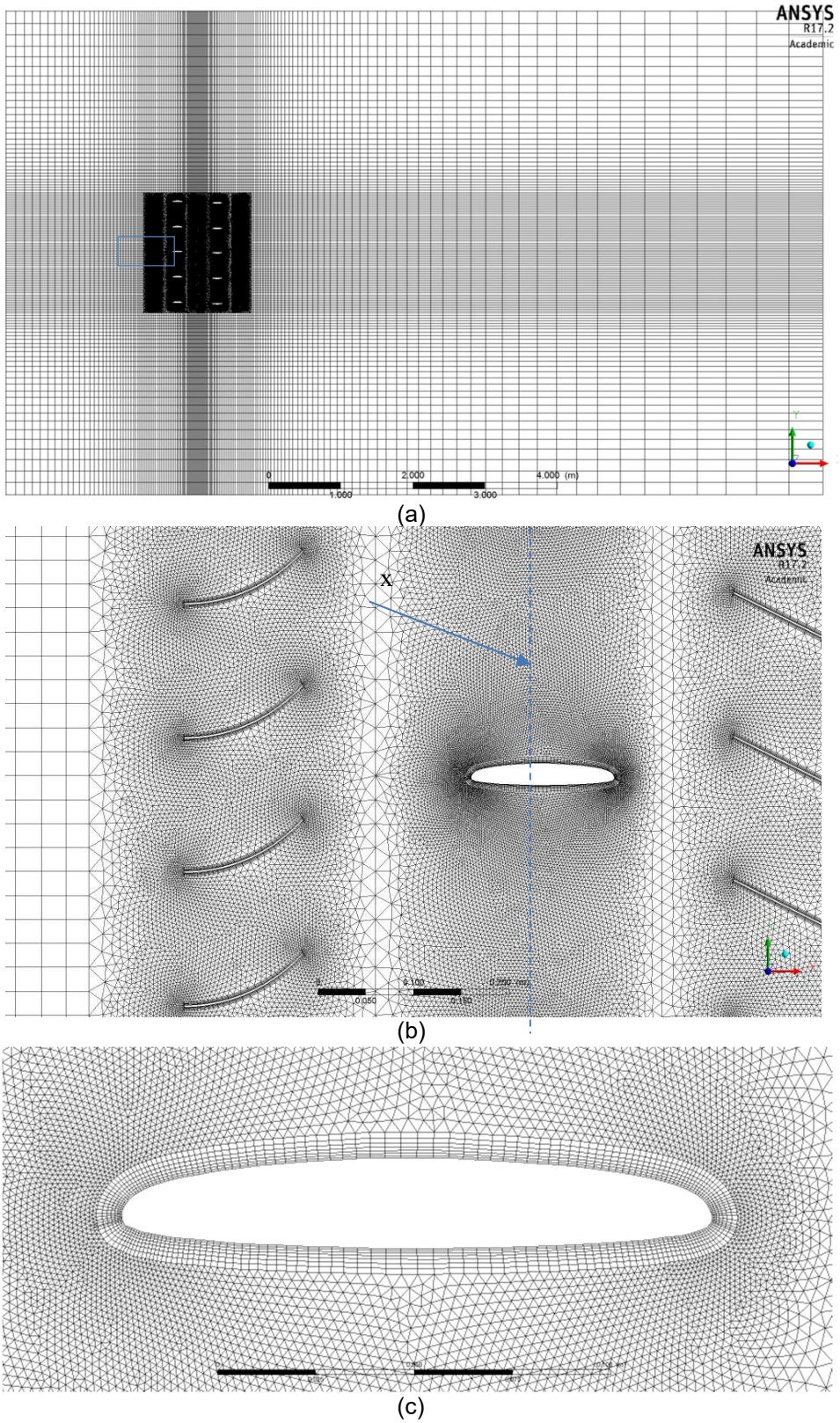

Figure 5-6: (a) Structured mesh generated around the unstructured region. (b) Combination of structured and unstructured mesh around the blades (a blue dash line shows x=0). (c) Fine structured rectangular elements adjacent to the blade surface.

5.5. Results and discussion

5.5.1. Power generation of stator-augmented PowerWindow model

In order to achieve similar power generation by the front and rear blades in the stator-augmented PowerWindow, in the preliminary configuration $\theta_{v,1}$ and $\theta_{v,3}$ were selected to have the same value as θ_2 ($\theta_{v,1} = \theta_{v,2} = \theta_{v,3} = 24°$). Number of blades are the same as the original PowerWindow which corresponds to the solidity: $\sigma = 0.428$. The value of ε is obtained from another study [103] and used in the developed BEM model. In order to validate the BEM model of the stator-augmented PowerWindow, the C_P achieved by this model has been compared with results obtained by the CFD model with the same approach wind velocity of $8m.s^{-1}$, and shown in Figure 5.7. P_f, P_r and P_t indicate the power generation performance of the front blades, rear blades and the total amount.

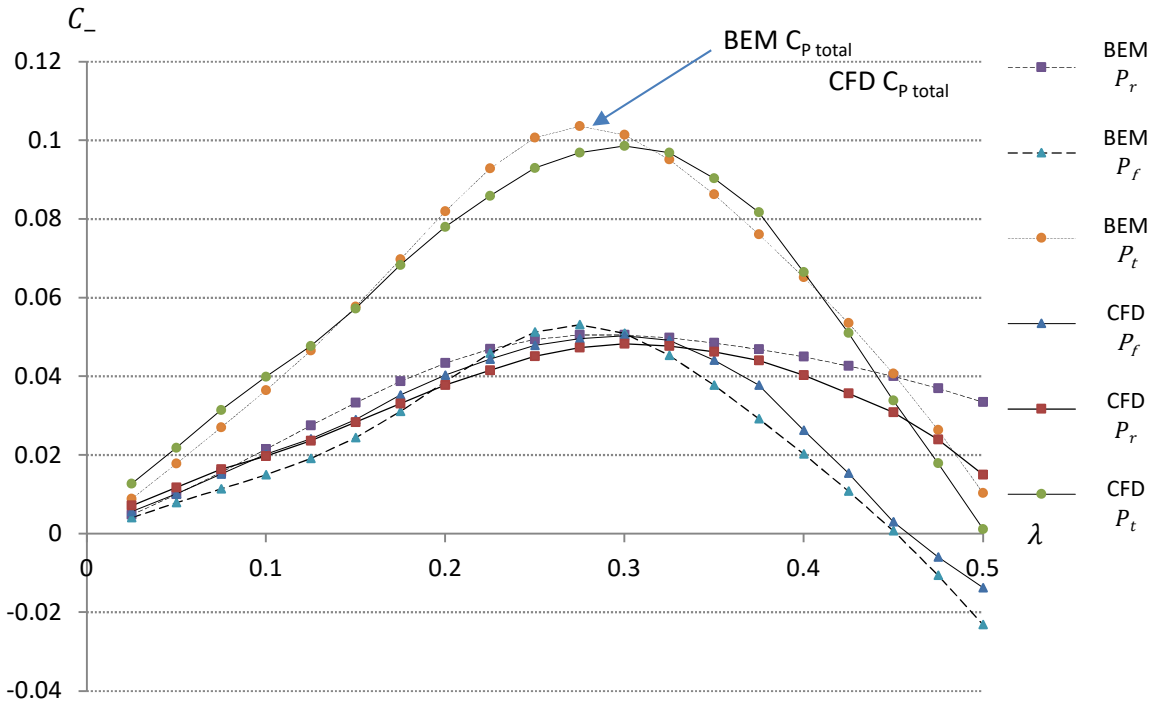

Figure 5-7: C_P of stator-aufmented PowerWindow when σ = 0.428 versus λ when $\theta_{v,1} = \theta_{v,2} = \theta_{v,3} = 24°$ using modified BEM and CFD models.

Figure 5.7 shows a reasonable agreement between the results achieved by the CFD model and those calculated by the modified BEM model. Both models have also detected different contributions to the total power generation for the front and rear blades at different λ, while $\theta_{v,1}$ and $\theta_{v,3}$ were selected to have the same value as $\theta_{v,2}$. The reason is that α_1 is dependent on $\theta_{v,1}, \alpha_f$, and λ (as shown in Equation 5.21 and 5.22) while $\alpha_2$is also dependent on ε (as shown in Equation 24 and 25). However, an active control system could adjust $\theta_{v,2}$ so that $\alpha_1 = \alpha_2$. It should be noted that the

results obtained by the BEM model are based on a number of simplifying assumptions, including neglecting viscous effects. Furthermore, simplifications such as selecting first-order scheme or considering uniform velocity profile at the inlet are generally reflected in the accuracy of the computed results obtained by the CFD model. Although the current results may have some inaccuracies in predicting the aerodynamic performance of the stator-augmented LCWT, they are considered sufficiently reliable to highlight the overall effect of stator vanes on the performance of the device.

5.5.2. Aerodynamic forces of stator-augmented PowerWindow model

Attaching the stator vanes to the PowerWindow blades increases friction and decreases the average velocity within the device, which is undesirable. Meanwhile, the stator vanes by changing the flow direction increase the vertical component of velocity toward the blades, which is desirable for power generation. This change demands a higher overall pressure gradient across the stator-augmented model compared with the original PowerWindow. Figure 5.8 (a) and (b) have plotted velocity and pressure contours in terms of velocity ratio (R_V) and surface pressure coefficient (C_{SP}) in and around the stator-augmented model. C_{SP} shows the ratio of the local air pressure to the dynamic pressure of the free stream and $R_V$shows the ratio of the local air velocity to the free stream velocity:

$$C_{SP} = \frac{P_{static}}{0.5\rho V^2} \tag{5-31}$$

$$R_V = \frac{V_{local}}{V_{wind}} \tag{5-32}$$

Flow streamlines are also mapped over both the C_{SP} and R_V contours. As can be seen in Figure 5.8 (a) the front stator vanes have effectively redirected the flow upward, which as expected increases the lift force over the front blades. However, the bottom blade has been located beneath the flow path which means that more stator vanes need to be attached below the front ones to cover the bottom blade. Between the front and rear blades, the middle stator vanes have redirected the flow downward (toward the rear blades). Some flow detachment can be observed over the top stator vanes which as shown in Figure 5.8 (b) have created a low-pressure region there. Such flow detachment is not desirable as it partially blocks the flow path and decreases the uniformity of the flow approaching the rear blades. One possible solution to reduce flow detachment from the surface of the middle vane is to use symmetric airfoil instead of regular flat vanes.

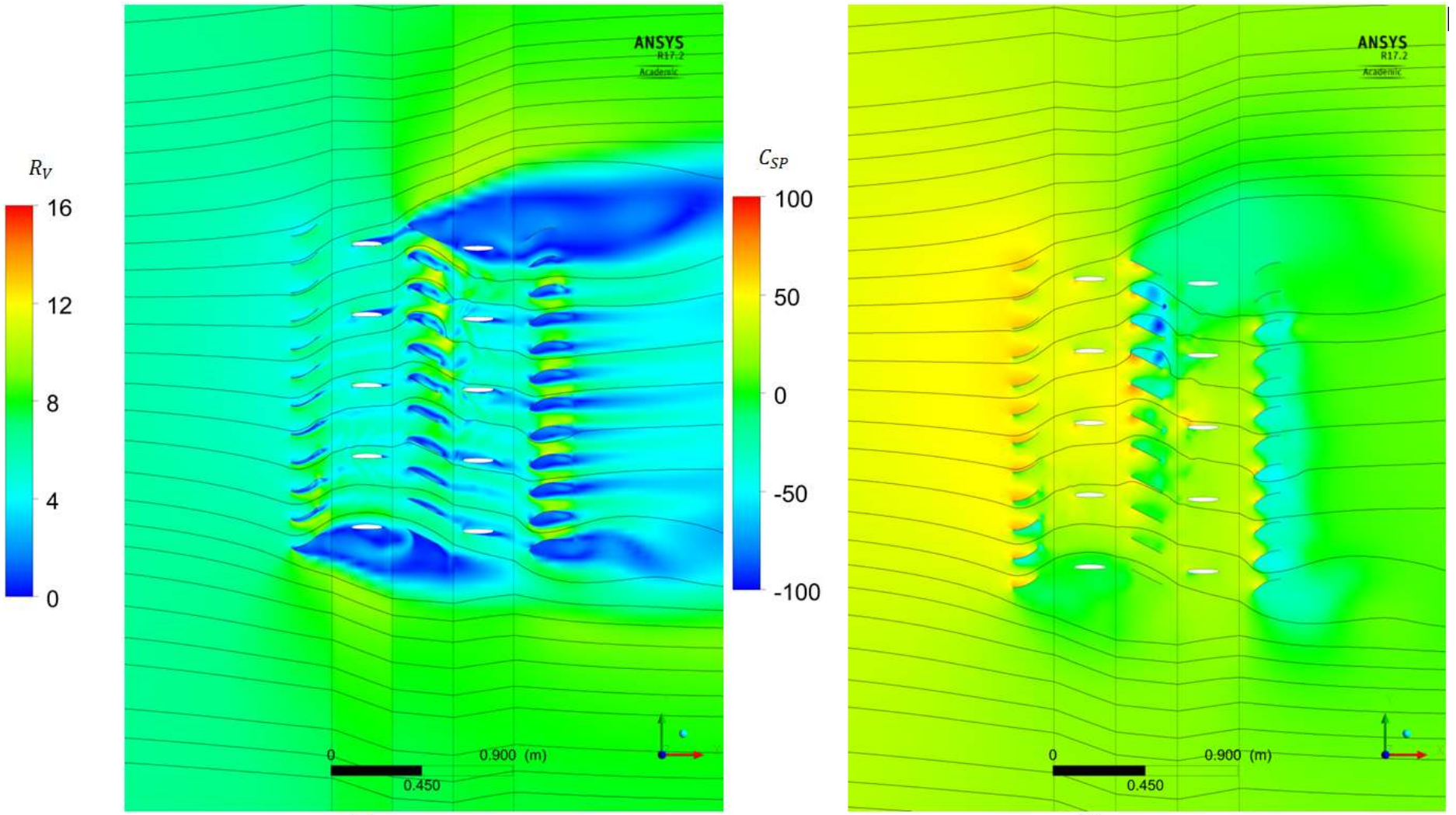

Figure 5-8: (a)R_V and (b) C_{SP} contours in and around the blades of the stator-augmented PowerWindow.

Similar to the bottom blade of the front ones, the top blades of the rear ones have been located outside the flow path which means that more stator vanes need to be attached above the middle ones to cover the top blade. As can be observed in both Figures 5.8 (a) and (b), flow detachment is created beneath the rear stator vanes which has created a low-pressure region at their downstream. Although it seems that the rear stator vanes have successfully redirected flow to the windward direction, they have resulted in high-pressure gradient there. Therefore, in future studies, the length of the front and rear vanes can be altered and/or the curvature of the vanes can be modified to minimize the flow detachment at the outlet.

For investigating the effect of changing flow direction on the aerodynamic forces over the PowerWindow blades, the vertical and axial (windward) aerodynamic forces over the blades of the stator-augmented configuration have been compared with the prototype configuration using CFD simulations.

Figure 5.9 shows C_T of the original and stator-augmented PowerWindow versus λ. T_f and T_r indicate the axial (windward) force over the front and rear blades. Comparison of F_x between the original and stator-augmented PowerWindow presented in Table 1 shows that the F_x of the stator-augmented PowerWindow is lower than the original one, and F_x would be negative ($F_x < 0$) if $F_D \cos\alpha$ be greater than $F_L \sin\alpha$ ($F_L \sin\alpha < F_D \cos\alpha$) which results in a negative C_T.

As shown later in the next figure (Figure 5.10), the operating point is around $0.15 - 0.175$ for the original PowerWindow and $0.275 - 0.325$ for the stator-augmented one. As a result, C_T would be around 0.035 for the original PowerWindow and -0.005 forthe stator-augmented one. Figure 5.9 shows that even at other λs, C_T is very low ($-0.005 < C_T < 0.005$) in the stator-augmented PowerWindow. The revealed result shows that the stator vanes are able to minimize/neutralize C_T on PowerWindow. However, C_T has not been completely neutralized by the proposed design and further improvements on the vanes are needed to make that possible.

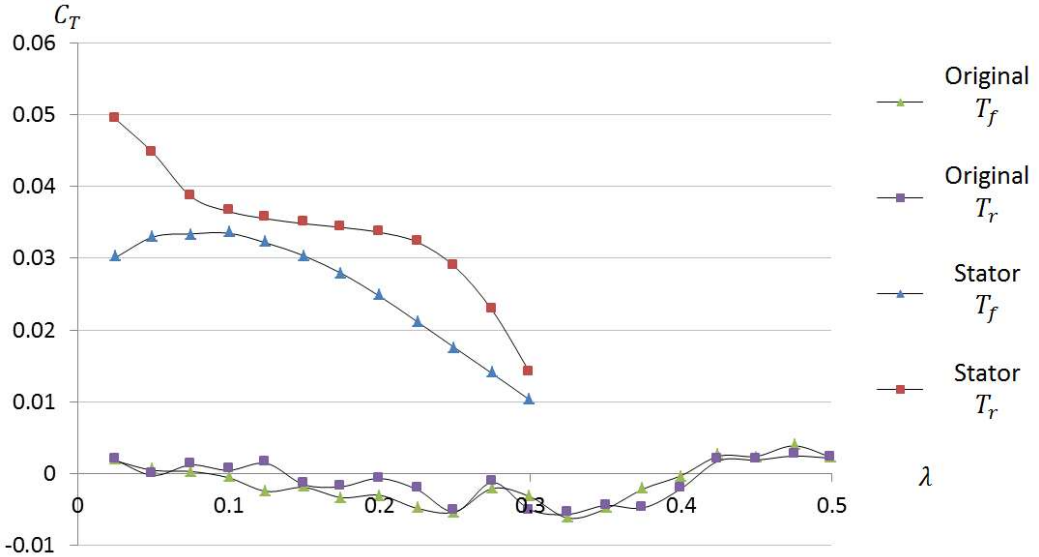

Figure 5-9: C_T on the original and stator-augmented PowerWindow versus λ.

Figure 5.10 compares C_P of the stator-augmented PowerWindow with the contribution of the front and rear blades in the total C_P with the original PowerWindow from another study [104]. P_f, P_r and P_t indicate the power generation by the front blades, rear blades and the total power generation. As a comparison between the experimental test on the prototype and its CFD model has shown [7], operating λ is expected to be around the optimum λ in PowerWindow, where the maximum C_P is achieved. As can be seen, using the stator vanes, PowerWindow can achieve higher C_P (around 10%) at much lower C_T. This result is very valuable because the main obstacle against enhancing C_P of the original model of PowerWindow with increasing α is the destructive axial force which would be inevitably created by increasing θ_b.

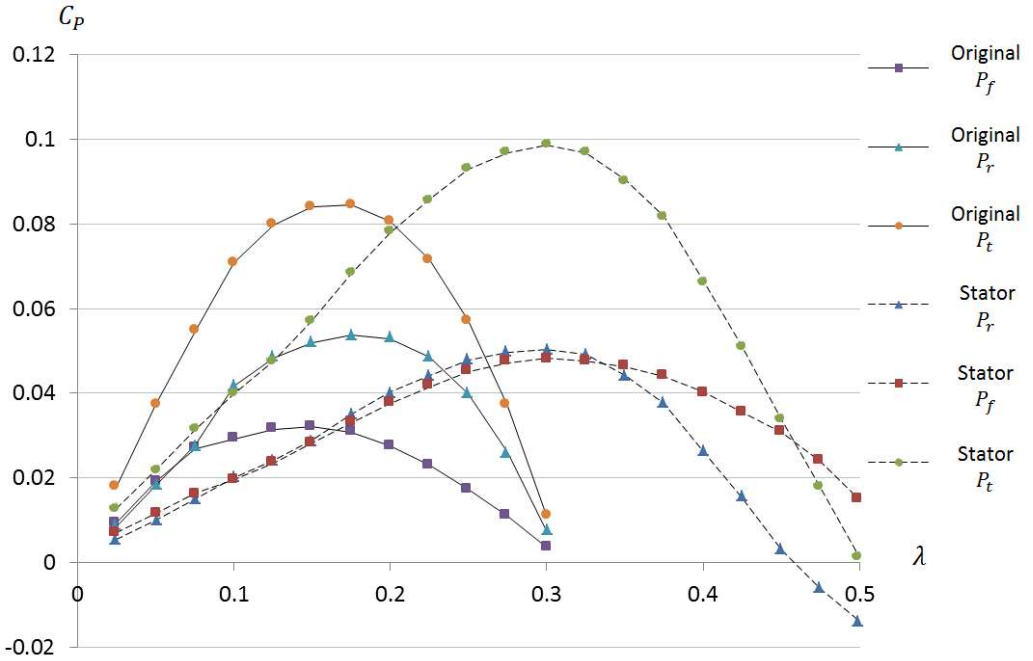

Figure 10: C_P of the original and stator-augmented PowerWindow versusλ.

As shown in the previous study [7], the relative position of the front blades to the rear ones can slightly change the aerodynamic forces on the LCWT blades. A similar interaction is expected between the vanes and the blades in the stator-augmented LCWT. The effect of the configuration of stator vanes and the relative position of the vanes to the blades will be investigated in future studies.

5.6. Conclusion

This study has proposed to attach stator vanes to PowerWindow, a linear cascade wind turbine, to improve the flow direction in the device. The stator vanes by controlling the angle of attack increase the acting force (vertical load) and decrease the undesirable force (axial load) on PowerWindow blades. An Analytical model using blade element momentum theory has been developed for the new configuration referred to as stator-augmented PowerWindow. The analytical model has been verified by a computational fluid dynamic model. The results have shown that the stator vanes are able to minimize/neutralize the undesirable force (axial load) on PowerWindow so that the thrust coefficient decreases from 0.035 in the original model to -0.005 in the stator-augmented one. It is shown that the stator vanes by increasing the acting force (vertical load) on PowerWindow blades have simultaneously enhanced the coefficient of performance from 0.85 to 0.1. It is also shown that another advantage of using stator vanes to control the angle of attack is that the direction of rotation of PowerWindow will remain the same regardless of the wind direction. In the original PowerWindow, when the wind direction is reversed, the turbine will also rotate in the opposite direction. The stator-augmented design, therefore, will be particularly useful for fixed in-building installations.

CHAPTER 6. BUILDING INTEGRATION OF STATOR_AUGMENTED POWERWINDOW, A LINEAR CASCADE WIND TURBINE

A reprint of this study entitles 'Building Integration of stator-augmented PowerWindow, a Linear Cascade Wind Turbine', Jafari SAH, Hassanli S, Kwok KCS, Safaei F, Kosasih B, Zhao M, published by the Journal of Energy Science & Engineering, 2019; 00: 1-18 (https://doi.org/10.1002/ese3.300) is appended in Appendix B4.

6.1. Introduction

Installation of small wind turbines on buildings can potentially generate a part of the energy demand in cities [47, 68]. One of the advantages of the application of wind turbines in the urban environment is the power generation at the point of use, and the reduction of the energy loss and cost of power distribution network [93]. Studies have shown that the performance of urban wind turbines strongly depends on the type and the location of the turbines. For example, horizontal axis wind turbines (HAWT) have better performance in flat-terrain applications, whereas vertical axis wind turbines VAWT show superior performance in high-density building environments [66]. Flow characteristics in urban areas are most often dominated by the boundary layer, which is characterized by unsteady turbulent flow passing over buildings and structures. Figure 6.1 shows the development of the surface boundary layer in an urban, suburban and open country terrain. The boundary layer development in an urban area is known to be the least well-developed. Wind turbines are generally operating in relatively low average wind speeds in urban areas [1]. Suitable locations in and around buildings currently being used for integrating wind turbine systems can be categorized into four groups: in between two buildings; inside a through-building opening; mounted on the roof; integrated into the façade of a building.

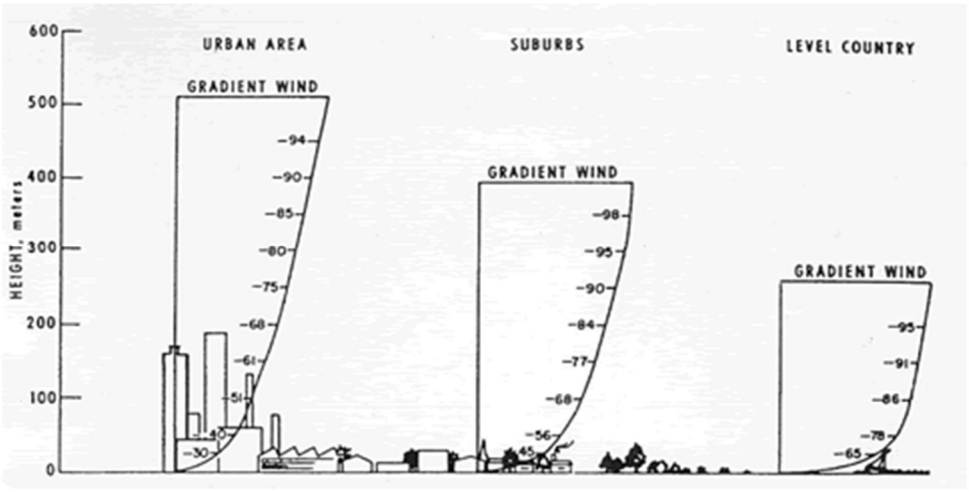

Figure 6-1: Development of surface boundary layer in an urban, suburban and country terrain [1].

Smaller wind turbines are usually mounted on the roofs and on the corners of buildings [109]. Abohela et al. [110] have investigated the effect of roof shape, wind direction, building height and urban configuration on energy yield and the positioning of roof-mounted wind turbines. This analysis has shown that the positioning of a roof-mounted wind turbine, for a particular roof shape, can enhance the energy harvesting from the acceleration of the wind above the building. Integrating a wind turbine system to the skin of buildings is also a possibility. It has been shown that by using

double skin façade for wind energy harvesting, the free-stream wind speed can be amplified up to a maximum of 1.8 times inside the corridors of the double skin façade [93-95].

Although the roughness of the terrain in urban environments can reduce the velocity and increase the turbulence of the flow compared to open spaces, it was reported that mounting turbines at high elevations on buildings may provide a perfect opportunity for onsite wind power harvesting [3]. The application of through-building openings for wind energy harvesting was investigated for Pearl River Tower [47] which was then extended by accommodating site-specific local wind climate data. The results indicated that power generation was improved, particularly at locations where the average wind speed was lower, and the wind was more turbulent.

Dannecker and Grant [111] developed a prototype of a building-mounted ducted wind turbine. They also conducted a series of wind tunnel and numerical tests to evaluate pressure and velocity for different duct configurations. These tests achieved velocity enhancements up to a factor of 1.3 for a wide range of incident wind angles up to ±60°. Grant and Kelly [112] developed a mathematical model by taking into account the pressure drop as a result of considering a wind turbine to predict the power output of a similar building-mounted ducted wind turbine. The annual energy budget of the same wind turbine system was assessed by Grant et al. [69], and it was concluded that retro-fitting ducted wind turbines into existing buildings has great potential to efficiently harvesting wind energy. By conducting a series of wind tunnel tests and CFD simulations, Chong et al. [113] studied the performance of a Sistan wind turbine with an augmented guide vane as a part of an integrated device for renewable energy harvesting in high-rise buildings. They concluded that the Power Augmentation Guide Vane could increase the rotational speed, torque and power output of a Sistan rotor by a factor of 1.75, 2.88 and 5.80, respectively. More recently, Krishnan and Paraschivoiu [114] studied the optimisation of the power coefficient of a building-mounted diffusor-augmented vertical axis wind turbine. They established that a performance enhancement factor of 2.5 could be achieved when the shroud was integrated with the wind turbine."

A properly designed through-building opening has more reliable flow characteristics because: (i) it channels the flow within a wide range of incident angles and makes it almost unidirectional; (ii) it acts similar to a high-pass turbulence filter and blocks the low-frequency turbulence; (iii) the confined area of opening limits high-pass turbulence intensity, compared with the outside free-stream flow. Therefore, a through-building opening has been chosen as the installation location for the selected wind turbines in this study.

This study aims to investigate the power generation of a linear cascade wind turbine (LCWT) integrated with through-building openings. LCWTs are a new generation of wind turbines. Unlike the conventional HAWTs and VAWTs, the blades of LCWTs do not rotate around the rotor axis but

move translationally in a direction perpendicular to the approach wind direction. PowerWindow [46], shown in Figure 6.2 (a), is a compact modular LCWT which can easily fit into any designated area in a building. The previous study has shown that PowerWindow has a greater performance in a ducted area compared with the free-stream condition [103]. Stator-augmented PowerWindow is an improved version of this LCWT. In this configuration as shown in Figure 6.2 (b), stator vanes are attached to the device. The stator vanes control the flow direction on the blades by (i) decreasing the undesirable axial force on the blades, (ii) enhancing its power generation by increasing the vertical force on the blades, and (iii) enabling the device to keep its operational direction when subjected to bi-directional approach wind [104]. This LCWT is also capable of generating electricity when the ratio of blade speed to wind speed (referred to as the blade speed ratio, λ) is quite low. These characteristics make stator-augmented PowerWindow a suitable and promising wind turbine to be integrated inside through-building openings.

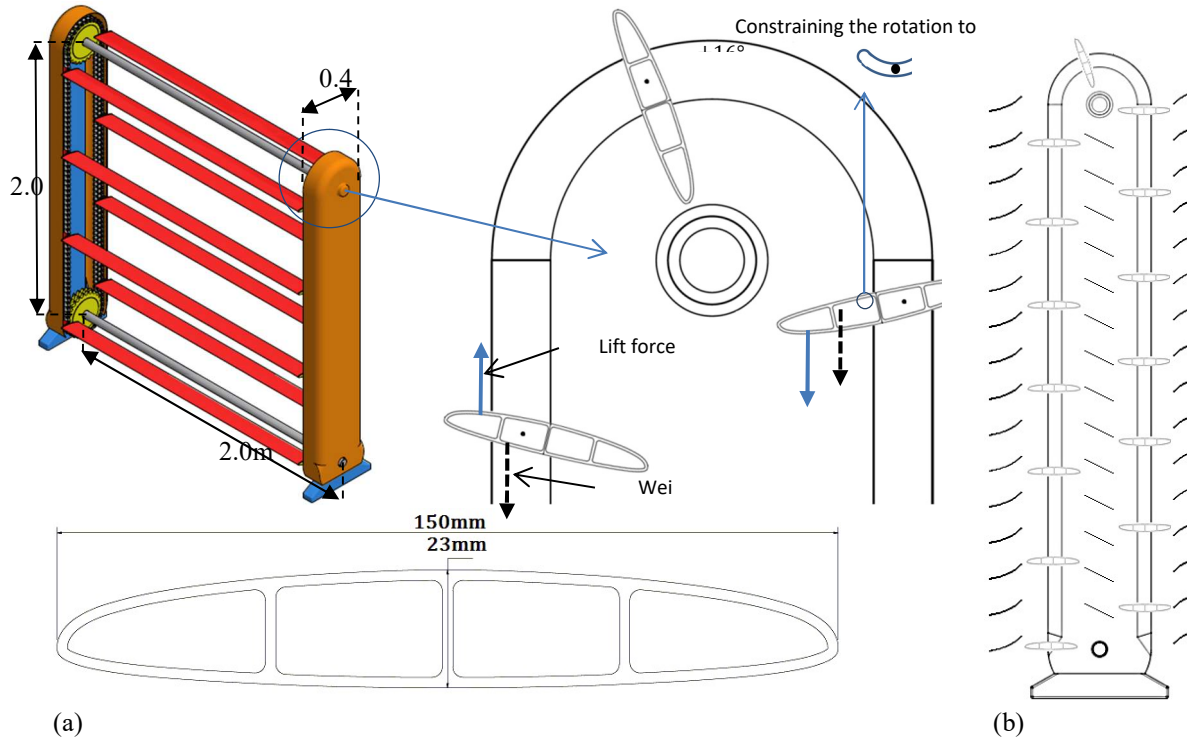

Figure 6-2: (a) Sketch of the PowerWindow prototype, its blade profile, and blades rotation mechanismat the top, (b) Sketch of the stator-augmented PowerWindowfrom side view[104].

This study also aims to compare the power generation of the selected LCWT with a conventional HAWT, referred to as Ampair 300, when both the wind turbines are integrated with the same through-building opening. The flow characteristics change inside the through-building opening once the turbine is installed. By capturing some momentum from the flow, the ducted turbine increases the pressure gradient and reduces the mean velocity across the opening. Therefore, for power generation analysis of the turbine(s), this study develops a method capable of estimating the influence of the turbine(s) on the flow characteristics inside the openings without explicitly modelling them. By

replacing the actual wind turbines with an equivalent momentum sink (EMS), this method estimates velocity, pressure gradient and turbulence intensity of the approach wind in the presence of wind turbine(s) in the through-building openings.

6.2. Methodology

Calculating the power generation of a building-integrated wind turbine is analytically difficult because of the unpredictable interactions between the building and the approach wind. Computational fluid dynamic (CFD) simulations can be an approach for this purpose. However, this would also be computationally expensive due to three reasons: (i) a building alone needs very fine and smooth boundary layer mesh on its surfaces, which would demand a massive mesh with numerous (usually millions of) elements in a 3D domain; (ii) each turbine needs a combination of very fine structured and unstructured mesh around it and along its upstream and downstream path; and (iii) once the turbine is installed in the through-building opening, it creates velocity reduction and pressure gradient along the opening, which depend on the operating λ of the turbine and is itself unknown. As a result, massive trial and error processes including different series of iterations are needed to be undertaken in order to find the operating λ of the turbine, pressure gradient and velocity reduction in the through-building opening.

In order to reduce the computation time, two approaches have recently been used for investigating the flow characteristics of a wind farm with several wind turbines. First one is based on the virtual blade model (VBM) of the commercial solver ANSYS FLUENT, in which a 3D Reynolds-averaged Navier–Stokes (RANS) calculation of the flow field is carried out for the outer domain, while the effect of the rotating blades on the fluid is simulated through a body force, acting inside a disk of fluid with an area equal to the swept area of the turbine [115]. The second one is based on an actuator disk model (ADM), in which the turbine presence is modelled as a sink of momentum, associated to the drag force exerted over it [116]. In many near and far wake calculations, the rotor is represented by an actuator disk acting as a momentum sink [117]. Such a representation circumvents the explicit calculation of the blade boundary layers, reducing computational cost and easing mesh generation [118].

To analyse wakes of wind turbines at different wind direction, Jiménez et al. [119] developed a momentum sink which could guarantee that the extraction of momentum by the whole disk was equal to the one predicted by the actuator disk theory. They compared the wake deflection and trajectories of a simple analytical model with experimental results. The results showed satisfactory agreement between the experiments and the analytical model. Jimenez et al. [120, 121] proposed a simplified large eddy simulation (LES) model to simulate the turbulent flow in the wake of a wind turbine. The turbine was simulated by a set of local sinks of momentum distributed across the rotor disk, without reproducing the blade details. The turbulence characteristics, at every point of the computational domain were obtained and found to be in good agreement with experimental results. Those results

indicated that the LES model, with the simplified momentum sink approach to simulate the rotor, was a very useful tool to simulate real turbulent characteristics in wakes [120, 121].

Therefore, by adopting a momentum sink of the drag force that the selected wind turbines exert on the ducted flow, this study develops a method, referred to as equivalent momentum sink (EMS) method, capable of estimating the flow characteristics and the power generation of a wind turbine installed in a through-building opening without generating a massive mesh and undertaking trial and error processes.

When a wind turbine is installed in a through-building opening, it extracts some momentum out of the ducted flow and converts that into electrical energy via the generator. Considering the momentum is decreasing in a control volume which would house the wind turbine(s), the pressure of the ducted flow reduces from the volume's inlet to the volume's outlet along the flow path. This pressure gradient cannot be provided unless if the velocity of the ducted flow reduces from its original condition (when no wind turbine was installed). By decreasing the inlet velocity, dynamic pressure decreases and static pressure increases instead. The higher static pressure at the inlet would provide a higher pressure gradient along the duct. The higher power generation needs higher momentum extraction for the ducted flow and creates greater velocity reduction in the through-building opening. As a result, ignoring other effects of the ducted wind turbine on the ducted flow characteristics such as turbulent kinetic energy, the control volume housing the ducted turbine(s) can be considered as a momentum sink which extracts momentum from the ducted flow.

FLUENT allows the momentum sink to be modelled as a simple homogeneous porous media, is dependent on the velocity magnitude. The sink is composed of two parts: (i) a viscous loss term and; (ii) an inertial loss term. Viscous loss or Darcy is the first term on the right-hand side of Equation 6.1 and inertial loss is the second term on the right-hand side of this equation:

$$S_i = -\left(\sum_{j=1}^{3} D_{ij}\mu v_j + \sum_{j=1}^{3} C_{ij}\frac{1}{2}\rho|v|v_j\right) \quad (6\text{-}1)$$

where S_i is the source term for the ith (x, y, or z) momentum equation, μ and ρ are the viscosity and density of air, $|v|$ is the magnitude of the velocity and D and C are prescribed matrices. The ratio of the inertial force to the viscous forces of the fluid is known as the Reynolds number (Re) and can be estimated using the following equation:

$$Re = \frac{\rho v L}{\mu} \quad (6\text{-}2)$$

Re of the LCWT within the target range of inlet wind velocity: $4\,m/s < V < 12m/s$ was $3.6 \times 10^4 < Re < 1.1 \times 10^5$ based on flow over a flat plate (blade surface). As a result, the inertial force is much greater than the viscous forces in this study and the viscous forces are negligible.

When a wind turbine is operating in the duct it exerts a reacting force on the ducted flow opposite to the flow direction, referred to as thrust. In order to find D and C, the thrust of the turbine should be measured at its operating blade speed at different velocities and divided by the ducted cross-section area. The resultant pressure drop versus the ducted flow velocities creates a parabolic curve. D and C values should be selected so that equation 1 matches the resultant curve. This equivalent momentum sink contributes to the pressure drop in the porous cell, creating a pressure drop equal to that created by the ducted wind turbine(s). The pressure drops (due to the viscous loss) that FLUENT computes in each of the three coordinate directions within the porous region are as follows:

$$\Delta p_x = \sum_{j=1}^{3} \frac{\mu}{\alpha_{ij}} v_j \Delta n_x \quad (6\text{-}3)$$

$$\Delta p_y = \sum_{j=1}^{3} \frac{\mu}{\alpha_{yj}} v_j \Delta n_y \quad (6\text{-}4)$$

$$\Delta p_z = \sum_{j=1}^{3} \frac{\mu}{\alpha_{zj}} v_j \Delta n_z \quad (6\text{-}5)$$

where $\frac{1}{\alpha_{ij}}$ are the entries in the matrix D in Equation 1, v_j are the velocity components in the x, y, and z directions, and Δn_x, Δn_y, and Δn_z are the actual thickness of the porous region in the x, y, and z directions.

This study replaces the explicit model of the LCWT and HAWT with an equivalent momentum sink (EMS) in the through-building openings, the description of which is presented in the following section. Then the CFD model calculates the pressure and ducted flow velocity in the presence of the relevant momentum sink. Eventually, using the explicit model of the ducted LCWT and ducted HAWT, by simulating the ducted wind turbines subjected to the resulted ducted flow characteristics, their power generation can be calculated accurately. The user-defined function (UDF) codes which apply the relevant EMSs to the CFD simulations are shown in Appendix C2.

6.2.1. Through-building openings

A building model with a square plan and the dimensions of $96\text{m} \times 32\text{m} \times 32\text{m}$ is considered for this study (Figure 6.3). Two through-building openings are created at a representative height of 3/4H at two ends of building breadth, where "H" refers to the building height. The cross-section area of the through-building openings is $4 \times 4\ \text{m}^2$. The 1/80 scaled model of the building is tested at the wind tunnel facility of the University of Sydney (Figure 6.4 a) mainly to compare with and validate the CFD results.

Before applying the selected velocity profiles to the inlet of the CFD model, a series of experimental tests were undertaken to verify the accuracy of the CFD simulations. A number of velocity measurements were acquired from the incident wind angle of zero to $60°$ with an interval of

15°, using a Cobra probe with the frequency response of 2 kHz. Cobra probe is a multi-hole pressure probe that resolves the three components of velocity and local static pressure. The setup configuration for the Cobra probe measurement is shown in Figure 6.4 (a). The tip of the probe would be located at the centre of the corridor and facing towards the free-stream wind.

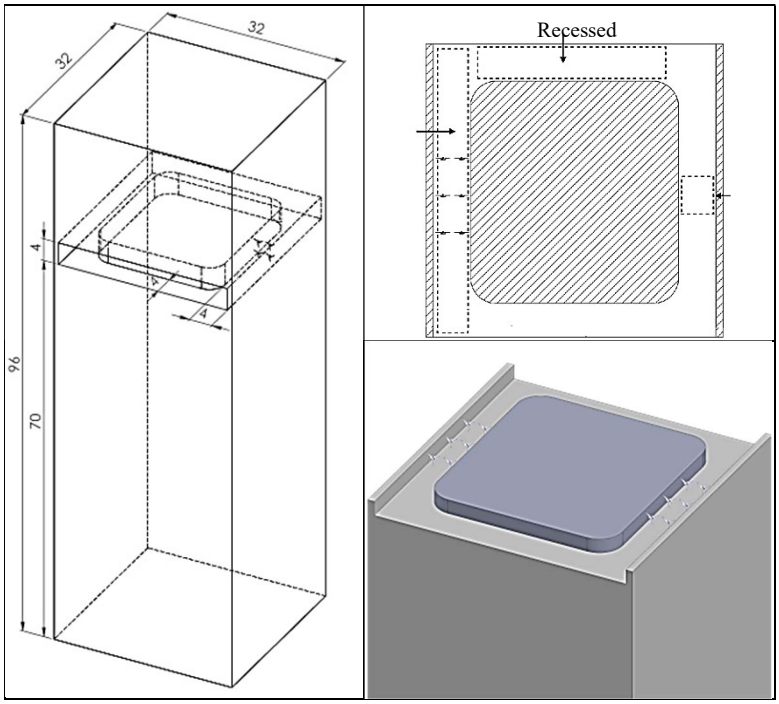

Figure 6-3: Dimensions of the building and schematic view of the wind turbines in the through-building openings [122, 123].

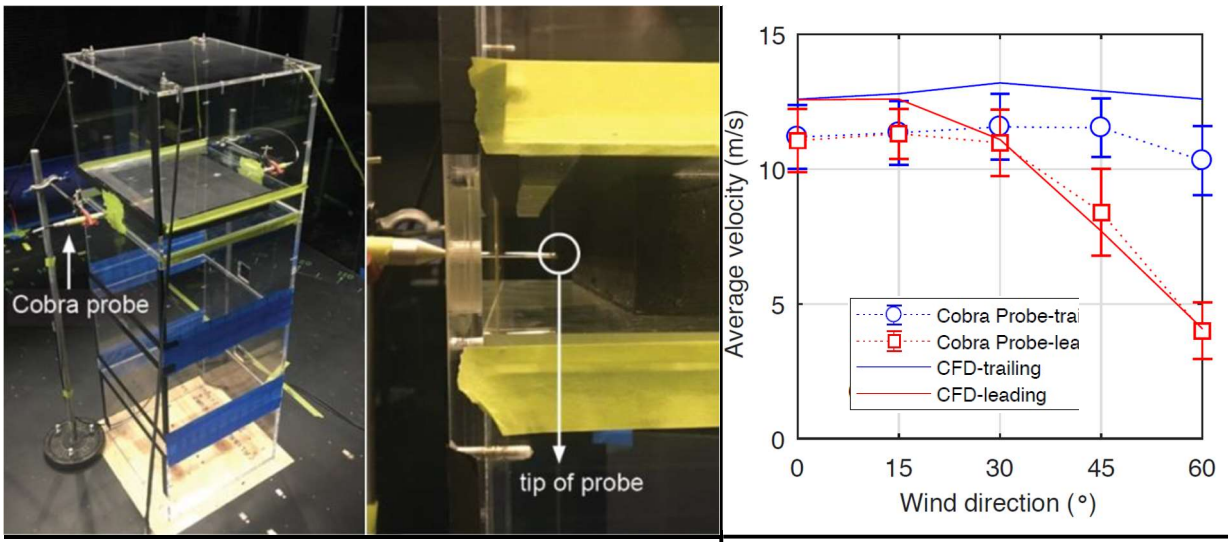

(a) (b)

Figure 6-4: (a) 1/80 scaled model of the building in the wind tunnel with setup configuration of Cobra probe inside the through-building opening and (b) The average velocity in the through-building opening measured by Cobra probe and computed by CFD simulations [124].

The PIV results have been compared with the Cobra probe measurements in the experimental test and shown that the results have an acceptable agreement with error bound of less than 7% [124]. It was also found that the Cobra probe showed the more accurate result when the flow angle to the tip of the probe was within $\pm 45°$. Considering the flow within the through-building opening, the flow angles relative to the cobra probe was far less than $\pm 45°$ [124]. The data is sampled at a frequency of 4 kHz for a duration of 180 seconds. The average velocity of the measured data at the wind tunnel and computed by the CFD simulations for different wind directions are shown in Figure 6.4 (b). As can be seen, although the average velocities predicted by the CFD simulations are slightly greater than the Cobra probe measurements, the discrepancy remains below 10% for all measured wind directions, which is an acceptable range in practice. The main reason of the slight discrepancy between the experimental and CFD results might be the simplification of the CFD model such as ignoring the roughness of the inner walls of the through-building opening and solving the simulation in steady-state condition.

6.2.2. EMS for the LCWT

In order to develop the EMS for the selected LCWT (stator-augmented PowerWindow), CFD model of the device developed in a previous study [104] has been scaled up by 2 times and located in a $4\text{m} \times 4\text{m} \times 32\text{m}$ duct. As explained in the previous study [7] PowerWindow is a scalable and modular LCWT. Therefore, that would be possible to scale it up so that it can tightly fit into the through-building opening. In this part of the study, the inlet velocity of the duct has been gradually increased from 3 m/s up to 15 m/s regardless of the pressure gradient needed along the duct. At each ducted flow velocity, power generation of the LCWT is calculated and the pressure gradient it creates along the duct is recorded. The thrust force which the EMS exerts out of the ducted flow at each velocity can be calculated by multiplying the duct area by the pressure gradient created along the duct.

The operating λ needs to be known to find the power generation of the LCWT at each ducted flow velocity using the following equation:

$$P = \lambda V F_v \tag{6-6}$$

where λ is the ratio of the blade speed to the wind speed and V is the velocity along the duct. Therefore, multiplying λ by V gives the absolute speed of the blades. It should be noted that the blades have only vertical velocity when moving up or down in the LCWT. F_v is the vertical aerodynamic force on the entire LCWT blades. Although the vertical aerodynamic force acting on each individual blade changes when moving from the bottom to the top or vice versa, the total vertical aerodynamic force acting on the entire blade assembly can be assumed to be constant, as each blade is taking the place of another one continuously. Therefore, the total power generation of the ducted LCWT can be calculated by multiplying λV by F_v.

Therefore, a series of CFD simulations have been undertaken at each ducted flow velocity with different λs, and coefficient of performance (C_P) has been calculated at each λ. C_P is the ratio of the power generation by a wind turbine to the total wind power passing through the wind turbine's area:

$$C_P = \frac{P}{\frac{1}{2}\rho V^3 A} \tag{6-7}$$

where A is the swept area of the turbine.

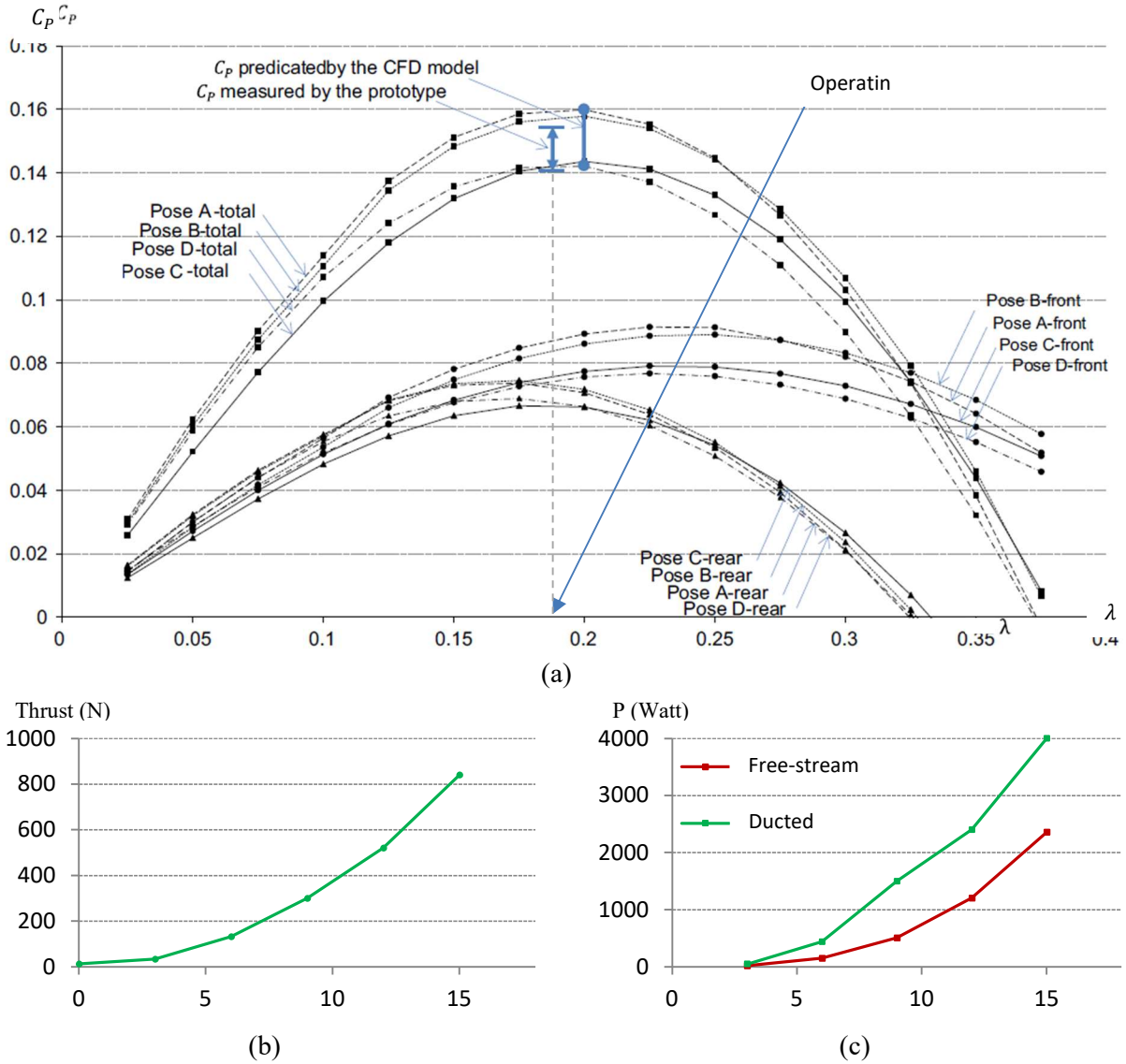

Figure 6-5: (a) Operating λ of PowerWindow detected by CFD simulation via calculating the maximumC_P, compared with the operating λmeasured in the experimental model [7], (b) The resultant thrust force of the LCWT on the ducted flow, and (c) Power generation of the LCWT in the ducted and free-stream conditions.

Ideally, a wind turbine operates at its maximum C_P which would only be possible at the optimum λ. But in practice, the operating λ is usually higher or lower than the optimum value. Nevertheless, in the previous study [7], a comparison between the experimental test undertaken in the wind tunnel and

CFD simulation of the original PowerWindow shows that this device operates at a λ close to the optimum value predicted by the CFD simulation. Therefore, this study has used the optimum λ as the operating one in order to calculate the power generation of the LCWT and pressure gradient which it creates along the duct at each ducted flow velocity. However, it should be noted that the efficiency of the generator is not included in the calculation of the power generation. Therefore, the overall C_P is expected to be slightly lower than this.

Figure 6.5 (a) shows that the operating λ measured in the experimental test is very close to the optimum λ predicted by the CFD simulations. Therefore, at every inlet velocity, the optimum (computed) λ is considered as the operational λ. Figure 6.5 (b) shows the thrust force which the EMS exerts on the ducted flow at each velocity. The process of finding power generation of the stator-augmented PowerWindow has been done once when it is located in the duct and once when it is located in the free-stream condition and the calculated power generations are shown in Figure 6.5 (c). As could be expected, the power generation of the ducted one is higher than the free-stream one. The reason is further explained in another study [103].

6.2.3. EMS for the HAWT

In order to develop the EMS for the HAWT, CFD model of the device developed in the previous study [13] has been located in the same duct. Four HAWTs have been located there to fit the cross-section area. The inlet velocity of the duct has been gradually increased from 4 m/s up to 18 m/s and at each velocity, power generation of the ducted wind turbines are calculated and the pressure gradient they create along the duct is recorded. The thrust force has also been calculated using a similar process, as discussed in the previous part.

For finding the power generation of the HAWT at each ducted flow velocity, rotational speed (ω) of the turbine is needed, which is provided by the manufacturer shown in Figure 6.6 (a) [125].

$$P = \omega \times \tau \tag{6-8}$$

where τ is the resultant torque on the rotor of the HAWT.

Using the operating ω at each wind velocity, CFD simulations have been undertaken at different ducted flow velocities. The power generation of the turbines is calculated and the pressure gradient they create along the duct is recorded. Figure 6.6 (b) shows the resultant thrust force that all four ducted HAWTs exert on the ducted flow at each velocity. The process of finding power generation of the four HAWTs has been done once when it is located in the duct and once in free-stream condition. Power generations are calculated and shown in Figure 6.6 (c). Power generation of four HAWTs

using the data provided by the manufacturer is also plotted in Figure 6.6 (c) to compare with the CFD results, which shows that the CFD results have a good agreement with the manufacturer results.

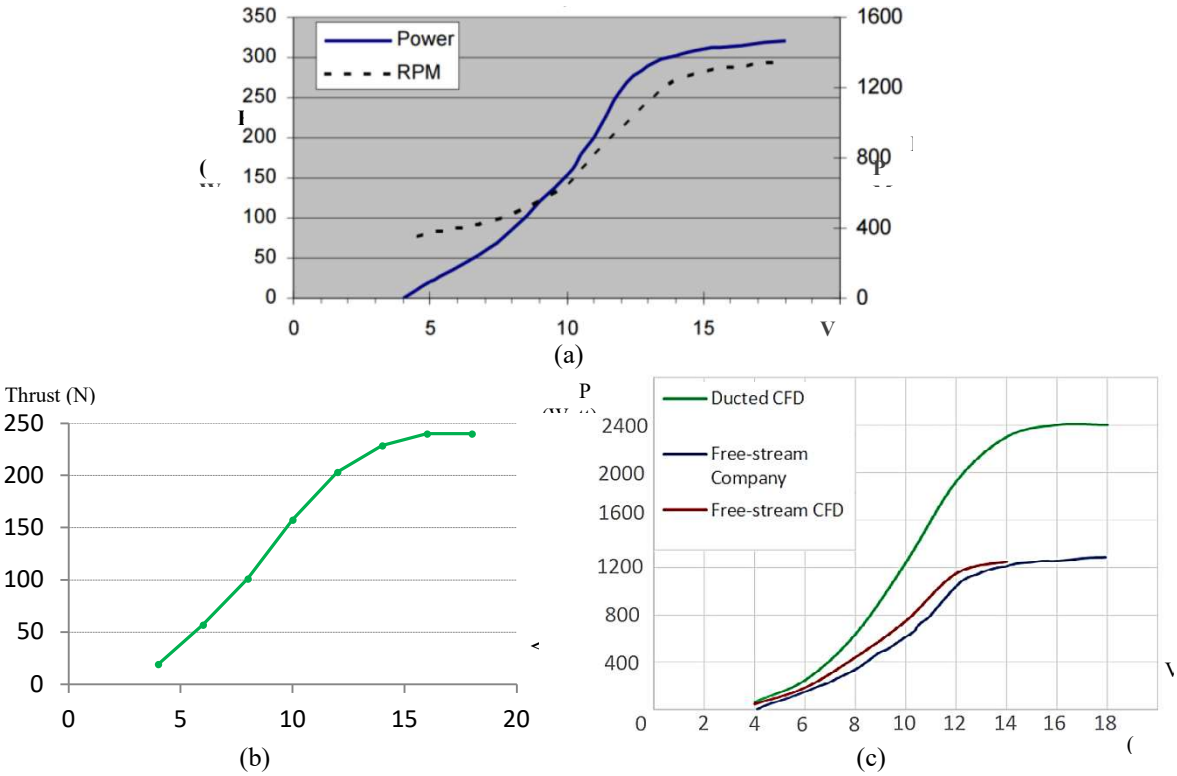

Figure 6-6: (a) power generation and rotational speed of Ampair 300 subjected to different approach wind velocities [125], (b)The resultant thrust force that all 4 HAWTs exert on the ducted flow, and (c) Power generation of 4 ducted and free-stream HAWTs, computed by CFD simulations and using the manufacturer's data.

6.3. CFD Setup

As discussed in the methodology section, the ducted flow characteristics need to be investigated in the through-building openings in two phases: (i) when the entire building is subjected to the approach wind and no wind turbine is installed and (ii) when a duct resembling the through-building opening is subjected to the approach wind and the wind turbines are installed. Section 6.3.1 presents the computational domain enclosing the building with the through-building openings, and Section 6.3.2 presents the computational domain of the through-building opening enclosing the wind turbines.

6.3.1. Building computational domain and boundary conditions

The dimensions and boundary conditions of the computational domain enclosing the building are shown in Figure 6.7 (a), which are in accordance with the CFD guidelines for flow simulations in the urban environment [126]. The building is located in a large domain where it has 3H distance from the inlet, 10H from the outlet, 1.25H from each side and 1.67H from the top (to be in consistence with the wind tunnel cross-section). The bottom and sides are set to no-slip condition and the top is set to zero shear stress.

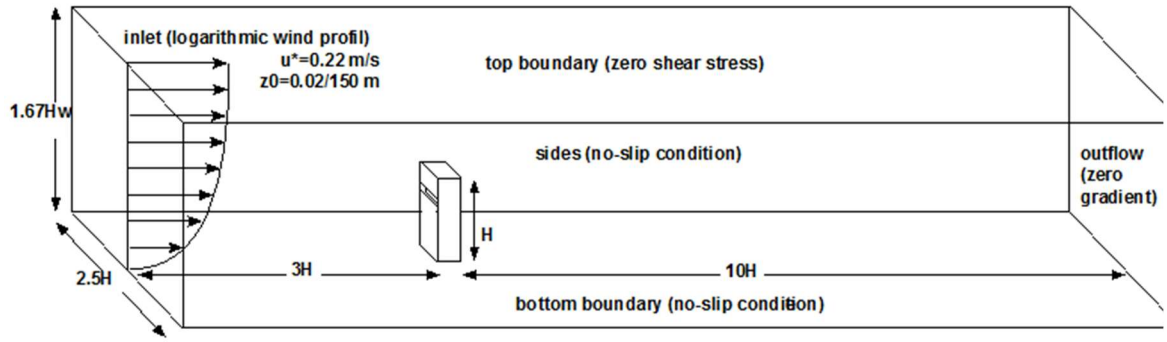

(a)

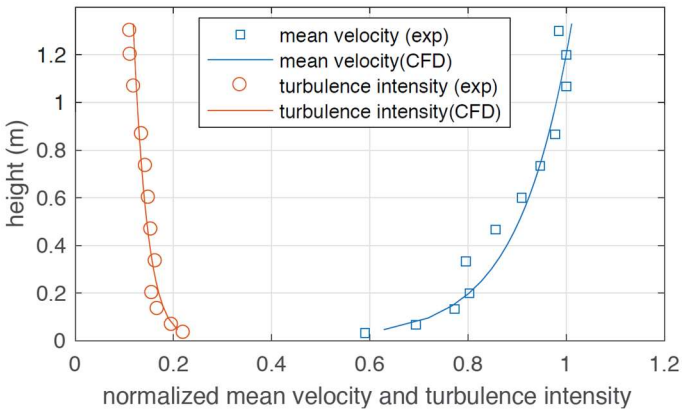

(b)

Figure 6-7: (a) The CFD domain and boundary conditions, (b) Normalized mean velocity and turbulence intensity profiles at the target location in an empty domain [127].

At the inlet boundary, a wind profile is imposed in accordance with the mean velocity and turbulent intensity corresponding to an open terrain (TC2) in the Australian Standards AS/NZS 1170.2:2011. As shown in Figure 6.7 (b), the velocity is normalized by the velocity magnitude at building height (H) at free-stream (U_{ref}). The outlet is set to outflow condition with zero velocity/turbulent intensity gradient.

The building is located in a cylindrical sub-domain, shown in Figure 6.8 (a), which can rotate similar to turn table in wind tunnels and enables the inlet flow to approach the building with different incident wind angles (ϕ). As shown in Figure 6.8 (b), the finer mesh has been generated on and around all the corners and edges of the building especially in those surfaces which are closer to the through-building openings. The EMS is placed in the middle of the through-building openings, instead of the wind turbines. By activating the sink of momentum, the simulations estimate the flow characteristics in the through-building opening in the presence of wind turbine(s) and by deactivating the sink of momentum, the simulations can estimate the flow characteristics of the empty through-building opening. Steady SST $k-\omega$ turbulence model with the SIMPLE scheme for pressure-velocity coupling and second-order discretization for pressure and momentum is considered and the value of y^+ is maintained below 300 on all walls. y^+ is a non-dimensional wall distance for a wall-bounded flow which can be calculated by the following equation:

$$y^+ = \frac{u_* y}{\nu} \tag{6-9}$$

where u_* is the friction velocity at the nearest wall, y is the distance to the nearest wall and ν is the local kinematic viscosity of the fluid.

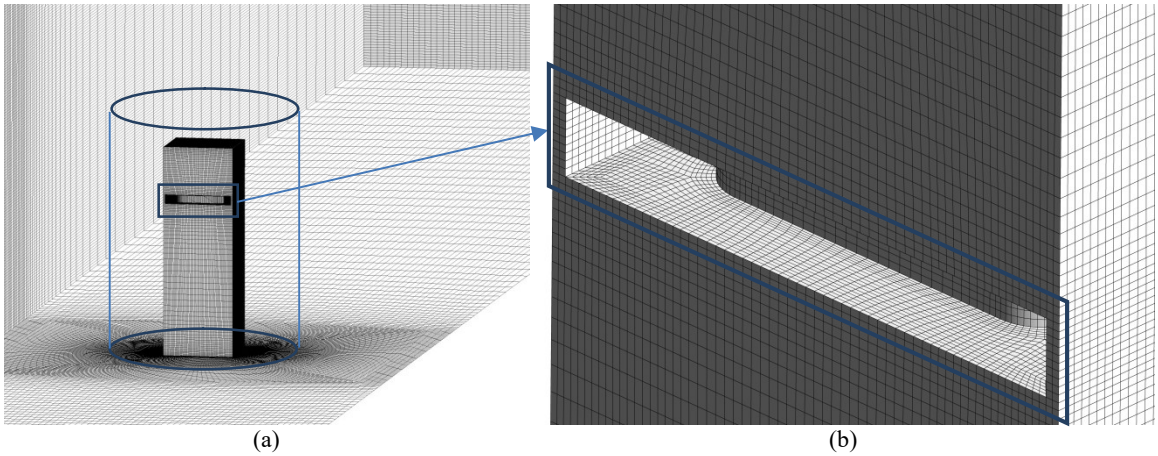

(a) (b)

Figure 6-8: (a) Cylindrical sub-domain containing the building, and (b) Fine mesh generated on and the surfaces in and around the through-building openings.

6.3.2. Wind turbines computational domain and boundary conditions

The through-building openings were created at two ends of 3/4H of the building's breadth. Each through-building opening is essentially a long duct where the LCWT or the HAWTs are installed in. Dimensions of the duct are $4\ \mathrm{m} \times 4\ \mathrm{m} \times 32\ \mathrm{m}$, and the wind turbine(s) is/are located at the middle as shown in Figure 9 (a) and (b). For the HAWTs, using the symmetry boundary condition, one quarter of the corridor housing one single turbine has been built up and extended to the other three quarters. Using Multiple Reference Frame (MRF), the rotor of the HAWTs and front and rear blades of the LCWT are located in a rotating disk and translating frames respectively. In order to achieve a balance between solution accuracy and calculation time, a combination of structured and unstructured mesh is used in this study. This technique helps to decrease the number of elements while having a high-quality mesh around the body [13]. A number of layers with structured rectangular elements are generated around the blades, and this fine mesh region is connected to the outer coarser structured region via unstructured triangular elements. The 3D model of the HAWT and the LCWT contain 1,678,320 and 5,128,740 elements respectively.

The frame of the hybrid region containing the front and rear blades are selected as moving frames which can move vertically within the domain. The boundaries of the blades are set to the moving wall with zero velocity relative to their adjacent cells. As a result, their vertical/rotational velocity would be equal to the MRF surrounding cells. The inlet boundary condition is changed within the target range. Turbulence intensity of 5% and turbulence viscosity ratio (the ratio of turbulent to laminar viscosity) of 10 is set for inlet, and outlet boundary condition is set as outflow. The standard pressure correction method and a first-order upwind scheme are used.

The operating λ applied on the rotating disk and the translating frames at each inlet velocity has been identified, as previously discussed in the methodology section. The inlet velocity, the pressure and the turbulent kinetic energy of the through-building opening extracted from the simulations undertaken for the whole building (explained in the previous section) are imposed at the inlet of the duct. The outlet is set as an outflow condition. Steady SST $k-\omega$ turbulence model with the SIMPLE scheme for pressure-velocity coupling and second-order discretization for pressure and momentum is considered for the simulations. The value of y^+ is maintained below 2 on the blade surface of the HAWTs and the LCWT and below 300 on inner duct surfaces.

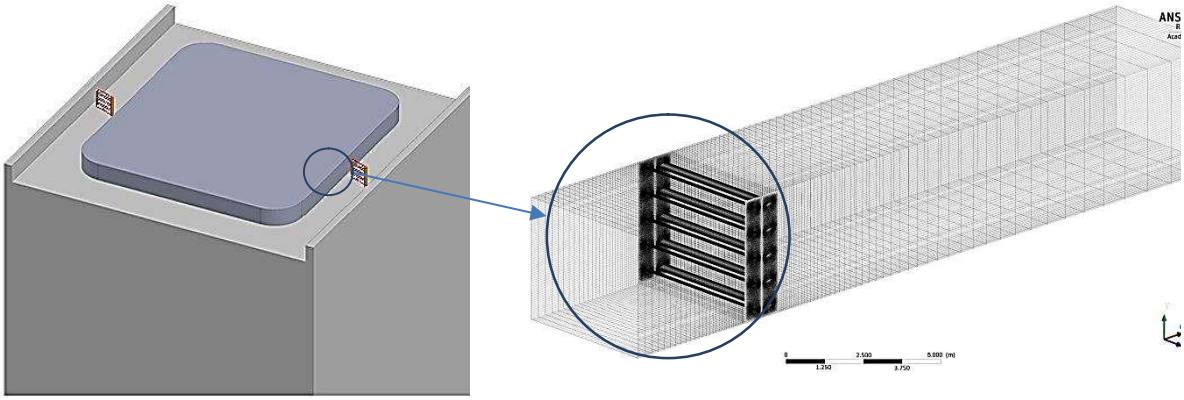

(a)

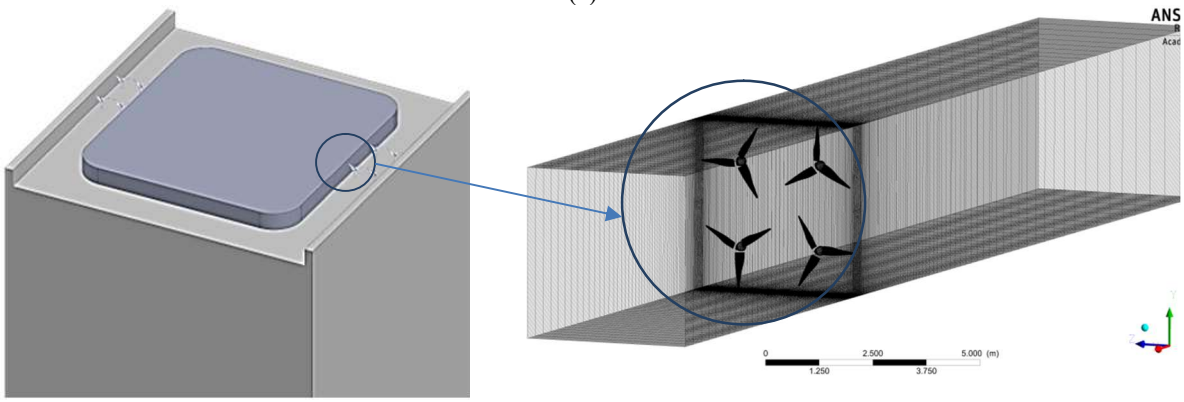

(b)

Figure 6-9: Through-building openings replaced by a simple duct containing (a) the LCWT and (b) the HAWTs.

6.4. Results and discussion

Using the MS method and explicit model of the wind turbines in the duct, flow characteristics and power generation has been done and presented in the following sections. Section 6.4.1 presents the effect of the building on the ducted flow in the empty through-building openings. Section 6.4.2 presents the effect of the LCWT on the ducted flow by installing the synchronised MS in the through-building openings. And considering the mutual effects of the building and the wind turbines on the ducted flow in the through-building openings, Section 6.4.3, presents and compares the total power generation of the LCWT and the HAWTs at different approach wind velocities and directions.

6.4.1. The effect of the building on the ducted flow

The geometrical parameters of the through-building openings (such as length, cross-section area, inlet and outlet shape) and the building itself (such as H and ϕ) strongly influence the characteristics of the ducted flow. Therefore, by deactivating the EMS located at the middle of the through-building opening, the effect of the mentioned parameters has been investigated on the ducted flow in the absence of HAWTs or LCWT. The velocity contours around the building and inside the through-building openings at $\phi = 0°$ when the free-stream velocity at H is 12 m/s ($U_{ref} = 12\ \mathrm{m/s}$) and at the 3/4H is 11 m/s ($\mathrm{U_{3/4H}} = 11.6\ \mathrm{m/s}$) and the EMS is deactivated, are shown in Figure 6.10 (a) and (b). These contours indicate that at $\phi = 0°$, the represented through-building opening enhances the velocity. As can be seen in the figures, on the windward side of the building, the recessed region has trapped the approach wind which would expect to increase the static pressure there, while the flow detachment at leeward side of the building would expect to decrease the static presser there. The overall effect should result in a high-pressure gradient along the through-building openings which has increased the velocity. The pressure contours are presented in Figure 6.11 (a). However, the flow characteristics inside and around the building and though-building openings are also strongly dependent on ϕ.

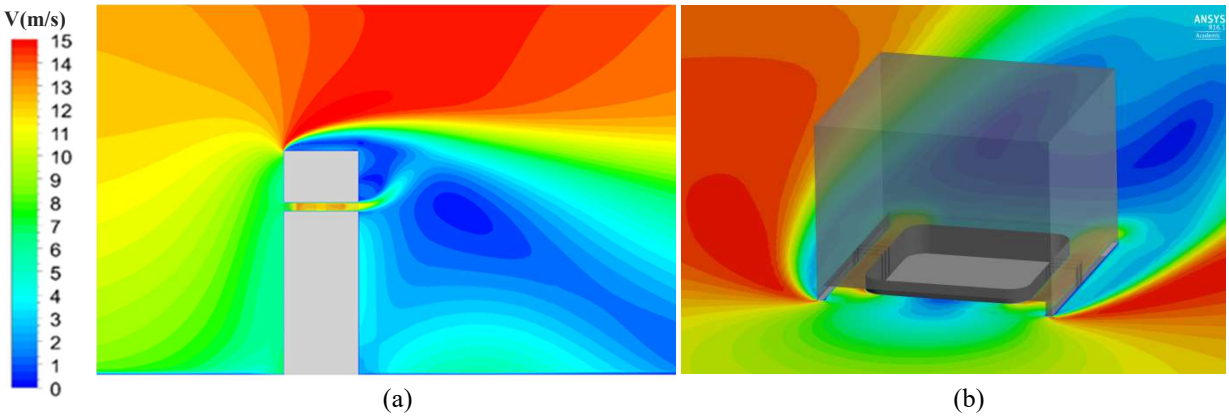

(a) (b)

Figure 6-10: (a) Transverse view and (b) isometric close-up view of mean velocity contours around the building and along the through-building openings [127].

For investigating the effect of ϕ on the ducted flow velocity in the through-building openings the building model has been rotated by 30° and 60° against the approach wind direction. Figure 6.11 (a-c) shows the static pressure and resultant velocity contour, in terms of surface pressure coefficient (C_{sp}) and velocity ratio (R_V) in the through-building openings at $= 0°, 30°$, and $60°$ when $U_{ref} = 12$ m/s and $\mathrm{U_{3/4H}} = 11.6\, m/s$. C_{sp} shows the ratio of the local static pressure to the free-stream dynamic pressure and $\mathrm{V_R}$ shows the local velocity to the free-stream velocity:

$$C_{sp} = \frac{P_{local}}{0.5\rho(U_{3/4H})^2} \tag{6-10}$$

$$V_R = \frac{U_{local}}{U_{3/4H}} \tag{6-11}$$

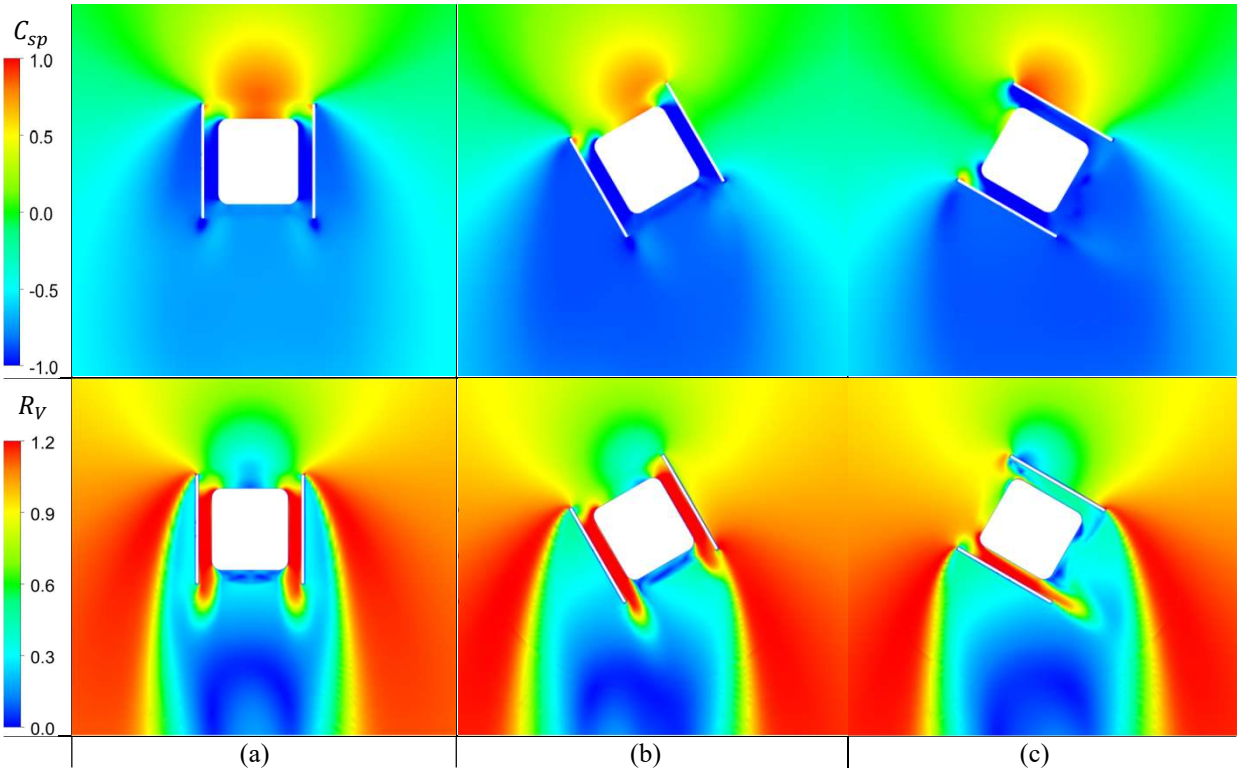

Figure 6-11: $C_{sp}$and $R_V$contours of the ducted flow at ϕ =(a) 0°, (b) 30° and (c) 60° whenU_{ref}= 12 m/s($U_{3/4H}$=11.6 m/s) and the EMSs for the LCWT are deactivated.

Figure 6.11 (a) shows that as expected at $\phi = 0°$ on the windward side of the building the trapped flow in the recessed region has increased the static pressure there and at the leeward side of the building the flow detachment has created a very low pressure there. Therefore, the high-pressure gradient created along the openings at 0° increase the ducted flow velocity in the through-building openings to above $U_{3/4H}$. Comparing Figures 6.11 (a) and (b) shows that the velocity of the ducted flow has even slightly increased at $\phi = 30°$ which should be due to the lower negative pressure

created at the outlet of the openings. Comparing Figures 6.11 (a) and (c) shows that at $\phi = 60°$ the ducted flow velocity has dropped below 6 m/s in the right opening while it is still above 12 m/s in the left one. The reason is that the flow detachment at the inlet of the right through-building opening has strongly decreased the static pressure and consequently the pressure gradient along this opening.

6.4.2. The effect of the LCWT on the ducted flow

For investigating the effect of ducted flow on power generation of the LCWT, $C_{sp}$and $R_V$contours are plotted at $\phi = 0°$,30°, and 60° when the free-stream velocity is 12 m/s at the 3/4H of the building, and the sink of momentums (adopted with the LCWT) are activated. As can be seen in Figure 6.12 (a-c), compared with Figure 6.11 (a-c), the pressure gradient is focused at the location of the EMS and the velocity has decreased in the through-building openings. According to R_V contours, the ducted flow has lower velocity than $U_{3/4H}$ in the openings at 0° when the LCWT is installed in the through-building openings.

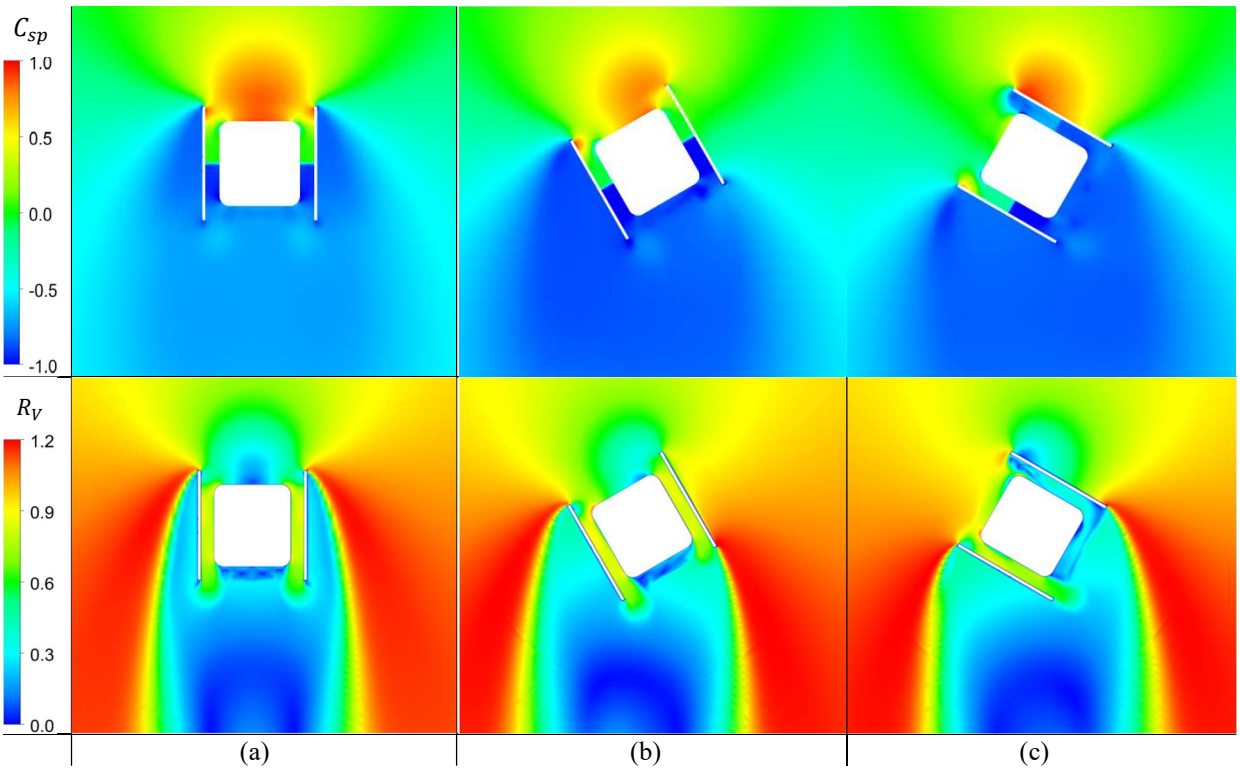

Figure 6-12: $C_{sp}$and $R_V$contours of the ducted flow at ϕ = (a) 0°, (b) 30° and (c) 60° when the U_{ref}= 12 m/s ($U_{3/4H}$=11.6 m/s) at and the EMSs for the LCWT are activated.

Similar to the empty through-building openings, at 30° the velocity is slightly higher than at 0° which should be due to the similar reason (lower pressure created at the outlet of the openings). Comparing Figures 6.12 (a) and (c) shows that at 60° the ducted flow velocity has dropped below

90% of the free-stream velocity in the left through-building opening and below 30% in the right one. On the other hand, according to Figure 6.4 (c), power generation of the LCWT in the duct is about $30-70\%$ higher than in the free-stream condition. Therefore, the overall effect of the through-building opening on the wind turbines at low ϕs may not be decreasing their power generation compared with the free-stream condition. However, the power generation will dramatically drop in one of the through-building openings when the ϕ increases.

Using EMS method, the mean velocity, inlet pressure and turbulent kinetic energy (TKE) of the ducted flow are estimated and recorded in the presence of the ducted LCWT and shown in Table 6.1 (a-d). U_{ref} is 6, 9, 12 and 15 m/s in Table 6.1 (a), (b), (c) and (d) respectively. $U_{3/4H}$ at each velocity profile is also presented.

Table 6-1: Characteristics of the ducted flow when the EMS of the LCWT is activated in the right and left through-building openings at different ϕ when U_{ref}= (a) 6 m/s, (b) 9 m/s, (c) 12 m/s and (d) 15 m/s.

Incident wind angle (°)	Through-building opening	Inlet gauge Pressure (Pa)	Mean Velocity (m/s)	TKE $(\frac{m^2}{s^2})$
0°	Left & right	0.99	4.72	0.65
30°	Left	0.08	4.94	0.58
	Right	-1.24	4.90	0.58
60°	Left	-3.91	4.35	0.42
	Right	-14.71	1.99	0.26

(a)$U_{3/4H} = 5.8$ m/s

Incident wind angle (°)	Through-building opening	Inlet gauge Pressure (Pa)	Mean Velocity (m/s)	TKE $(\frac{m^2}{s^2})$
0°	Left & right	2.25	7.18	1.49
30°	Left	0.08	7.40	1.62
	Right	-1.24	7.46	1.33
60°	Left	-32.39	6.66	0.96
	Right	-8.29	3.14	0.64

(b)$U_{3/4H}$ = 8.7 m/s

Incident wind angle (°)	Through-building opening	Inlet gauge Pressure (Pa)	Mean Velocity (m/s)	TKE $(\frac{m^2}{s^2})$
0°	Left & right	3.84	9.61	2.66
30°	Left	-0.34	10.00	2.89
	Right	-5.67	9.94	2.37
60°	Left	-17.35	8.90	1.69
	Right	-64.32	4.32	1.17

(c)$U_{3/4H} = 11.6$ m/s

Incident wind angle (°)	Through-building opening	Inlet gauge Pressure (Pa)	Mean Velocity (m/s)	TKE $(\frac{m^2}{s^2})$
0°	Left & right	5.85	12.03	4.15
30°	Left	-1.28	12.54	4.53
	Right	-9.63	12.45	3.72
60°	Left	-23.11	11.24	2.68
	Right	-98.43	5.58	1.86

(d)$U_{3/4H} = 14.5$ m/s

6.4.3. The effect of the ducted flow on power generation of the LCWT and HAWT

The resultant flow characteristics of the approach wind in the through-building opening in the presence of the LCWTs are applied to the inlet of the simple duct which explicitly houses the LCWTs. Power generation of the ducted wind turbines installed in the left and right through-building openings at $\phi = 0°$, 30° and 60° are computed and compared with each other and their free-stream condition. In Figures 6.13 (a-d), the left axis shows the resultant power generation of the LCWT installed in the through-building openings at $\phi = 0°$, 30° and 60° and the right axis shows the power generation ratio (R_P) of the ducted LCWT to the free-stream one when U_{ref} is 6, 9, 12 and 15 m/s respectively.

The resultant R_Ps of the HAWTs show that similar to the LCWTs, their installation in the selected through-building openings enhances their performance compared with their free-stream condition. However, the comparison of Figures 6.13 and 6.14 shows that the power generation of the LCWT has not increased as much as the HAWTs. The reason is the higher solidity of the LCWT which demands higher pressure gradient along the through-building opening, and subsequently by decreasing the mass flow rate in the opening decreases the ducted velocity.

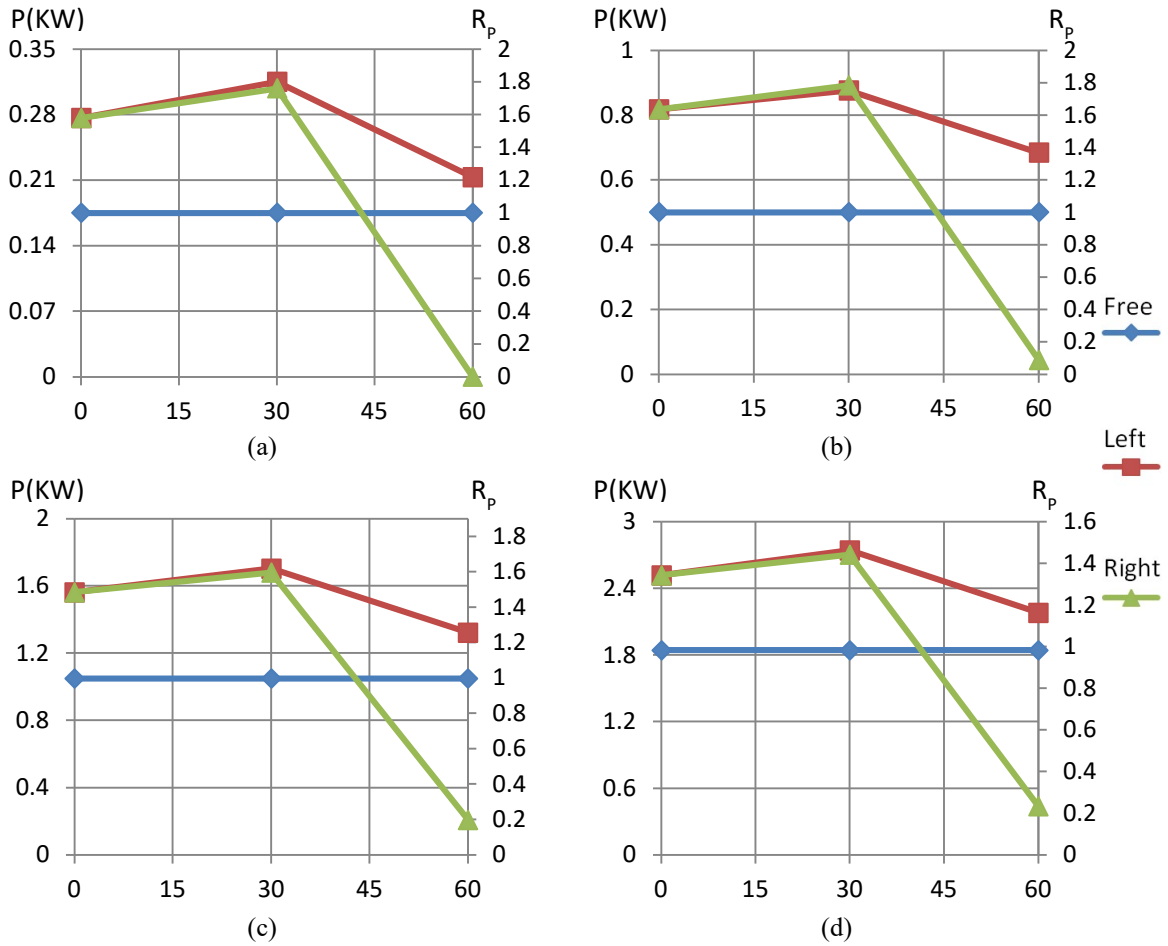

Figure 6-13: Power generation and power generation ratio of the LCWTs installed in the left and right through-building openings at $\phi = 0°$, 30° and 60°, when U_{ref}= (a) 6 m/s, (b) 9 m/s, (c) 12 m/s and (d) 15 m/s.

Flow characteristics of the approach wind in the through-building opening have also been investigated and recorded in the presence of the HAWTs and the resultant flow characteristics are applied to the inlet of the simple duct which explicitly houses the HAWTs. Power generation of the ducted wind turbines installed in the left and right through-building openings at $\phi = 0°$, 30° and 60° are computed and compared with each other and their free-stream condition. Similar to Figure 6.13, in Figures 6.14 (a-d), the left axis shows the resultant power generation of the HAWTs installed in the through-building openings at $\phi = 0°$, 30° and 60° and the right axis shows R_P of the ducted HAWTs to the free-stream one when U_{ref} is 6, 9, 12 and 15 m/s respectively.

The resultant R_Ps of the HAWTs show that similar to the LCWTs, their installation in the selected through-building openings enhances their performance compared with their free-stream condition. However, a comparison of Figures 13 and 14 shows that the power generation of the LCWT has not increased as much as the HAWTs. The reason is the higher solidity of the LCWT which demands higher pressure gradient along the through-building opening, and subsequently by decreasing the mass flowrate in the opening decreases the ducted velocity.

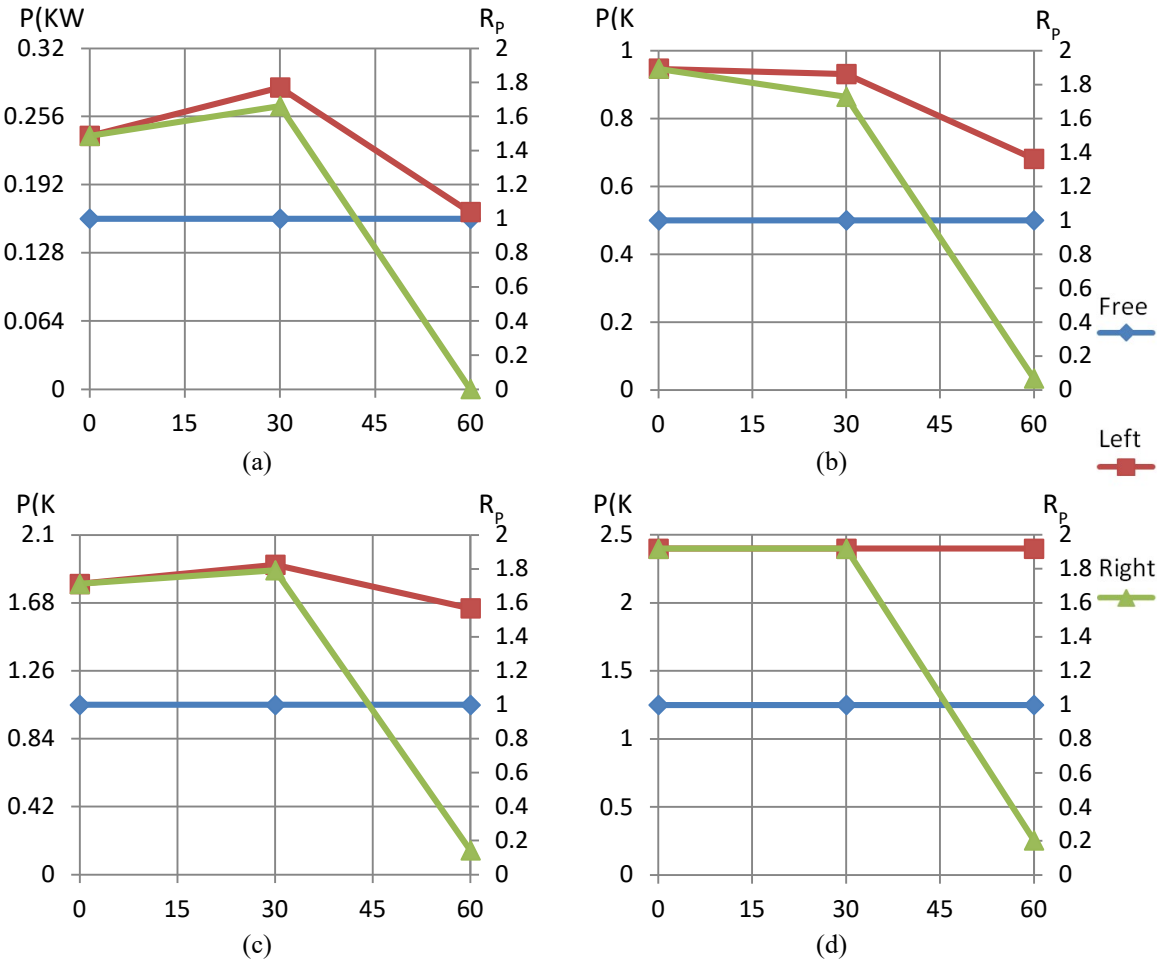

Figure 6-14: Power generation and power generation ratio of the HAWTs installed in the left and right through-building openings at $\phi = 0°$, $30°$ and $60°$, when U_{ref}= (a) 6 m/s, (b) 9 m/s, (c) 12 m/s and (d) 15 m/s.

The sum of the generated power of the right and left LCWTs and HAWTs are calculated when the building is exposed to different velocity profiles and different ϕs and shown in Table 6.2. As can be seen in the table, at $\phi = 0°$, $30°$ and $60°$the total power generation of both the ducted wind turbines are relatively close (maximum 20% higher or lower than one another). It should be noted that, the maximum power generation of the selected HAWT (Ampair 300) is not normally above 0.35KW in free-stream condition but the studies have shown that its capacity increases when it is operating in a ducted configuration [128]. The increase in power generation is due to the increase of τ (in Equation 3). Even though power generation of each ducted HAWT cannot exceed 0.6KW. Therefore, at higher

approach wind velocities (15 m/s or higher) is a constant 0.6KW. The other important issue is that, due to the geometrical symmetry of the selected building, the total power generation of the wind turbines are identical at $\phi = 30°$ and $-30°$ or $60°$ and $-60°$, as the power generation of the right and left wind turbines integrated with the trough-building openings would only be swapped with one another at these ϕs. The free-stream velocity at 10 metres above sea level (U_{10}) at each U_{ref} is also presented.

Table 6-2: Total power generation of the right and left wind turbines integrated with the through-building opening when the building is exposed to different velocity profiles and ϕs.

U_{ref} (m/s)	U_{10} (m/s)	Incident wind angle (°)	Power generation of the LCWTs (KW)	Power generation of the HAWTs (KW)
6	**4.4**	0	0.55	0.47
		30	0.62	0.55
		60	0.21	0.17
		90	0	0
		120	0.21	0
		150	0.62	0
		180	0.55	0
9	**6.06**	0	1.63	1.89
		30	1.77	1.79
		60	0.73	0.71
		90	0	0
		120	0.73	0
		150	1.77	0
		180	1.63	0
12	**8.07**	0	3.12	3.60
		30	3.38	3.80
		0	1.53	1.80
		90	0	0
		120	1.53	0
		150	3.38	0
		180	3.12	0
15	**10.09**	0	5.03	4.80
		30	5.45	4.80
		60	2.62	2.65
		90	0	0
		120	2.62	0
		150	5.45	0
		180	5.03	0

The main difference between the power generations of the LCWT and HAWT appears when ϕ exceeds $90°$. When the approach wind comes from the other side of the building, regardless of the exact value of ϕ, the ducted flow direction changes by $180°$ and the passive yaw mechanism of the HAWT is not capable of responding to this change of flow direction. Therefore, the HAWTs cannot operate unless by using an active yaw mechanism. However, as shown in the previous study [104], the LCWT (stator-augmented PowerWindow) is designed and configured to be capable of operating continuously regardless of wind direction. This is a prime advantage for the LCWT. To demonstrate

the value of this advantage, the annual operating probability of these two wind turbines can be compared when installed in the selected through-building openings of a building located in the Sydney region.

Figure 6.15 shows the probability distributions of hourly mean wind speeds with direction for Sydney Airport at 45° intervals at the height of 10 m over open country. It can be seen that, if the building faces North West, the approach wind has a great probability to channel through the openings. In this case, the HAWT, by collecting the wind energy at $\phi = -45°, 0$ and $45°$, excluding the probability of having $U_{10} < 2.8\, m/s$ (which is below the cut-in speed of both the wind turbines), it has the annual operating probability of about 24%, while the LCWT by collecting the wind energy at $\phi = -135°, -45°, 0, 45°, 135°$ and $180°$, excluding the probability of having $U_{10} < 2.8\, m/s$ has the annual operating probability of about 56%. A more detailed analysis of the total annual energy production of LCWT in different wind climates and urban terrains needs further investigation which can be considered as a recommendation for future research.

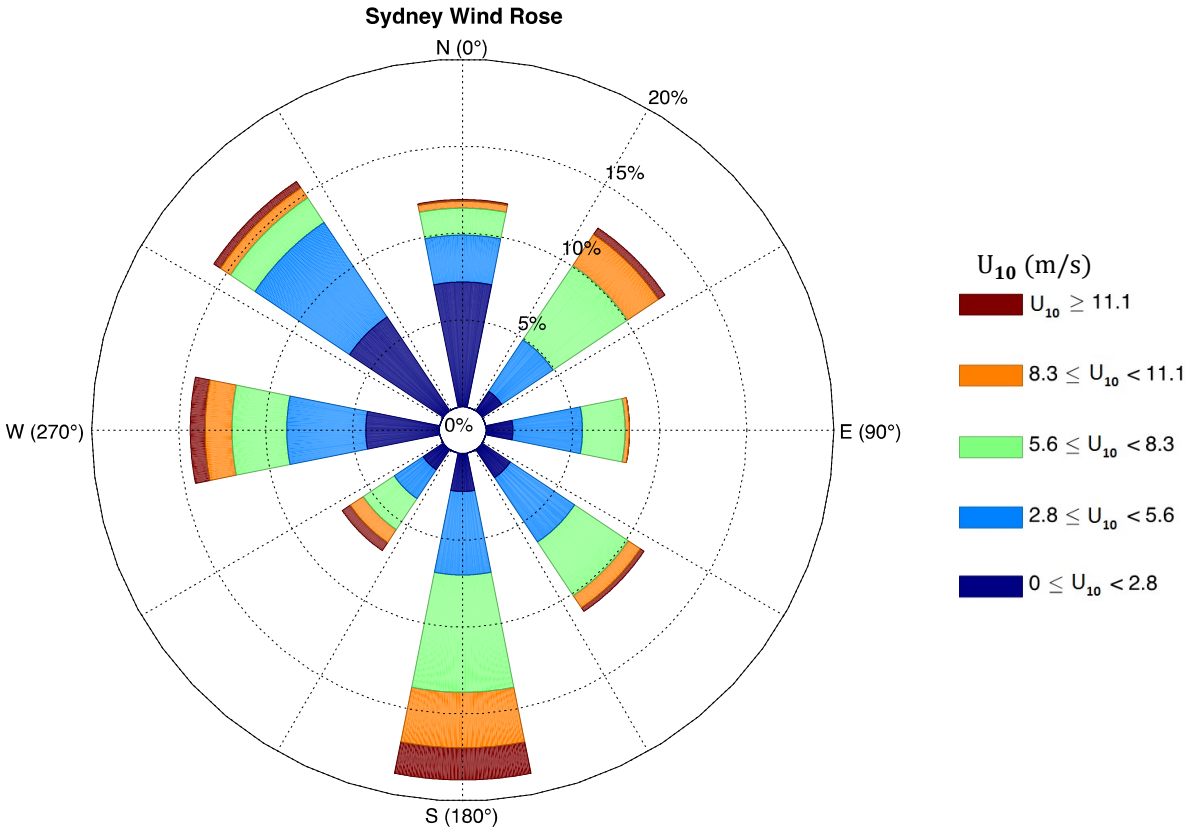

Figure 6-15: Wind rose of Sydney [129].

Creating one more pair of the through-building openings (e.g., on the next floor of the building), perpendicular to these, enables the potential of wind energy harvesting in any direction. In other words, at any given time, at least two of the turbines are operating, provided that the wind speed

exceeds the cut-in speed of wind turbines. Based on the wind rose of Sydney (Figure 6.15), excluding the probability of having $U_{10} < 2.8\, m/s$ (which is below the cut-in speed of the LCWT), a minimum of (0 + 0.55=) 0.55 KW and maximum of (2.45 + 2.62 =) 8.07 KW power generation can be guaranteed 72% of the times throughout the year. Although this power generation is not sufficient for the whole building, it is sufficient to supply a portion of the electricity consumption of the building facilities.

6.5. Conclusion

Employing the equivalent momentum sink method developed in this study, characteristics of the ducted flow are predicted in the presence of stator-augmented PowerWindow, a linear cascade wind turbine (LCWT), and power generation capacity of the LCWT is investigated when it is installed in a through-building opening in a tall building. The equivalent momentum sink method enables the estimation of pressure, velocity and turbulence intensity of the flow in the through-building opening integrated with a wind turbine and subjected to different wind directions. It is shown that the selected through-building openings with a properly designed layout can maintain the velocity of the flow in the openings in a wide range of wind directions ($-60° < \varphi < 60°$) and enhances the power generation by 50-80%. Power generation of the LCWT is also compared with a conventional horizontal axis wind turbine (HAWT), Ampair 300, installed in the same through-building opening. The results show that in certain incident wind angles, the velocity of the ducted flow is higher than the free-stream velocity at the same elevation. By installing the LCWT in the through-building opening the ducted flow velocity decreased below the free-stream velocity at the same elevation due to the increase in the pressure gradient demanded along the opening. It is computed and shown that power generation of the ducted LCWT is close to the ducted HAWTs in some incident wind angles, but the LCWT is also able to effectively operate at above $90°$ wherethe ducted HAWTs are not. As a result, with 56% annual power generation probability, the LCWT is superior to the HAWT with 24% annual power generation probability for building integration in Sydney. As a case study, it is also shown that in Sydney area by embedding four thorough-building openings integrated with stator-augmented PowerWindow in the selected building, a minimum of 0.55 KW and maximum of 8.07 KW power generations can be guaranteed 72% of the times throughout the year which is sufficient to supply a portion of the electricity consumptions of the building facilities.

CHAPTER 7. CONCLUSION

Linear Cascade Wind Turbines (LCWTs) are a new generation of wind turbines. Unlike conventional horizontal or vertical axis wind turbines (HAWTs and VAWTs), where the blades have rotational movement around the rotor axis, LCWTs have two sets of blades in a linear cascade configuration. One of the major advantages of this configuration is derived from the translational movement of both sets of blades moving in the opposite direction and perpendicular to the approach wind direction. PowerWindow, which is a special type of LCWT, has recently been developed based on a modular approach to provide flexibility for different applications. Furthermore, PowerWindow is capable of generating power in low wind velocity conditions which makes it an effective and safe wind turbine for application in urban environments. However, the Coefficient of Performance of the first generation PowerWindow is noticeably lower than existing commercialised HAWTs and VAWTs. Moreover, similar to other wind turbines, the application of PowerWindow is constrained by unfavourable urban wind conditions such as low and/or intermittent wind velocity and continuously variable direction particularly to urban environments. Therefore, this research project has aimed to improve the design of PowerWindow to enhance the Coefficient of Performance (C_P) and practical applications in urban environments.

An analytical model was developed based on the blade element momentum (BEM) theory for the analysis of PowerWindow. The BEM model was used to predict the C_P of PowerWindow. Computational fluid dynamic (CFD) models were generated and used to verify the accuracy of this model. Investigations on the aerodynamic mechanism of the elevated PowerWindow showed that the front blades increase the angle of attack (α) on the rear blades and consequently enhance their contribution to the total power generation. Solidity (σ) and blade pitch angle (θ_b) were also investigated to determine their effects on the performance of the elevated PowerWindow. It was shown that increasing θ_b enhances the power generation, so that $C_P$was enhanced from 0.075 to 0.15 by increasing θ_0 from 16° to 24°. However, increasing θ_b beyond an optimum point raises the possibility of stall, which may result in a degradation of C_P. Similarly, increasing σ from 0.428 to 0.857 was shown to enhance C_P from 0.08 to 0.12. Moreover, it was shown that increasing σ results in postponing the stall condition and allowing θ_b to be above 24° to achieve a higher power generation. The BEM model showed that optimizing σ and θ_b can strongly enhance the aerodynamic performance of PowerWindow.

Due to the limited suitable locations for installing PowerWindow in grounded configuration, elevated and ducted installation configurations were investigated for the device. A 3D CFD model of PowerWindow was developed and validated with the experimental data from the wind tunnel test of the prototype. Elevated and ducted installation configurations were proposed for PowerWindow. In

the elevated configuration PowerWindow is installed on top of a tall building. In the ducted configuration it is installed inside a ducted area such as a through-building opening. Aerodynamic performances of the elevated and ducted PowerWindow were investigated and compared using computational fluid dynamic simulations. The undertaken results indicated that with the current design parameters, the elevated and ducted configurations have respectively 8% and 12% C_P and in both configurations the front blades enhance the power generation of the rear ones. The effect of σ was also investigated on the flow mechanism and power generation of an elevated and ducted PowerWindow. It was shown that σ of the front blades has a significant effect on the flow direction approaching the rear ones which increases their contribution in power generation. It was also shown that increasing σ results in greater C_P in both configurations. However, the optimum σ of the ducted configuration depends on the inlet and outlet design of the through-building opening and needs to be investigated for each design.

In order to enhance the power generation capacity and the probability of PowerWindow by improving the flow direction in the device, stator vanes were proposed to be attached to the PowerWindow. The stator vanes by controlling α increase the acting force (vertical load) and decrease the undesirable force (axial load) on PowerWindow blades. An Analytical model using BEM theory was developed for the new configuration referred to as stator-augmented PowerWindow. The analytical model was verified by a CFD model. The results showed that the stator vanes are able to minimise/neutralise the undesirable force (axial load) on PowerWindow so that the thrust coefficient (C_T) decreases from 0.035 in the original model to -0.005 in the stator-augmented one. It was shown that the stator vanes by increasing the acting force (vertical load) on PowerWindow blades have simultaneously enhanced C_P from 0.85 to 0.1. It is also shown that another advantage of using stator vanes to control α is that the direction of rotation of PowerWindow will remain the same regardless of the wind direction. In the original PowerWindow, when the wind direction was reversed, the turbine would also rotate in the opposite direction. The stator-augmented design, therefore, is particularly useful for fixed in-building installations.

An equivalent momentum sink (EMS) method was developed to investigate the power generation capacity of stator-augmented PowerWindow when the device was installed in through-building openings of a tall building. The EMS method enables prediction of the flow characteristics in a duct at the presence of stator-augmented PowerWindow. Power generation capacity of the ducted stator-augmented PowerWindow was investigated when it was installed in a through-building opening in a tall building. It was shown that the selected through-building openings with a properly designed layout could maintain the velocity of the flow in the openings in a wide range of wind directions ($-60° < \varphi < 60°$) and enhanced the power generation by 50-80%. Power generation of the LCWT was also compared with a conventional HAWT, Ampair 300, which was installed in the same

through-building opening. The results showed that in certain incident wind angles, the velocity of the ducted flow was higher than the free-stream velocity at the same elevation. By installing the LCWT in the through-building opening the ducted flow velocity decreased below the free-stream velocity at the same elevation due to the increase in the pressure gradient demanded along the opening. It was computed and shown that power generation of the ducted LCWT was close to the ducted HAWTs in some incident wind angles, but the LCWT was also able to effectively operate at above 90° where the ducted HAWTs were not. As a result, with 56% annual power generation probability, the LCWT was superior to the HAWT with 24% annual power generation probability for building integration in Sydney. As a case study, it was shown that in the Sydney area by embedding four thorough-building openings integrated with stator-augmented PowerWindow in the selected building, a minimum of 0.55 KW and maximum of 8.07 KW power generations could be guaranteed 72% of the times throughout the year which would be sufficient to supply a portion of the electricity consumptions of the building facilities.

This study proposed and investigated approaches to increase the C_P and application of PowerWindow, particularly in urban areas. It was shown that improving the design and installation configuration of PowerWindow could make this device an efficient and reliable wind turbine for being integrated with urban buildings.

REFERENCES

1. Duffy, M.J., *SMALL WIND TURBINES MOUNTED TO EXISTING STRUCTURES* in *Aerospace Engineering*. 2010, Georgia Institute of Technology

2. Li, Q.S., Z.R. Shu, and F.B. Chen, *Performance assessment of tall building-integrated wind turbines for power generation.* Applied Energy, 2016. **165**: p. 777-788.

3. Dayan, E., *Wind energy in buildings: Power generation from wind in the urban environment - where it is needed most.* Refocus, 2006. **7**(2): p. 33-38.

4. Tabassum, A., et al., *Wind energy: Increasing deployment, rising environmental concerns.* Renewable and Sustainable Energy Reviews, 2014. **31**: p. 270-288.

5. Sharpe, T. and G. Proven, *Crossflex: Concept and early development of a true building integrated wind turbine.* Energy and Buildings, 2010. **42**: p. 2365-2375.

6. Chong, W., et al., *Early development of an innovative building integrated wind, solar and rain water harvester for urban high rise application.* Energy and Buildings, 2012. **47**: p. 201-207.

7. Jafari, S.A.H., et al., *Power generation analysis of PowerWindow, a linear wind generator, using computational fluid dynamic simulations.* Journal of Wind Engineering and Industrial Aerodynamics, 2015. **147**: p. 226-238.

8. Wei, D. and Z. Feng. *Loading Analysis and Strength Calculation of Wind Turbine Blade Based on Blade Element Momentum Theory and Finite Element Method*. in *Power and Energy Engineering Conference (APPEEC), 2010 Asia-Pacific*. 2010.

9. Lanzafame, R., S. Mauro, and M. Messina, *Wind turbine CFD modeling using a correlation-based transitional model.* Renewable Energy, 2013. **52**(0): p. 31-39.

10. O'Doherty, T., et al. *Considerations of a horizontal axis tidal turbine*. Proceedings of the ICE - Energy, 2010. **163**, 119-130.

11. Vermeer, L.J., J.N. Sørensen, and A. Crespo, *Wind turbine wake aerodynamics.* Progress in Aerospace Sciences, 2003. **39**(6–7): p. 467-510.

12. Whale, J., et al., *An experimental and numerical study of the vortex structure in the wake of a wind turbine.* Journal of Wind Engineering and Industrial Aerodynamics, 2000. **84**(1): p. 1-21.

13. Jafari, S.A.H. and B. Kosasih, *Flow analysis of shrouded small wind turbine with a simple frustum diffuser with computational fluid dynamics simulations.* Journal of Wind Engineering and Industrial Aerodynamics, 2014. **125**(0): p. 102-110.

14. Guo, T., et al., *A CFD/CSD model for aeroelastic calculations of large-scale wind turbines.* Science China Technological Sciences, 2013. **56**(1): p. 205-211.

15. David, C., et al., *Investigating Aeroelastic Performance of Multi-Mega Watt Wind Turbine Rotors Using CFD*, in *53rd AIAA/ASME/ASCE/AHS/ASC Structures, Structural Dynamics and Materials Conference*. 2012, American Institute of Aeronautics and Astronautics.

16. Sanderse, B., S.P. van der Pijl, and B. Koren, *Review of computational fluid dynamics for wind turbine wake aerodynamics.* Wind Energy, 2011. **14**(7): p. 799-819.

17. Raciti Castelli, M., A. Englaro, and E. Benini, *The Darrieus wind turbine: Proposal for a new performance prediction model based on CFD.* Energy, 2011. **36**(8): p. 4919-4934.

18. Lanzafame, R. and M. Messina, *Fluid dynamics wind turbine design: Critical analysis, optimization and application of BEM theory.* Renewable Energy, 2007. **32**(14): p. 2291-2305.

19. Glauert, H., *Airplane propellers, Aerodynamic theory, Julius Springer (Berlin.* Germany), 1935: p. 169-360.

20. Rajagopalan, R.G. and S.R. Mathur, *Three dimensional analysis of a rotor in forward flight.* Journal of the American Helicopter Society, 1993. **38**(3): p. 14-25.

21. Pratumnopharat, P. and P.S. Leung, *Validation of various windmill brake state models used by blade element momentum calculation.* Renewable Energy, 2011. **36**(11): p. 3222-3227.

22. Sørensen, J.N. and C.W. Kock, *A model for unsteady rotor aerodynamics.* Journal of Wind Engineering and Industrial Aerodynamics, 1995. **58**(3): p. 259-275.

23. Bohorquez, F., D. Pines, and P.D. Samuel, *Small Rotor Design Optimization Using Blade Element Momentum Theory and Hover Tests.* Journal of Aircraft, 2010. **47**(1): p. 268-283.

24. Ohyama, K. and T. Nakashima. *Wind turbine emulator using wind turbine model based on blade element momentum theory*. in *Power Electronics Electrical Drives Automation and Motion (SPEEDAM), 2010 International Symposium on*. 2010.

25. Hu, Y. and S.S. Rao, *Robust Design of Horizontal Axis Wind Turbines Using Taguchi Method.* Journal of Mechanical Design, 2011. **133**(11): p. 111009-111009.

26. Bedon, G., M. Raciti Castelli, and E. Benini, *Optimization of a Darrieus vertical-axis wind turbine using blade element – momentum theory and evolutionary algorithm.* Renewable Energy, 2013. **59**(0): p. 184-192.

27. Islam, M., D.S.K. Ting, and A. Fartaj, *Aerodynamic models for Darrieus-type straight-bladed vertical axis wind turbines.* Renewable and Sustainable Energy Reviews, 2008. **12**(4): p. 1087-1109.

28. Masters, I., et al., *A robust blade element momentum theory model for tidal stream turbines including tip and hub loss corrections.* Proceedings of IMarEST - Part A - Journal of Marine Engineering and Technology, 2011. **10**(1): p. 25-35.

29. Malki, R., et al., *Planning tidal stream turbine array layouts using a coupled blade element momentum – computational fluid dynamics model.* Renewable Energy, 2014. **63**(0): p. 46-54.

30. Buckland, H.C., et al., *Cavitation inception and simulation in blade element momentum theory for modelling tidal stream turbines.* Proceedings of the Institution of Mechanical Engineers, Part A: Journal of Power and Energy, 2013. **227**(4): p. 479-485.

31. Bai, C.J.H., F.B. *Using CFD Computation for Aerodynamic Performance Design and Analysis of Horizontal Axis Wind Turbine Blade*. in *15th National Computational Fluid Dynamics Conference*. 2008. Tainan, Taiwan.

32. Lanzafame, R., S. Mauro, and M. Messina, *HAWT Design and Performance Evaluation: Improving the BEM Theory Mathematical Models.* Energy Procedia, 2015. **82**: p. 172-179.

33. Robin, L., G. Janusz, and M. Florian, *Predicting 2D Airfoil and 3D Wind Turbine Rotor Performance using a Transition Model for General CFD Codes*, in *44th AIAA Aerospace Sciences Meeting and Exhibit*. 2006, American Institute of Aeronautics and Astronautics.

34. Xu, G. and L.N. Sankar, *Development of engineering aerodynamics models using a viscous flow methodology on the NREL phase VI rotor.* Wind Energy, 2002. **5**(2-3): p. 171-183.

35. Shen, W.Z., et al., *Tip loss corrections for wind turbine computations.* Wind Energy, 2005. **8**(4): p. 457-475.

36. Madsen, H.A., et al., *Validation and modification of the Blade Element Momentum theory based on comparisons with actuator disc simulations.* Wind Energy, 2010. **13**(4): p. 373-389.

37. Carroll, J. and D. Marcum, *Comparison of a Blade Element Momentum Model to 3D CFD Simulations for Small Scale Propellers.* SAE International Journal of Aerospace, 2013. **6**(2): p. 721-726.

38. Malki, R., et al., *A coupled blade element momentum – Computational fluid dynamics model for evaluating tidal stream turbine performance.* Applied Mathematical Modelling, 2013. **37**(5): p. 3006-3020.

39. Esfahanian, V., et al., *Numerical analysis of flow field around NREL Phase II wind turbine by a hybrid CFD/BEM method.* Journal of Wind Engineering and Industrial Aerodynamics, 2013. **120**(0): p. 29-36.

40. Tavares Dias do Rio Vaz, D.A., et al., *An extension of the Blade Element Momentum method applied to Diffuser Augmented Wind Turbines.* Energy Conversion and Management, 2014. **87**: p. 1116-1123.

41. Joselin Herbert, G.M., et al., *A review of wind energy technologies.* Renewable and Sustainable Energy Reviews, 2007. **11**(6): p. 1117-1145.

42. *V164-9.5 MW*. 2011 [cited 2019 January]; Available from: http://www.mhivestasoffshore.com/category/v164-9-5-mw/.

43. *E-126 7.5MW*. 2007 [cited 2019 January]; Available from: https://www.enercon.de/en/products/ep-8/e-126/.

44. Arndt, C., *The global energy revolution and developing countries*. 2018, International Food Policy Research Institute (IFPRI).

45. Eriksson, S., H. Bernhoff, and M. Leijon, *Evaluation of different turbine concepts for wind power.* Renewable and Sustainable Energy Reviews, 2008. **12**(5): p. 1419-1434.

46. Jafari, S.A., *Performance Analysis of PowerWindow: a Linear Wind Generator*, in *Mechanical, Materials and Mechatronic (MMM)*. 2014, University of Wollongong.

47. Ishugah, T.F., et al., *Advances in wind energy resource exploitation in urban environment: A review.* Renewable and Sustainable Energy Reviews, 2014. **37**: p. 613-626.

48. Mohamed, M.H., *Performance investigation of H-rotor Darrieus turbine with new airfoil shapes.* Energy, 2012. **47**(1): p. 522-530.

49. Aslam Bhutta, M.M., et al., *Vertical axis wind turbine – A review of various configurations and design techniques.* Renewable and Sustainable Energy Reviews, 2012. **16**(4): p. 1926-1939.

50. Mohamed, M.H., et al., *Optimal blade shape of a modified Savonius turbine using an obstacle shielding the returning blade.* Energy Conversion and Management, 2011. **52**(1): p. 236-242.

51. Akwa, J.V., H.A. Vielmo, and A.P. Petry, *A review on the performance of Savonius wind turbines.* Renewable and Sustainable Energy Reviews, 2012. **16**(5): p. 3054-3064.

52. Gupta, R. and A. Biswas, *Computational fluid dynamics analysis of a twisted three-bladed H-Darrieus rotor.* Journal of Renewable & Sustainable Energy, 2010. **2**(4): p. 043111.

53. Debnath, B.K., A. Biswas, and R. Gupta, *Computational fluid dynamics analysis of a combined three-bucket Savonius and three-bladed Darrieus rotor at various overlap conditions.* Journal of Renewable & Sustainable Energy, 2009. **1**(3): p. 033110.

54. Mertens, S., *The energy yield of roof mounted wind turbines.* Wind Engineering, 2003. **27**(6): p. 507-518.

55. Wang, Y., et al., *Numerical investigation on aerodynamic performance of a novel vertical axis wind turbine with adaptive blades.* Energy Conversion and Management, 2016. **108**: p. 275-286.

56. Ragner, G.D., *Axial-mode linear wind-turbine*. 2003, Google Patents.

57. Ponta, F.L., J.J. Seminara, and A.D. Otero, *On the aerodynamics of variable-geometry oval-trajectory Darrieus wind turbines.* Renewable Energy, 2007. **32**(1): p. 35-56.

58. Ponta, F.L. and L.I. Lago, *Analysing the suspension system of variable-geometry oval-trajectory (VGOT) Darrieus wind turbines.* Energy for Sustainable Development, 2008. **12**(2): p. 5-16.

59. Otero, A.D. and F.L. Ponta, *On the structural behaviour of variable-geometry oval-trajectory Darrieus wind turbines.* Renewable Energy, 2009. **34**(3): p. 827-832.

60. *Cape Bouvard Energy* 2014 [cited 2014 October]; http://www.lineartechnologies.com.au/index.html]. Available from: http://www.lineartechnologies.com.au/index.html.

61. Drew, D.R., J.F. Barlow, and T.T. Cockerill, *Estimating the potential yield of small wind turbines in urban areas: A case study for Greater London, UK.* Journal of Wind Engineering and Industrial Aerodynamics, 2013. **115**(0): p. 104-111.

62. Sharma, R.N. and U.K. Madawala, *The concept of a smart wind turbine system.* Renewable Energy, 2012. **39**(1): p. 403-410.

63. Müller, G., M.F. Jentsch, and E. Stoddart, *Vertical axis resistance type wind turbines for use in buildings.* Renewable Energy, 2009. **34**(5): p. 1407-1412.

64. Ledo, L., P.B. Kosasih, and P. Cooper, *Roof mounting site analysis for micro-wind turbines.* Renewable Energy, 2011. **36**(5): p. 1379-1391.

65. Billinton, R. and G. Bai, *Generating capacity adequacy associated with wind energy.* Energy Conversion, IEEE Transactions on, 2004. **19**(3): p. 641-646.

66. Toja-Silva, F., A. Colmenar-Santos, and M. Castro-Gil, *Urban wind energy exploitation systems: Behaviour under multidirectional flow conditions—Opportunities and challenges.* Renewable and Sustainable Energy Reviews, 2013. **24**: p. 364-378.

67. Walker, S.L., *Building mounted wind turbines and their suitability for the urban scale—A review of methods of estimating urban wind resource.* Energy and Buildings, 2011. **43**(8): p. 1852-1862.

68. Ayhan, D. and Ş. Sağlam, *A technical review of building-mounted wind power systems and a sample simulation model.* Renewable and Sustainable Energy Reviews, 2012. **16**(1): p. 1040-1049.

69. Grant, A., C. Johnstone, and N. Kelly, *Urban wind energy conversion: The potential of ducted turbines.* Renewable Energy, 2008. **33**(6): p. 1157-1163.

70. Park, J., et al., *A new building-integrated wind turbine system utilizing the building.* Energies, 2015. **8**(10): p. 11846-11870.

71. Wang, F., et al., *Development of small domestic wind turbine with scoop and prediction of its annual power output.* Renewable Energy, 2008. **33**(7): p. 1637-1651.

72. Wang, F., et al., *The methodology for aerodynamic study on a small domestic wind turbine with scoop.* Journal of Wind Engineering and Industrial Aerodynamics, 2008. **96**(1): p. 1-24.

73. *PowerWindow*. 2015 [cited 2015; https://youtu.be/XM5SFx-IJJ0]. Available from: https://youtu.be/XM5SFx-IJJ0.

74. Døssing, M., H.A. Madsen, and C. Bak, *Aerodynamic optimization of wind turbine rotors using a blade element momentum method with corrections for wake rotation and expansion.* Wind Energy, 2012. **15**(4): p. 563-574.

75. Bazilevs, Y., et al., *3D simulation of wind turbine rotors at full scale. Part I: Geometry modeling and aerodynamics.* International Journal for Numerical Methods in Fluids, 2011. **65**(1-3): p. 207-235.

76. Li, Y., et al., *Dynamic overset CFD simulations of wind turbine aerodynamics.* Renewable Energy, 2012. **37**(1): p. 285-298.

77. Hailiang, X., H. Jiabing, and H. Yikang, *Operation of Wind-Turbine-Driven DFIG Systems Under Distorted Grid Voltage Conditions: Analysis and Experimental Validations.* Power Electronics, IEEE Transactions on, 2012. **27**(5): p. 2354-2366.

78. Utsunomiya, T., et al., *At Sea Experiment of a Hybrid Spar for Floating Offshore Wind Turbine Using 1/10-Scale Model.* Journal of Offshore Mechanics and Arctic Engineering, 2013. **135**(3): p. 034503-034503.

79. Wei, K., et al. *Modeling analysis and experimental research on a combined-type vertical axis wind turbine*. in *Electronics, Communications and Control (ICECC), 2011 International Conference on*. 2011.

80. Lee, S., et al., *Effects of design parameters on aerodynamic performance of a counter-rotating wind turbine.* Renewable Energy, 2012. **42**(0): p. 140-144.

81. Yousif, A.H., J.M. Hassan, and O.A. Khudar, *Effect of Surface Roughness Height on the Aerodynamics Performance of Axial Compressor Cascade Blades.* Al-Nahrain Journal for Engineering Sciences, 2015. **18**(1): p. 128-139.

82. Ingram, G., *Wind Turbine Blade Analysis using the Blade Element Momentum Method*. 2005.

83. Shives, M. and C. Crawford, *Developing an empirical model for ducted tidal turbine performance using numerical simulation results.* Proceedings of the Institution of Mechanical Engineers, Part A: Journal of Power and Energy, 2011.

84. El-Behery, S.M. and M.H. Hamed, *A comparative study of turbulence models performance for separating flow in a planar asymmetric diffuser.* Computers & Fluids, 2011. **44**(1): p. 248-257.

85. Menter, F.R., *Review of the shear-stress transport turbulence model experience from an industrial perspective.* Int. J. Comput. Fluid Dyn., 2009. **23**(4): p. 305-316.

86. *Gambit*. 2015 [cited 2015; http://www.arl.hpc.mil/software/description.html?sw=Gambit]. Available from: http://www.arl.hpc.mil/software/description.html?sw=Gambit.

87. Mohamed, M.H., *Impacts of solidity and hybrid system in small wind turbines performance.* Energy, 2013. **57**(0): p. 495-504.

88. Peacock, A.D., et al., *Micro wind turbines in the UK domestic sector.* Energy and Buildings, 2008. **40**(7): p. 1324-1333.

89. Rafailidis, S., *Influence of Building Areal Density and Roof Shape on the Wind Characteristics Above a Town.* Boundary-Layer Meteorology, 1997. **85**(2): p. 255-271.

90. Mirecki, A., X. Roboam, and F. Richardeau, *Architecture Complexity and Energy Efficiency of Small Wind Turbines.* IEEE Transactions on Industrial Electronics, 2007. **54**(1): p. 660-670.

91. Wood, D., *Small Wind Turbines*, in *Advances in Wind Energy Conversion Technology*, M. Sathyajith and G.S. Philip, Editors. 2011, Springer Berlin Heidelberg: Berlin, Heidelberg. p. 195-211.

92. Pagnini, L.C., M. Burlando, and M.P. Repetto, *Experimental power curve of small-size wind turbines in turbulent urban environment.* Applied Energy, 2015. **154**: p. 112-121.

93. Hassanli, S., et al., *Potential application of double skin façade incorporating aerodynamic modifications for wind energy harvesting.* Journal of Wind Engineering and Industrial Aerodynamics, 2018. **174**: p. 269-280.

94. Hassanli, S., et al., *Utilizing cavity flow within double skin façade for wind energy harvesting in buildings.* Journal of Wind Engineering and Industrial Aerodynamics, 2017. **167**: p. 114-127.

95. Hassanli, S., K.C.S. Kwok, and M. Zhao, *Performance assessment of a special Double Skin Façade system for wind energy harvesting and a case study.* Journal of Wind Engineering and Industrial Aerodynamics, 2018. **175**: p. 292-304.

96. Jafari, S.A.H., et al., *Aerodynamic analysis of a linear cascade wind turbine.* Wind Energy, 2018. **21**(11): p. 1141-1154.

97. Incropera, F.P. and P. David, *De Witt.* Fundamentals of heat and mass transfer, 1990. **4**.

98. Jafari, S.A.H., S. Hassanli, and K.C.S. Kwok, *Performance analysis of a small wind turbine mounted inside a tall building*, in *18th Australasian Wind Engineering Society Workshop*. 2016: Serafino Convention Centre, McLaren Vale, South Australia, Australia.

99. Blocken, B., et al., *Numerical study on the existence of the venturi effect in passages between perpendicular buildings.* Journal of Engineering Mechanics, 2008. **134**(12): p. 1021-1028.

100. Blocken, B., T. Stathopoulos, and J. Carmeliet, *Wind environmental conditions in passages between two long narrow perpendicular buildings.* Journal of Aerospace Engineering, 2008. **21**(4): p. 280-287.

101. Li, B., et al., *Revisiting the 'Venturi effect' in passage ventilation between two non-parallel buildings.* Building and Environment, 2015. **94**: p. 714-722.

102. Lu, L. and K.Y. Ip, *Investigation on the feasibility and enhancement methods of wind power utilization in high-rise buildings of Hong Kong.* Renewable and Sustainable Energy Reviews, 2009. **13**(2): p. 450-461.

103. Jafari, S.A.H., et al., *The effects of installation configuration and solidity on the power generation of a linear cascade wind turbine.* Journal of Wind Engineering and Industrial Aerodynamics, 2018. **180**: p. 122-135.

104. Jafari, S.A.H., et al., *Aerodynamic Analysis of a Stator-augmented Linear Cascade Wind Turbine.* Wind Energy, 2018. **uner peer review**.

105. Perry, R.H. and D.W. Green, *Perry's Chemical Engineers' Handbook*. 2007: McGraw Hill.

106. DiPietro, A.L., *Integrated fan-core twin spool counter-rotating turbofan gas turbine engine*. 2002, Google Patents.

107. Hwang, B., S. Lee, and S. Lee, *Optimization of a counter-rotating wind turbine using the blade element and momentum theory.* Journal of Renewable and Sustainable Energy, 2013. **5**(5).

108. Lawn, C.J., *Optimization of the power output from ducted turbines.* Proceedings of the Institution of Mechanical Engineers, Part A: Journal of Power and Energy, 2003. **217**(1): p. 107-117.

109. Park, J., et al., *A New Building-Integrated Wind Turbine System Utilizing the Building.* Energies, 2015. **8**(10): p. 11846-11870.

110. Abohela, I., N. Hamza, and S. Dudek, *Effect of roof shape, wind direction, building height and urban configuration on the energy yield and positioning of roof mounted wind turbines.* Renewable Energy, 2013. **50**: p. 1106-1118.

111. Dannecker, R.K.W. and A.D. Grant, *Investigations of a building-integrated ducted wind turbine module.* Wind Energy, 2002. **5**(1): p. 53-71.

112. Grant, A. and N. Kelly, *A ducted wind turbine model for building simulation.* Building Services Engineering Research and Technology, 2004. **25**(4): p. 339-349.

113. Chong, W.T., et al., *Performance investigation of a power augmented vertical axis wind turbine for urban high-rise application.* Renewable Energy, 2013. **51**: p. 388-397.

114. Krishnan, A. and M. Paraschivoiu, *3D analysis of building mounted VAWT with diffuser shaped shroud.* Sustainable Cities and Society, 2016. **27**: p. 160-166.

115. Bianchini, A., et al., *Comparative Analysis of Different Numerical Techniques to Analyze the Wake of a Wind Turbine.* 2017(50961): p. V009T49A017.

116. Migoya, E., et al., *Comparative study of the behavior of wind-turbines in a wind farm.* Energy, 2007. **32**(10): p. 1871-1885.

117. Barthelmie, R.J., et al., *Modelling and measuring flow and wind turbine wakes in large wind farms offshore.* Wind Energy, 2009. **12**(5): p. 431-444.

118. Sanderse, B., S.P. Pijl, and B. Koren, *Review of computational fluid dynamics for wind turbine wake aerodynamics.* Wind Energy, 2011. **14**(7): p. 799-819.

119. Jiménez, Á., A. Crespo, and E. Migoya, *Application of a LES technique to characterize the wake deflection of a wind turbine in yaw.* Wind Energy, 2010. **13**(6): p. 559-572.

120. Jimenez, A., et al., *Advances in large-eddy simulation of a wind turbine wake.* Journal of Physics: Conference Series, 2007. **75**(1): p. 012041.

121. Jimenez, A., et al., *Large-eddy simulation of spectral coherence in a wind turbine wake.* Environmental Research Letters, 2008. **3**(1): p. 015004.

122. Jafari, S., et al. *Effect of Incident Wind Angle on Power Generation of Building Integrated Wind Turbines*. in *9th Asia-Pacific Conferences on Wind Engineering*. 2017.

123. Hassanli, S., et al. *Performance Assessment of Cascaded Wind Turbines inside Through-building Openings*. in *9th Asia-Pacific Conferences on Wind Engineering*. 2017.

124. Hassanli, S., et al., *Application of through-building openings for wind energy harvesting in built environment.* Journal of Wind Engineering and Industrial Aerodynamics, 2019. **184**: p. 445-455.

125. *Ampair*. 2016 [cited 2016 January]; http://www.nfenergies.com/documents/Ampair%20300%20Data%20Sheet.pdf]. Available from: http://www.nfenergies.com/documents/Ampair%20300%20Data%20Sheet.pdf.

126. Franke, J., *Best practice guideline for the CFD simulation of flows in the urban environment*. 2007: Meteorological Inst.

127. Hassanli, S., S.A.H. Jafari, and K.C.S. Kwok, *Performance assessment of cascaded wind turbines inside through-building openings*. 2017, 9th Asia-Pacific Conference on Wind Engineering.

128. Jafari, S.A.H., K.C.S. Kwok, and S. Hassanli, *Integration of wind turbines in tall buildings for wind power generation*, in *8th International Colloquium on Bluff Body Aerodynamics and Applications*. 2016: Northeastern University, Boston, Massachusetts, USA.

129. *Wind Roses for Selected Locations in Australia*. 2016 [cited 2018 August]; http://www.bom.gov.au/climate/averages/wind/selection_map.shtml]. Available from: http://www.bom.gov.au/climate/averages/wind/selection_map.shtml.

Appendix A

A.1. Confugration of PowerWindow

Linear Cascade Wind Turbines are a new generation of wind turbines, in which the blades move within a rectangular frame. This type of wind turbine is capable of generating electricity at relatively low wind velocities ($< 10\, m.s^{-1}$) with relatively low blade speed ($\approx 2\, m.s^{-1}$).LCWTs owing to their design are safe and architecturally suitable for use in urban environments [60]. PowerWindow is a LCWT, in which, two series of blades are arranged in a linear cascade configuration and move (vertically or horizontally) in opposite directions perpendicular to the approaching wind direction (Figure A.1).

PowerWindow design is similar to Variable-Geometry Oval-Trajectory (VGOT) Darrieus turbine [57-59], modified version of a straight-blade Darrieus or H-rotor Vertical Axis Wind Turbine(VAWT) [27]. Similar to VGOT, PowerWindow has an adjustable blade design angle (θ_0), which enables optimizing the angle of attack (α) when exposed to different approach wind velocities. Here, θ_0 refers to the angle between the cord length of the blades and the horizontal axis. Therefore, α equals θ_0 if the blades are stationary and reduces to below θ_0 as the blades' speed increases. Moreover, PowerWindow is a compact modular unit which can be installed alone or in numbers. Further information on the configuration and power generation mechanism of PowerWindowcan be found in previous studies [7, 73].

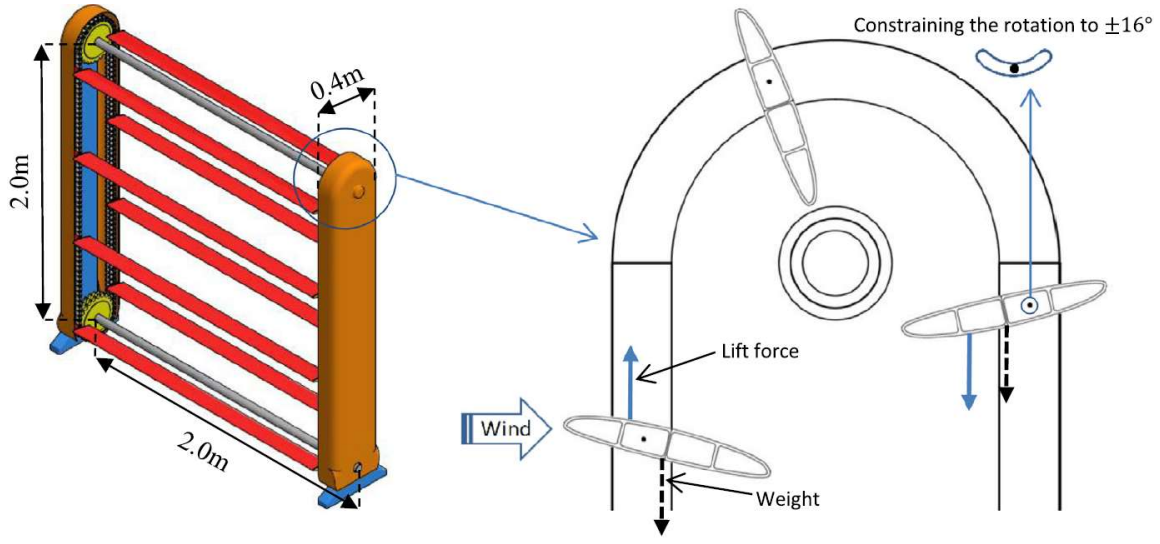

(a) (b)

Figure A 1: (a) Sketch of the PowerWindow prototype, (b) Front blades and rear blades move vertically in opposite direction [7].

A.2. Modified blade element momentum model

This appendix presents the aerodynamics of cascade and the BEM model developed in Mphil thesis by Jafari (2014).

A.2.1. Aerodynamics of cascade

The first step in developing the analytical model was to calculate C_L and C_D of the PowerWindow blades. For most of the well-known airfoils, C_L and C_D have been extracted for a limited range of angle of attack (α), Reynolds and Mach numbers, and the recorded databases are available. However, it has been reported that the values are usually higher than those which are typically experienced by wind turbine blades during the operation [26]. In this study, $k-\omega$ shear stress transport (SST), a transitional model was used in the CFD simulations to extract the C_L and C_D values for an isolated airfoil and similar airfoil in a linear cascade configuration with solidity (σ) of the PowerWindow prototype: $\sigma = 0.428$. The C_L and C_D values of an airfoil cascade configuration are different from an isolated one and strongly depends on σ. Due to the higher surface area, cascade configuration increases drag. Meanwhile, by restraining the flow, it postpones stall. Studies have shown that the influence of surface height roughness reduces, while C_D increases with an increase in the height of roughness. The height of roughness does eliminate the operating condition of the cascade blades, which reduces the value of the stall angle [81]. A cross-section of the PowerWindow airfoil is shown in Figure A 2.

In PowerWindow σ is the ratio of the total surface area of the windward side of the (front/rear) blades to the total area of PowerWindow exposed to the approach wind:

$$\sigma = NB/A \quad \text{(A 1)}$$

Where *N*, *B* and *A* represents the number of the blades, area of the blades and area of PowerWindow respectively.

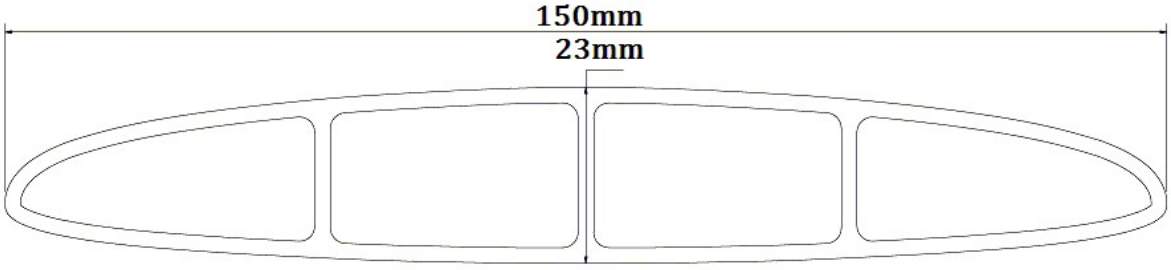

Figure A 2: Cross section view of the airfoil shows its symmetry which enables flow to efficiently create lift when the blade is located at both the front or rear side of PowerWindow.

The C_L and C_D of the linear cascade configuration are also extracted for some higher σ values: $\sigma = 0.857$ and 1.714, to demonstrate the influence of σ on the aerodynamic performance of

PowerWindow. Infinite numbers of airfoils are located above each other using periodic boundary conditions on a line perpendicular to the approach wind. Inlet flow direction is constant and α is created by rotating the airfoil(s). In all simulations, the inlet wind velocity was set to $8\ m/s$, which is achievable in appropriate places in urban environments. The Reynolds and the Mach number are 7.1×10^4 and 2.33×10^{-2} based on cord length the airfoil and room temperature (300K).

Figures A 3 (a) and (b) show C_L and C_D extracted for the isolated airfoil and the linear cascade configuration with $\sigma = 0.428,\ 0.857$ and 1.714 against a range of α:$-14° < \alpha < 36°$. Polynomial curves have been fitted to the undertaken results for C_L and C_D in the prototype condition: $\sigma = 0.428$. This function facilitates calculation of the lift and drag forces in the BEM model by making them dependent on α.

As can be seen in Figure A 3 (a) the maximum C_Ls of cascade airfoils are lower than the maximum C_L of the isolated airfoil. In addition, asσincreases, the maximum C_L decreases and shifts to higher α. It can also be seen that for $10° < \alpha$, C_D of the higher σ cascades lie below the lower σ cascades. The reason lies in the effect of multi cascade blades on flow direction, separation and pressure distribution on and around the PowerWindow blades. Figure 3.3 (a-c) has illustrated surface pressure coefficient (C_{SP}) and velocity ratio (R_V) of the flow around the isolated blade and the linear cascade configurations on left and right side respectively. The results have been undertaken at $\alpha = 16°$ with $\sigma = 0.428,\ 0.857$ and 1.714 for the linear cascade configurations. $\alpha = 16°$ is equal to θ_0 of the prototype which happens when PowerWindow is in stationary condition.

The optimum lift to drag ratio is not investigated in this study because, in the experimental test, increasing the design angle resulted in a destructive fluctuating drag.

C_{SP} shows the ratio of the local air pressure to the dynamic pressure of the free stream and R_V shows the local air velocity ratio to the approach wind velocity, respectively shown in Equations A 2 and A 3:

$$R_V = \frac{V_{local}}{V_{wind}} \quad \text{(A 2)}$$

$$C_{SP} = \frac{P}{1/2(\rho A {V_{wind}}^2)} \quad \text{(A 3)}$$

A comparison of C_{SP} contours around the isolated airfoil and linear cascade configurations show that increasing the blades' area, decreased the intensity of the high- and low-pressure regions on their surface but a higher pressure gradient was created between the upstream and downstream of the blades. Therefore, as the blades' area increased a lower lift is created on each single blade of the linear cascade configuration. However, by multiplying the resultant vertical force by the number of

the blades, the overall lift may increase. This study investigates the overall effect of increasing σ on power generation of PowerWindow in the developed BEM model.

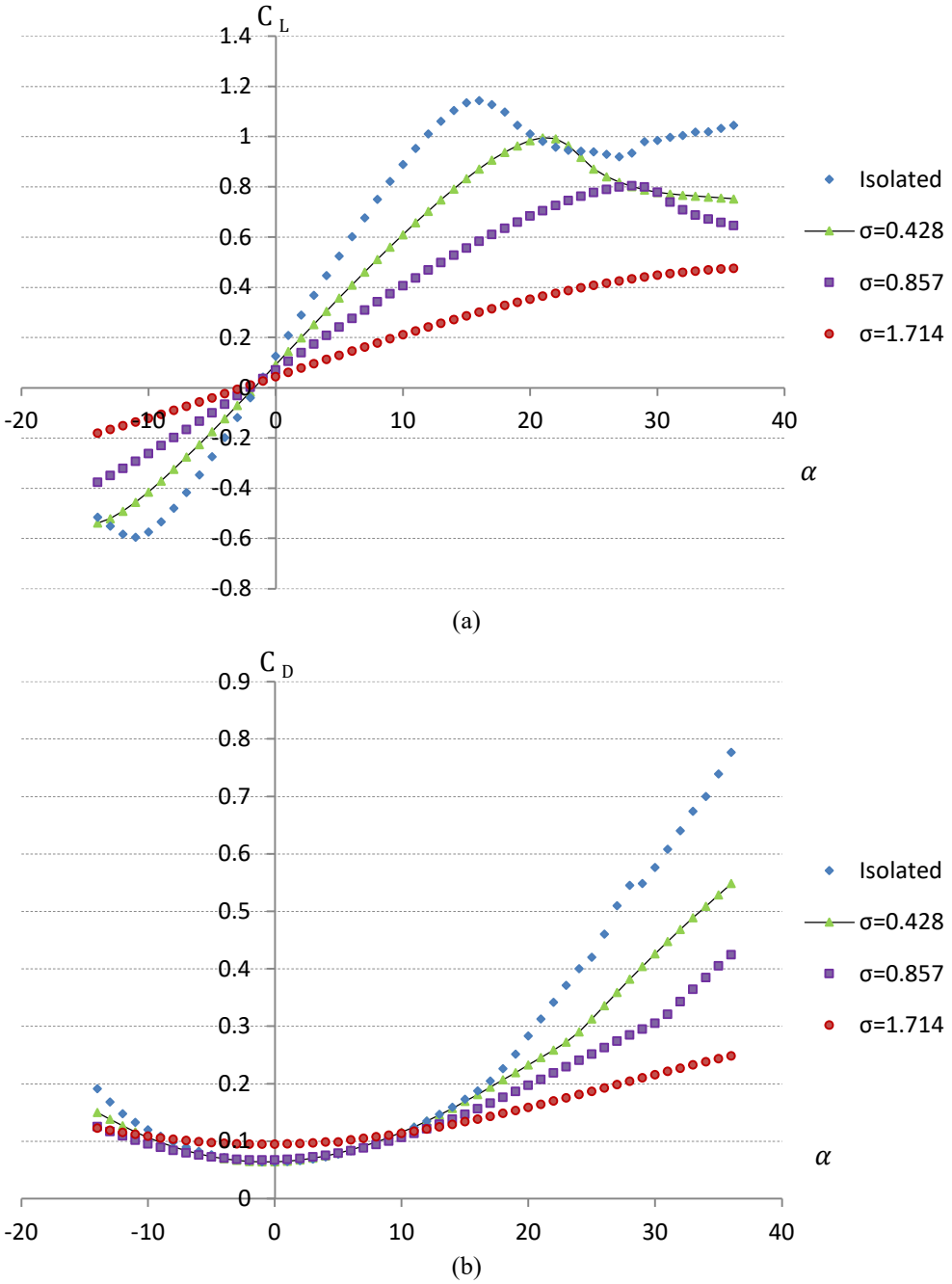

Figure A 3: (a) C_L and (b) C_D of the PowerWindowisolated and linear cascade configurationswith $\sigma =$ 0.428, 0.857 and 1.714 against α. For $\sigma = 0.428$:$C_L = 3.93 \times 10^{-1}\ \alpha^{11} - 4.35 \times 10^{-13}3\alpha^{10} + 1.47 \times 10^{-11}\alpha^{9} - 2.55 \times 10^{-11}\alpha^{8} - 6.89 \times 10^{-9}\alpha^{7} + 7.05 \times 10^{-8}\alpha^{6} + 9.76 \times 10^{-7}\alpha^{5} - 1.14 \times 10^{-5}\alpha^{4} - 8.05 \times 10^{-5}\alpha^{3} + 5.68 \times 10^{-4}\alpha^{2} + 5.48 \times 10^{-2}\alpha + 8.73 \times 10^{-2}andC_D = -3.02 \times 10^{-9}\alpha^{5} + 1.86 \times 10^{-7}\alpha^{4} - 4.39 \times 10^{-6}\alpha^{3} + 4.07 \times 10^{-4}\alpha^{2} + 9.43 \times 10^{-4}\ \alpha + 6.63 \times 10^{-2}$.

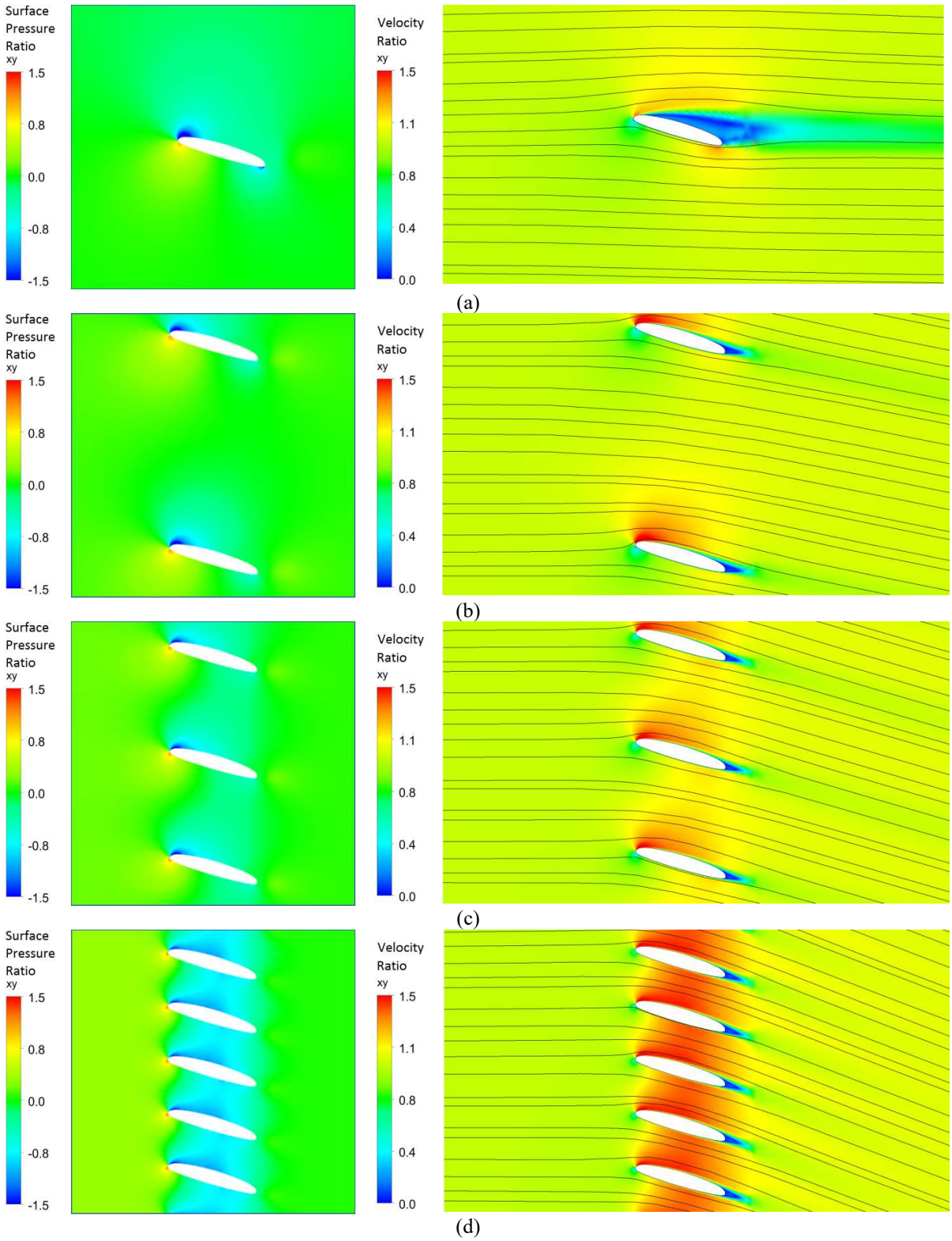

Figure A 4: C_{SP} (on the left side) and R_V (on the right side) contours and stream lines around (a) isolated PowerWindow airfoil and cascade configurations with (b) $\sigma = 0.428$ and (c) $\sigma = 0.857$and (d) $\sigma = 1.714$ at $\alpha = 16°$.

Comparing R_V contours around the isolated airfoil and linear cascade configurations show that increasing the number of the blades (i) increases the velocity of the flow between the blades, (ii) shifts the separation point toward the trailing edge of the blades and (iii) increases flow redirection parallel to the cord line of the blades. Increasing the velocity between the blades due to preservation of continuity justifies the lower pressure created between the blades in linear cascade configurations, particularly for the highest one with $\sigma = 1.714$. Shifting the separation point to the trailing edge of the blades in the linear cascade configurations with higher σ because of the flow being trapped between two blades justifies shifting the maximum C_L to higher α in Figure A 3 (a). On the other hand, although increasing σ creates a higher total drag on the blades, by trapping flow between the blades it reduces the separation, which increases the drag and eventually reduces the contribution of each blade to the total C_D. Increasing flow redirection in the linear cascade configurations with higherσ raisesquestions about the influence of the front blades on the direction of the flow approaching the rear ones in PowerWindow; this is also investigated in this study.

A.2.2. Application of the modified BEM model for PowerWindow

A.2.2.1. The modified momentum theory

Figure 3.4 shows a flow stream tube around PowerWindow. It is assumed that the flow expands equally at the top and bottom of PowerWindow. The approach wind has an almost uniform velocity profile at the inlet of the elevated PowerWindow. The analytical model calculates the forces exerted on each blade based on the local pressure and velocity. However, that would make the calculations significantly difficult to consider one particular zone for every single blade. Therefore, a reasonable assumption that facilitates the calculations by considering the uniform velocity profile at the inlet of the elevated PowerWindow is needed. In this assumption, the entire front blades are exposed to one uniform flow in one union zone, and similarly the entire rear blades are exposed to another uniform flow in another union zone. 5 zones emerge out of this division in and around PowerWindow which are bounded by 6 boundaries/interfaces from each other and flow characteristics of the approach wind can assume to be changing while proceeding from one zone to the next one. These 6 boundaries are shown in Figure A 5.

The upstream flow far from PowerWindow is before Boundary 0. Boundaries 1 and 2 are the leading edge and the trailing edge of the front blades of PowerWindow. Boundaries 3 and 4 are the leading edge and trailing edge of the rear blades of PowerWindow. After Boundary 5 is the downstream flow far from PowerWindow. The velocity and pressure at each boundary $i = \{0, 1, \dots 5\}$ is denoted by $\mathrm{V_i}$ and p_i, respectively.

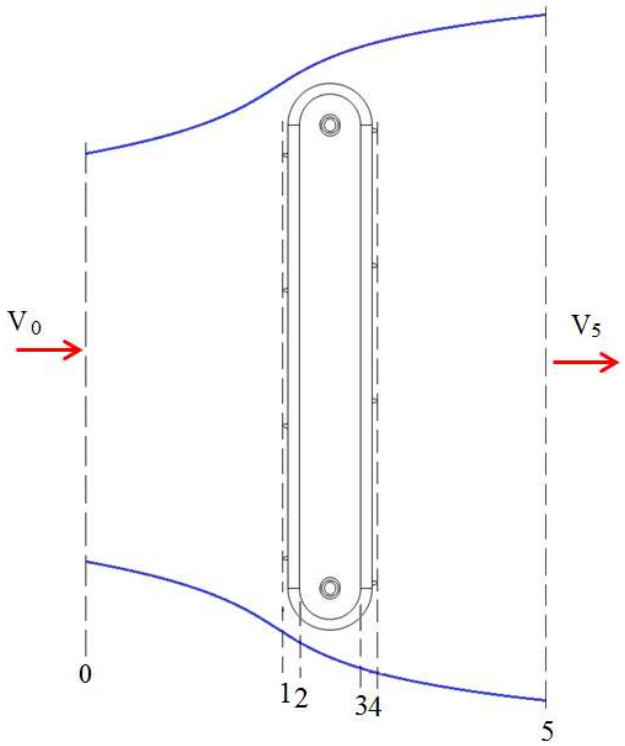

Figure A 5: Approach flow passing the elevated PowerWindow from far upstream to far downstream through 6 identified boundaries.

Distance between the leading and trailing edge of the PowerWindow blades is short. Therefore, it is assumed that $V_{1,x} = V_{2,x}$ and $V_{3,x} = V_{4,x}$, however pressure of the flow drops from p_2 to $p_1 (p_2 < p_1)$ and p_3 to $p_4 (p_4 < p_3)$ across the front blade and rear blades respectively. Distance between the front and rear blades in PowerWindow prototype is also equal to the blades cord length. Within the space of the front and rear blades the flow does not expand, so it can reasonably be assumed that $p_2 = p_3$ and $V_{2,x} = V_{3,x}$. But, prior to entering PowerWindow between 0 and 1, flow expands, and its velocity reduces from $V_{0,x}$ to $V_{1,x}$ and air pressure increases from p_0 to p_1 (note that $p_0 = p_{atm}$). This expansion will magnify the pressure in 1 and create enough pressure-gradient for air to pass through both front and rear blades, so in one zone the pressure in 1 decreases to pressure in 2 and in another zone pressure in 3 decreases to pressure in 4 with an axial induction factor (a_f). In the second expansion air velocity reduces from $V_{4,x}$ to $V_{5,x}$ and its pressure increases from p_4 to p_5 ($p_5 = p_{atm}$).

a_f is the ratio of decrease in velocity to the approach velocity:

$$a_f = \frac{V_{0,x} - V_{1,x}}{V_{0,x}} = \frac{V_{4,x} - V_{5,x}}{V_{5,x}} \quad \text{(A 4)}$$

It should be noted that a unified a_f is considered for the entire blade system since the gap between the front and rear blades in the prototype configuration is not large enough for wind to recover its

velocity/pressure. Otherwise, an induvial a_{f_1} needs to be considered for the front blades and a_{f_2} for the rear ones, which will be investigated in further studies. When $p_3 = p_2$ and $V_{1,x} = V_{2,x} = V_{3,x} = V_{4,x}$, the power extracted by the front and rear blades can be calculated by Equations A 5 and A 6:

$$P_{PW,front} = V_{1,x}A(p_1 - p_2) = V_{0,x}A(1 - a_f)(p_1 - p_2) \quad \text{(A 5)}$$
$$P_{PW,rear} = V_{3,x}A(p_3 - p_4) = V_{0,x}A(1 - a_f)(p_2 - p_4) \quad \text{(A 6)}$$

And the total power captured by PowerWindowis:

$$P_{PW,total} = V_{0,x}A(1 - a_f)(p_1 - p_4) \quad \text{(A 7)}$$

As a_f assumes equal air velocity reduction rates at upstream and downstream of PowerWindow, V_5 can be calculated based on V_1 as follows:

$$V_{5,x} = V_{1,x}A(1 - a_f) = V_{1,x}A(1 - a_f)^2 \quad \text{(A 8)}$$

Considering $P_0 = P_5 = P_{atm}$ and $V_{0,x}$=V_{wind}, multiplying the dynamic pressure reduction of the approach wind by its average velocity, $P_{PW,total}$ can be calculated as follows:

$$P_{PW,total} = \tfrac{1}{2}\rho A {V_{wind}}^3(1 - a_f)^2 \quad \text{(A 9)}$$

Effect of the tangential momentum and induction factor (a'_f) is assumed to be negligible on power generation of PowerWindow because the front and rear blades are chained together, and the inlet flow simultaneously moves the front blades up and the rear ones down with the same velocity.

A.2.2.2. The modified blade element theory for PowerWindow

Blade element theory divides a blade into small elements so that the forces on each of these small elements can be individually calculated. These forces are then integrated along the entire blade and over one rotor revolution in order to obtain the forces produced by the entire propeller or rotor [82]. Since PowerWindow blades are not twisted and have the similar airfoil shape along the spanwise, the vertical and horizontal forces can be calculated along entire the span of the front and rear blades ($i = 1,2$) by the following equations:

$$F_{x_i} = (F_{L_i}sin\beta_i + F_{D_i}cos\beta_i) \quad \text{(A 10)}$$
$$F_{y_i} = (F_{L_i}cos\beta_i - F_{D_i}sin\beta_i) \quad \text{(A 11)}$$

β is effective angle (the angle between the drag direction and the horizontal axis and/or between the lift direction and the vertical axis), α is the angle of attack and θ_0 is the blade design angle (the angle between the cord line and the horizontal axis). Therefore, β is equal to the difference between

θ_0 and α: $\beta = \theta_0 - \alpha$. Figure 3.5 shows four blades located in different regions in PowerWindow: front blade in Region A; rear blade in Region B; front blade in the turning Region C; and rear blade in the turning in Region D. θ_0 is constant in Regions A and B but θ is variable in the semicircular Regions C and D. The variation of θ is dependent on both θ_0 and φ, where φ is the angular location of the blades centre to the rotating axis in Regions C and D.

Wind exerts a lift force on the blade causes the belt to roll and moves the blade from Region A to B. As the belt goes around φ increases and moves the blade from Region C to D, the blade changes side and orientation (θ) as shown in Figure 3.5. If the attachment between blades and the belt were fixed, the lift forces acting on the front and the rear blades would oppose each other. Hence PowerWindow is designed such that blades 'flip over' and adjust their angle of attack as they move from Region A to B. The adjustment is done passively without any additional control mechanism. This is achieved by observing that the force of gravity acts at the centre of mass, while the lift force acts at the centre of pressure which for most profiles is closer to the leading edge of the blade. In PowerWindow, the blade is attached to the belt at a point which is forward of the centre of mass but behind the centre of pressure in the upwind state. In the current prototype and based on the blade profile shown, the point of attachment is at about a third of the cord length. The blade is free to rotate around within a certain degree at the point of attachment so that a positive and negative angle of attack can be obtained in the front and rear blades respectively. The blade's angular rotation is constrained by a simple pin-and-groove mechanism shown in Figure 3.1 (b), which in the current prototype limits the angles of attack to ±16° [7].

Equations A 12, shows the relations between θ and φ and θ_0 in Regions C and D:

$$\theta = \theta_0 \left(1 - \frac{\varphi}{90}\right) + \varphi \qquad \text{(A 12)}$$

Power generation of the single blade located in Region C and D is assumed to be negligible compared to the (ten) blades located at Regions A and B.

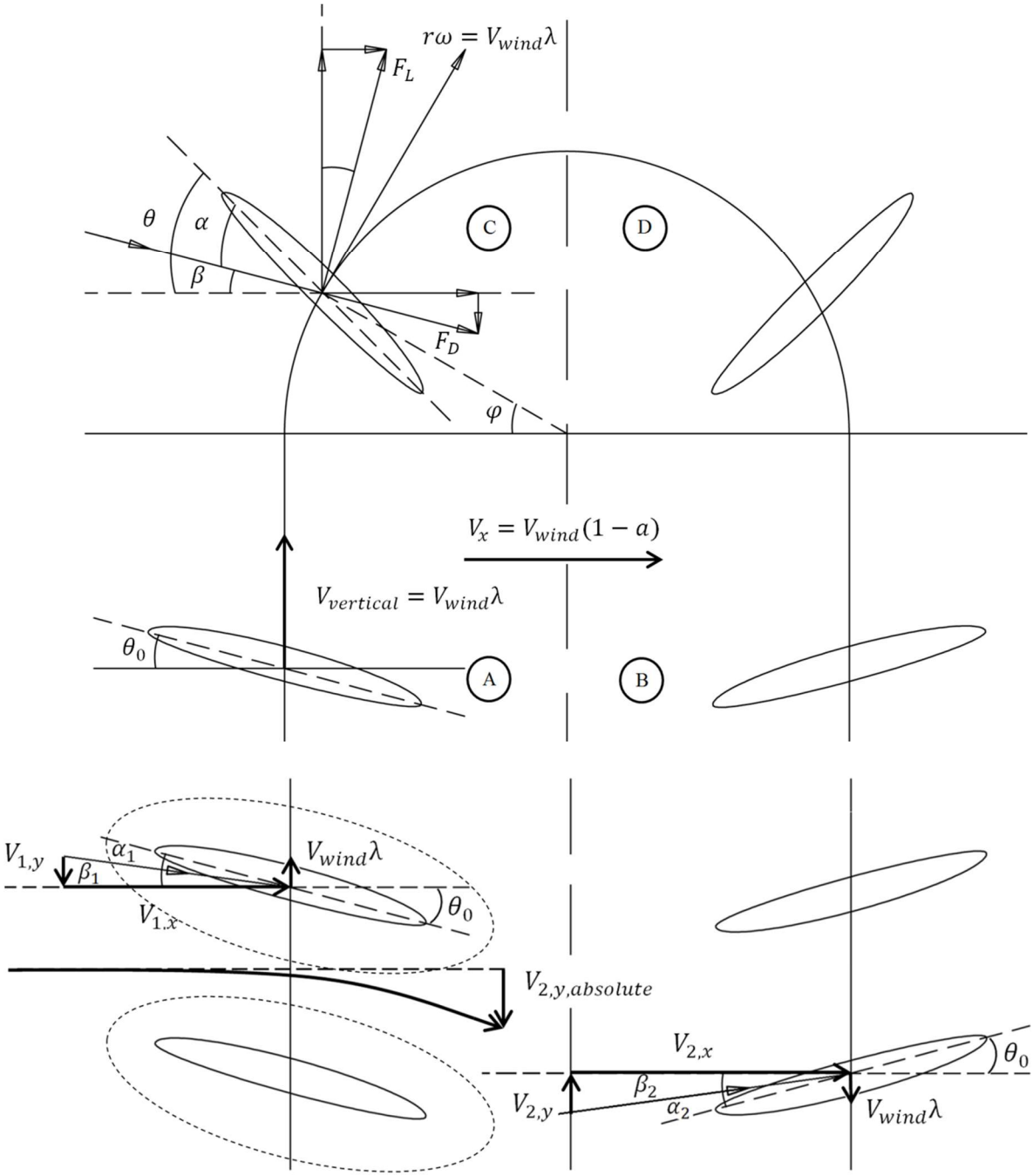

Figure A 6: Schematic view of the path followed by the blades of PowerWindowin Regions A, B, C and D, and the velocity vectors of the wind facing the front and rear blades.

Blade Speed Ratio denoted by λ is the ratio of the blade's speed to the approach wind velocity, where blade's speed is the vertical component of the relative velocity of the flow approaching the front:

$$\lambda = \frac{V_{blade}}{V_{wind}} = \frac{V_{rel_{1,y}}}{V_{wind}} \quad \text{(A 13)}$$

As the blades move in Regions A and B, power generation can be calculated by integration of the resultant vertical force exerted on each blade multiplied by its vertical velocity:

$$Power = \sum_1^N \left(\frac{\rho B}{2}\right) {V_{rel}}^2 \left[C_L cos\beta - C_D sin\beta\right](V_{wind}\lambda) \quad \text{(A 14)}$$

The vertical forces exerted on the blades (F_y) have been calculated using F_L and F_D from Equations A 10 and A 11. V_{rel} shows the relative wind velocity with respect to a blade and can be calculated by Equation 3.16 ($i = 1,2$):

$${V_{rel_i}}^2 = {V_{rel_{i,y}}}^2 + {V_{rel_{i,x}}}^2 \quad \text{(A 15)}$$

Considering the far upstream velocity is equal to the approach wind velocity ($V_{wind} = V_{0,x}$), the horizontal velocity of the flow passing through the front and rear blades can be calculated by Equation A 16:

$$V_{1,x} = V_{2,x} = V_{wind}\left(1 - a_f\right) \quad \text{(A 16)}$$

The vertical component of the relative velocity of the flow approaching the front blades equals to the PowerWindow blades speed:

$$V_{1,x} = \lambda V_{wind} \quad \text{(A 17)}$$

Then, β_1 and α_1 can be calculated as follow:

$$\beta_1 = tan^{-1}\left(V_{1,y}/V_{1,x}\right) = tan^{-1}\left(\lambda/\left(1 - a_f\right)\right) \quad \text{(A 18)}$$

$$\alpha_1 = \theta_0 - tan^{-1}\left(\lambda/\left(1 - a_f\right)\right) \quad \text{(A 19)}$$

Substituting β_1 and α_1 (from Equations A 18 and A 19) in Equation A 14 gives the power captured by the front blades ($P_{PW,front}$):

$$P_{PW,front} = N\left(\frac{\rho B}{2}\right) {V_{wind}}^3 \lambda\left(\left(1 - a_f\right)^2 + \lambda^2\right)\left[\begin{array}{l} C_{L_{\alpha 1}} cos\left(tan^{-1}\left(\frac{\lambda}{(1-a_f)}\right)\right) - \\ C_{D_{\alpha 1}} sin\left(tan^{-1}\left(\frac{\lambda}{(1-a_f)}\right)\right) \end{array}\right] \quad \text{(A 20)}$$

As shown in Figure 4, that linear cascade blades redirect the flow stronger when the σ is higher. Therefore, the relative vertical velocity of the flow approaching the rear blades is affected by both the slope (θ_0) and number of the front blades (σ). These two parameters lead the flow downward. Meanwhile, the relative vertical velocity of the flow approaching the rear blades is affected by the upward translation of the front blades (λ) which leads the flow upward. Hence, the overall effect of the front blades on the flow may result in redirecting it upward or downward which needs to be elucidated.

However, if σ is sufficiently high, the front blades can influence the entire flow passing through them. Then, the vertical component of the wind in the middle of PowerWindow can be calculated by Equation A 21:

$$V_{2,y} = \lambda V_{wind} - V_{wind}(1 - a_f)tan\theta_0 = V_{wind}(\lambda - (1 - a_f)tan\theta_0) \quad \text{(A 21)}$$

The rear blades have downward vertical velocity equal to the upward vertical velocity of the front blades. Hence, the relative vertical velocity of the flow approaching the rear blades can be calculated by Equation A 22:

$$V_{relative_{2,y}} = V_{2,y} + \lambda V_{wind} = V_{wind}(2\lambda - (1 - a_f)tan\theta_0) \quad \text{(A 22)}$$

Considering Equation A 16 and A 22, β_2 and α_2 can be calculated using Equations A 23 and A 24 as follow:

$$\beta_2 = tan^{-1}\left(\frac{V_{2y}}{V_{2x}}\right) = tan^{-1}\left(\frac{2\lambda - (1-a_f)tan\theta_0}{1-a_f}\right) \quad \text{(A 23)}$$

$$\alpha_2 = \theta_0 - tan^{-1}\left(\frac{((2\lambda - (1-a_f)tan\theta_0)}{(1-a_f)}\right) \quad \text{(A 24)}$$

Assuming uniform aerodynamic force exerted on every blade in the elevated position, and applying the velocities calculated by Equations A 15, A 16 and A 22 and substituting β_2 and α_2 into Equation A 14, power generated by the rear blades ($P_{Pw,rear}$) can be calculated as follow:

$$P_{Pw,rear} = N\left(\frac{\rho B}{2}\right){V_{wind}}^3\,\lambda\left((1 - a_f)^2 + (2\lambda - (1 - a_f)tan\theta)^2\right)\left[C_{L_{\alpha 2}}cos\left(tan^{-1}\left(\frac{(2\lambda - (1-a_f)tan\theta_0)}{(1-a_f)}\right)\right) - C_{D_{\alpha 2}}sin\left(tan^{-1}\left(\frac{(2\lambda - (1-a_f)tan\theta_0)}{(1-a_f)}\right)\right)\right] \quad \text{(A 25)}$$

Equation A 25 can accurately calculate the power generation by the rear blades when the entire flow is affected by the front blades. However, if a portion of the flow is not affected by the front blades, Equations A 21-25 does not give the accurate answer. In practice when σ is very low ($\sigma \ll 1$) or the approach wind velocity is very high, the front blades may only affect the air adjacent to their surface. The area within the dashed line in Figure A 6 shows such an area. In this case, the affected flow ratio ε is defined and represents the ratio of the flow affected by the front blades to the entire flow passing through PowerWindow. Applying ε into Equations A 21-24, results in Equations A 26-29:

$$V_{2y,absolute} = \varepsilon V_{wind}(\lambda - (1 - a_f)tan\theta_0) \quad \text{(A 26)}$$

$$V_{2y} = V_{2y,absolute} + \lambda V_{wind} = V_{wind}\left((\varepsilon + 1)\lambda - \varepsilon(1 - a_f)tan\theta_0\right) \quad \text{(A 27)}$$

$$\beta_2 = tan^{-1}\left(\frac{V_{2y}}{V_{2x}}\right) = tan^{-1}\left(\frac{\left((\varepsilon+1)\lambda - \varepsilon(1-a_f)tan\theta_0\right)}{(1-a_f)}\right) \quad \text{(A 28)}$$

$$\alpha_2 = \theta_0 - tan^{-1}\left(\frac{\left((\varepsilon+1)\lambda-\varepsilon(1-a_f)tan\theta_0\right)}{(1-a_f)}\right) \quad \text{(A 29)}$$

Replacing the resultant velocity and angles in Equation A 25 results in Equation A 30:

$$P_{PW,rear} = N\left(\frac{\rho B}{2}\right){V_{wind}}^3\,\lambda\left(\frac{(1-a_f)^2 + \left((\varepsilon+1)\lambda-\varepsilon(1-a_f)tan\theta_0\right)^2}{}\right)\left[C_{L_{\alpha 2}}cos\left(tan^{-1}\left(\frac{\left((\varepsilon+1)\lambda-\varepsilon(1-a_f)tan\theta_0\right)}{(1-a_f)}\right)\right) - C_{D_{\alpha 2}}sin\left(tan^{-1}\left(\frac{\left((\varepsilon+1)\lambda-\varepsilon(1-a_f)tan\theta_0\right)}{(1-a_f)}\right)\right)\right] \quad \text{(A 30)}$$

A.2.2.3. The modified BEM formulation derived for PowerWindow

Equating the total power generation (Equation A 10) from momentum theory with the total power generation of the front and rear blades (Equations A 20 and A 30) results in Equation A 31. Equation 3.32 calculates a_f and then the power generation of the front and rear blades of PowerWindow:

$$\tfrac{1}{2}\rho A{V_{wind}}^3(1-a_f)^2 = B\left(\frac{\rho C}{2}\right){V_{wind}}^3\lambda\left[\left(\left((1-a_f)^2+\lambda^2\right)\left[C_{L_{\alpha 1}}cos\left(tan^{-1}\left(\frac{\lambda}{(1-a_f)}\right)\right) - C_{D_{\alpha 1}}sin\left(tan^{-1}\left(\frac{\lambda}{(1-a_f)}\right)\right)\right]\right) + \left((1-a_f)^2 + \left((\varepsilon+1)\lambda-\varepsilon(1-a_f)tan\theta_0\right)^2\right)\left[C_{L_{\alpha 2}}cos\left(tan^{-1}\left(\frac{\left((\varepsilon+1)\lambda-\varepsilon(1-a_f)tan\theta_0\right)}{(1-a_f)}\right)\right) - C_{D_{\alpha 2}}sin\left(tan^{-1}\left(\frac{\left((\varepsilon+1)\lambda-\varepsilon(1-a_f)tan\theta_0\right)}{(1-a_f)}\right)\right)\right]\right] \quad \text{(A 31)}$$

MATLAB is used in this study for solving Equation A 31, calculating a_f and power generation at various λ. The λ whichprovides the maximum total power generation indicates the ideal operating condition for PowerWindow. Based on the prototype configuration, the analytical model has considered 5 blades at the front and 5 others at the rear of PowerWindow ($N = 5$), surface area of the blades equals 0.3 m^2 ($B = 0.3\ m^2$) and the swept area (the effective area which wind passes through) of PowerWindow is 3.35 m^2 ($A = 3.35\ m^2$), solidity of PowerWindow is 0.428 ($\sigma = 0.428$),blade design angle is 16° ($\theta_0 = 16°$), approach wind velocity is 8 $m.s^{-1}$ ($V = 8\ m.s^{-1}$) and affected flow ratio is not known but has been checked for 0.5 and 1 ($\varepsilon = 0.5\ and\ 1$).

The accurate value of ε depends on σ and λ and needs to be investigated in future studies.

A.3. Computational fluid dynamics model

This appendix presents the computational fluid dynamics model developed in the MPhil thesis by Jafari (2014).

A.3.1. Turbulence model

The Shear Stress Transport (SST) model has been extensively validated for separating 2D flows with Reynolds-averaged Navier–Stokes (RANS) models [83].El-Behery and Hamed [84] approved that the SST model outperforms the 4-equation, v2-f (transition SST) model in predicting separating velocity profiles for the NACA 4412 airfoil case. Menter [85] suggested that considering that the flow over the rotor blades can be subject to significant region of laminar-turbulence transition and the transition process can strongly affect the separation behavior of the boundary layer on the blade surface, the v2-f model is the best model in case of separation.

The v2-f model is a modified SST k-ω RANS turbulence model by the addition of two other transport equations for γ (the intermittency) and the transition onset criteria. Menter [85] expressed that this approach has two main advantages. The first is that it improves the robustness of the model because the intermittency does not enter directly into the momentum equations. The second advantage is that it allows the model to predict the effects of high free stream turbulence levels on buffeted laminar boundary layers. The reason is that for large free stream eddy viscosities, the small values of intermittency in the boundary layer do not cancel out the local eddy viscosity. It is shown that separation has a significant effect on the lift and drag characteristics of the linear cascade configurations in this study. Therefore, v2-f (transition SST) model has been used in FLUENT 16.1 for the CFD models.

A.3.2. Mesh and boundary conditions

In order to achieve a balance between solution accuracy and calculation time, a combination of structured and unstructured mesh was used. This technique decreases the number of elements while still ensuring a high-quality mesh around the body. Therefore, a number of layerswith very fine structured rectangular elements, as shown in Figure A 7 (c), are generated around the blades. This very fine mesh region is connected to the outer coarser structured region via unstructured triangular elements shown in Figure A 7 (b). The structured mesh generated for the surrounding region is shown in Figure A 7 (a). To ensure acceptable accuracy of the simulation results and to balance between the mesh quality and computation speed, a grid independence study has been undertaken and the findings are published in [7]. Since the PowerWindow used in this study and the range of wind velocity is the same as those in [7], grid dependency study was not repeated.

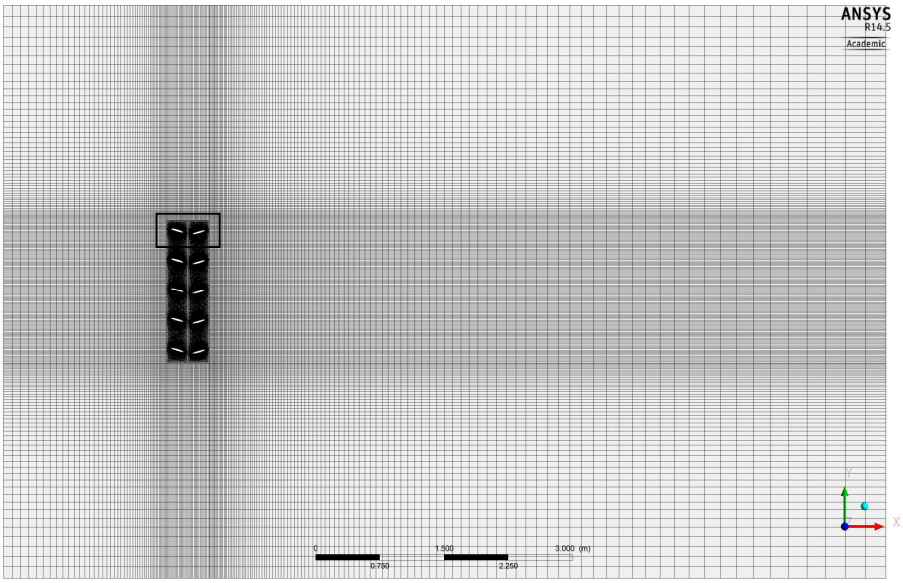

(d)

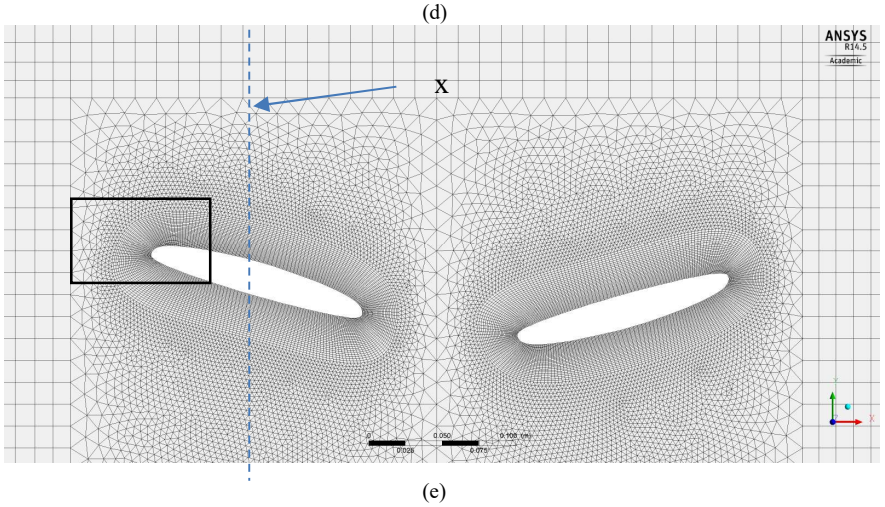

(e)

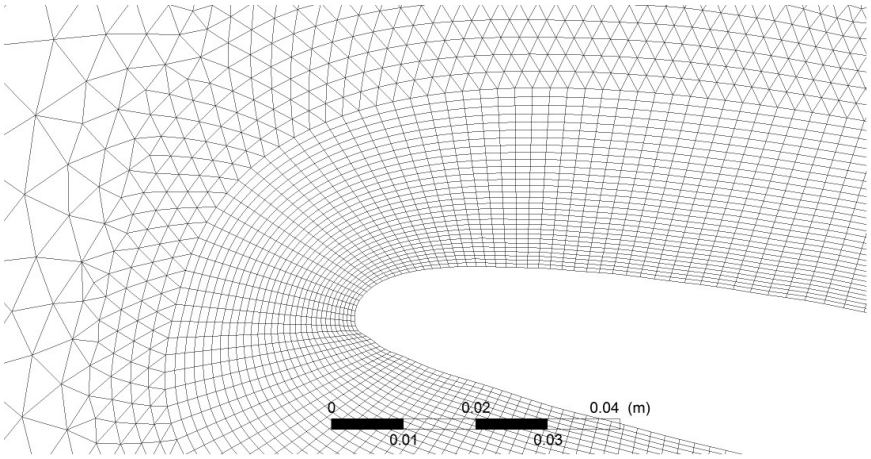

(f)

Figure A 7: (a) Structured mesh generated around the unstructured region. (b) Combination of structured and unstructured mesh around the blades (a blue dash line shows x=0). (c) Fine structured rectangular elements adjacent to the blade surface [7].

A.4. Sensitivity analysis of the coefficient of performance to blade design angle

As previously discussed, the relative vertical velocity of the flow approaching the rear blades was affected by θ_0, σ and λ. Therefore, the amount of ε is not easily ascertainable. However, Figure A 5 (b), which illustrates the velocity contours around the PowerWindow linear cascade configuration, indicates a significant redirection when $\sigma = 0.428$ and ε should be closer to 1 rather than 0. Hence, a reasonable range of ε can be considered that: $0.5 < \varepsilon < 1.0$. Although the accurate value for ε is unknown, the analytical model can calculate the aerodynamic forces and power generation with both values ($\varepsilon = 0.5$, and $\varepsilon = 1.0$) and predict the power generation based on both conditions.

Figures A 8 (a-c) show the power generation performance of the elevated PowerWindow in terms of C_P versus λ whe $\sigma = 0.428$ and $\theta_0 = 14°, 16°$ and $18°$ calculated bymodified BEM and undertaken by CFD models. P_f, P_r and P_t indicate the power generated by the front blades, rear blades and the total power. These figures show that the results achieved by the CFD model agree with those calculated by the modified BEM model. An unexpected result shown is in Figure A 8 (a-c) is that both the analytical and the CFD results agree that the contribution of the rear blades to the total power generation of PowerWindow is interestingly greater than the front blades. As the front and the rear blades are exposed to similar approach flow in terms of velocity magnitude, the reason behind this unexpected contribution should have been laid in the direction of the flow over the blades and influence of the front blades on redirecting the flow approaching the rear ones.

Comparing Equations A 19 and A 24 (or A 29 when $\varepsilon \neq 1$) shows that α_2 is higher than α_1 when $\lambda < (1 - a_f)\tan\theta_0$. BEM results show that in these configurations provide a particular condition in which for the identified of λ, α_2 is greater than α_1 hence: $0° < \alpha_1 < 20°$.The reason is that the overall effect of the front blades on the flow passing them is redirecting them downward and creating greaterαover the rear blades. On the other hand, Figure A 3 (a) shows that in the linear cascade configurations when $0° < \alpha < 20°$, C_L increases by α. The vertical force on the blades increases by increasing C_L. Eventually, the power generated by the rear blades would be greater than the power generated by the front ones.

Comparing Figures A 8 (a), (b), and (c) also shows that the C_P of PowerWindow strongly depends on θ_0 so that, 2° deviation in θ_0 from 16°can increase C_P from .085 to 0.1 or decrease it to 0.65. The reason is that as shown in Equations A 19 and A 24 (or 30 when $\varepsilon \neq 1$), α increases with θ_0 and before the stall condition lift increases by α. Therefore, increasing θ_0 results in creating higher lift and eventually higher power generation. On the other hand, as θ_0 increases a similar α can be created at higher λ and as shown in Equation A 31, the power generation directly increases by increasing λ.

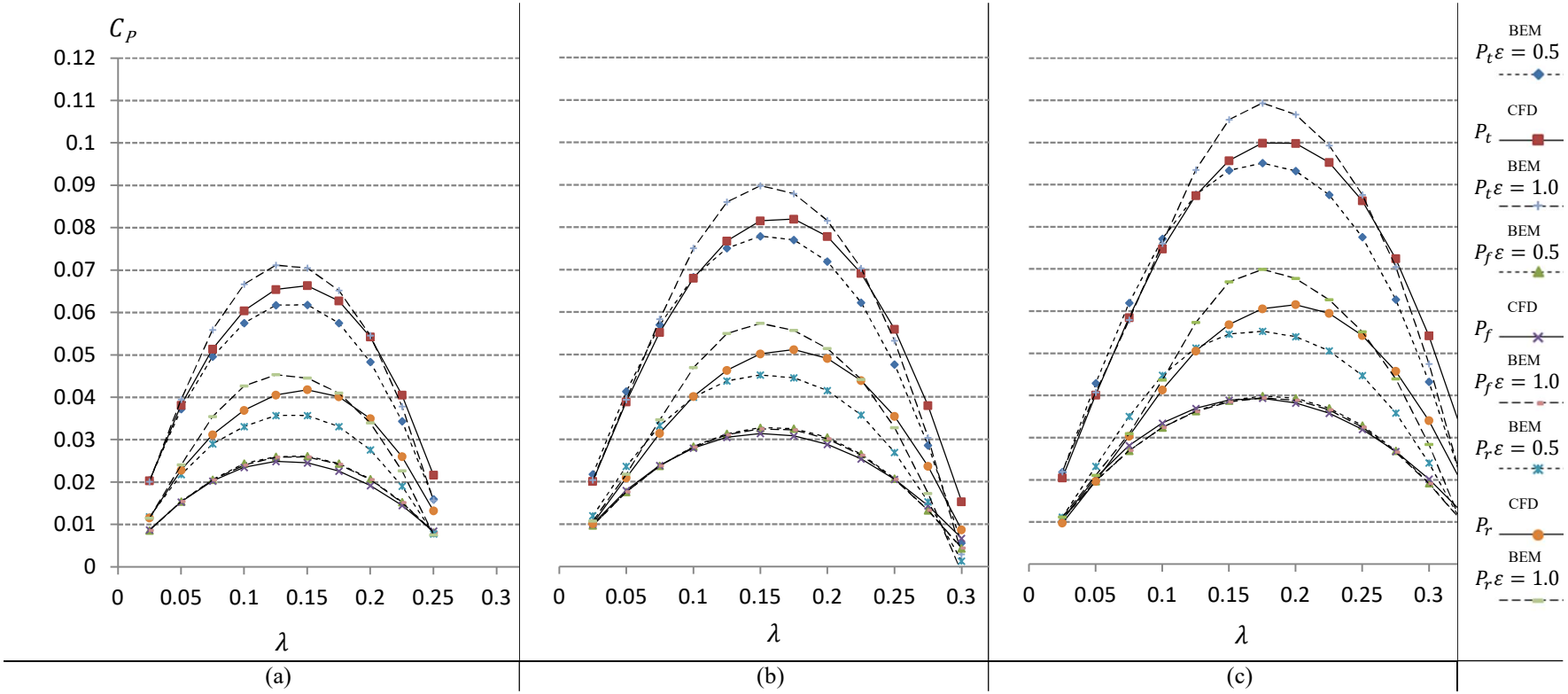

Figure A 8: C_P of the PowerWindow in elevated when $\sigma = 0.428$ versus λ when $\theta_0 =$ (a)14°, (b)16°and (c)18° using modified BEM and CFD models.

Appendix B1

Aerodynamic Analysis of a Linear Cascade Wind Turbine, Jafari SAH, Kwok KCS, Safaei F, Kosasih B, Zhao M, *Journal of Wind Energy*, 2018; 21 (11): 1141-1154.

https://doi.org/10.1002/we.2219

Received: 20 July 2017 | Revised: 11 May 2018 | Accepted: 24 May 2018

DOI: 10.1002/we.2219

RESEARCH ARTICLE

WILEY

Aerodynamic analysis of a linear cascade wind turbine

S. A. H. Jafari[1] | K. C .S. Kwok[2] | F. Safaei[3] | B. Kosasih[4]

[1] Western Sydney University, Center for Infrastructure Engineering, Kingswood, New South Wales 2747, Australia

[2] University of Sydney, School of Civil Engineering, Camperdown, New South Wales 2006, Australia

[3] University of Wollongong, School of Electrical, Computer and Telecommunications Engineering, Wollongong, New South Wales 2500, Australia

[4] University of Wollongong, School of Mechanical, Materials and Mechatronic Engineering, Wollongong, New South Wales 2500, Australia

Correspondence
S. A H. Jafari, Center for Infrastructure Engineering, Western Sydney University, Kingswood, New South Wales 2747, Australia.
Email: s.jafari@westernsydney.edu.au

Abstract

This paper develops an analytical model to investigate the aerodynamic of the power generation of a linear cascade wind turbine, referred to as PowerWindow. Based on blade element momentum theory, this analytical model elucidates some flow characteristics of PowerWindow such as axial induction factor and local instantaneous angle of attack along the blades. The model also provides an understanding of the effects of blade pitch angle, blade speed ratio, and solidity on the angle of attack, axial induction factor, and power generation of PowerWindow when operating in "elevated" position. In elevated position, PowerWindow is installed on a tower as opposed to directly mounted on a roof. The validity and accuracy of the analytical model are verified with computational fluid dynamic simulations. The results indicate that by doubling the solidity or increasing the blade pitch angle by 8°, the coefficient of performance of PowerWindow increases from 8% to 12% and 16%, respectively. The analytical model can serve as the tool to find the design parameters of PowerWindow and their influence on power generation for given life wind condition.

KEYWORDS

blade element momentum theory, computational fluid dynamics, linear cascade, solidity, wind turbine

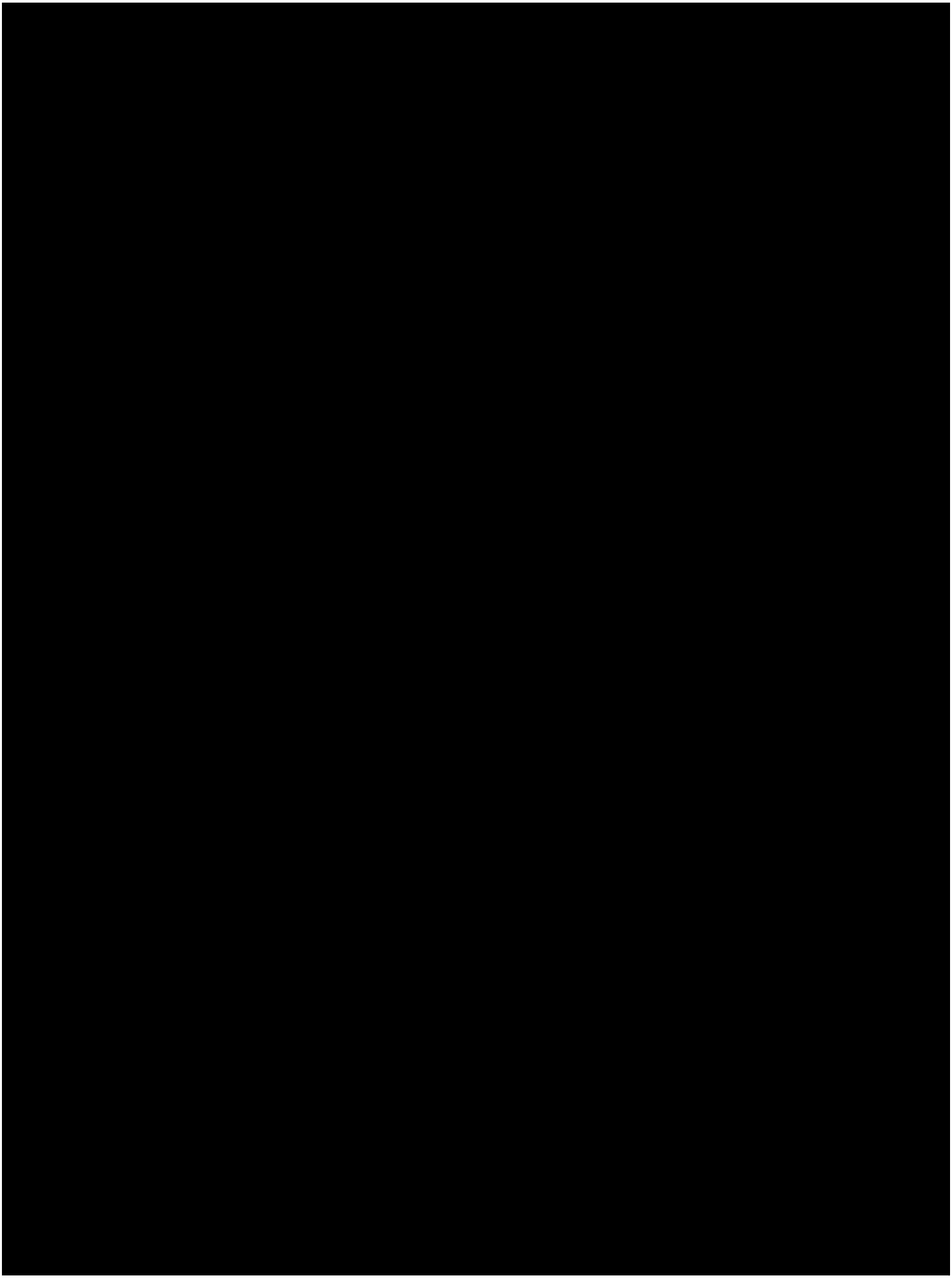

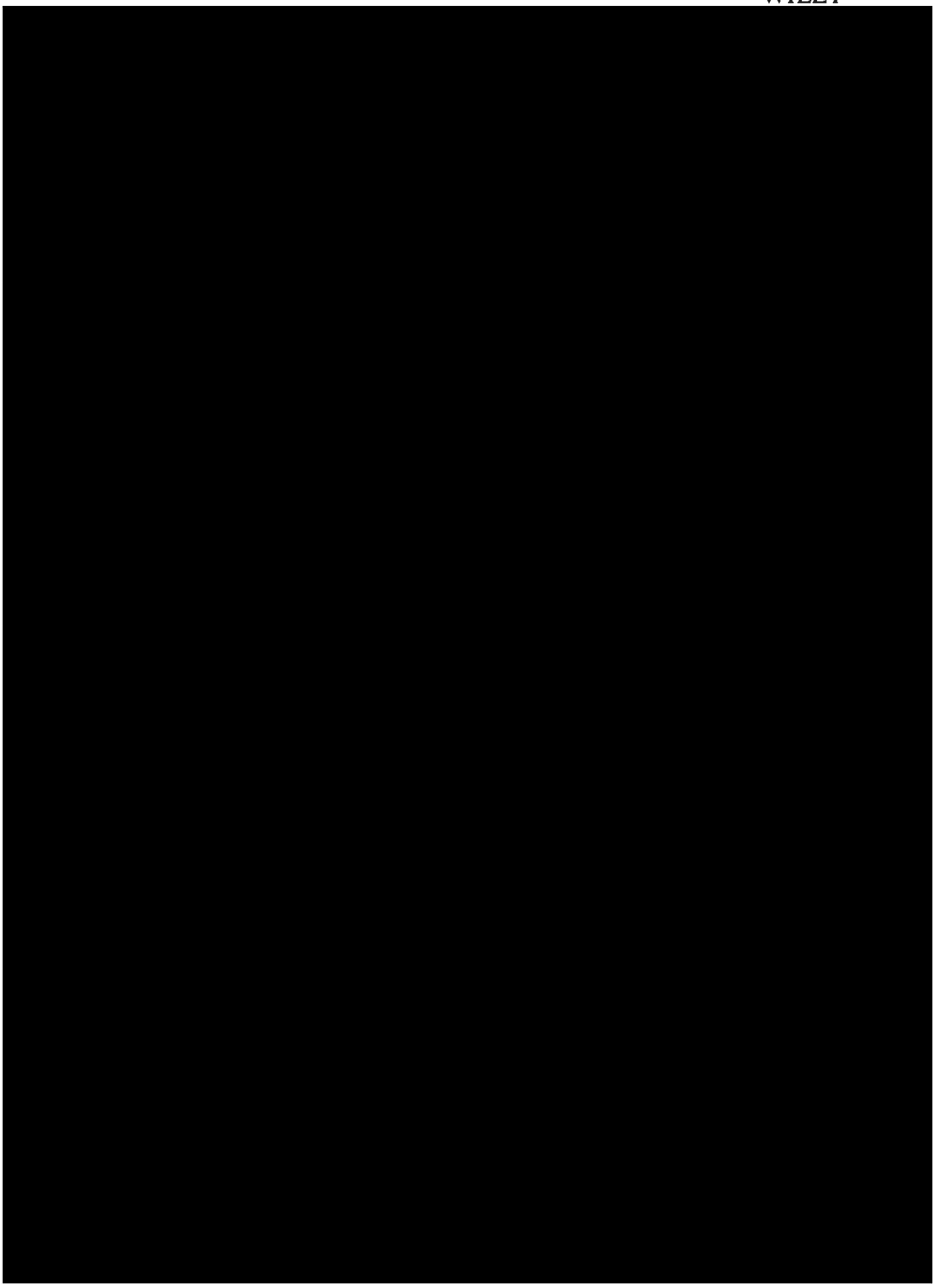

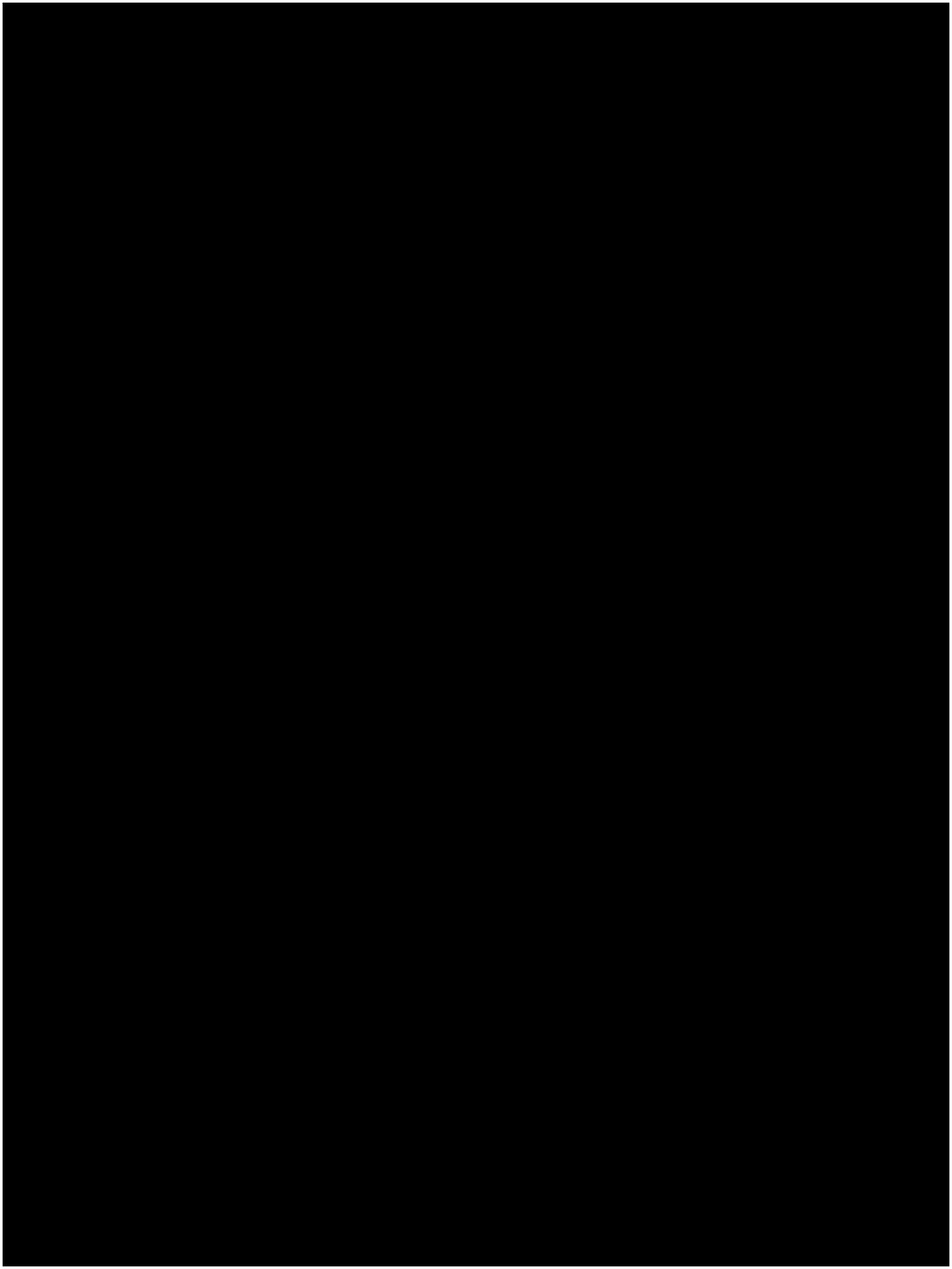

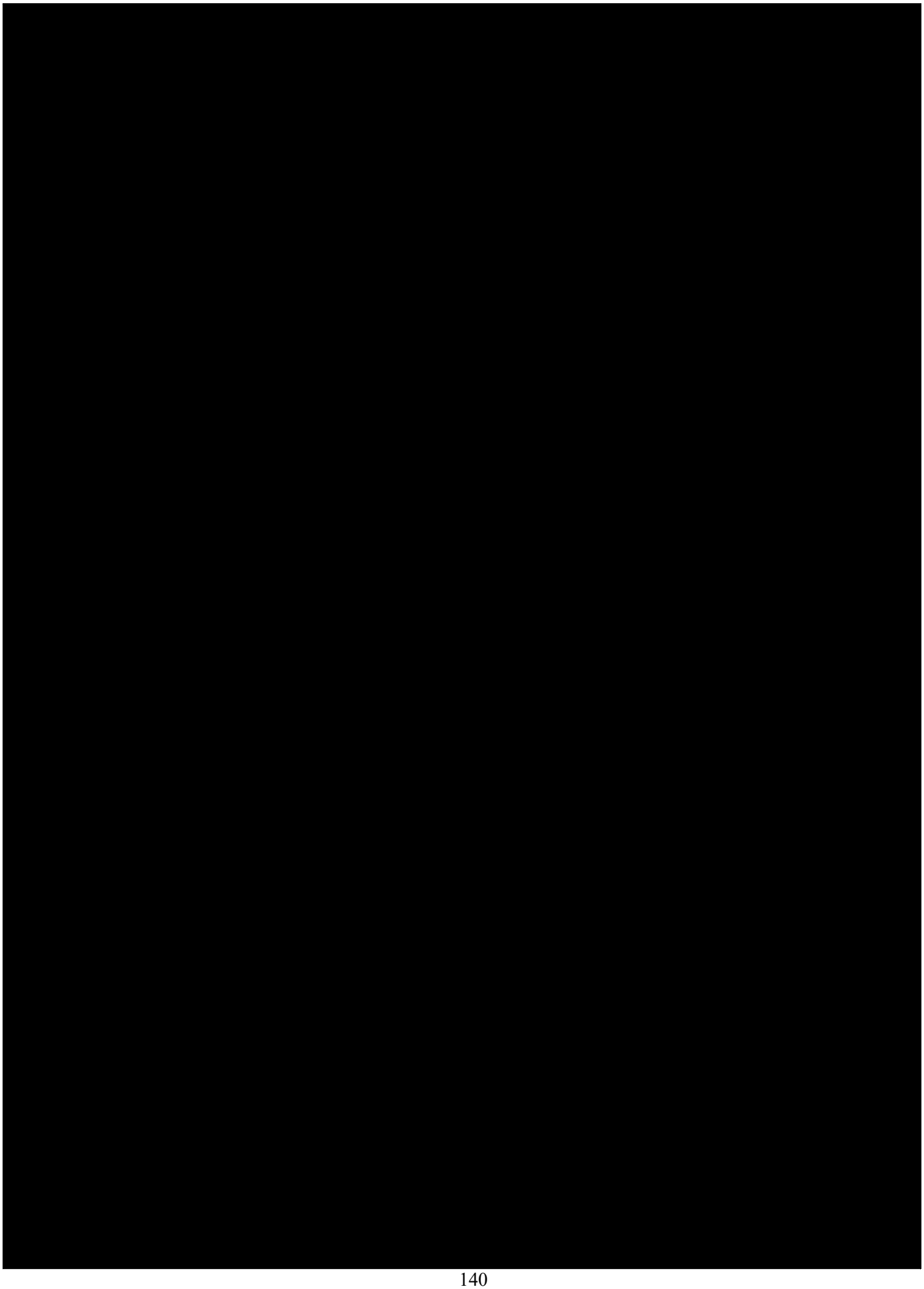

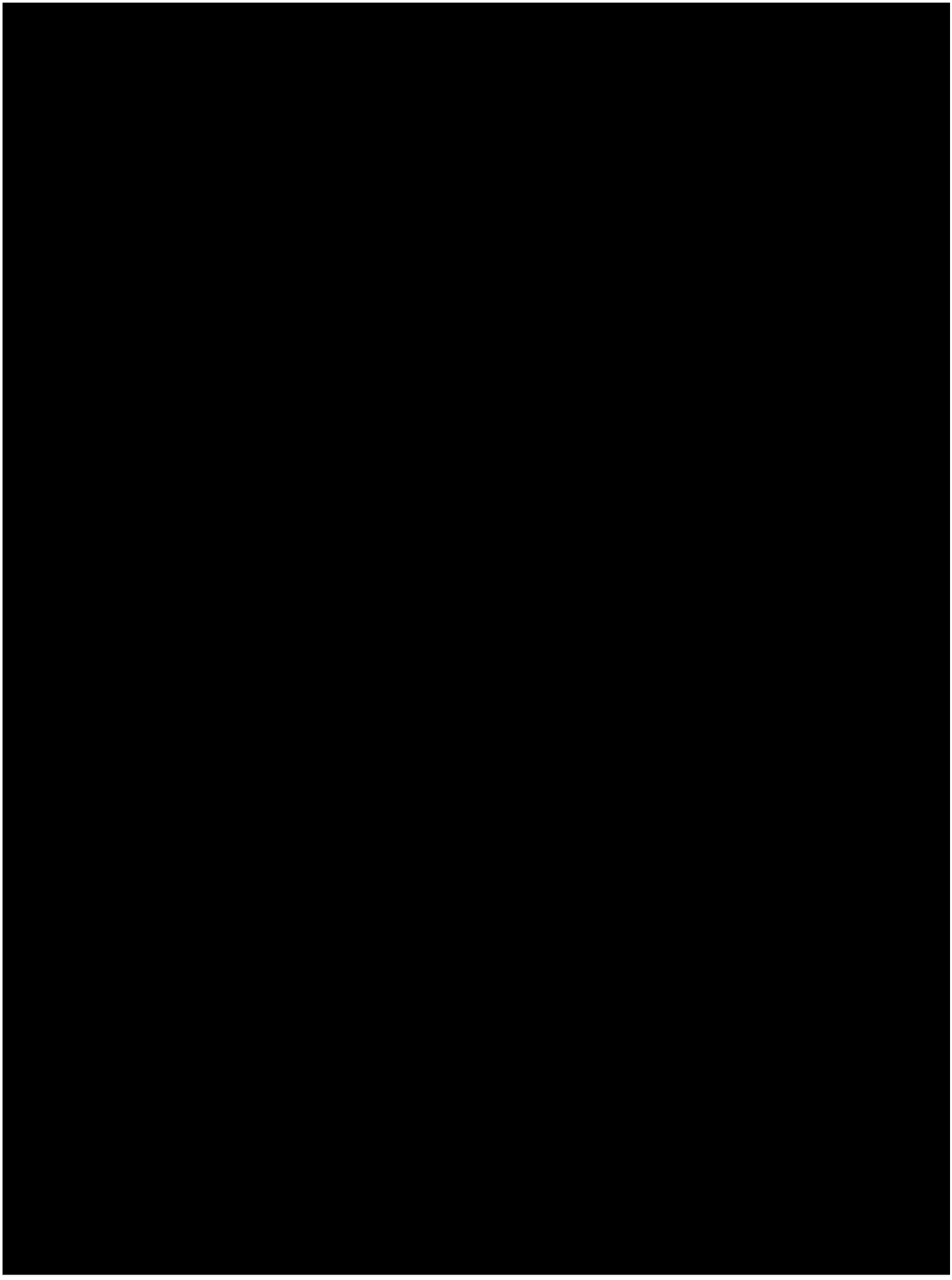

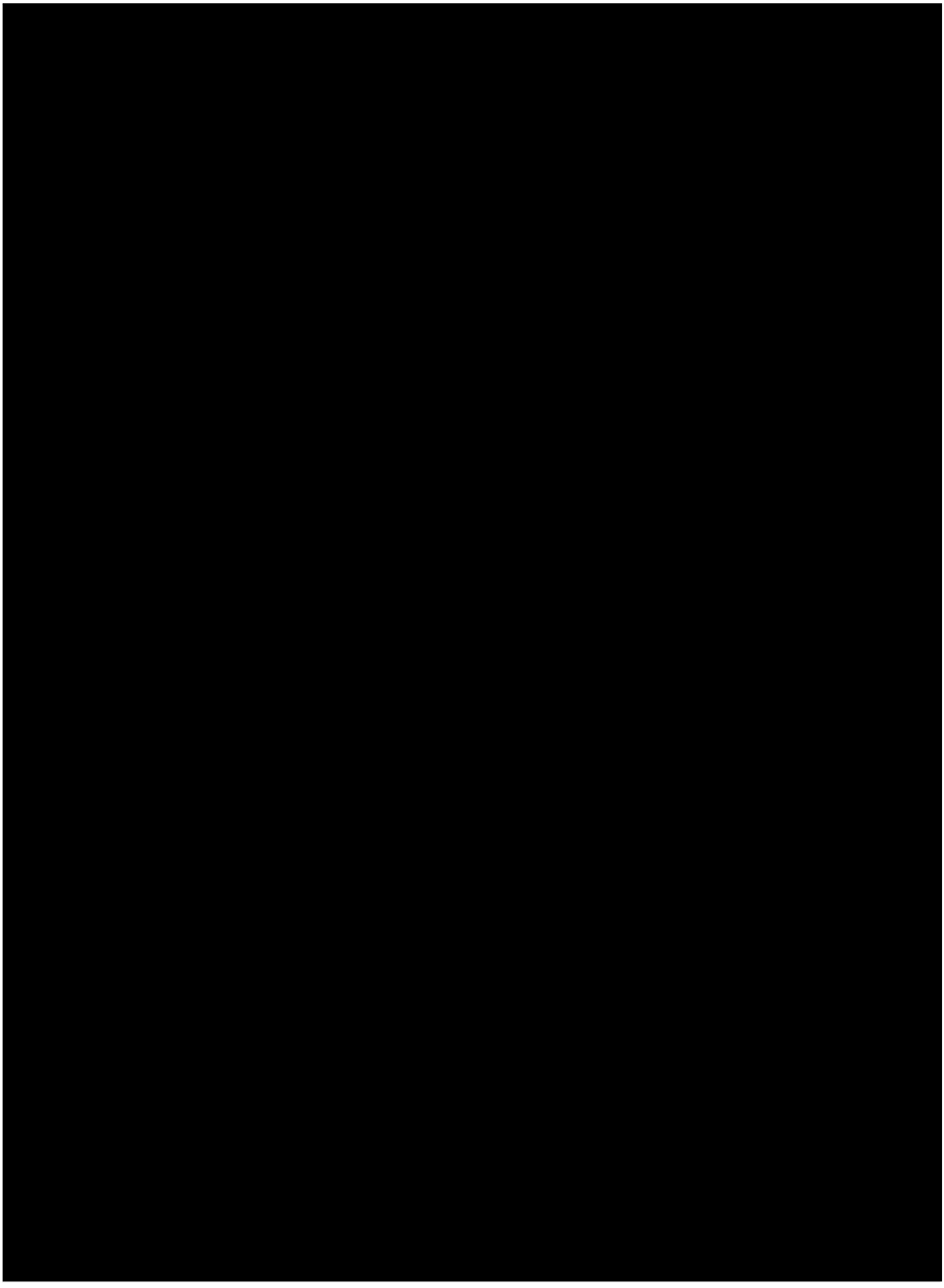

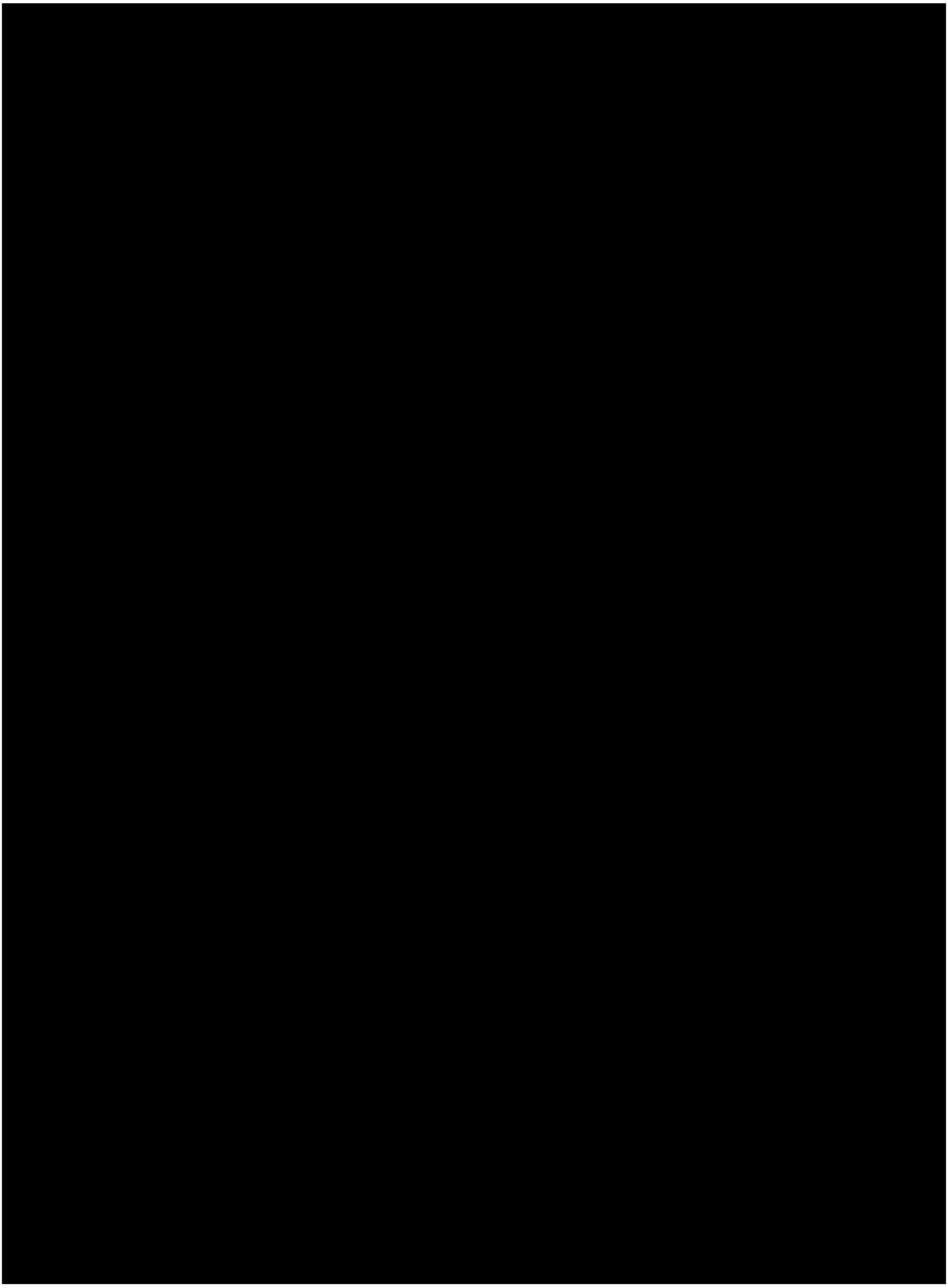

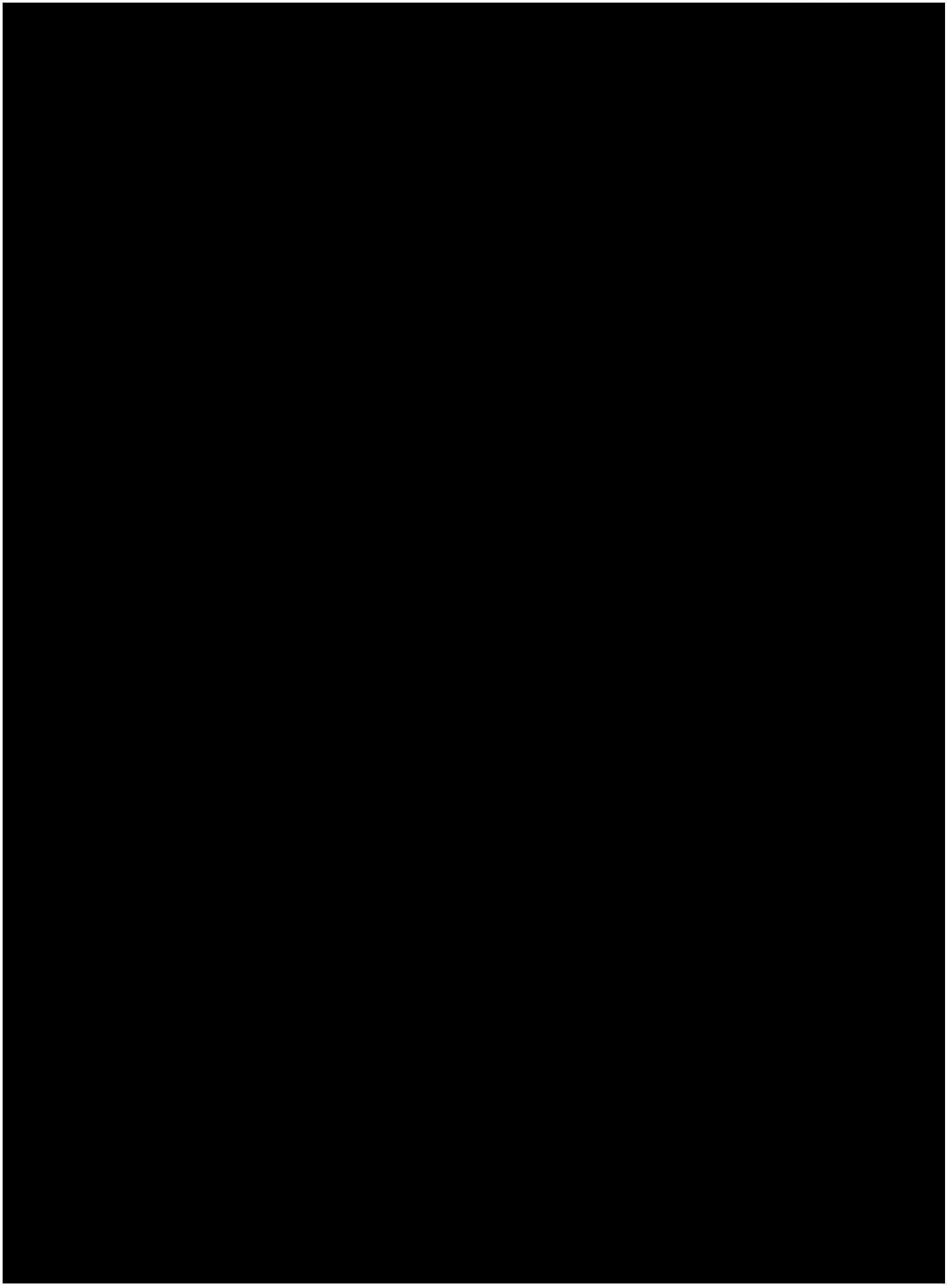

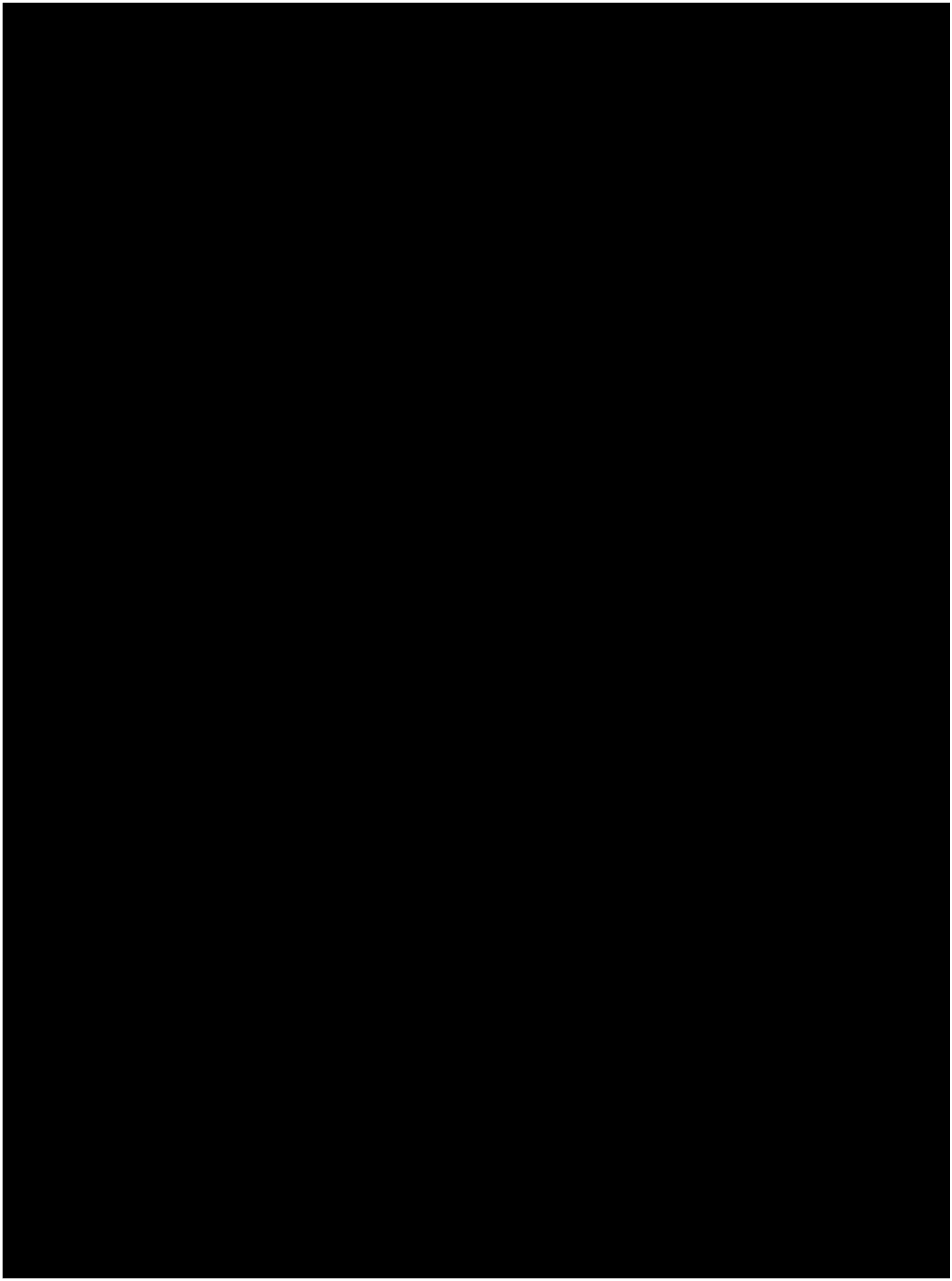

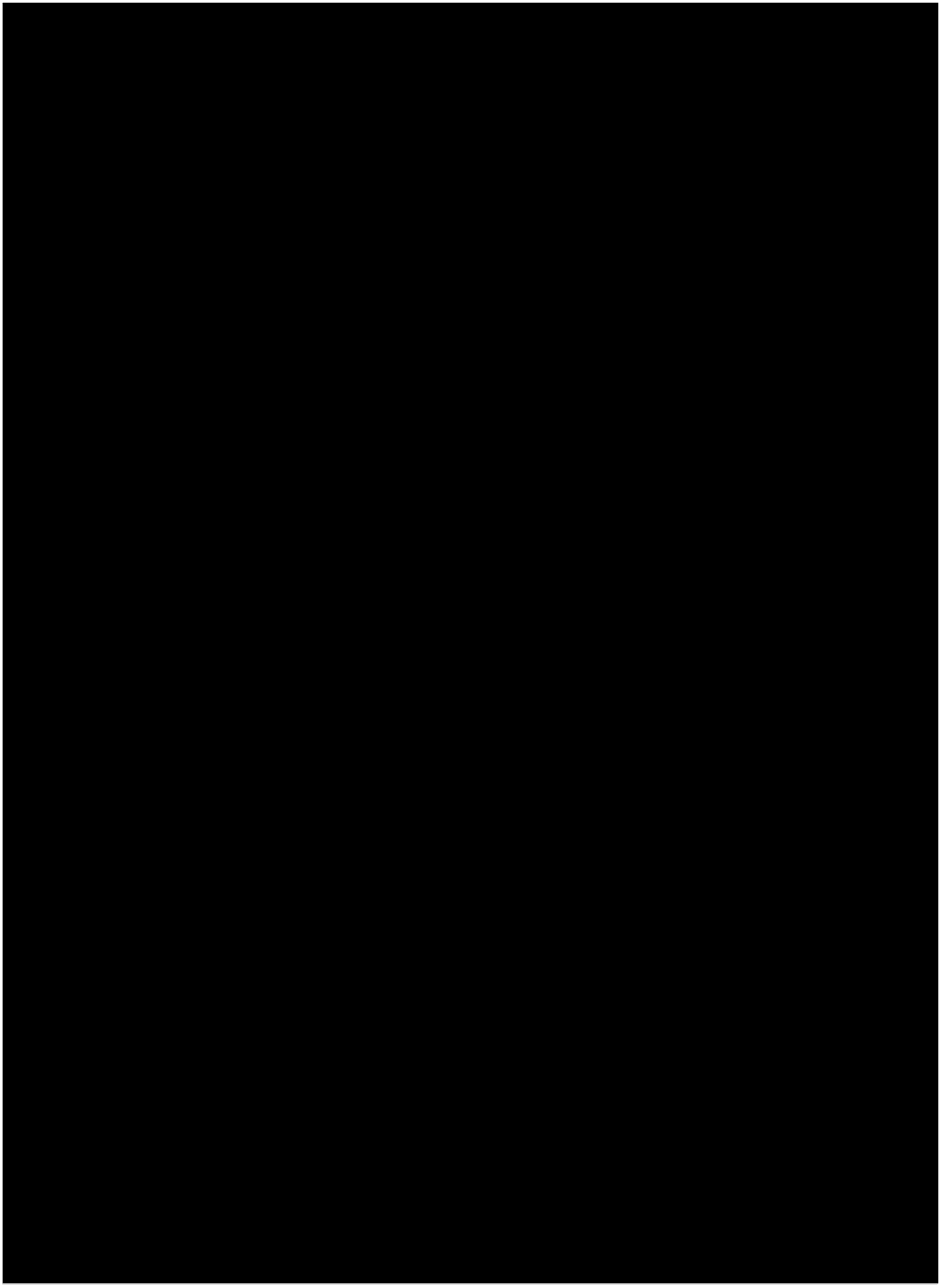

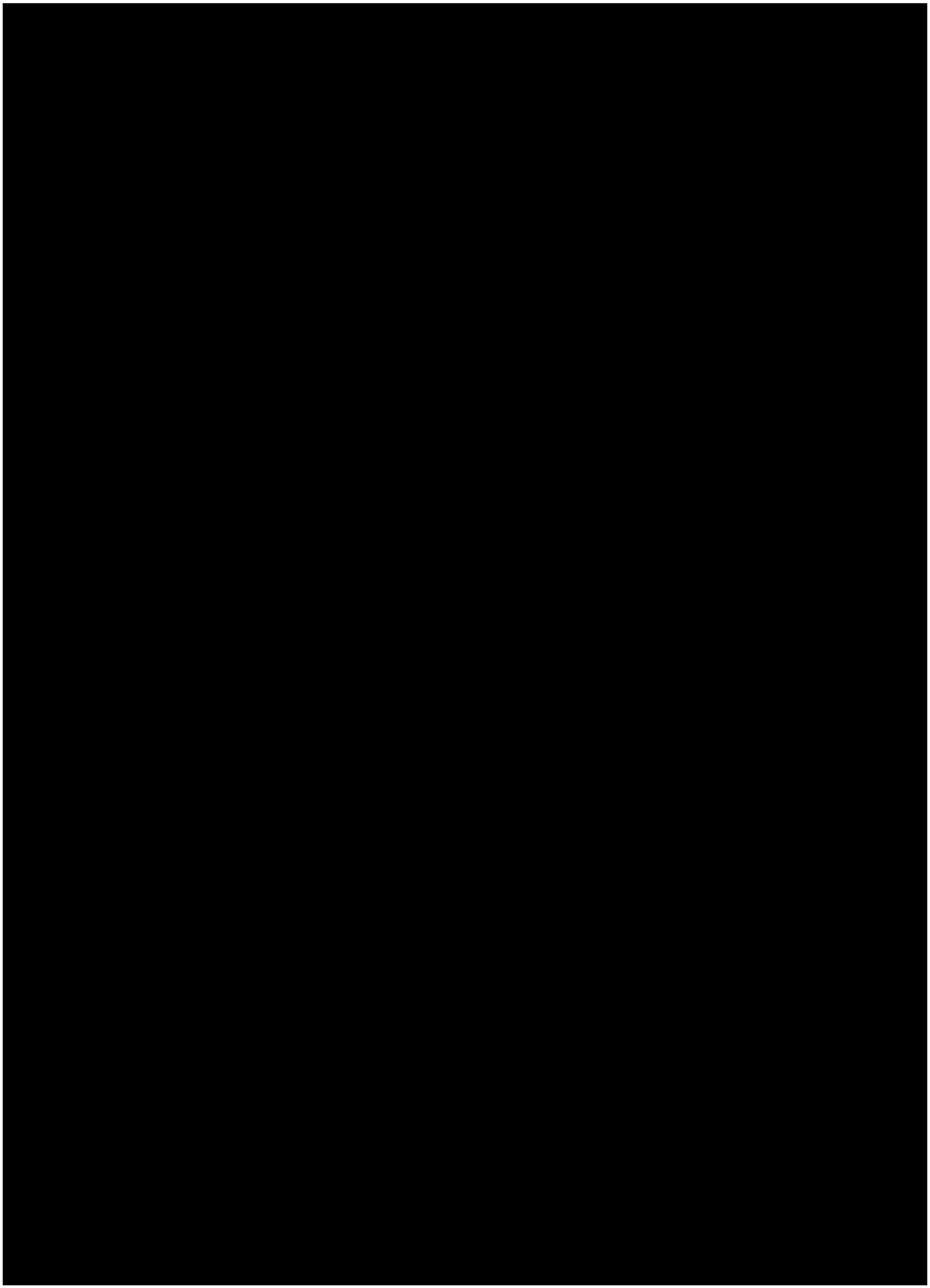

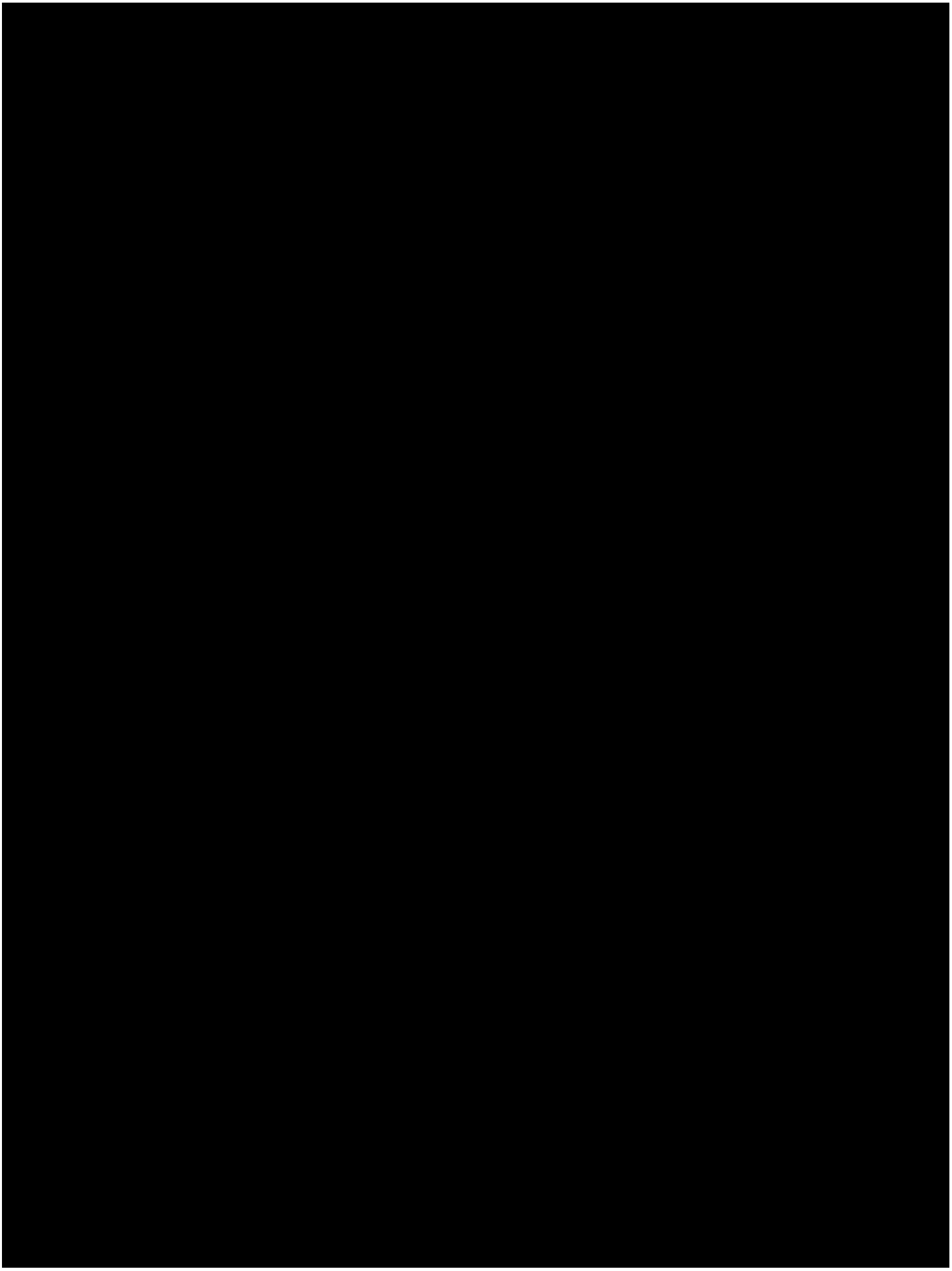

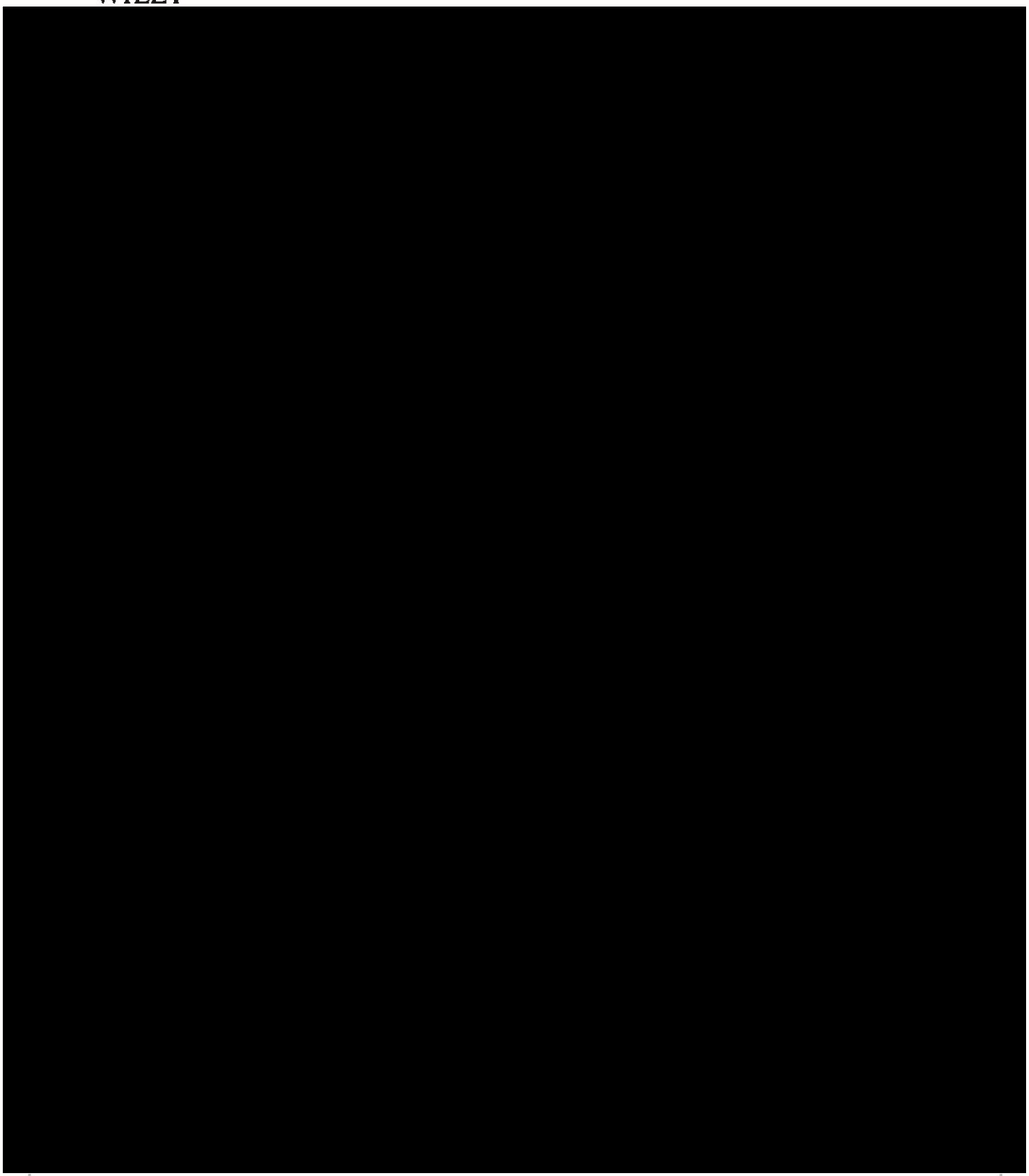

How to cite this article: Jafari SAH, Kwok KCS, Safaei F, Kosasih B. Aerodynamic analysis of a linear cascade wind turbine. *Wind Energy*. 2018;1–14. https://doi.org/10.1002/we.2219

Appendix B2

The effects of installation configuration and solidity on the power generation of a linear cascade wind turbine, Jafari SAH, Kwok KCS, Safaei F, Kosasih B, Zhao M, *Journal of Wind Engineering and Industrial Aerodynamics*, 2018; 180: 122-135.

https://doi.org/10.1016/j.jweia.2018.07.015

Journal of Wind Engineering & Industrial Aerodynamics 180 (2018) 122–135

Contents lists available at ScienceDirect

Journal of Wind Engineering & Industrial Aerodynamics

journal homepage: www.elsevier.com/locate/jweia

The effects of installation configuration and solidity on the power generation of a linear cascade wind turbine

S.A.H. Jafari [a,*], K.C.S. Kwok [b], F. Safaei [c], B. Kosasih [d], M. Zhao [e]

[a] Center for Infrastructure Engineering, Western Sydney University, Kingswood, NSW, 2747, Australia
[b] School of Civil Engineering, The University of Sydney, Camperdown, NSW, 2006, Australia
[c] School of Electrical, Computer and Telecommunications Engineering, University of Wollongong, Wollongong, NSW, 2500, Australia
[d] School of Mechanical, Materials and Mechatronic Engineering, University of Wollongong, Wollongong, NSW, 2500, Australia
[e] School of Engineering, Western Sydney University, Kingswood, NSW, 2747, Australia

ARTICLE INFO

Keywords:
PowerWindow
Installation configuration
Computational fluid dynamics
Elevated configuration
Ducted configuration

ABSTRACT

PowerWindow is a Linear Cascade Wind Turbine (LCWT) capable of generating electricity in very low blade speed ratios, which makes it a safe power generator in built environments. The power generation mechanism and aerodynamic performance of PowerWindow were investigated using experimental prototyping and computational fluid dynamic simulations in a previous study. Due to the limited suitable locations for installing the device in grounded configuration, this study investigates *elevated* and *ducted* installation configurations. In the elevated configuration PowerWindow is installed on a tower or in between two tall buildings. In ducted configuration it is installed inside a ducted area such as a through-building opening. Aerodynamic performances of the elevated and ducted PowerWindow are investigated and compared, using computational fluid dynamic simulations. It is shown that the coefficient of performance of the ducted PowerWindow with 12% is about 50% higher than the elevated one with 8%. The effect of solidity is also investigated on the flow mechanism and power generation. The results show that increasing solidity results in greater increase in power generation of the ducted configuration compared to the elevated one. This study also investigates effect of increasing solidity on the required pressure gradient and recommends an efficient solidity for each configuration based on the installation circumstances.

1. Introduction

Significant efforts to adopt renewable energy technologies in suburban and urban environments have been made worldwide during the last decades due to the growing public awareness of the rising level of greenhouse gas emissions. Building-integrated wind turbines are potential low-cost renewable energy devices that could be adopted in these environments (Ledo et al., 2011). Small scale wind turbines integrated in urban buildings have attracted increasing interest, because they have the advantage of being installed and generate power at the point of use (Sharma and Madawala, 2012; Drew et al., 2013). Therefore, it is expected that more and more buildings with integrated wind turbines will be built as sustainability becomes an increasing design driver in the future (Peacock et al., 2008). Efforts have also been made to overcome the hurdles which restrain the installation of wind turbines in urban built environments such as: (i) lack of suitable area for medium-large size wind turbines; (ii) noise pollution in high wind velocity conditions; and (iii) relatively low power output and unreliable performance due to unfavourable urban wind conditions such as low wind velocity, continuously variable wind directions and high turbulence level (Drew et al., 2013; Rafailidis, 1997; Mertens and Mertens, 2003).

PowerWindow as a Linear Cascade Wind Turbine (LCWT) is capable of generating electricity at very low blade speed ratios (λ) (Jafari et al., 2015). Operating at low λ is an advantage as for both remote and grid-tied turbines, controlling the blade speed is necessary for two reasons: first, it is desirable that blade speed remain proportional to the wind velocity (U) over a large range of U, for maximum power generation at the optimal λ. The process to achieve the optimal λ is called Maximum Power Point Tracking (MPPT) (Mirecki et al., 2007). The second reason to control blade speed is for safety at high wind speeds. In the event that the controller loses power, the turbine must be protected aerodynamically and/or mechanically (Wood et al., 2011). Furthermore, PowerWindow is designed to operate efficiently even at very low λ, thus making it a safe option for application in built environments.

* Corresponding author.
E-mail address: S.jafari@westernsydney.edu.au (S.A.H. Jafari).

https://doi.org/10.1016/j.jweia.2018.07.015
Received 27 December 2017; Received in revised form 25 June 2018; Accepted 23 July 2018

PowerWindow is modular and can easily fit into any designated area in a building. A PowerWindow module (Shown in Fig. 1) is composed of a light frame that could be mounted on the support tower or structural frame. A couple of rotating disks connected together with a shaft are mounted at the top and bottom of side frame. The generator is attached to the bottom shaft. There are two chains running over these disks and several blades of appropriate aerofoil profile are attached to the chain. For the direction of wind shown in the figure, the blades that encounter wind first are referred to as 'front' blades and the ones behind are referred to as 'rear' blades. Unlike those of conventional wind turbines: horizontal axis wind turbine (HAWT) and vertical axis wind turbine (VAWT), the blades of the LCWT move in opposite directions perpendicular to the approach wind direction, instead of around rotor axis. Since the LCWT does not create trailing swirl like a conventional wind turbines, it allows another unit behind it to operate efficiently.

Investigations have proved that the installation of small wind turbines on urban buildings has great potential to generate energy efficiently. Investigating the wind characteristics in urban environment and in close proximity of common types of wind turbines currently being used in urban environment has shown that although simplicity in construction and low cost of materials has been a major driving factor in the decision making process, VAWTs have been preferred for small scale power production in urban environment as they possess the required design factors to take advantage of urban wind flow's low and turbulent wind speed characteristics, installation space challenges, vibration and noise reduction, among others (Ishugah et al., 2014).

Studies have shown that the performance of urban wind turbines strongly depends on the location where the turbines are installed. For example, HAWT has better performance in flat-terrain applications, whereas in high-density building environments, VAWT is superior (Toja-Silva et al., 2013). An investigation on the power production of two small-size commercial wind turbines, a HAWT and a VAWT characterized by the same rated power installed in the same area has shown that the overall energy production of the HAWT is higher than that of the VAWT. but, the HAWT has shown to be strongly affected by gusts wind speed and direction fluctuations while the VAWT has shown to be less affected by wind fluctuations so that it could be operational also at higher wind velocities (Pagnini et al., 2015). Although the roughness of the terrain in urban environments can reduce the velocity and increase turbulence of the flow compared to open spaces, it is reported that mounting turbines at high elevations on buildings may provide a perfect opportunity for onsite wind power harvesting (Dayan, 2006). By investigating the wind flow over the buildings based on local meteorological data and local building characteristics, it is reported that the wind speed amplification effects associated with the grouping of buildings and the heights of buildings may enhance wind power utilization by increasing the wind power density by 3–8 times (Ayhan and Sağlam, 2012). Some studies have investigated possibility of using double skin façade for wind energy harvesting purposes and shown that free-stream wind speed can be amplified up to a maximum of 1.8 times along with wind power density of 4.2 times inside the corridors of the double skin façade (Hassanli et al., 2018a,b; Hassanli et al, 2017, 2018a, b).

Due to the limitation for grounded installation of PowerWindow in urban areas, this study investigates two alternative installation configurations: *elevated* and *ducted* configurations for PowerWindow. In the elevated configuration, PowerWindow is installed on top of a tall building referred to as on top of building mounted or between two tall buildings referred to as between two building mounted position (Ayhan and Sağlam, 2012). In the ducted configuration PowerWindow is installed inside a ducted area such as a through-building opening referred to as building-integrated position (Li et al., 2016). Based on the inlet and outlet design of the duct and the approach wind direction, the ducted flow may have a higher speed than the free stream at the same elevation. Fig. 1(a–c) show PowerWindow installed in the (a) grounded (in wind tunnel), (b) elevated (between two buildings) and (c) ducted (in a through-building opening) configurations. The first scope of this study is to estimate power generation performance of the proposed configurations and compare them with each other.

Power generation performance of any wind turbine is dependent on different design parameters. Airfoil shape, solidity, pitch angle and rotating speed are among the most important parameters which have been investigated in recent studies. Mohamed et al. (2011) investigated

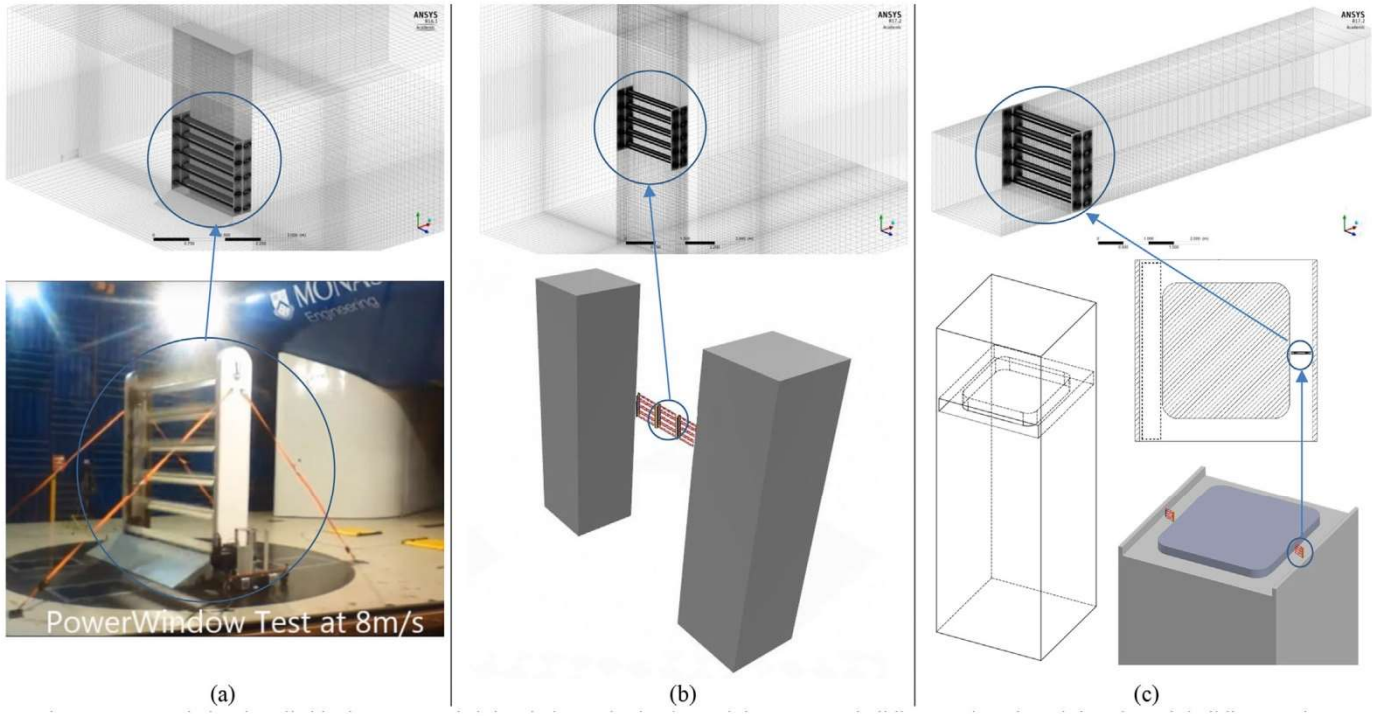

Fig. 1. PowerWindow installed in the (a) grounded (in wind tunnel), (b) elevated (between two buildings) and (c) ducted (in a through-building opening) configurations.

the optimal blade shape of a modified Savonius turbine and obtained almost 40% increase in the power output coefficient. Lee e al (Lee et al., 2012). investigated effects of pitch angle and rotating speed on aerodynamic performance of a counter-rotating wind turbine. Mohamed (2012) investigated performance of a H-rotor Darrieus turbine with new airfoil shapes and obtained almost 27% increase in the power output coefficient. In another study Mohamed (2013) investigated impacts of solidity on a small H-rotor Darrieus turbines and reported that optimizing solidity has a significant effect on performance of the wind turbine. He also reported rotating speed of the turbine at the operating condition strongly depends on solidity.

Among the mentioned design parameters, solidity is the most influential on the required pressure gradient (ΔP) across a wind turbine. In PowerWindow, solidity, shown by σ, presents the ratio of total area of the blades projected to the approach wind to the total area of the wind turbine which the approach wind is passing through:

$$\sigma = NB/A \tag{1}$$

when N, B and A represents the number of the blades, area of the blades and area of PowerWindow respectively.

Higher σ demands higher ΔP across the wind turbine which may or may not be realistically available in some installation configurations. Studies have also shown increasing σ results in decreasing the operating speed ratio (λ) of the turbine (Mohamed, 2012, 2013). λ, known as blade speed ratio in the LCWTs, shows the ratio of the blade's speed to the approach wind velocity:

$$\lambda = \frac{V_{blade}}{U_{wind}} \tag{2}$$

Another study has investigated effect of the blade pitch angle (θ_b) on power generation performance of PowerWindow and shown that the angle of attack (α) of the approach wind is strongly dependent on λ (Jafari et al., 2018). The second scope of this study is to investigate the effect of σ on the power generation performance of PowerWindow in both the elevated and ducted installation configurations.

2. Model geometry and CFD setup

2.1. Experimental setup

Fig. 2 (a) shows the PowerWindow prototype mounted directly on the floor in Monash University wind tunnel with a 12m(Length) × 9m(Width) × 5m(Height) test section. Fig. 2 (b) shows dimensions of the prototype (2m × 2m × 0.4m). The prototype has 12 blades (which results in σ = 0.428), and each blade has a 2 m span length, 150 mm chord length and 23 mm thickness (Fig. 3). The reason for using a mid-chord symmetrical blade is to have power generation by both the front and rear blades. A standard airfoil could result in a higher aerodynamic vertical force when the blades were located at the front but, this would locate the trailing edge of the blades toward the wind at the rear side and dramatically decrease the aerodynamic vertical force on them. θ_b was set to 16° in the experimental test.

In the experimental test on the prototype, the inlet wind velocity was set to 8 m/s with a Turbulence Intensity of 5%, which results in the Reynolds number of 7.1×10^4, based on flow over the length of the chord. A torque sensor was attached to the lower shaft to measure the power output. A variable electrical load and associated power electronics were also developed to measure the electrical power output produced by the generator (after accounting for the losses in the gearbox and generator). Unfortunately, the torque sensor showed some instability in its readings during the test. Therefore, only the electrical power output is considered. The records showed a maximum electrical power output of 140 W from the prototype's generator. The wind tunnel setup has been further explained in (Jafari et al., 2015).

2.2. Numerical setup

2.2.1. Transition – turbulence model

In CFD simulations accuracy of flow separation prediction on every wind turbine blades is significantly dependent on selecting an appropriate turbulence model. The shear stress transport (SST) k-ω models have been validated extensively for separating 2D flows with Reynolds-averaged Navier–Stokes (RANS) - based models (Shives and Crawford, 2012). Menter (2009) reports that flow over the rotor blades can be subject to significant region of laminar-turbulence transition and because the transition process can affect the separation behavior of the boundary layer on the blade surface. Therefore, transition SST 4 eqn k − ω maybe a more accurate model in case of separation. Based on flow over a flat plate (Incropera et al., 1990), Reynold number of 7.1×10^4 is calculated on the PowerWindow blades in the wind tunnel test, which indicates that blades are located in a laminar-turbulent transition region. Therefore, transition SST 4 eqn model seems to be the most accurate model for these simulations. However, transition SST 4 eqn model needs more (almost twice) calculation time than SST 2 eqn model so, the accuracy level of these two models are investigated and compared.

The undertaken results indicated that SST 2 eqn model predicts the vertical aerodynamic force on PowerWindow blades 3–5% higher than SST eqn model. Fig. 4(a) and (b) show velocity vectors and turbulent kinetic energy (TKE) contours around the middle blades of PowerWindow achieved by SST 2 eqn and SST 4 eqn model. Separation region

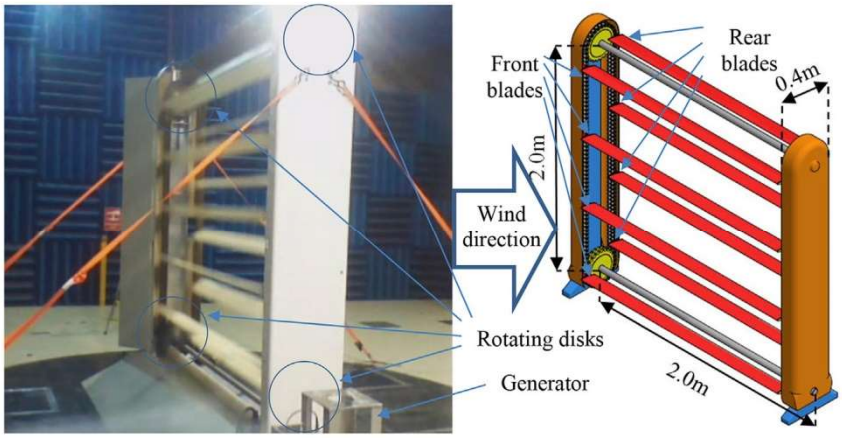

Fig. 2. (a) PowerWindow prototype in the wind tunnel (grounded position), (b) Sketch of the PowerWindow prototype showing its dimensions.

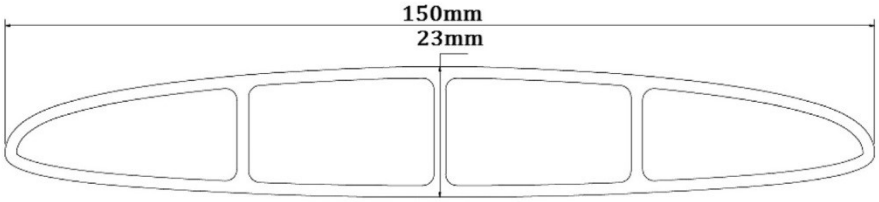

Fig. 3. Cross section view of PowerWindow blade showing chord C and thickness T.

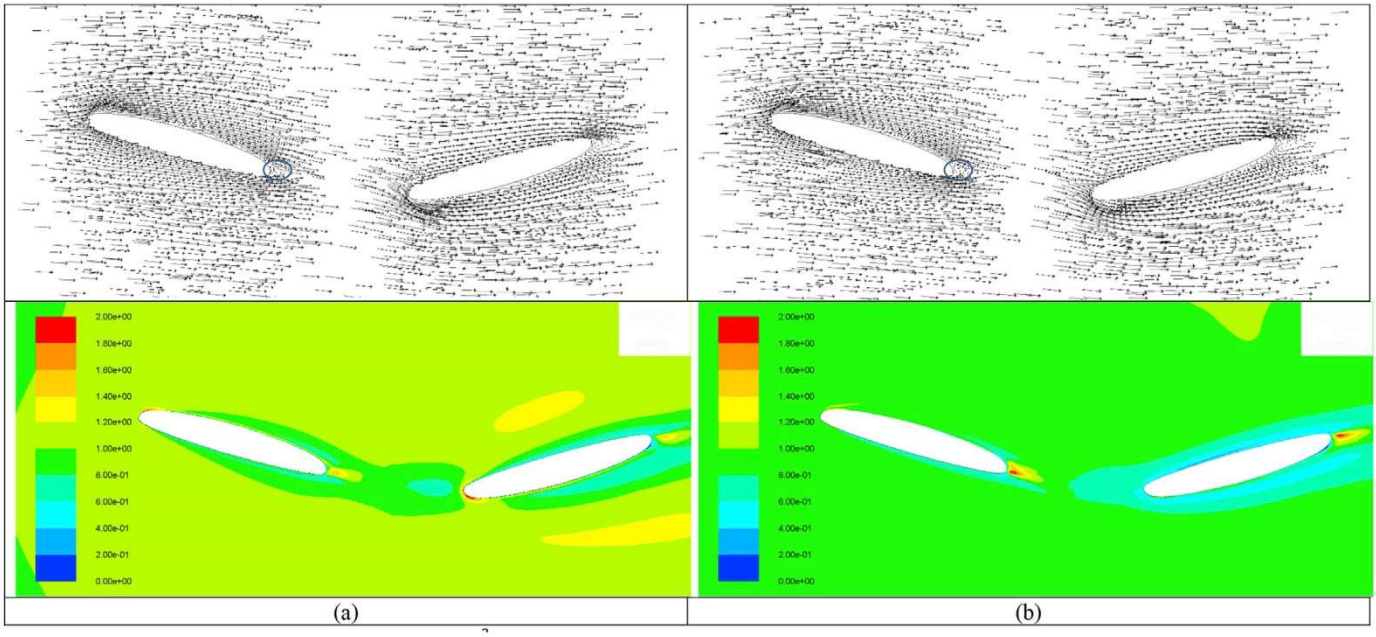

Fig. 4. Velocity vectors and TKE (m^2/s^2) contours around PowerWindow blades by (a) SST 2 eqn and (b) SST 4 eqn model.

is indicated within a blue circle near the trailing edge of the front and rear blades in all figures. Comparison shows that both models have predicted very similar locations for flow separation over the front and rear blades while, SST 4 eqn model has predicted higher TKE level around the blades and separation region compared to SST 2 eqn model. As the TKE level is higher, energy loss is greater and power generation is lower. For more accuracy and minimizing the error in critical circumstances this study uses SST 4eq k − ω model (in ANSYS-Fluent 16.1) for the simulations.

SST 4 eqn model is a modified SST k − ω RANS turbulence model by the addition of two other transport equations for γ (the intermittency) and the transition onset criteria. The transport equation for γ is defined as

$$\frac{\partial(\rho\gamma)}{\partial t}+\frac{\partial(\rho U_j\gamma)}{\partial x_j}=P_{\gamma 1}-E_{\gamma 1}+P_{\gamma 2}-E_{\gamma 2}+\frac{\partial}{\partial x_j}\left[\left(\mu+\frac{\mu_t}{\sigma_\gamma}\right)\frac{\partial\gamma}{\partial x_j}\right] \tag{3}$$

Where x is length (m), t is time (s), ρ is air density (kg m^{-3}), U is velocity of air (m s^{-1}), P is pressure (Pa) and μ is molecular viscosity (Pa s) and the second transport equation for the transport of the transition momentum thickness Reynolds number, $\tilde{R}e_{\theta e}$ (local transition onset momentum thickness Reynolds number) is

$$\frac{\partial(\rho\tilde{R}e_{\theta t})}{\partial t}+\frac{\partial(\rho U_j\tilde{R}e_{\theta t})}{\partial x_j}=P_{\theta t}+\frac{\partial}{\partial x_j}\left[\sigma_{\theta t}(\mu+\mu_t)\frac{\partial\tilde{R}e_{\theta t}}{\partial x_j}\right] \tag{4}$$

These equations are coupled with the SST turbulence model

$$\frac{\partial}{\partial t}(\rho k)+\frac{\partial}{\partial x_j}(\rho u_j k)=\tilde{P}_k-\tilde{D}_k+\frac{\partial}{\partial x_j}\left[(\mu+\sigma_k\mu_t)\frac{\partial k}{\partial x_j}\right] \tag{5}$$

$$\frac{\partial}{\partial t}(\rho\omega)+\frac{\partial}{\partial x_j}(\rho u_j\omega)=\alpha\frac{P_k}{\nu_t}-D_\omega+C\,d_\omega+\frac{\partial}{\partial x_j}\left[(\mu+\sigma_k\mu_t)\frac{\partial\omega}{\partial x_j}\right] \tag{6}$$

$$P_k=\gamma_{eff}\,P_k \tag{7}$$

$$\tilde{D}_k=\min\left[\max(\gamma_{eff},0.1),1.0\right]\,D_k \tag{8}$$

P_k and D_k are the turbulent kinetic energy (TKE) production and destruction terms in the original SST turbulence model and γ_{eff} is the effective intermittency calculated by the additional two equations. Menter (2009) expressed that this approach has two main advantages. The first is that it improves the robustness of the model because the intermittency does not enter directly into the momentum equations. The second advantage is that it allows the model to predict the effects of high free stream turbulence levels on buffeted laminar boundary layers. The reason is that for large free stream eddy viscosities, the small values of intermittency in the boundary layer do not cancel out the local eddy viscosity.

2.2.2. Mesh and boundary conditions

In CFD simulations a high mesh quality is primarily achievable by using a fine structured mesh. But, a fully structured mesh usually needs numerous elements which is computationally expensive. In order to achieve a balance between solution accuracy and calculation time, a combination of structured and unstructured mesh is used in this study. This technique helps to decrease the number of elements while having a high quality mesh around the body (Jafari and Kosasih, 2014). Therefore, as previously investigated in the mesh independence study on the CFD model the PowerWindow prototype (Jafari et al., 2016), 200 structured

rectangular elements (1.5mm length of each cell along the chord-wise) with y+ below 2.0 are generated adjacent to the blade surface while this structured region is connected to the surrounding structured region via unstructured triangular elements with maximum skewness of 0.17, as shown in Fig. 5(b). Structured coarser mesh is generated around the hybrid region in both the ducted and elevated model as shown in Fig. 5(a). The 3D model contains 3,698,740 elements in the wind tunnel model, 3,103,560 elements in the ducted model and 4,078,320 elements in the elevated model. In the elevated model assuming the PowerWindow frame as a solid blocking area (with 100% porosity which is over-estimated) would result in 11% blockage effect. In both the models distance of the device from inlet and outlet are 2 m and 8 m respectively.

The frame of the hybrid region containing the front and rear blades is selected as multiple reference frame (MRF) which can move vertically within the domain. The reason for selecting MRF model was that unlike the rotating geometries, in PowerWindow the frame containing the blades will not remain inside the domain by time transition. Therefore, MRF as a steady state model capable of solving moving reference frame equations has been used in the study. In MRF, flow in each moving cell zone is solved using the moving reference frame equations. If the zone is stationary, the stationary equations are used. At the interfaces between cell zones, a local reference frame transformation is performed to enable flow variables in one zone to be used to calculate fluxes at the boundary of the adjacent zone.

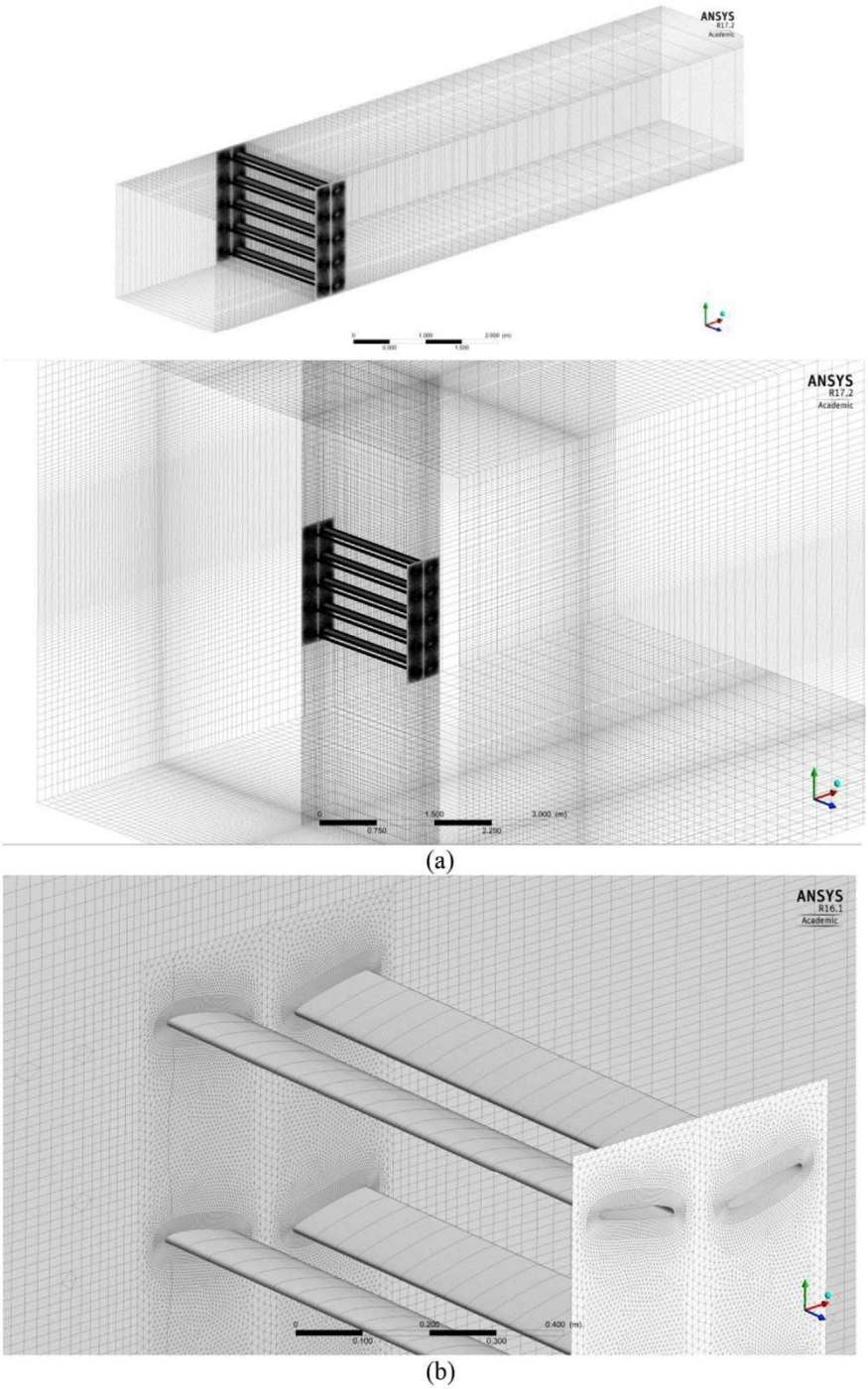

Fig. 5. (a) Structured coarse mesh generated around the unstructured region. (b) Structured-unstructured hybrid mesh around the blades including fine structured rectangular elements adjacent to the blade surface.

Moving mesh has not been used in this study, as it needs periodic boundary condition and, using periodic boundary condition would change the continuity equations around the blades so that it led some flow in and out from the top and bottom of the blades and significantly changed the flow direction accordingly. In the MRF (front and rear) moving zones, 50 cells have been generated span-wise along the blade's surface which has resulted in $45 < y+ < 115$ over the inner and outer side of the frame's surfaces. It should be noted that on both sides of the blades, there are a pair of interfaces laid on each other with structured mash over the outer surface (facing the stationary zone) and unstructured mesh over the inner surface (facing the moving zone).

The boundaries of the blades are set to moving wall with zero velocity relative to their adjacent cells. As a result, their vertical velocity would be equal to the MRF surrounding cells. The inlet boundary condition has a uniform velocity of 8 m/s and the outlet boundary of the domain is set to atmospheric pressure. Turbulence intensity of 5% and turbulence viscosity ratio of 10 is set for inlet, while outflow was selected for outlet boundary conditions. In the elevated configuration, a realistic wind profile strongly depends on the elevation from the ground and topology of the area. In the ducted configuration, wind profile at upstream of PowerWindow strongly depends on distance of the device from the duct inlet and also the entry design. Therefore, uniform wind profile is considered at the inlet of the models in this study. The standard pressure correction method and a first order upwind scheme is used. The top and bottom boundaries of the domain are selected as stationary wall. Gambit (2015) is used as the mesh generation tool in this study. The CFD simulations are at prototype scale, thus avoiding the need to accommodate any scaling dictated by similarity criteria.

3. Validation of the CFD model

Due to the lack of experimental data on the proposed installation configurations (elevated and ducted configurations) for PowerWindow, the experimental data is used to validate the CFD wind tunnel configuration. The accuracy of the CFD model is investigated by comparing the power generation predicted by the CFD model and with that recorded in

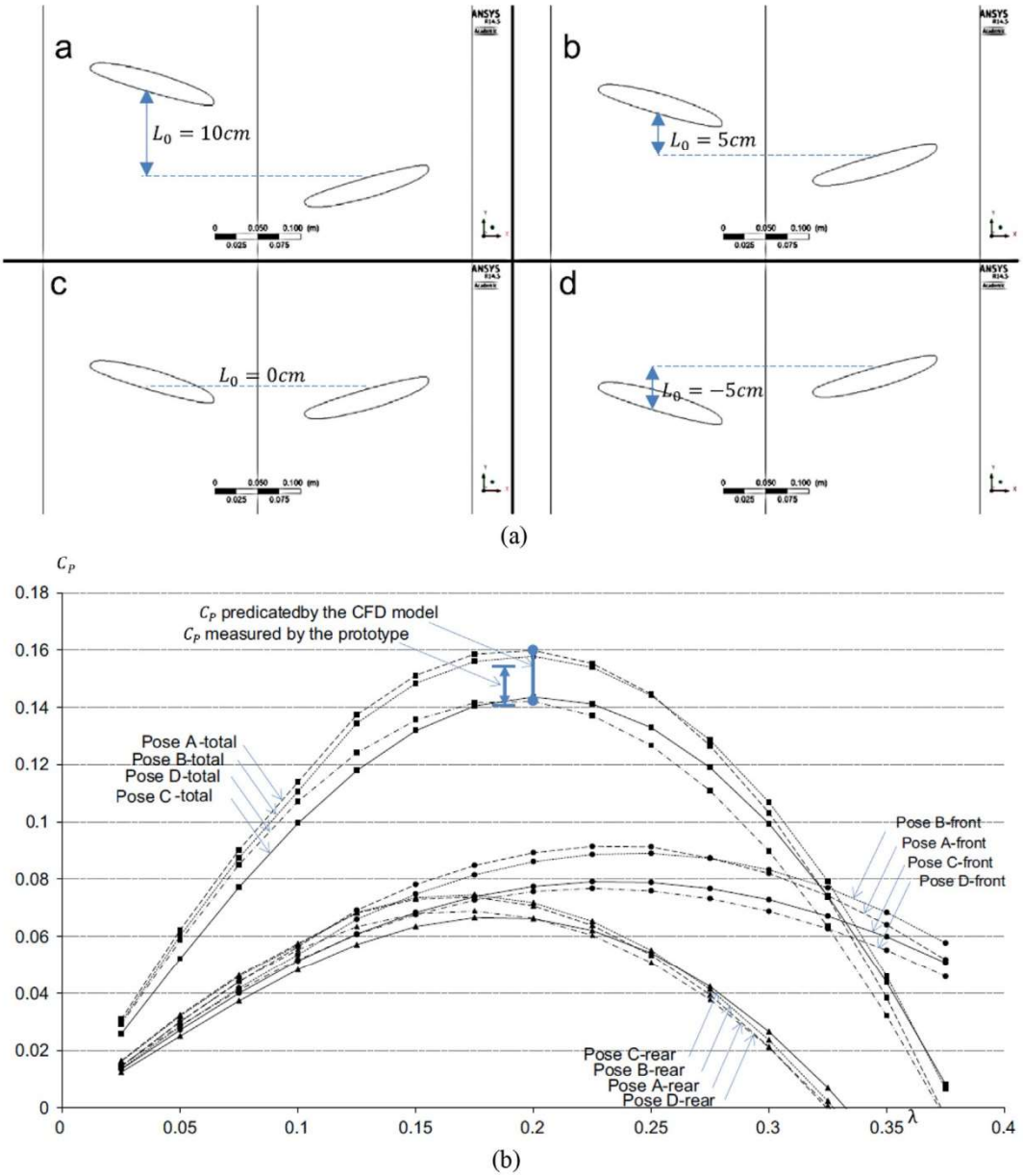

Fig. 6. (a) Front and rear blades of the PowerWindow CFD model in poses (a) when $L_0/C = 2/3$, (b) when $L_0/C = 1/3$, (c) when $L_0/C = 0$ and (d) when $L_0/C = -1/3$ (C = 15cm). (b) C_P of the PowerWindow prototype recorded in the experimental test and predicted by the CFD simulations against λ.

the experimental test. CFD model of the grounded PowerWindow has been built with $\sigma = 0.428$ and $\theta_b = 16°$ (similar to the prototype). The CFD model has been tested in four different poses, shown in Fig. 6(a), to investigate the effect of position of the front blades to the rear ones on their aerodynamic force and power generations. In each pose L_0 shows the elevation of the front blade to its adjacent rear blade. The L_0/C ratio is $2/3$, $1/3$, 0 and $-1/3$ respectively in pose a, b, c and d while the chord length of each blade is 15cm (C = 15cm). The vertical and horizontal forces exerted on the front and rear blades are found via simulations.

Coefficient of performance (C_P) is selected to measure the power generation efficiency of PowerWindow prototype and the CFD models in this study. C_P shows the ratio of the power captured by the wind energy device to the entire wind energy passing through its swept area. The total power captured by the CFD model, ignoring the power generated by the single top and bottom blades, can be calculated via multiplying the total vertical force exerted on both front and rear blade by their velocity. C_P is calculated by dividing this power by the total wind power passing the swept area of the model.

$$C_P = \frac{P_{measured}}{P_{wind}} = \frac{\sum_1^n (Lift_{front} \times U\lambda) + \sum_1^n (Lift_{rear} \times U\lambda)}{1/2(\rho U^3)A} = \frac{Lift_{total} \times U\lambda}{\frac{1}{2}\rho U^3 A} \quad (9)$$

Unlike in the HAWTs and some VAWTs, in a LCWTs such as PowerWindow, λ does not depend on the distance of a particular part of blade to the rotating centre but, is constant along the blades and can be measured by multiplying the angular velocity of the gear by its radius:

$$V_{blade} = \omega_{gear} \times r_{gear} \quad (10)$$

Fig. 6(b) shows the C_P achieved by the front, rear and the total blades of the CFD model versus λ. The arrow between the horizontal solid lines shows the C_P achieved by the prototype in the experimental test. The curved lines show the C_P predicted by the CFD model in different values of λ. The operating condition of the CFD model is λ at which the maximum C_P is achieved ($\lambda = 0.2$). It can be seen that the prototype C_P in the experimental test has validated the CFD results. Operating conditions predicted by the CFD model is indicated by a blue solid line within two circles which shows $0.14 < C_P < 0.16$ at $\lambda = 0.2$. Operating recorded in the wind tunnel test is indicated by a blue arrow within to blue lines indicating shows $0.14 < C_P < 0.155$ at $\lambda = 0.1875$. The generated results show a close agreement between the experimental test and the CFD simulations, which verifies the validity of the CFD model. The verification has been further reported in (Jafari et al., 2015).

4. Results and discussion

4.1. Effect of installation configuration on power generation

This study investigates elevated and ducted installation configurations and their effect on the power generation. PowerWindow is a modular LCWT and the aerodynamic performance of a multiple unit can be different from a single unit. An illustration of the pressure distribution on the prototype blades using the 3D model is presented in Fig. 7. This figure shows that the pressure difference between the high and low pressure sides of the bottom blades is greater than that of the top blades, which is mainly due to the ramp installed at the bottom inlet. The ramp accelerates the flow toward the bottom blades and increases velocity magnitude there, resulting in a higher dynamic pressure and consequently the stagnation pressure (on the higher pressure side of the blades). The vertical velocity also increases as the wind passes over the ramp. The increase in the vertical velocity results in a higher α and consequently the pressure created on the bottom blades. Therefore, such a difference in the pressure distribution over the top and bottom blades is not expected to be observed in the elevated and ducted configuration, where there are no ramps.

Fig. 6 also shows that the pressure distribution over the blades changes along the span so that the pressure difference across the sides of a blade at the middle is greater than that near the ends of the blade. The dissimilarity between the pressure distributions on the middle and both sides of the blades is because near the sides, the flow can easily bypass the frame instead of passing through it. As a result, the axial velocity toward

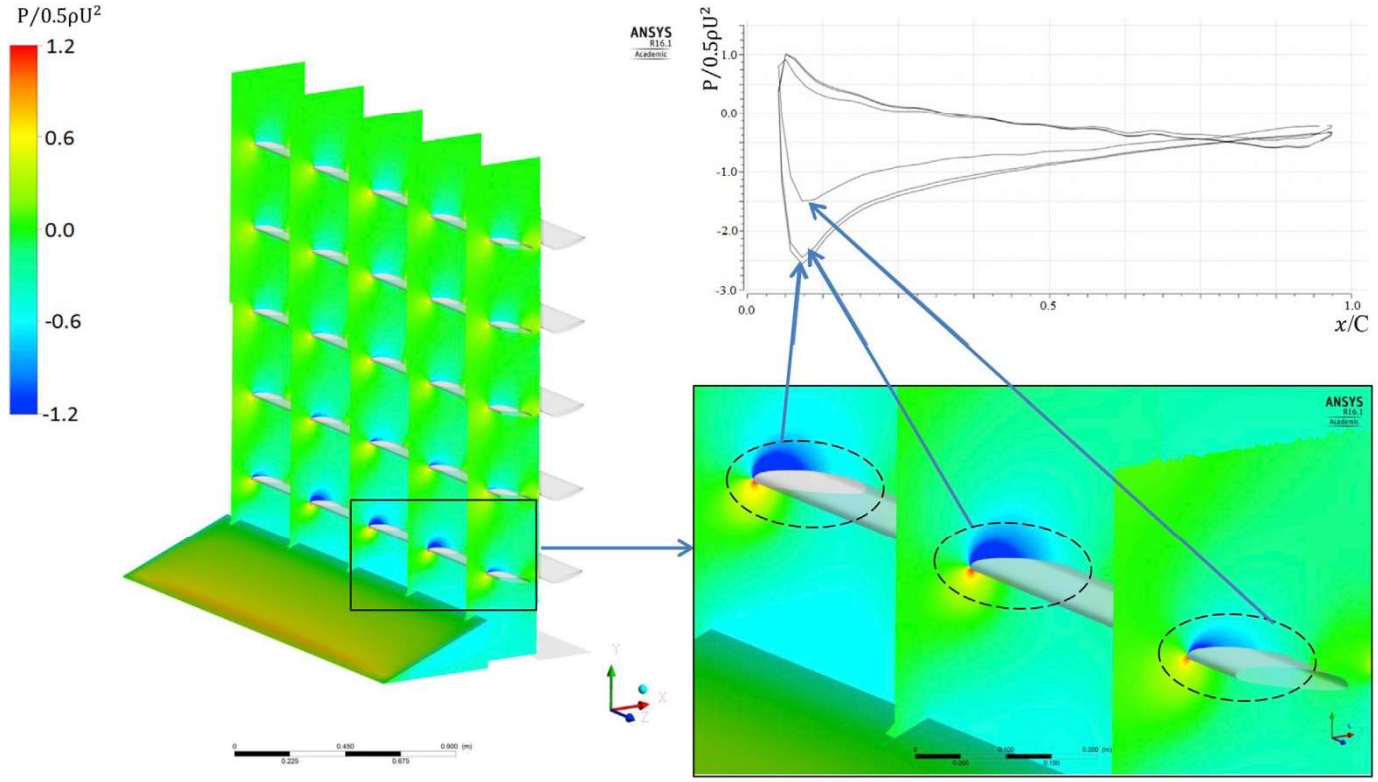

Fig. 7. Pressure distribution around the blades of the PowerWindow prototype (in wind tunnel configuration) at different sections along the span.

the blades decelerates, which consequently reduces the pressure difference between the high and low pressure sides of the blades near the sides. This study illustrates and compares flow characteristics around the PowerWindow blades, at the mid-span in the elevated and ducted configurations.

Fig. 8 shows velocity contours around the PowerWindow blades at the mid-span when PowerWindow is installed in the (a) elevated, and (b) ducted configurations at $\lambda = 0.15$. It can be seen that the free stream velocity has slightly decreased below 8m/s at upstream of the front blades in the elevated configuration while the stream velocity has increased to up to 9m/s between the front and rear blades of the ducted configuration. The mean velocity between the front and rear blades of the elevated model has been measured 7.2m/s while it has remained 8m/s between the front and rear blades of the ducted model. The reason is absence of the bypass flow in the ducted configuration which forces the flow to pass through PowerWindow. Higher velocity creates a lower α at the same λ on the blades of the ducted configuration. Therefore, λ at the operating condition increases in this configuration to optimize α.

The higher velocity also creates greater pressure gradient between the higher and lower pressure sides of the ducted PowerWindow and the blades, which results in a higher vertical force on them and evidently higher power generation. Fig. 9 shows pressure contours around the PowerWindow blades and streamlines around the middle blades at the mid-span when installed in the (a) elevated, and (b) ducted configurations and operating at $\lambda = 0.15$. This figure agrees that the pressure gradient around the blades is higher in the ducted configuration and shows that this configuration demands a higher pressure gradient between the upstream and downstream sides of the PowerWindow (ΔP), which may not be available in the duct particularly at higher σ. Comparison of the stream lines between the elevated and ducted configuration shows that the lower pressure side of the rear blades of the elevated PowerWindow is mainly located in the separation area, while the separation has been postponed to the trailing edge in the ducted PowerWindow and flow is mainly attached to the blade's surface. This can result in a major difference between the pressure distributions over the blade surface of the elevated and ducted PowerWindow.

For more accurate comparison, pressure distribution in terms of surface pressure coefficient ($C_{SP} = P/0.5\rho U^2$) along the chord-length of the front and rear blades of the elevated (blue color) and ducted (red color) PowerWindow are presented in Fig. 10. This figure shows that in both configurations, pressure difference between the high and low pressure sides of the rear blades is greater than the front ones. As a result, they are expected to have a greater contribution in the total power generation. The reason is that the front blades accelerate the flow downward and increase α over the rear blades and higher α results in higher ΔP between the high and low pressure sides of the rear blades. As shown in Fig. 9, the higher α creates flow separation over a major part of the rear blades of the elevated PowerWindow, while the separation area has been diminished to a very smaller part in the ducted PowerWindow. Nevertheless, Fig. 10 shows a slight difference between C_{SP} along the chord-length of the rear blades of the elevated and ducted PowerWindow. The only major difference is around the trailing edge of the rear blades.

It can be seen that on the trailing edges of the elevated configuration, high and low pressure lines have crossed each other which creates a reverse force there and decreases the total vertical force on them. As a result, the total vertical force on the blades of the ducted configuration and its power generation at the same λ is expected to be greater than the elevated one. The reason behind this phenomenon lies in the flow separation from the blade's surface. Separation begins as the flow passes along the chord-length of the pressure side of the blades and reaches the trailing edge. In the elevated configuration, the flow is less confined and can more freely separate from the blade's surface while in the ducted configuration, the flow is relatively confined and is forced to pass over the blade's surface.

Fig. 11 shows C_P obtained by the CFD model for the elevated and ducted PowerWindow configuration in comparison with the prototype (wind tunnel configuration). As expected from the pressure distribution on the blades, the ducted configuration with $C_P = 0.12$ has 50% higher power generation performance than the elevated one with $C_P = 0.08$. However, the wind tunnel configuration with $C_P = 0.14$ has the highest performance. It can also be seen that in the ducted and elevated configurations, the rear blades have 30 − 50% greater contribution to the total power generation compared to the front blades while in the wind tunnel configuration the front blades have greater contribution in the total power generation. The higher performance of the wind tunnel configuration in power generation particularly for the front blades is due to the ramp installed at the bottom inlet which accelerates the flow upward and increases α over the front blades there.

Fig. 11 also shows that the operating λ in the ducted configuration with $\lambda = 0.2$ is higher than in the elevated one with $\lambda = 0.15$. The reason is that the maximum vertical force exerted on the blades depends on α and the optimum α over the blades of the elevated configuration is higher than the optimum α in the elevated one due to the flow separation and higher α can be achieved in lower λ.

Comparing Figs. 6 and 11 shows that C_P of both the elevated and ducted configurations are still lower than the C_P of the wind tunnel configuration when all the models are exposed to an identical 8 m/s approach wind velocity which is mainly due to the ramp effect in the wind tunnel configuration. However, some amplification factors will be applied to the approach wind velocity for the elevated and ducted configurations which may results in greater power generation in them.

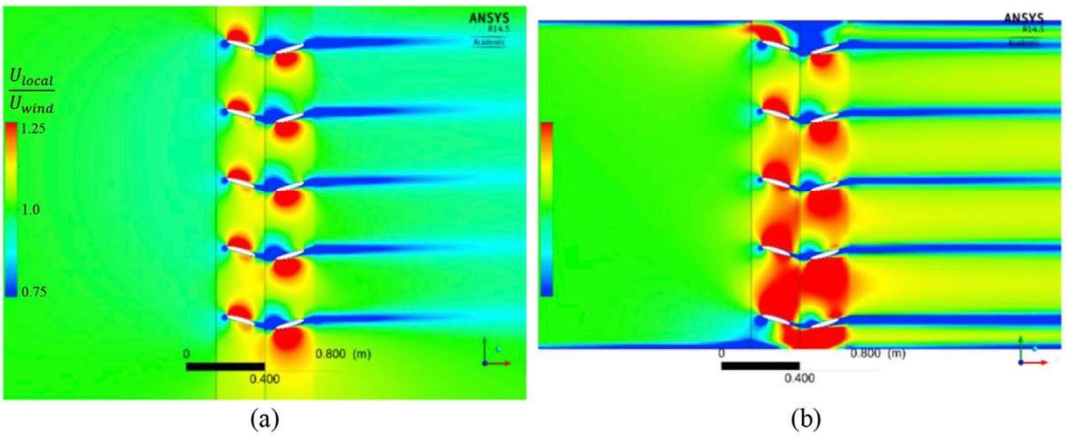

Fig. 8. Velocity contours around the PowerWindow blades at the mid-span when installed in the (a) elevated, and (b) ducted configurations at $\lambda = 0.15$.

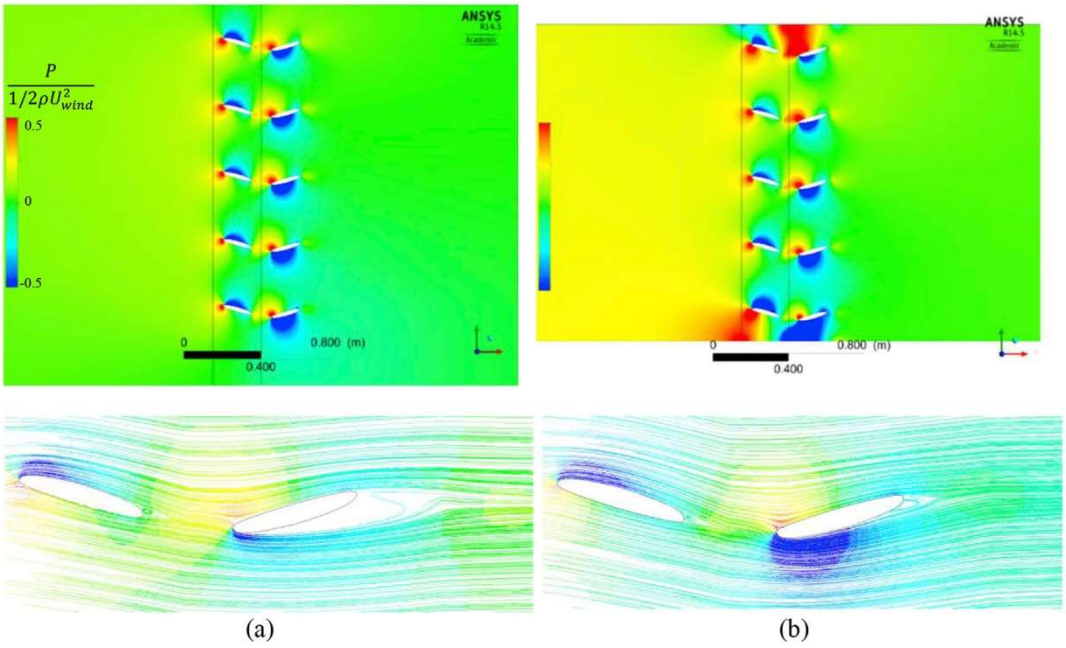

Fig. 9. Pressure contours around the PowerWindow blades and streamlines around the middle blades at the mid-span when installed in the (a) elevated, and (b) ducted configurations and operating at $\lambda = 0.15$.

The passages between two buildings can be treated as a potential location for wind energy harvesting. A study on Venturi effect of two perpendicular buildings by Blocken, Moonen (Blocken et al., 2008a) showed that wind speed amplification factors for converging passages at ground level is greater than the upper levels. The reason is that wind flow bypasses over the buildings rather than being forced to pass through the buildings. In another study by Blocken, Stathopoulos (Blocken et al., 2008b) for the same model, it was found that the wind speed amplification factors in diverging directions are most often larger than converging directions. The study was extended by Li, Luo (Li et al., 2015) who investigated the wind amplification factor with the building orientation varying from 0° to 180°. Lu and Ip (2009), investigated the flow characteristics between two identical neighbour buildings with dimensions of 25m × 25m × 70m and distances of 10, 15, 20m from each other. It was concluded that the wind speed increases by factor of 2 from the inlet wind speed of about 7.5 m/s.

In the ducted configuration PowerWindow is installed inside a ducted area such as a through-building opening. Based on the inlet and outlet design of the duct and the approach wind direction, the ducted flow may have a higher speed than the free stream at the same elevation. To achieve greater performance, through-building openings can be embedded toward the dominant wind direction. Li et al. (2016) provided a performance assessment of four wind turbines installed in four through-building openings in a tall building, Pearl River Tower, conducting a 1:150 scale wind tunnel test and reported that the wind speeds in the tunnels can be intensified by average factor of 1.90.

4.2. Effect of solidity on power generation

As previously mentioned, σ is one of the most influential design parameters on power generation of every wind turbine including PowerWindow. The C_L and C_D values of an airfoil cascade configuration is different from an isolated one and strongly depends on σ. Due to the higher surface area, cascade configuration increases drag. Meanwhile, by restraining the flow, it postpones stall. Studies have shown that the influence of surface height roughness reduces, while C_D increases with an increase in the height of roughness. The height of roughness does eliminate the operating condition of the cascade blades, which reduce the value of the stall angle (Yousif et al., 2015). Simple domains containing one airfoil blade with periodic boundaries at the top and bottom were generated for this part of study. C_L and C_D of the linear cascade configuration have been extracted for some selected higher σ values: $\sigma = 0.857$ and 1.714. Similar to the prototype test condition, in all simulations, the inlet wind velocity was set to 8 ms^{-1}, and the Reynolds and the Mach number are 7.1×10^4 and 2.33×10^{-2} based on chord length the airfoil and room temperature (300 K).

Fig. 12(a) and (b) show C_L and C_D extracted for the isolated airfoil and the linear cascade configuration with $\sigma = 0.428$, 0.857 and 1.714 against a range of α: $-14° < \alpha < 36°$. Polynomial curves have been fitted to the undertaken results for C_L and C_D in the prototype condition: $\sigma = 0.428$. This function facilitates calculation of the lift and drag forces in the BEM model by making them dependent on α. As can be seen in Fig. 12(a) the maximum C_L s of cascade airfoils are lower than the maximum C_L of the isolated airfoil. In addition, as σ increases, the maximum C_L decreases and shifts to higher α (postpones stall). Therefore, the cut-in speed (the minimum wind speed that the wind can overcome inertia and start moving the blades without the help of the generator) of PowerWindow is expected to be lower with higher σ.

As previously reported, results also show that in elevated and ducted configurations the flow redirection by the front blades enhances the vertical force created on the rear blades and thus, their contribution in the total power. The influence of the front blades on the flow direction when meeting the rear blades (β_2) depends on σ of the cascade. Higher σ results in more intense flow redirection and higher α_2 on the rear blades. The flow redirection also depends on λ, because the higher momentum that the air gives to the blades the more it will be redirected to the opposite of the blades moving direction. Therefore, β needs to be investigated against both σ and λ.

Fig. 13(a–c) shows flow streamlines when flow passes through linear cascade configuration of PowerWindow blades (at the mid-section) with σ = (a) 0.428, (b) 0.857 and, (c) 1.714 against a range of λ ($0.025 < \lambda < 0.25$). In the prototype $\sigma = 0.428$ and $\sigma = 0.857$ and $\sigma = 1.714$ are selected by doubling the number of the cascade blades. As can be seen in the figure, β increases by increasing both σ and λ. However, it can be

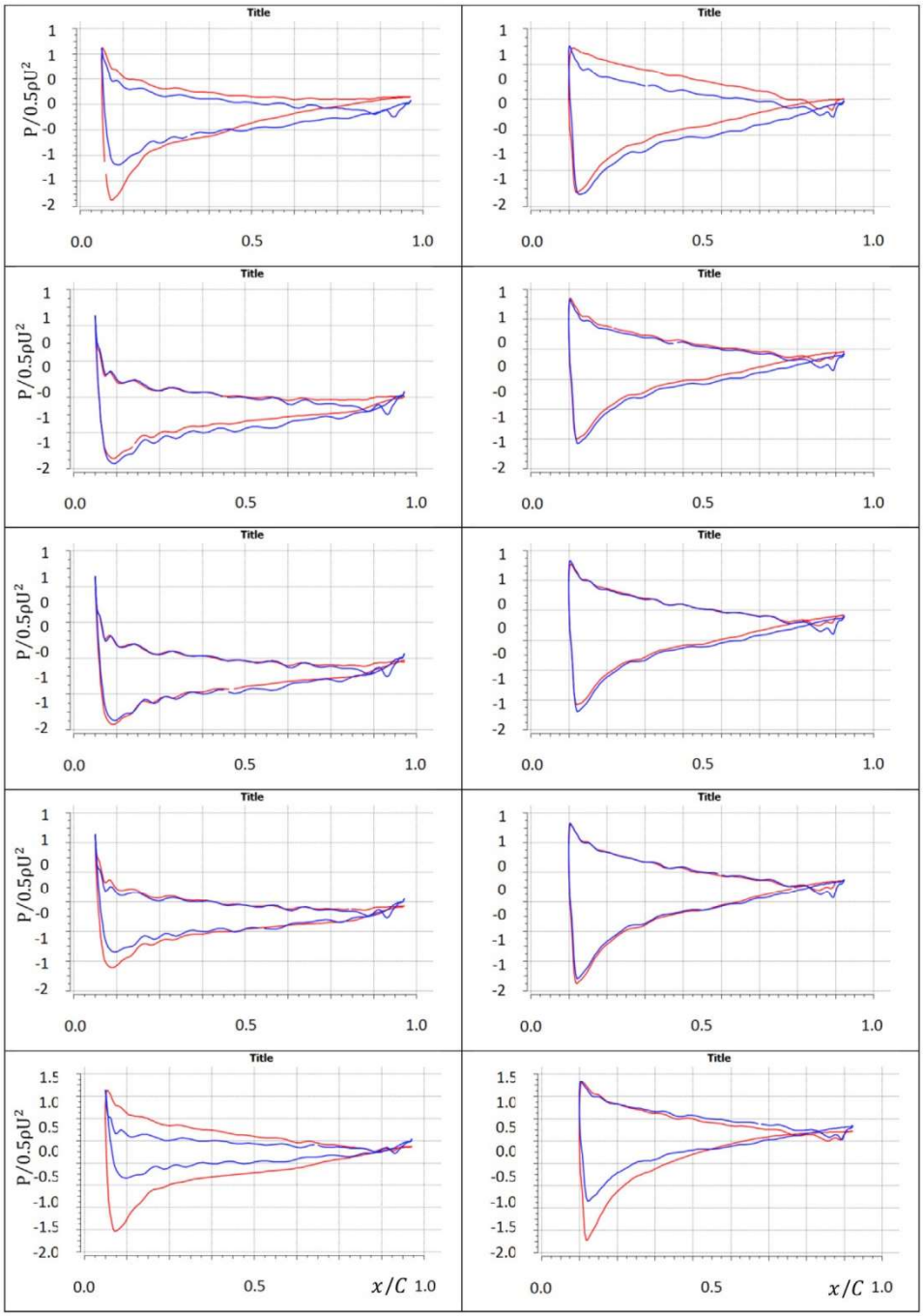

Fig. 10. Pressure distribution along the chord-length of the front (left) and rear (right) blades of the elevated (blue curves) and ducted (red curves) PowerWindow at $\lambda = 0.15$. (For interpretation of the references to color in this figure legend, the reader is referred to the Web version of this article.)

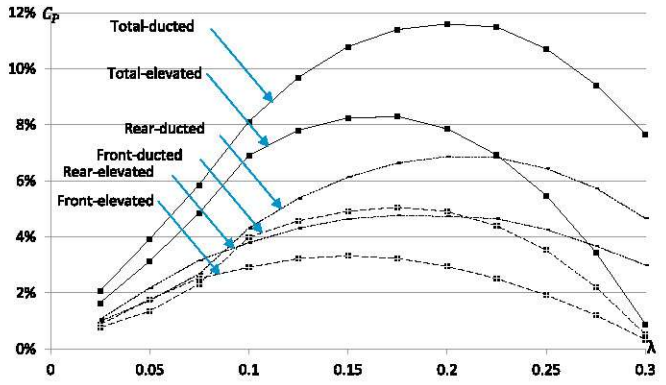

Fig. 11. C_P of PowerWindow in elevated and ducted configurations against λ.

seen that increasing σ diminishes the effect of λ on β so that, in σ = 0.428, β increases from 11° to 16° by increasing λ from 0.025 to 0.25 while in σ = 1.714, β increases only from 21° to 22° by a similar increase in λ.

Based on these results, Fig. 14 shows the relationships between β and λ at different values of solidity, σ = 0.428, 0.857 and 1.714. The governed relations between the β and λ at each σ helps to calculate the angle of attack over the rear blades, α_2, and derive a more accurate analytical model. α_2 can be calculated using Equation (11) (Jafari et al., 2018):

$$tan\alpha_2 = tan\alpha_2(\theta_b + \beta) - \left(2\lambda/(1-a_f)\right) \tag{11}$$

Where, a_f is the reduction ratio in velocity to the approach wind velocity. Power generation of the rear blades can be calculated using Equation (12) (Jafari et al., 2018):

$$Power = \sum_{1}^{N}\left(\frac{\rho B}{2}\right)V_{rel}^2[C_L cos(\theta_b - \alpha_2) - C_D sin(\theta_b - \alpha_2)](V_{wind}\lambda) \tag{12}$$

Equation (11) shows how α_2 increases by increasing β and Equation (12) shows how increasing α_2 to an optimum point increases power generation by the rear blades. Using the relationships between β and λ at each σ helps to calculate the power generation of the rear blades with different configurations in further studies.

Among the design parameters, σ is the most influential on the required ΔP across a wind turbine. Increasing σ results in higher vertical force by increasing the projected area of the cascade while, higher σ demands a greater ΔP across PowerWindow which may not be available/achievable everywhere. Using CFD simulations, C_P of the elevated and ducted PowerWindow with different σ s has been calculated. The maximum C_P at the operating λ has been identified for each configuration and presented against σ in Fig. 15. This figure shows that C_P of the elevated PowerWindow increases by 50% by doubling σ (at σ = 0.857) while further increase in σ is less effective. In the ducted configuration C_P steadily increases by increasing σ. The results show that increasing σ from 0.428 to 0.857 makes a significant enhancement (≈ 55%) in C_P, increasing σ from 0.428 to 1.284 enhances C_P by 90%, and increasing σ from 0.428 to 1.714 enhances C_P by 145%. The reason is that the flow cannot bypass PowerWindow and is forced to pass through the unit. However, higher σ demands grater pressure gradient which may result in lower ducted flow velocity. Therefore, appropriate ΔP needs to be investigated before increasing σ.

For investigating the optimum ΔP, maximum power generation of the ducted turbine needs to be calculated. The required ΔP for the maximum power generation would be the optimum ΔP. Ignoring every energy loss at the inlet; due to the wall friction; and by the device itself, and by assuming atmospheric pressure at leeward face of the building, the entire reduction in the momentum of the air entering the duct will be captured by the ducted turbine. Considering u as the reduced velocity of the approach wind at the inlet of the through-building opening, and assuming uniform cross section area along the through-building opening

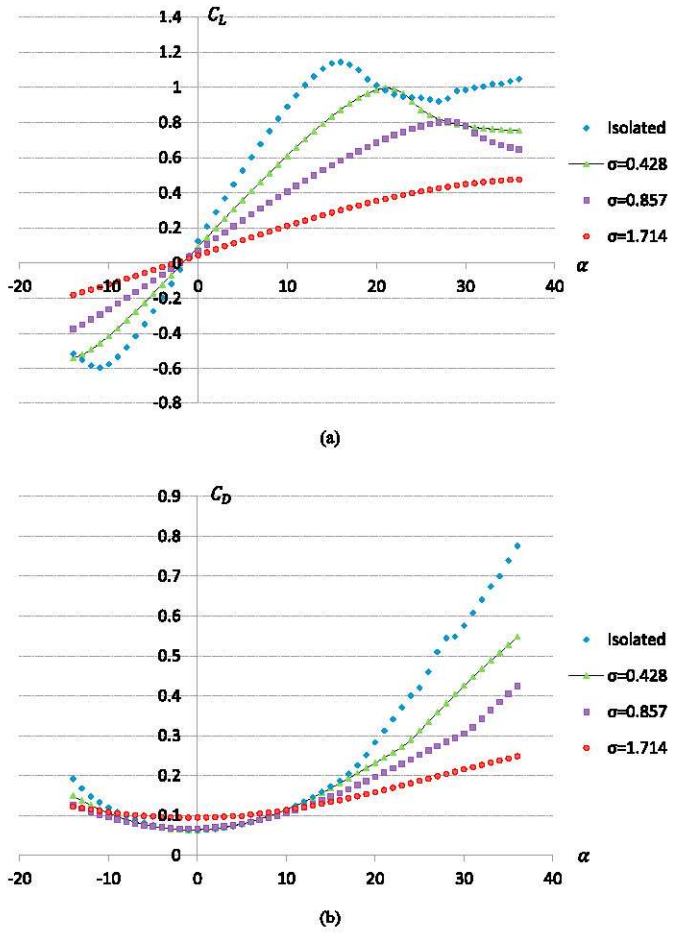

Fig. 12. (a) C_L and (b) C_D of the PowerWindow isolated and linear cascade configurations with σ 0.428, 0.857 and 1.714 against α.

(from the inlet to the outlet), ideal power generation of a ducted turbine can be calculated as below:

$$P = 0.5\rho u\left(U^2 - u^2\right)A \tag{13}$$

Derivation of the power generation equation for the ducted turbine gives the optimum u at which, the maximum power generation will be achieved:

$$\frac{dP}{du} = 0 \rightarrow u = \frac{\sqrt{3}}{3}U \tag{14}$$

The maximum C_P of the ducted turbine can be calculated using the optimum u as below:

$$P_{max} : u = \frac{\sqrt{3}}{3}U \rightarrow C_{Pmax} = \frac{2\sqrt{3}}{9} \tag{15}$$

Assuming atmospheric pressure at the leeward face of the building, where the outlet of the duct is located, the optimum ΔP can be calculated as follows:

$$\left(\Delta P/0.5\rho U^2\right)_{opt} = \left(P_{inlet} - P_{outlet}\right)/0.5\rho U^2 = \left(0.5\rho U^2 - 0.5\rho u^2\right)/0.5\rho U^2 = 2/3 \cong 0.66 \tag{16}$$

The measured ΔP between the inlet and outlet of the ducted PowerWindow at each σ is presented in Table 1.

Table 1 shows that the ratio of ΔP to the dynamic pressure of the approach wind at higher selected σ s is still below the optimum value (which is 0.66 as calculated in Equation (16)). Therefore, increasing σ by 300% can ideally increase C_P of the ducted PowerWindow. Regardless of

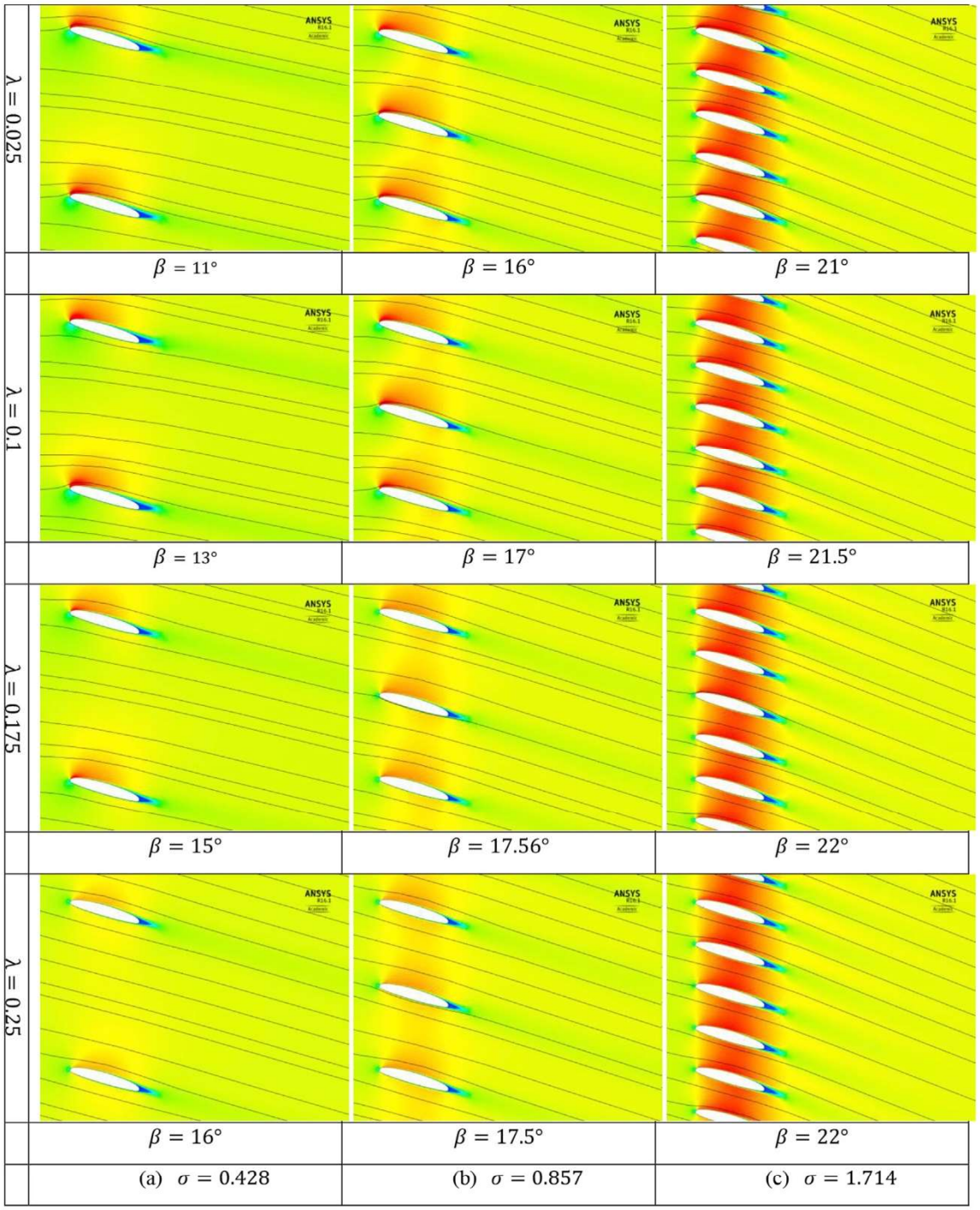

Fig. 13. Flow streamlines when passing through linear cascade configuration of PowerWindow blades with $\sigma = 0.428$, $\theta_b = 16°$, (b) 0.857 and, (c) 1.714 when $0.025 < \lambda < 0.25$.

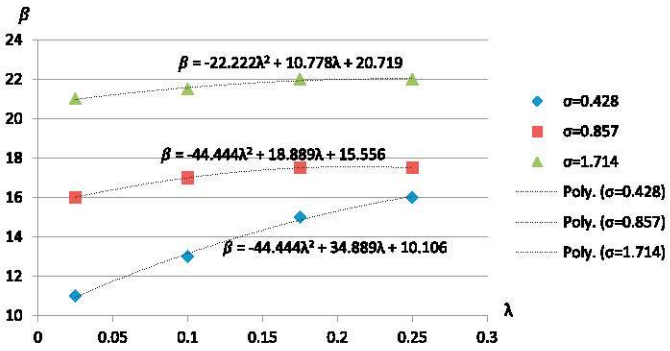

Fig. 14. Relation between the redirection angle of the flow and λ at with σ 0.428, 0.857 and 1.714 when θ_b 16°.

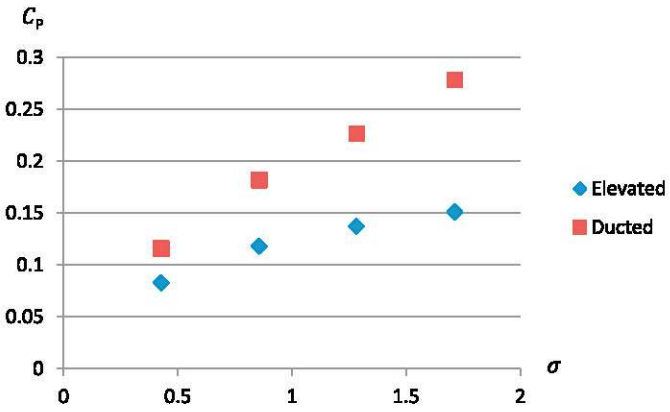

Fig. 15. C_P of the elevated and ducted PowerWindow with different σ s.

σ, if the ratio of ΔP to the dynamic pressure of the approach wind exceeds 0.66, u drops inefficently. Such a drop in u decreases the power generation. However, it should be noted that, in a through-building opening with inlet and outlet larger than the cross section area of the duct, u increases due to the continuity. In such a case, the optimum u/U ratio and ΔP to the dynamic pressure of the approach wind will change, and the optimum σ needs to be investigated accordingly.

Table 1
The ration of ΔP to the dynamic pressure of the approach wind at different σ.

σ	$\Delta P/0.5\rho U^2$
0.428	0.2
0.857	0.33
1.284	0.4
1.714	0.5

5. Conclusion

A 3D CFD model of PowerWindow was developed and validated with the experimental data from the wind tunnel test of the prototype. Elevated and ducted installation configurations were proposed for PowerWindow. In elevated configuration PowerWindow is installed on top of a tall building. In ducted configuration it is installed inside a ducted area such as a through-building opening. Aerodynamic performances of the elevated and ducted PowerWindow were investigated and compared using computational fluid dynamic simulations. The undertaken results indicated that with the current design parameters, the elevated and ducted configurations have respectively 8% and 12% coefficient of performance and in both configurations the front blades enhance the power generation of the rear ones. The effect of solidity was also investigated on the flow mechanism and power generation of elevated and ducted PowerWindow. It was shown that solidity of the front blades has a significant effect on the flow direction approaching the rear ones which increases their contribution in power generation. It was also shown that increasing solidity results in greater coefficient of performance in both configurations. However, the optimum solidity of the ducted configuration depends on the inlet and outlet design of the through-building opening at needs to be investigated for each design.

Nomenclature

A	Air swept area (m^2)
C_P	Coefficient of performance (dimensionless)
C_{sp}	Surface pressure coefficient (dimensionless)
D_k	Turbulent kinetic energy destruction (m^2 s^{-2})
k	Turbulent kinetic energy (m^2 s^{-2})
P	Power (W)
P	Pressure (Pa)
ΔP	Pressure gradient across PowerWindow (Pa)
P_k	Turbulent kinetic energy production (m^2 s^{-2})
$\tilde{R}e_{\theta t}$	Local transition onset momentum thickness Reynolds number (dimensionless)
r_{gear}	Gear radius (m)
U	Wind velocity (m s^{-1})
u	Air velocity in the duct (m s^{-1})
$u_x^{'}$	Velocity deviation in x direction (m s^{-1})
$u_y^{'}$	Velocity deviation in y direction (m s^{-1})
$u_z^{'}$	Velocity deviation in z direction (m s^{-1})
α	Angle of attack (degree)
β	Flow direction when meeting the rear blades (degree)
θ_b	Blade pitch angle (degree)
ω_{gear}	Gear angular velocity (rad s^{-1})
γ	Distance to nearest wall (m)
γ_{eff}	Effective intermittency (dimensionless)
μ	Molecular viscosity (Pa s)

μ_t Eddy viscosity (Pa s)
?? Air density (kg m ^{3})
λ Blade speed ratio (dimensionless)

Appendix A. Supplementary data

Supplementary data related to this article can be found at https://doi.org/10.1016/j.jweia.2018.07.015.

References

Ayhan, D., Sağlam, Ş., 2012. A technical review of building-mounted wind power systems and a sample simulation model. Renew. Sustain. Energy Rev. 16 (1), 1040 1049.

Blocken, B., et al., 2008a. Numerical study on the existence of the venturi effect in passages between perpendicular buildings. J. Eng. Mech. 134 (12), 1021 1028.

Blocken, B., Stathopoulos, T., Carmeliet, J., 2008b. Wind environmental conditions in passages between two long narrow perpendicular buildings. J. Aero. Eng. 21 (4), 280 287.

Dayan, E., 2006. Wind energy in buildings: power generation from wind in the urban environment - where it is needed most. Refocus 7 (2), 33 38.

Drew, D.R., Barlow, J.F., Cockerill, T.T., 2013. Estimating the potential yield of small wind turbines in urban areas: a case study for Greater London, UK. J. Wind Eng. Ind. Aerod. 115 (0), 104 111.

Gambit. 2015 cited 2015; http://www.arl.hpc.mil/software/description.html?sw=Gambit. Available from: http://www.arl.hpc.mil/software/description.html?sw=Gambit.

Hassanli, S., et al., 2017. Utilizing cavity flow within double skin façade for wind energy harvesting in buildings. J. Wind Eng. Ind. Aerod. 167, 114 127.

Hassanli, S., et al., 2018a. Potential application of double skin façade incorporating aerodynamic modifications for wind energy harvesting. J. Wind Eng. Ind. Aerod. 174, 269 280.

Hassanli, S., Kwok, K.C.S., Zhao, M., 2018b. Performance assessment of a special Double Skin Façade system for wind energy harvesting and a case study. J. Wind Eng. Ind. Aerod. 175, 292 304.

Incropera, F.P., David, P., Witt, De, 1990. Fundamentals of Heat and Mass Transfer, p. 4.

Ishugah, T.F., et al., 2014. Advances in wind energy resource exploitation in urban environment: a review. Renew. Sustain. Energy Rev. 37, 613 626.

Jafari, S.A.H., Kosasih, B., 2014. Flow analysis of shrouded small wind turbine with a simple frustum diffuser with computational fluid dynamics simulations. J. Wind Eng. Ind. Aerod. 125 (0), 102 110.

Jafari, S.A.H., et al., 2015. Power generation analysis of PowerWindow, a linear wind generator, using computational fluid dynamic simulations. J. Wind Eng. Ind. Aerod. 147, 226 238.

Jafari, S.A.H., Hassanli, S., Kwok, K.C.S., 2016. Performance analysis of a small wind turbine mounted inside a tall building. In: 18th Australasian Wind Engineering Society Workshop. Serafino Convention Centre, McLaren Vale, South Australia, Australia.

Jafari, S.A.H., Kwok, K.C.S., Safaei, F., Kosasih, B., 2018. Aerodynamic analysis of a linear cascade wind turbine. Wind Energy 1 14. https://doi.org/10.1002/we.2219 M.

Ledo, L., Kosasih, P.B., Cooper, P., 2011. Roof mounting site analysis for micro-wind turbines. Renew. Energy 36 (5), 1379 1391.

Lee, S., et al., 2012. Effects of design parameters on aerodynamic performance of a counter-rotating wind turbine. Renew. Energy 42 (0), 140 144.

Li, B., et al., 2015. Revisiting the 'Venturi effect' in passage ventilation between two non-parallel buildings. Build. Environ. 94, 714 722.

Li, Q.S., Shu, Z.R., Chen, F.B., 2016. Performance assessment of tall building-integrated wind turbines for power generation. Appl. Energy 165, 777 788.

Lu, L., Ip, K.Y., 2009. Investigation on the feasibility and enhancement methods of wind power utilization in high-rise buildings of Hong Kong. Renew. Sustain. Energy Rev. 13 (2), 450 461.

Menter, F.R., 2009. Review of the shear-stress transport turbulence model experience from an industrial perspective. Int. J. Comput. Fluid Dynam. 23 (4), 305 316.

Mertens, Mertens, S., 2003. The energy yield of roof mounted wind turbines. Wind Eng. 27 (6), 507 518.

Mirecki, A., Roboam, X., Richardeau, F., 2007. Architecture complexity and energy efficiency of small wind turbines. IEEE Trans. Ind. Electron. 54 (1), 660 670.

Mohamed, M.H., 2012. Performance investigation of H-rotor Darrieus turbine with new airfoil shapes. Energy 47 (1), 522 530.

Mohamed, M.H., 2013. Impacts of solidity and hybrid system in small wind turbines performance. Energy 57 (0), 495 504.

Mohamed, M.H., et al., 2011. Optimal blade shape of a modified Savonius turbine using an obstacle shielding the returning blade. Energy Convers. Manag. 52 (1), 236 242.

Pagnini, L.C., Burlando, M., Repetto, M.P., 2015. Experimental power curve of small-size wind turbines in turbulent urban environment. Appl. Energy 154, 112 121.

Peacock, A.D., et al., 2008. Micro wind turbines in the UK domestic sector. Energy Build. 40 (7), 1324 1333.

Rafailidis, S., 1997. Influence of building areal density and roof shape on the wind characteristics above a town. Boundary-Layer Meteorol. 85 (2), 255 271.

Sharma, R.N., Madawala, U.K., 2012. The concept of a smart wind turbine system. Renew. Energy 39 (1), 403 410.

Shives, M., Crawford, C., 2012. Developing an empirical model for ducted tidal turbine performance using numerical simulation results. Proc. IME J. Power Energy 226, 112 125.

Toja-Silva, F., Colmenar-Santos, A., Castro-Gil, M., 2013. Urban wind energy exploitation systems: behaviour under multidirectional flow conditions opportunities and challenges. Renew. Sustain. Energy Rev. 24, 364 378.

Wood, D., 2011. Small wind turbines. In: Sathyajith, M., Philip, G.S. (Eds.), Advances in Wind Energy Conversion Technology. Springer Berlin Heidelberg, Berlin, Heidelberg, pp. 195 211.

Yousif, A.H., Hassan, J.M., Khudar, O.A., 2015. Effect of surface roughness height on the aerodynamics performance of axial compressor cascade blades. Al-Nahrain J. Eng. Sci. 18 (1), 128 139.

Appendix B3

Aerodynamic Analysis of a Stator-augmented Linear Cascade Wind Turbine, Jafari SAH, Kwok KCS, Safaei F, Kosasih B, Zhao M, *Journal of Wind Energy*, 2019. 22 (8): p. 1148-1163.

https://doi.org/10.1002/we.2346

Received: 21 August 2018 | Revised: 1 February 2019 | Accepted: 6 March 2019

DOI: 10.1002/we.2346

RESEARCH ARTICLE

WILEY

Aerodynamic analysis of a stator-augmented linear cascade wind turbine

Seyed Amir Hosein Jafari[1] | Kenny C.S. Kwok[2] | Farzad Safaei[3] | Buyung Kosasih[4] | Ming Zhao[5]

[1] Center for Infrastructure Engineering, Western Sydney University, Kingswood, NSW 2747, Australia

[2] School of Civil Engineering, The University of Sydney, Camperdown, NSW 2006, Australia

[3] School of Electrical, Computer and Telecommunications Engineering, University of Wollongong, Wollongong, NSW 2500, Australia

[4] School of Mechanical, Materials and Mechatronic Engineering, University of Wollongong, Wollongong, NSW 2500, Australia

[5] School of Engineering, Western Sydney University, Kingswood, NSW 2747, Australia

Correspondence
Seyed AmirHosein Jafari, Center for Infrastructure Engineering, Western Sydney University, Kingswood, NSW 2747, Australia.
Email: s.jafari@westernsydney.edu.au

Abstract

This study proposes to attach stator vanes to PowerWindow, a linear cascade wind turbine, to improve the flow direction in the device. By controlling the angle of attack, the stator vanes increase the acting force and decrease the undesirable force on PowerWindow blades. An analytical model using blade element momentum theory is developed for the new configuration, referred to as stator-augmented PowerWindow. The analytical model has been verified by a computational fluid dynamic simulation. This study shows that the stator vanes are able to minimize/neutralize the undesirable axial force on PowerWindow so that the thrust coefficient decreases from 0.035 in the original model to −0.005 in the stator-augmented one. In addition, by increasing the acting force on the blades, the stator augmentation will simultaneously enhance the coefficient of performance by up to 10%. This study also shows that by using stator vanes to control the angle of attack, unlike in the original PowerWindow, the direction of rotation of the stator-augmented PowerWindow will remain the same regardless of the wind direction, increasing the utility of the device in practice.

KEYWORDS

angle of attack, blade element momentum theory, coefficient of performance, computational fluid dynamics, linear cascade, PowerWindow, stator vanes, wind turbine

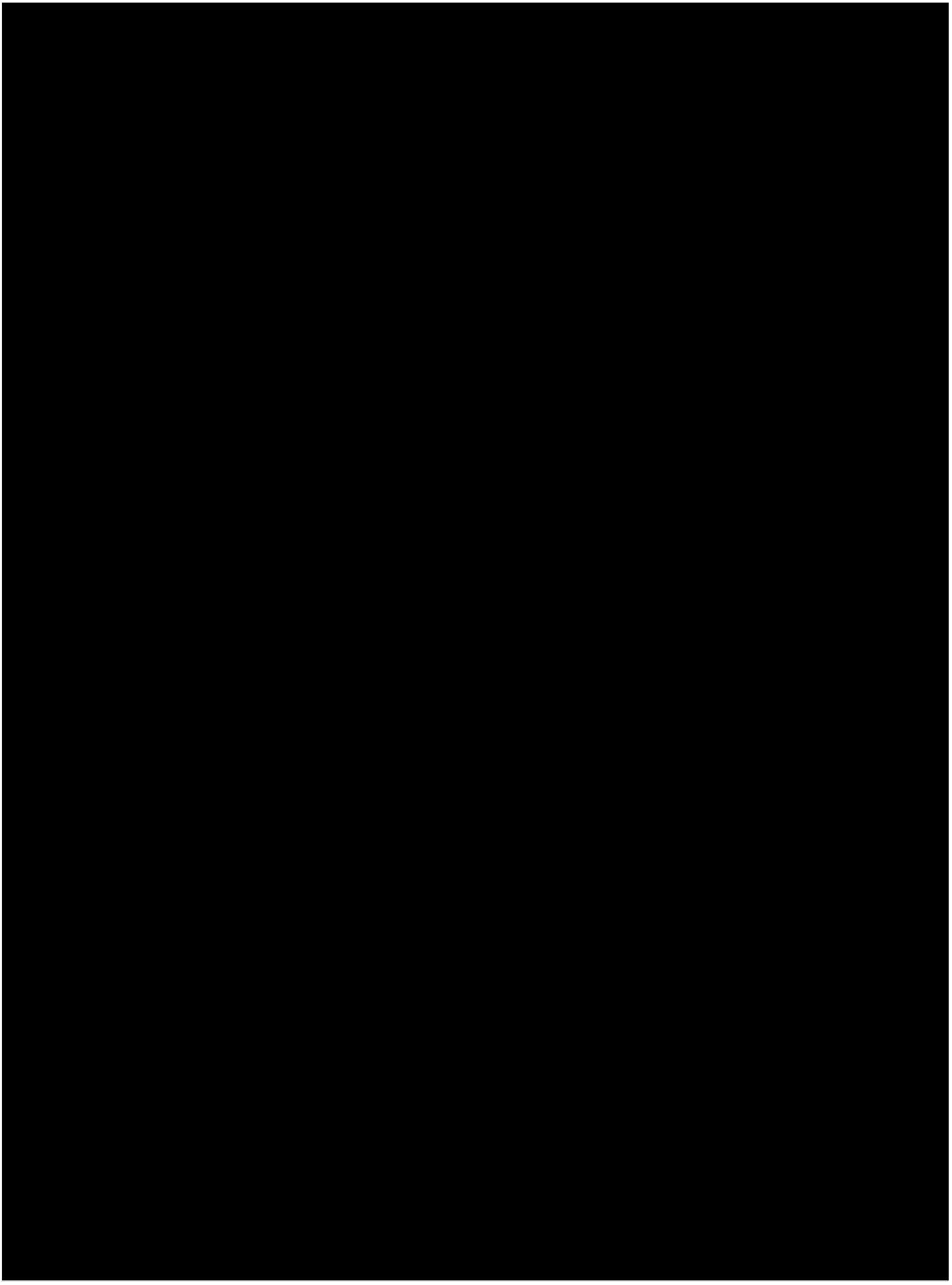

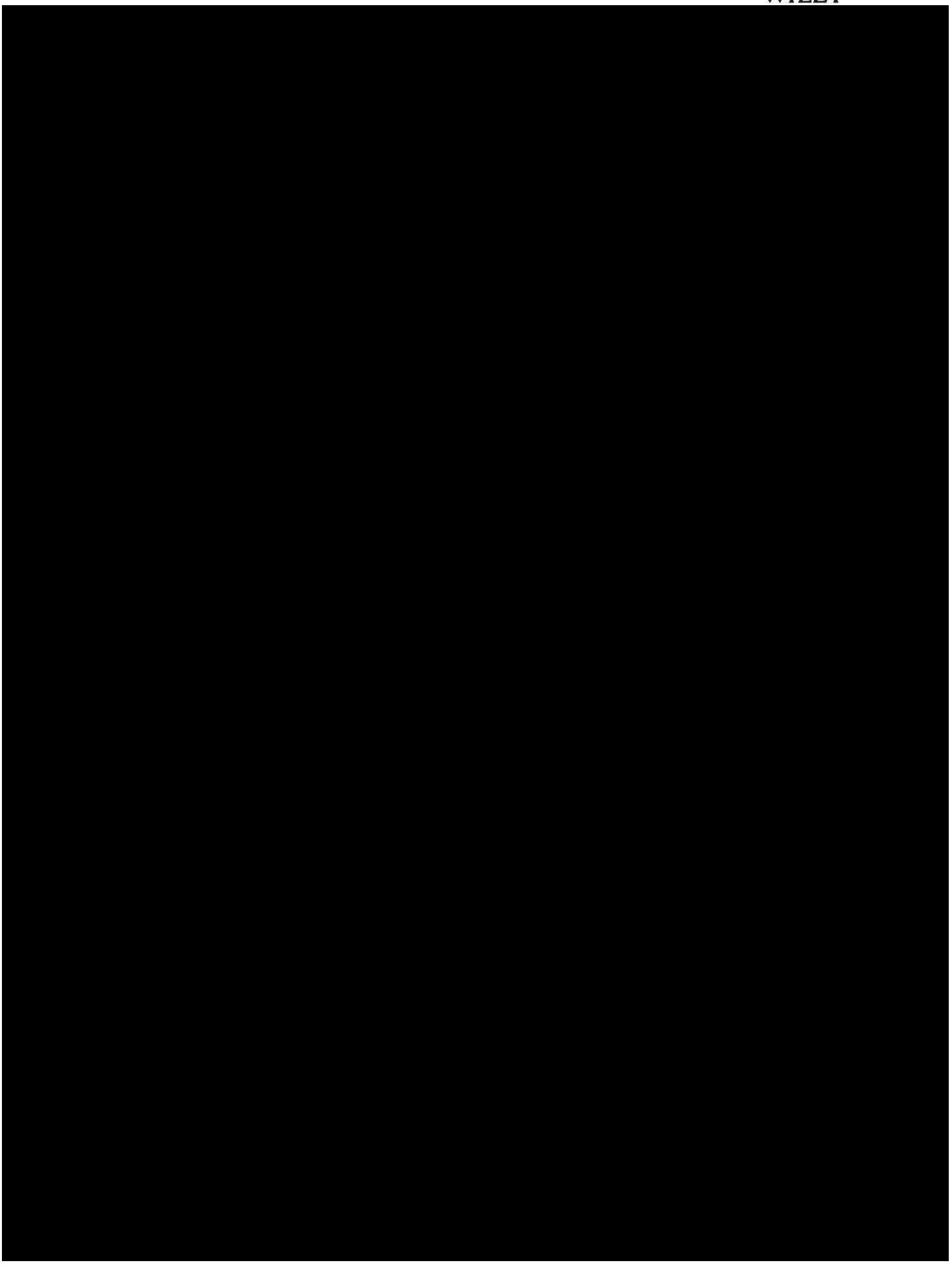

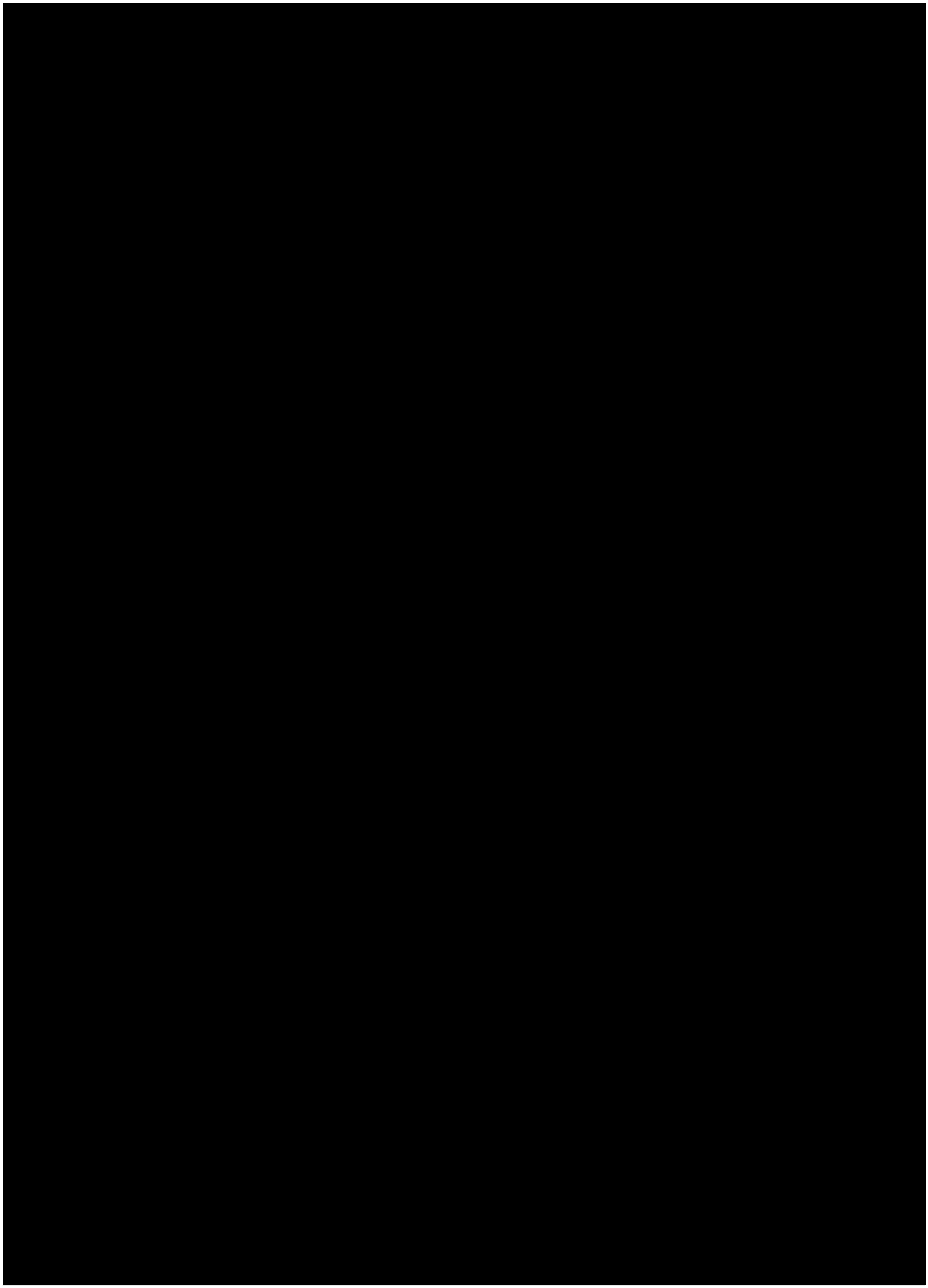

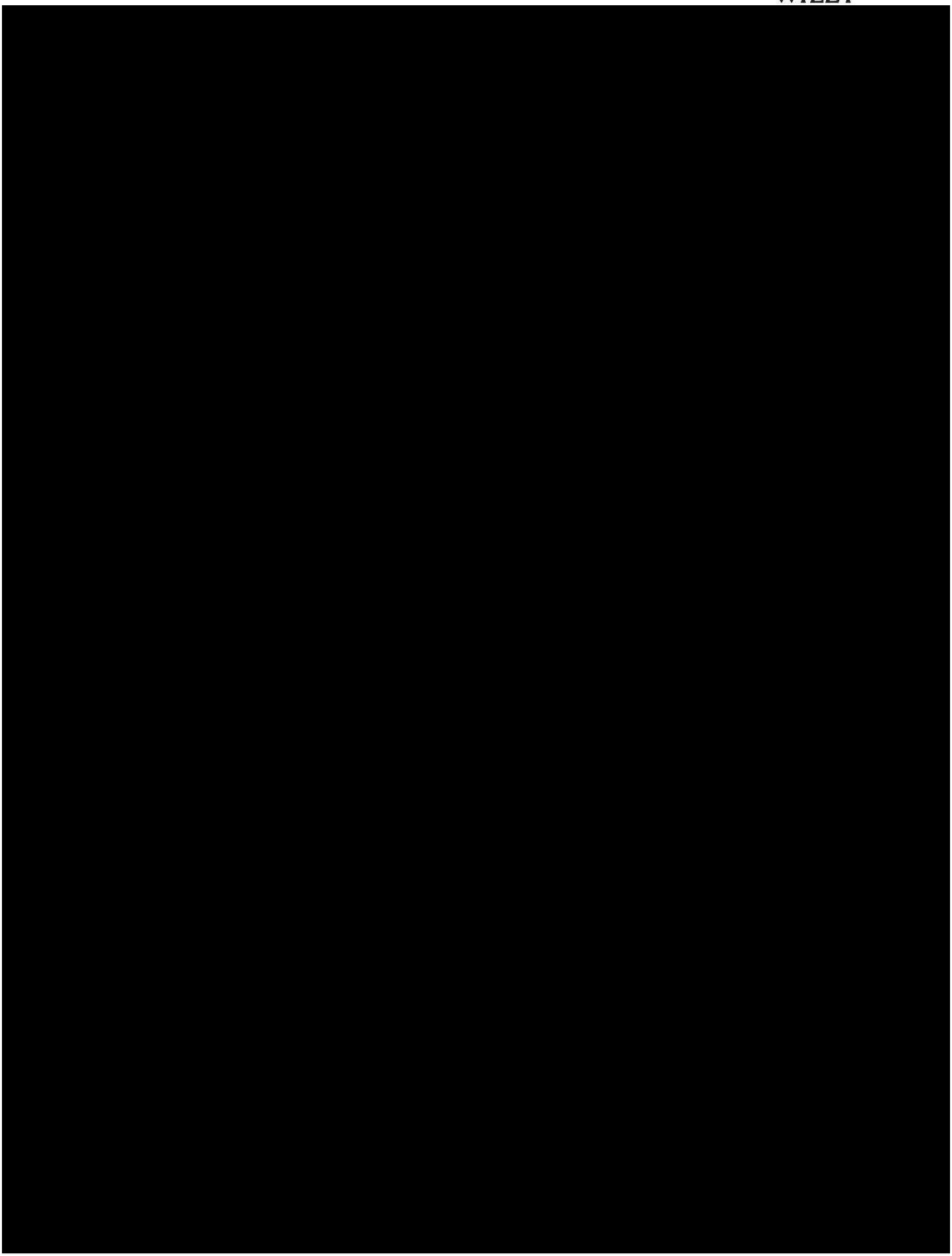

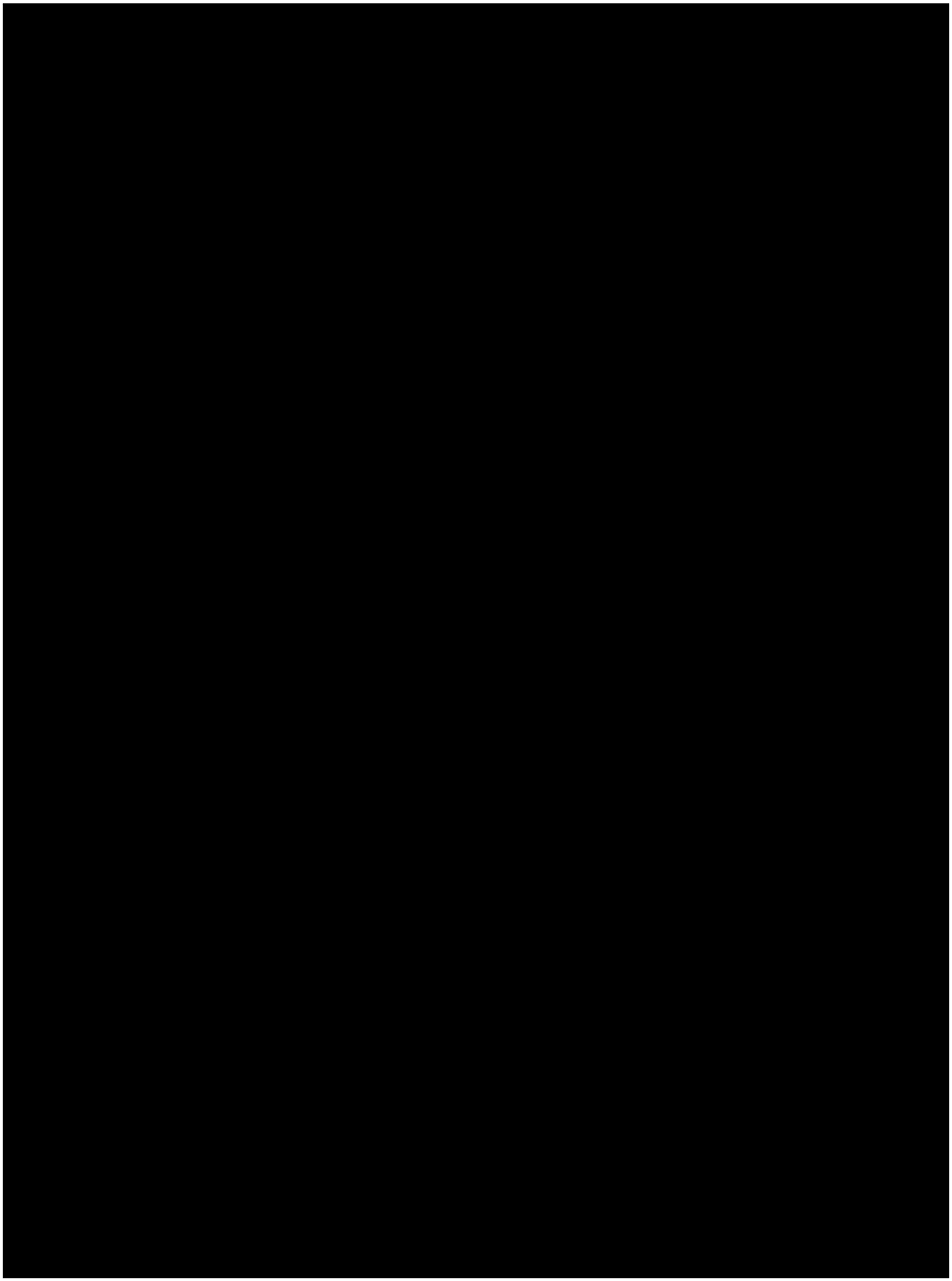

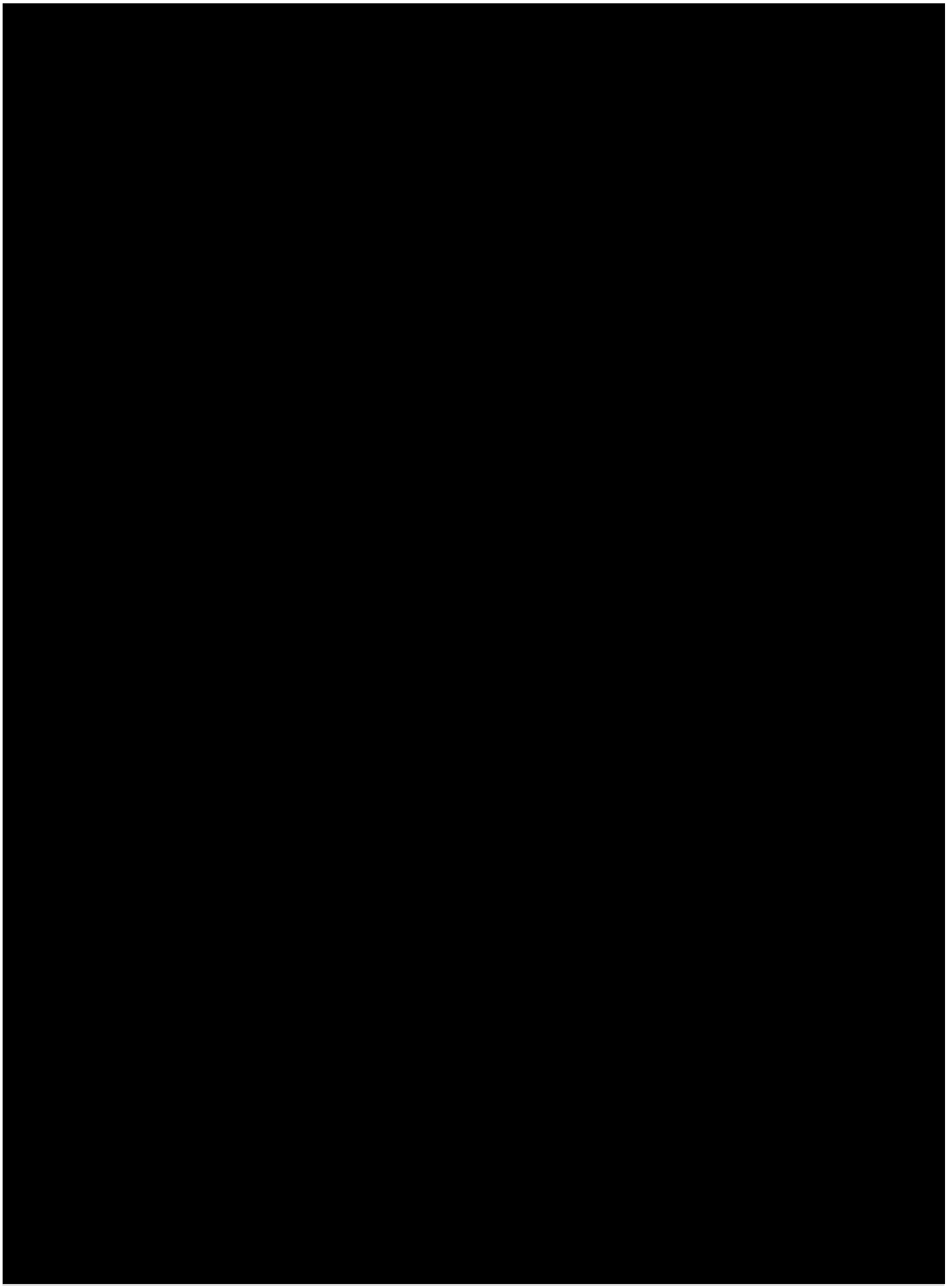

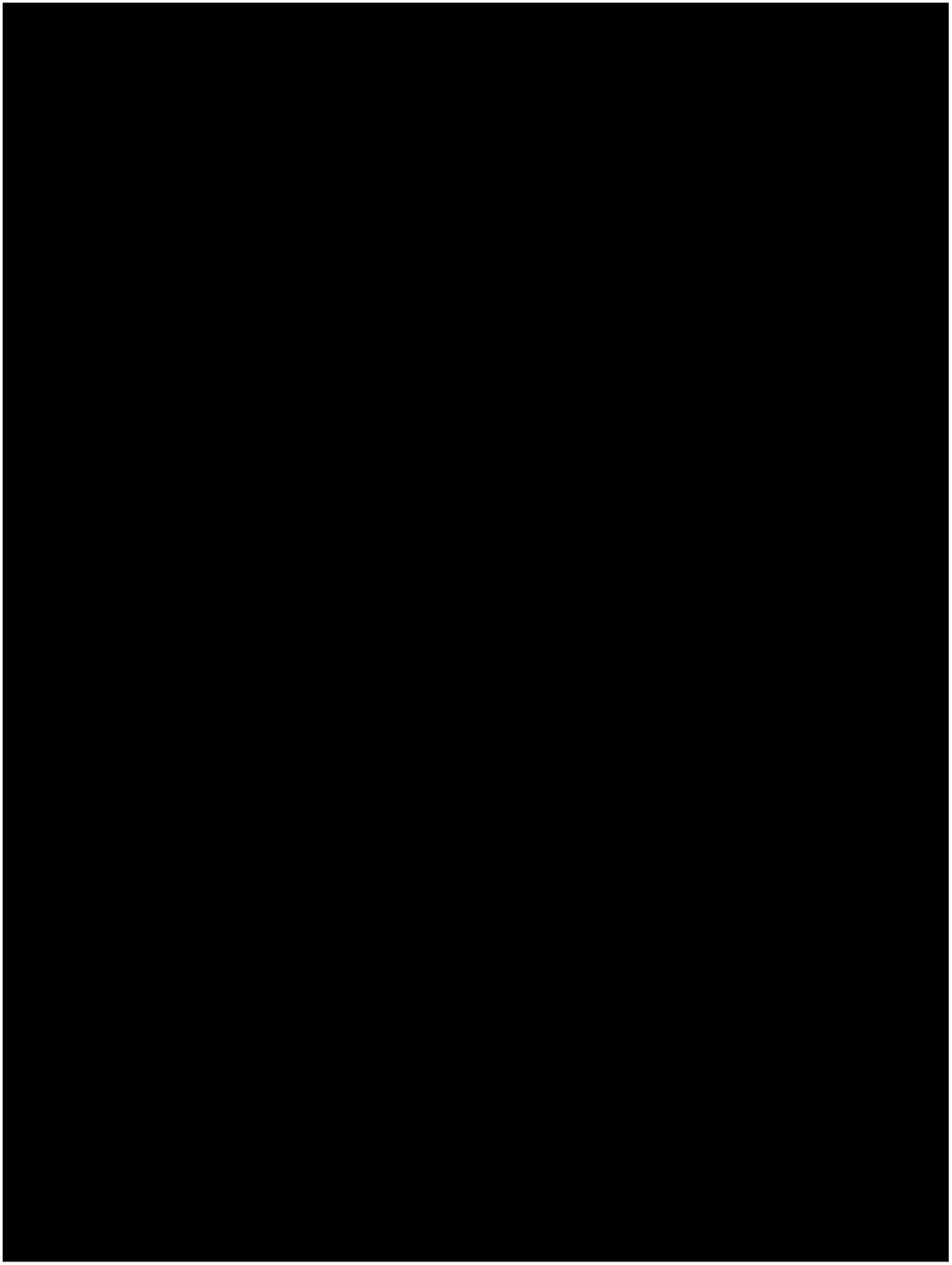

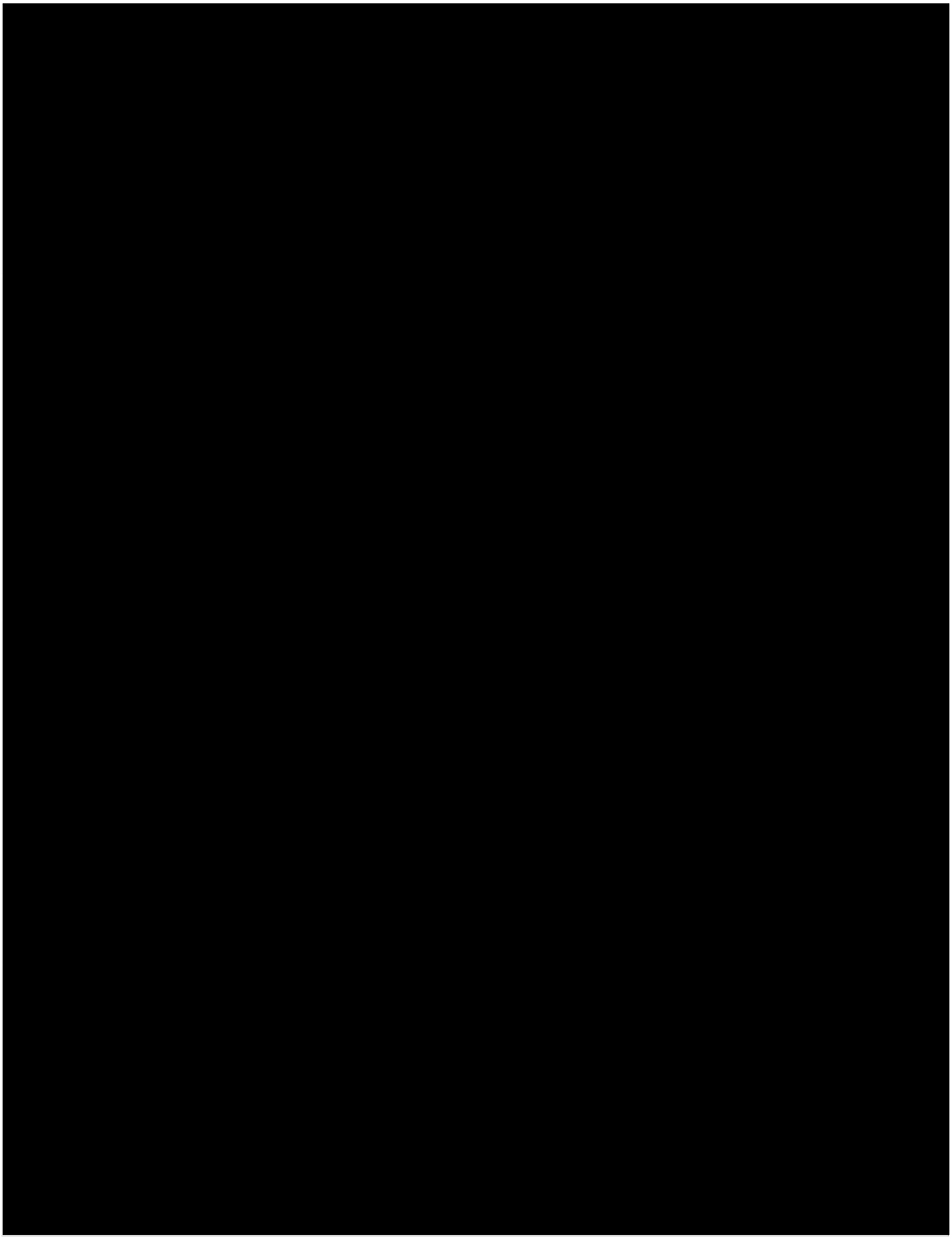

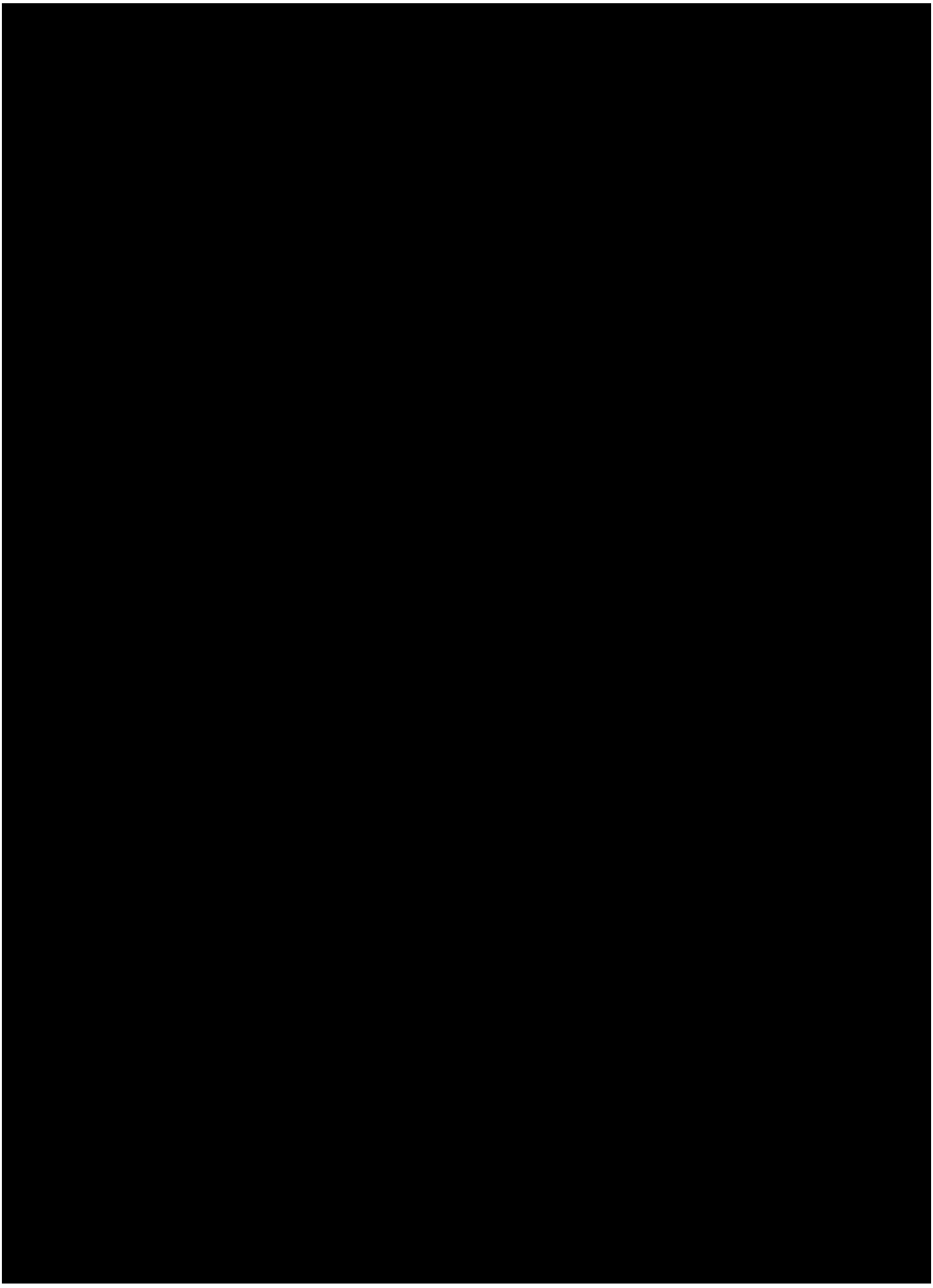

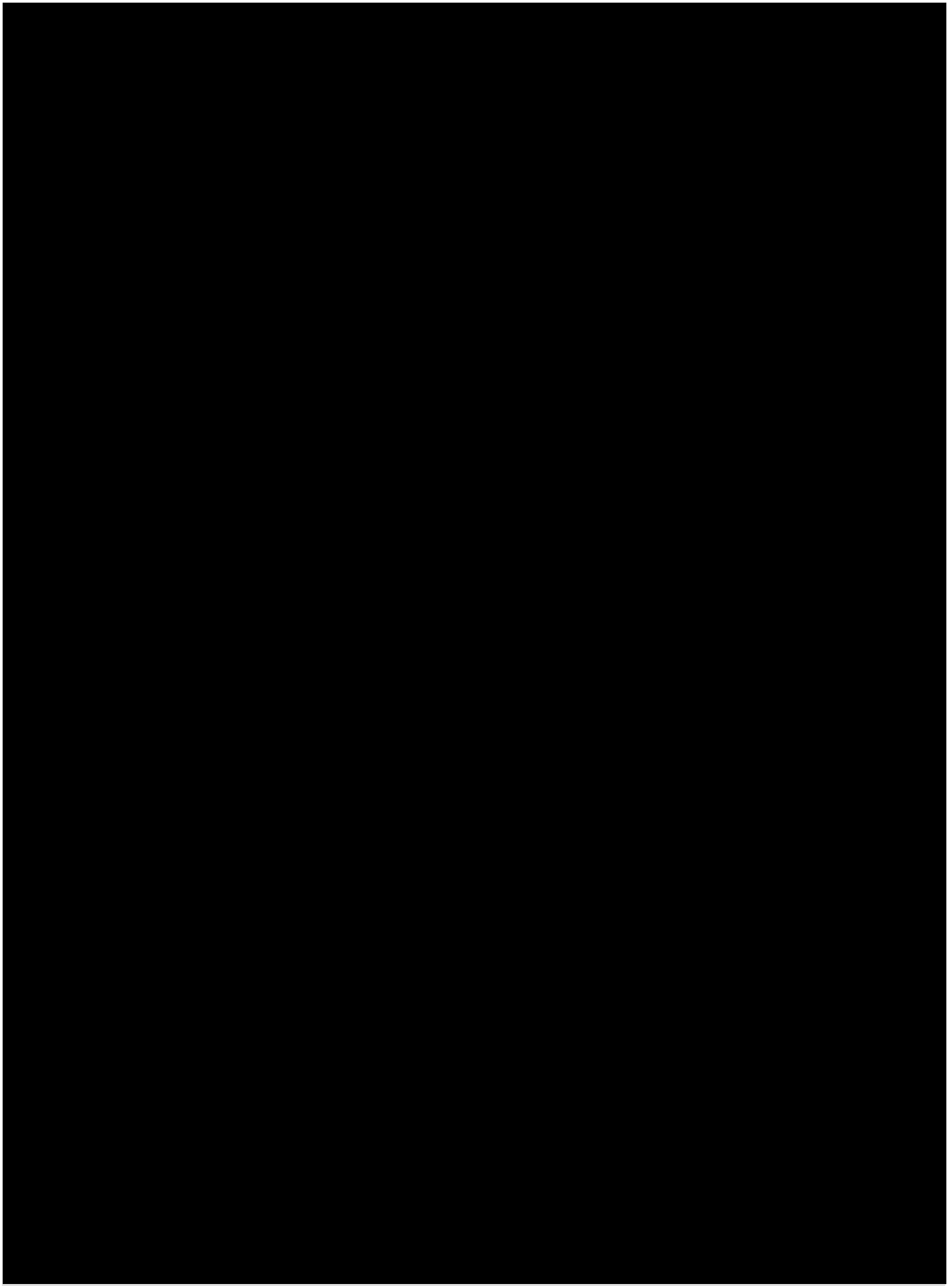

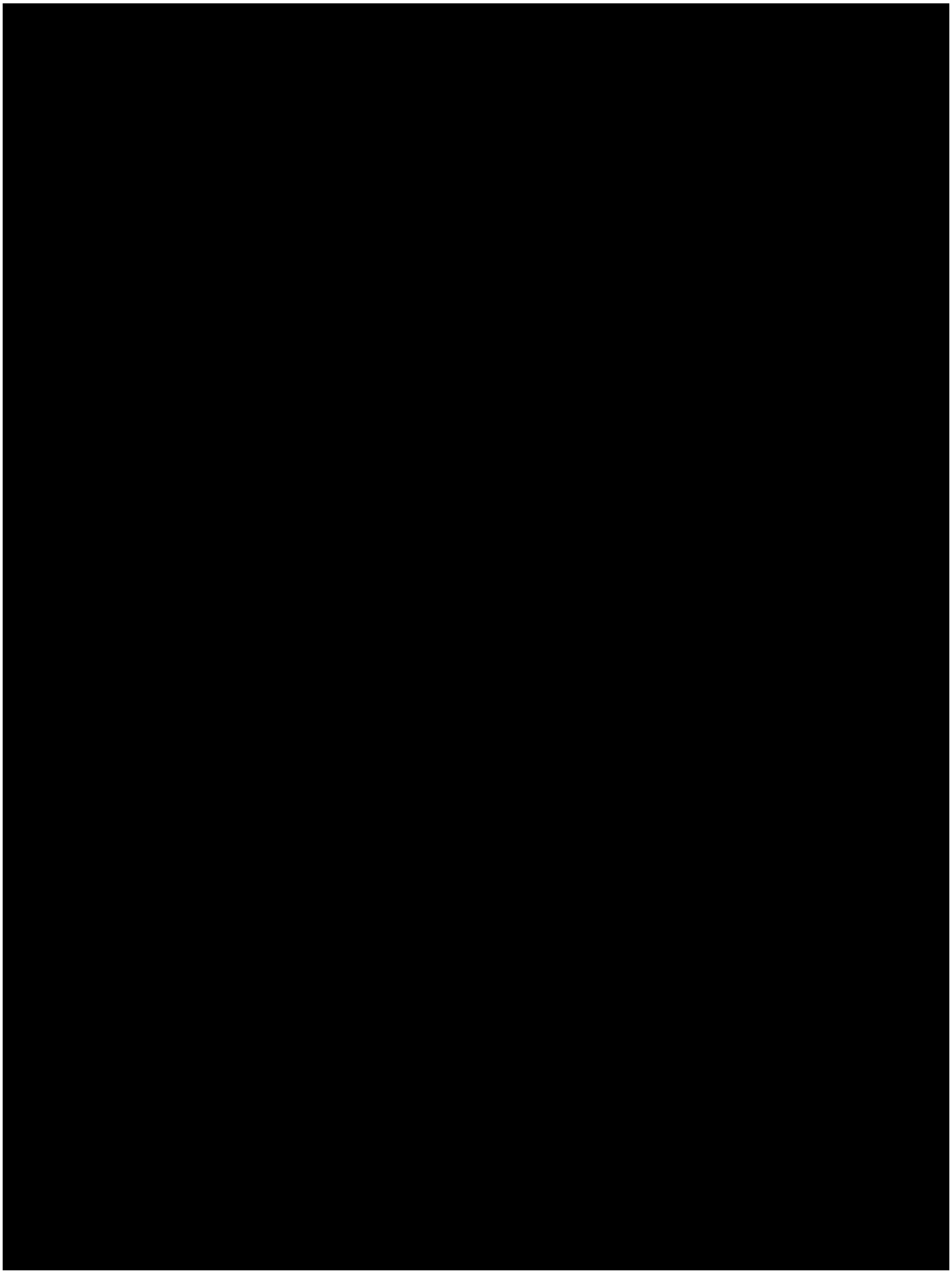

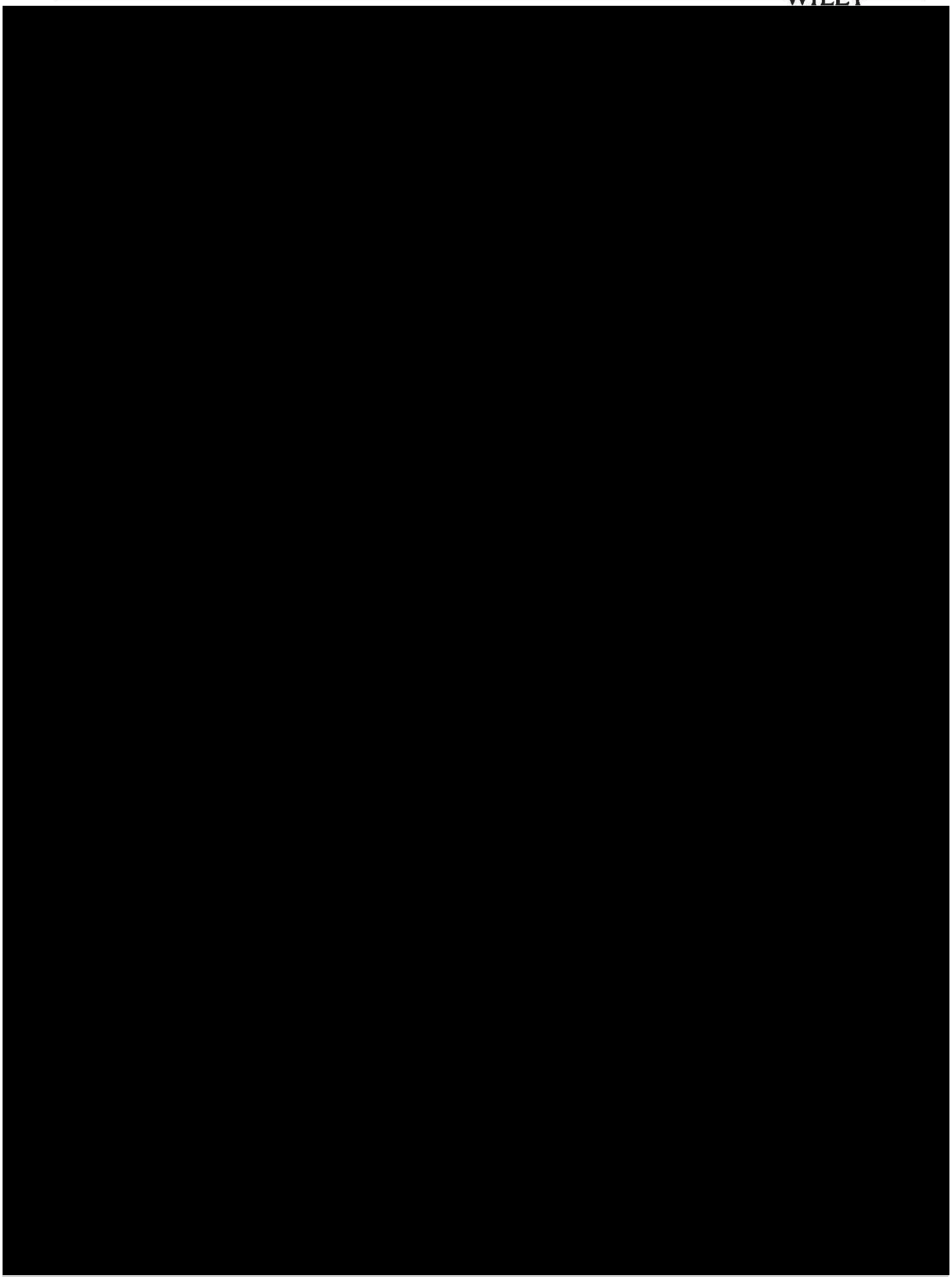

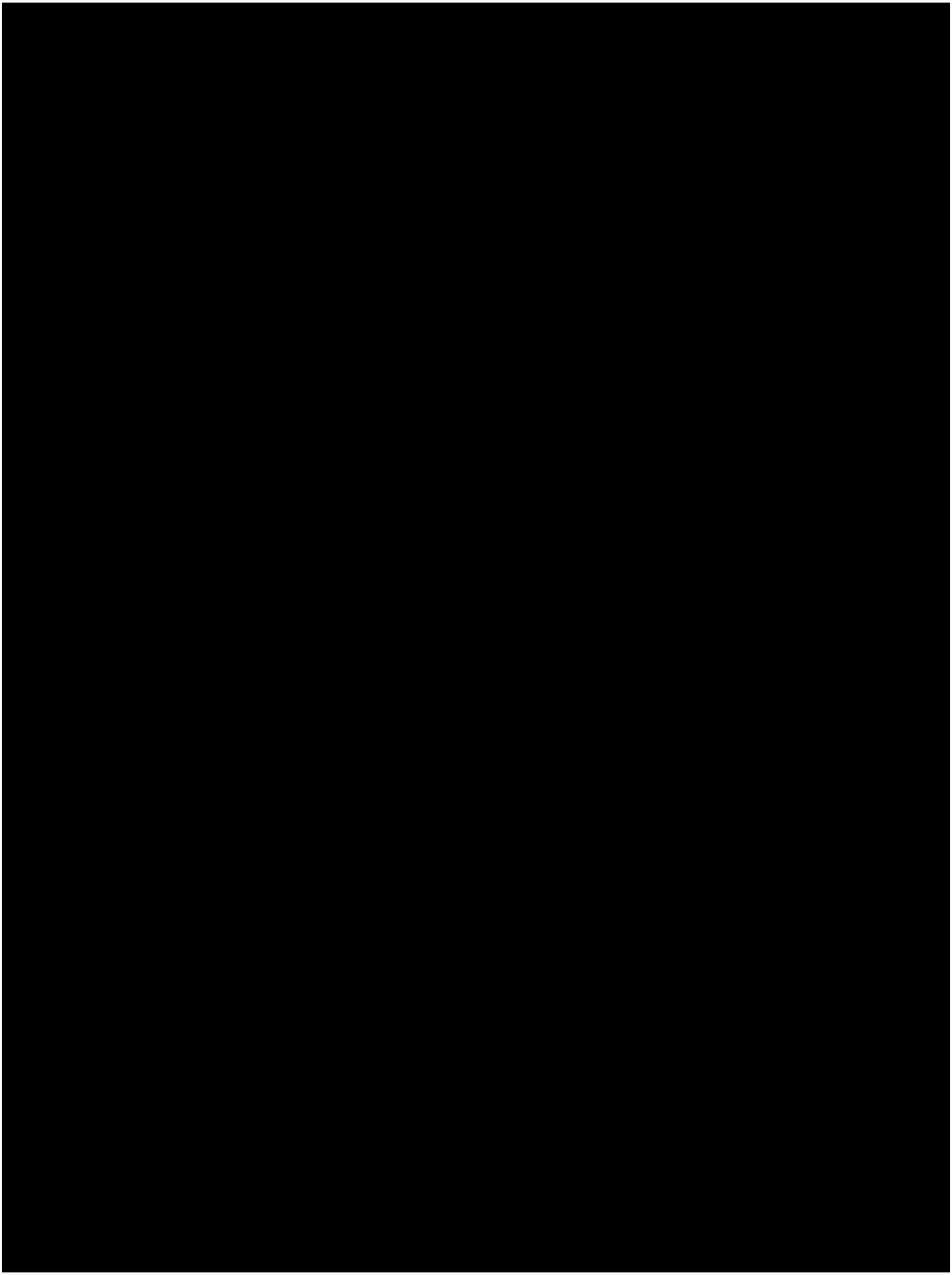

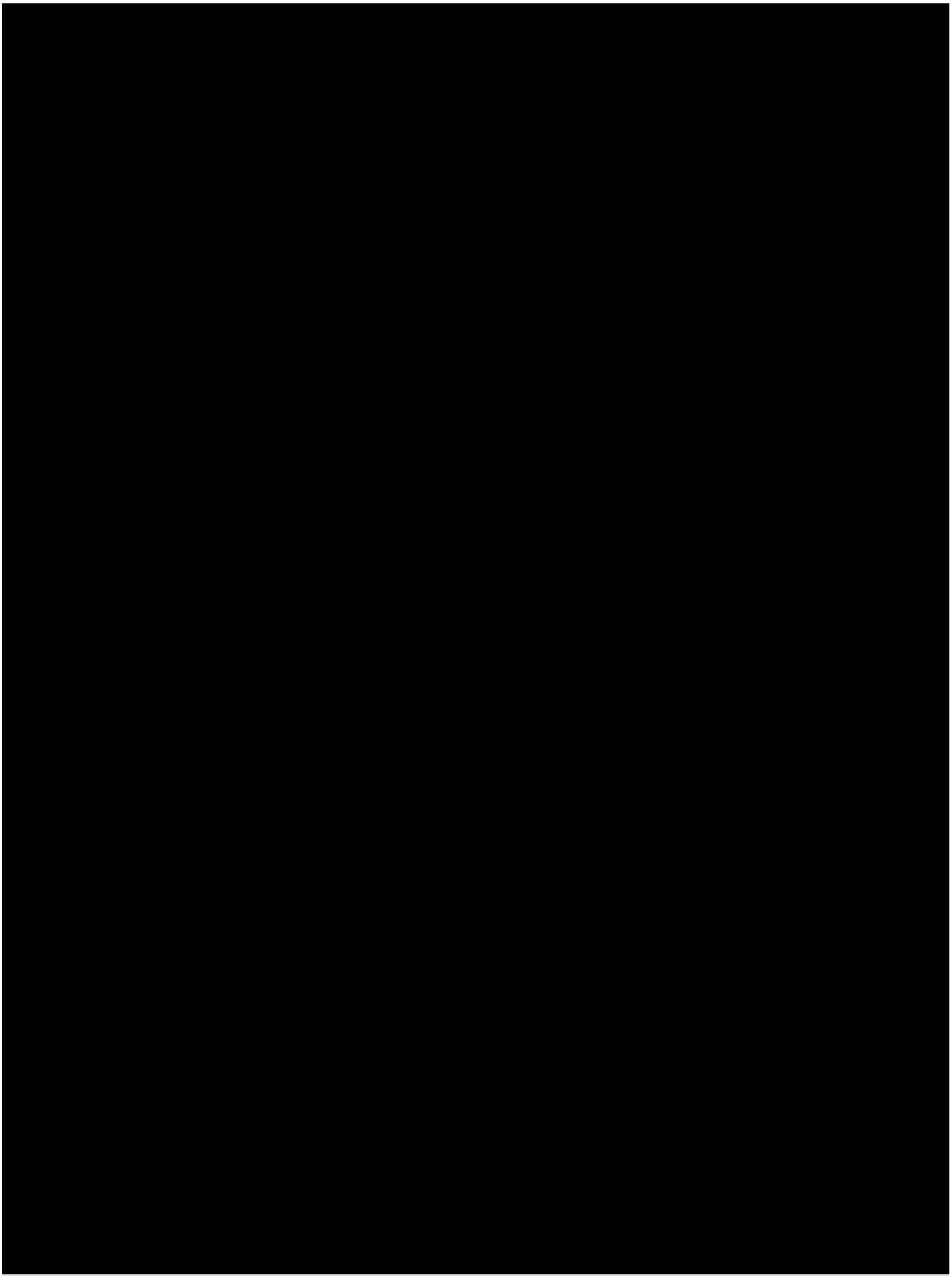

How to cite this article: Jafari SAH, Kwok KCS, Safaei F, Kosasih B, Zhao M. Aerodynamic analysis of a stator-augmented linear cascade wind turbine. *Wind Energy*. 2019;1–16. https://doi.org/10.1002/we.2346

Appendix B4

Building Integration of stator-augmented PowerWindow, a Linear Cascade Wind Turbine, Jafari SAH, Hassanli S, Kwok KCS, Safaei F, Kosasih B, Zhao M, *Journal of Energy Science & Engineering*, 2019; 00: 1-18.

https://doi.org/10.1002/ese3.300

Received: 3 November 2018 | Revised: 1 February 2019 | Accepted: 1 February 2019

DOI: 10.1002/ese3.300

RESEARCH ARTICLE

Energy Science & Engineering Open Access

Building integration of stator-augmented PowerWindow, a linear cascade wind turbine

Seyed AmirHosein Jafari[1] | **Sina Hassanli**[1] | **Kenny Kwok**[2] | **Farzad Safaei**[3] | **Buyung Kosasih**[4] | **Ming Zhao**[5]

[1]Center for Infrastructure Engineering, Western Sydney University, Sydney, New South Wales, Australia

[2]School of Civil Engineering, The University of Sydney, Sydney, New South Wales, Australia

[3]School of Electrical, Computer and Telecommunications Engineering, University of Wollongong, Wollongong, New South Wales, Australia

[4]School of Mechanical, Materials and Mechatronic Engineering, University of Wollongong, Wollongong, New South Wales, Australia

[5]School of Engineering, Western Sydney University, Kingswood, New South Wales, Australia

Correspondence
Seyed Amir Hosein Jafari, Center for Infrastructure Engineering, Western Sydney University, Sydney, NSW, Australia.
Email: S.jafari@westernsydney.edu.au

Abstract

This study investigates power generation capacity of stator-augmented PowerWindow, a linear cascade wind turbine, when installed in through-building openings of a tall building. By employing a new approach, referred to as equivalent momentum sink method, the flow characteristics of the ducted flow, such as its pressure, velocity, and turbulence intensity are predicted when subjected to different wind directions in presence of a wind turbine. This study shows that a properly designed layout maintains the velocity in the through-building openings for a wide range of wind directions and enhances the power generation by 50%-80% in comparison with the free-stream wind turbine installed at the same elevation. This study also compares the power generation of stator-augmented PowerWindow with a conventional horizontal axis wind turbine, Ampair 300, installed in the same through-building openings. The results show that the power generation of the ducted stator-augmented PowerWindow is close to that of the ducted Ampair 300 in certain wind directions. However, it can also effectively generate power at those wind directions that the ducted Ampair 300 is unable to operate. The analysis shows that this advantage significantly increases the annual power generation probability of the building-integrated stator-augmented PowerWindow. As a case study, it is shown that by embedding four through-building openings integrated with stator-augmented PowerWindow in a tall building in Sydney area, a portion (0.55-8.07 KW) of the electricity consumption of the building facilities can be supplied 72% of times.

KEYWORDS

Ampair 300, building-integrated wind turbine, equivalent momentum sink method, incident wind angle, linear cascade wind turbine, PowerWindow, stator-augmented

1 | INTRODUCTION

Installation of small wind turbines on buildings can potentially generate a part of the energy demand in cities.[1,2] One of the advantages of the application of wind turbines in urban environment is the power generation at the point of use, and the reduction of the energy loss and cost of power distribution network.[3] Studies have shown that the performance of urban wind turbines strongly depends on the type and the location of the turbines. For example, horizontal axis wind turbines

(HAWT) have better performance in flat-terrain applications, whereas vertical axis wind turbines VAWT show superior performance in high-density building environments.[4] Flow characteristics in urban area are most often dominated by the boundary layer which is characterized by unsteady turbulent flow passing over buildings and structures. Figure 1 shows the development of the surface boundary layer in an urban, suburban, and open country terrain. The boundary layer development in urban area is known to be the least well-developed. Wind turbines are generally operating in relatively low average wind speeds in urban areas.[5] Suitable locations in and around buildings currently being used for integrating wind turbine systems can be categorized into four groups: in between two buildings; inside a through-building opening; mounted on the roof; and integrated into the façade of a building.

Smaller wind turbines are usually mounted on the roofs and on the corners of buildings.[6] Abohela et al[7] have investigated the effect of roof shape, wind direction, building height and urban configuration on energy yield and the positioning of roof mounted wind turbines. This analysis has shown that the positioning of a roof mounted wind turbine, for a particular roof shape, can enhance the energy harvesting from the acceleration of the wind above the building. Integrating a wind turbine system to the skin of buildings is also a possibility. It has been shown that by using double skin façade for wind energy harvesting, the free-stream wind speed can be amplified up to a maximum of 1.8 times inside the corridors of the double skin façade.[3,8,9]

Although the roughness of the terrain in urban environments can reduce the velocity and increase turbulence of the flow compared to open spaces, it has been reported that mounting turbines at high elevations on buildings may provide a perfect opportunity for onsite wind power harvesting.[10] The application of through-building openings for wind energy harvesting was investigated for Pearl River Tower[2] which was then extended by accommodating a site-specific local wind climate data. The results indicated that power generation was improved particularly at locations where the average wind speed was lower and wind was more turbulent.

Dannecker and Grant[11] developed a prototype of a building-mounted ducted wind turbine. They also conducted a series of wind tunnel and numerical tests to evaluate pressure and velocity for different duct configurations. These tests achieved velocity enhancements up to a factor of 1.3 for a wide range of incident wind angles up to ±60°. Grant and Kelly[12] developed a mathematical model by taking into account the pressure drop as a result of the presence of a wind turbine to predict the power output. The annual energy budget of the same wind turbine system was assessed by Grant et al[13] and it was concluded that retro-fitting ducted wind turbines into existing buildings has great potential for efficient harvesting of wind energy. By conducting a series of wind tunnel tests and CFD simulations, Chong et al[14] studied the performance of a Sistan wind turbine with an augmented guide vane as part of an integrated device for renewable energy harvesting in high-rise buildings. They concluded that the Power Augmentation Guide Vane can increase the rotational speed, torque and power output of a Sistan rotor by a factor of 1.75, 2.88, and 5.80, respectively. More recently, Krishnan and Paraschivoiu[15] studied the optimization of the power coefficient of a building-mounted diffusor-augmented vertical axis wind turbine. They established that a performance enhancement factor of 2.5 could be achieved when the shroud was integrated with the wind turbine."

A properly designed through-building opening has more reliable flow characteristics because: (a) it channels the flow within a wide range of incident angles and makes it almost unidirectional; (b) it acts similar to a high-pass turbulence filter and blocks the low frequency turbulence; and (c) the confined area of opening limits high-pass turbulence intensity, compared with the outside free-stream flow. Therefore, through-building opening has been chosen as the installation location for the selected wind turbines in this study.

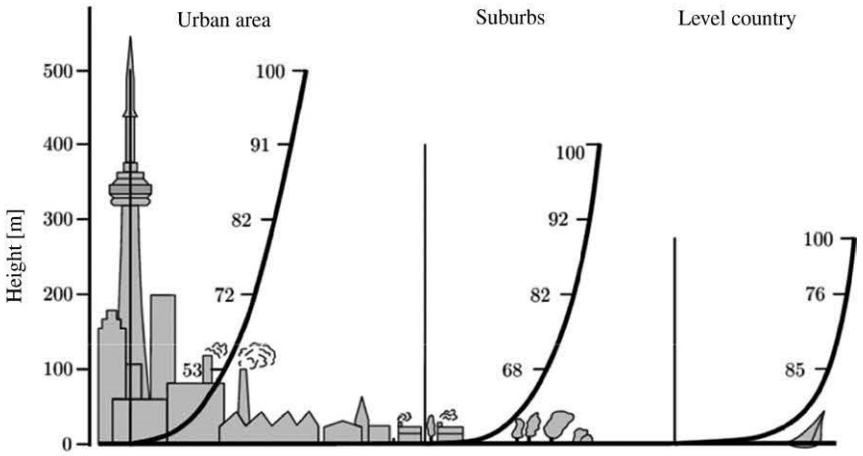

FIGURE 1 Development of surface boundary layer in an urban, suburban and country terrain[5]

This study aims to investigate the power generation of a linear cascade wind turbine (LCWT) integrated with through-building openings. LCWTs are a new generation of wind turbines. Unlike the conventional HAWTs and VAWTs, the blades of LCWTs do not rotate around the rotor axis but move translationally in a direction perpendicular to the approach wind direction. PowerWindow,[16,17] shown in Figure 2A, is a compact modular LCWT which can easily fit into any designated area in a building. Previous study has shown that PowerWindow has a greater performance in a ducted area compared with free-stream condition.[18] Stator-augmented PowerWindow is an improved version of this LCWT. In this configuration as shown in Figure 2B, stator vanes are attached to the device. The stator vanes control the flow direction on the blades by (a) decreasing the undesirable axial force on the blades; (b) enhancing its power generation by increasing the vertical force on the blades; and (c) enabling the device to keep its operational direction when subjected to bi-directional approach wind (SAH Jafari, KCS Kwok, F Safaei, B Kosasih, M Zhao, 2018, Under review). This LCWT is also capable of generating electricity when the ratio of blade speed to wind speed (referred to as the blade speed ratio, λ) is quite low. These characteristics make stator-augmented PowerWindow a suitable and promising wind turbine to be integrated inside through-building openings.

This study also aims to compare the power generation of the selected LCWT with a conventional HAWT, referred to as Ampair 300, when both the wind turbines are integrated with the same through-building opening. The flow characteristics change inside the through-building opening once the turbine is installed. By capturing some momentum from the flow, the ducted turbine increases pressure gradient and reduces the mean velocity across the opening. Therefore, for power generation analysis of the turbine(s), this study develops a method capable of estimating the influence of the turbine(s) on the flow characteristics inside the openings without explicitly modeling them. By replacing the actual wind turbines with an equivalent momentum sink (EMS), this method estimates velocity, pressure gradient, and turbulence intensity of the approach wind in the presence of wind turbine(s) in the through-building openings.

2 | METHODOLOGY

Calculating power generation of a building-integrated wind turbine is analytically difficult because of the unpredictable

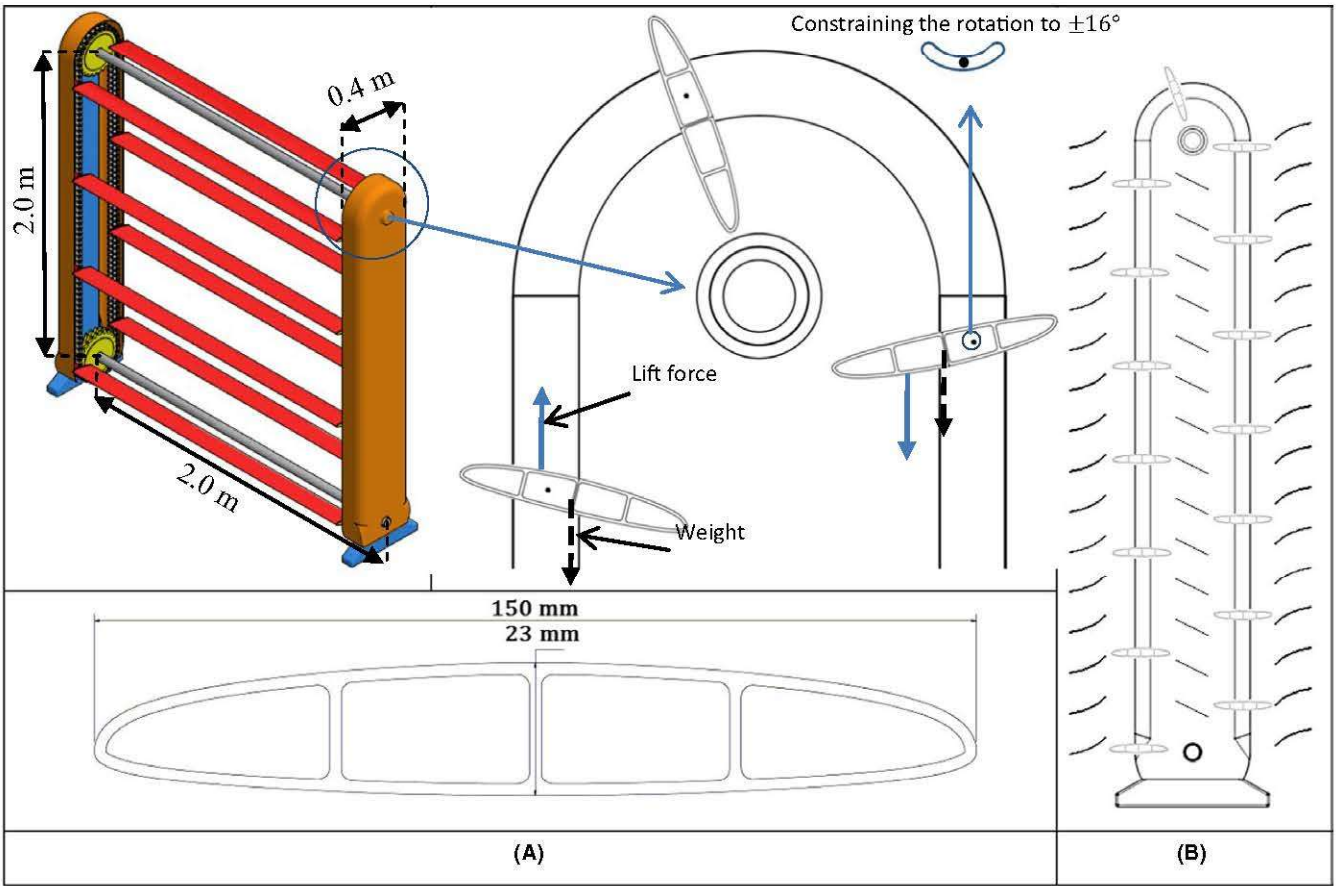

FIGURE 2 A, Sketch of the PowerWindow prototype, its blade profile, and blades rotation mechanism at the top; B, Sketch of the stator-augmented PowerWindow from side view.

interactions between the building and the approach wind. Computational fluid dynamic (CFD) simulations can be an approach for this purpose. However, this would also be computationally expensive due to three reasons: (a) a building alone needs very fine and smooth boundary layer mesh on its surfaces, which would demand a massive mesh with numerous (usually millions of) elements in a 3D domain; (b) each turbine needs a combination of very fine structured and unstructured mesh around it and along its upstream and downstream path; and (c) once the turbine is installed in the through-building opening, it creates velocity reduction and pressure gradient along the opening, which depend on the operating λ of the turbine and is itself unknown. As a result, massive trial and error processes including different series of iterations are needed to be undertaken in order to find the operating λ of the turbine, pressure gradient, and velocity reduction in the through-building opening.

In order to reduce the computation time, two approaches have recently been used for investigating the flow characteristics of a wind farm with several wind turbines. First one is based on the virtual blade model (VBM) of the commercial solver ANSYS FLUENT, in which a 3D Reynolds-averaged Navier-Stokes (RANS) calculation of the flow field is carried out for the outer domain, while the effect of the rotating blades on the fluid is simulated through a body force, acting inside a disk of fluid with an area equal to the swept area of the turbine.[19] The second one is based on an actuator disk model (ADM), in which the turbine presence is modeled as a sink of momentum, associated to the drag force exerted over it.[20] In many near and far wake calculations, the rotor is represented by an actuator disk acting as a momentum sink.[21] Such a representation circumvents the explicit calculation of the blade boundary layers, reducing computational cost and easing mesh generation.[22]

To analyze wakes of wind turbines at different wind direction, Jiménez et al[23] developed a momentum sink which could guarantee that the extraction of momentum by the whole disk was equal to the one predicted by the actuator disk theory. They compared the wake deflection and trajectories of a simple analytical model with experimental results. The results showed satisfactory agreement between the experiments and the analytical model. Jimenez et al[24,25] proposed a simplified large eddy simulation (LES) model to simulate the turbulent flow in the wake of a wind turbine. The turbine was simulated by a set of local sinks of momentum distributed across the rotor disk, without reproducing the blade details. The turbulence characteristics, at every point of the computational domain were obtained and found to be in good agreement with experimental results. Those results indicated that the LES model, with the simplified momentum sink approach to simulate the rotor, was a very useful tool to simulate real turbulent characteristics in wakes[24,25]

Therefore, by adopting a momentum sink of the drag force that the selected wind turbines exert on the ducted flow, this study develops a method, referred to as equivalent momentum sink (EMS) method, capable of estimating the flow characteristics and the power generation of a wind turbine installed in a through-building opening without generating a massive mesh and undertaking trial and error processes.

When a wind turbine is installed in a through-building opening, it extracts some momentum out of the ducted flow and converts that into electrical energy via the generator. By decreasing the momentum in the control volume housing the wind turbine(s), pressure of the ducted flow drops from the inlet to the outlet of the volume along the flow direction. This momentum extraction cannot happen unless the velocity of the ducted flow is reduced compared to a situation when no wind turbine is installed. Installing the wind turbine(s) in the through-building opening creates an adverse pressure gradient at the inlet of the opening, which by decreasing the inlet velocity, increases the static pressure at the inlet. A higher static pressure at the inlet would result in a higher pressure drop along the duct. A higher power generation demands a higher momentum extraction, a greater pressure drop and hence a greater velocity reduction in the through-building opening. Therefore, ignoring other effects of the wind turbine on the ducted flow characteristics such as turbulent kinetic energy, the control volume housing the ducted turbine(s) can be considered as a momentum sink which extracts momentum from the ducted flow.

FLUENT allows the momentum sink to be modeled as a simple homogeneous porous media, is dependent on the velocity magnitude. The sink is composed of two parts: (a) a viscous loss term and (b) an inertial loss term. Viscous loss or Darcy is the first term on the right-hand side of Equation 1 and inertial loss is the second term on the right-hand side of this equation:

$$S_i = -\left(\sum_{j=1}^{3} D_{ij}\mu v_j + \sum_{j=1}^{3} C_{ij}\frac{1}{2}\rho|v|v_j\right), \quad (1)$$

where S_i is the source term for the ith (x, y, or z) momentum equation, μ and ρ are the viscosity and density of air, $|v|$ is the magnitude of the velocity and D and C are prescribed matrices. The ratio of the inertial force to the viscous forces of the fluid is known as the Reynolds number (Re) and can be estimated using the following equation:

$$\mathrm{Re} = \frac{\rho v L}{\mu}, \quad (2)$$

where L is the characteristic of linear dimension.

Re of the LCWT within the target range of inlet wind velocity: 4 m/s $< V <$ 12 m/s was $3.6 \times 10^4 < \mathrm{Re} < 1.1 \times 10^5$ based on flow over a flat plate (blade surface). As a result, the inertial force is much greater than the viscous forces in this study and the viscous forces are negligible.

When a wind turbine is operating in the duct, it exerts a reacting force on the ducted flow opposite to the flow direction, referred to as thrust. In order to find D and C, the thrust of the turbine should be measured at its operating blade speed at different velocities and divided by the ducted cross-section area. The resultant pressure drop vs the ducted flow velocities creates a parabolic curve. D and C values should be selected, so that equation 1 matches the resultant curve. This equivalent momentum sink contributes to the pressure drop in the porous cell, creating a pressure drop equal to that created by the ducted wind turbine(s). The pressure drops (due to the viscous loss) that FLUENT computes in each of the three coordinate directions within the porous region are as follows:

$$\Delta p_x = \sum_{j=1}^{3} \frac{\mu}{\alpha_{ij}} v_j \Delta n_x \tag{3}$$

$$\Delta p_y = \sum_{j=1}^{3} \frac{\mu}{\alpha_{yj}} v_j \Delta n_y \tag{4}$$

$$\Delta p_z = \sum_{j=1}^{3} \frac{\mu}{\alpha_{zj}} v_j \Delta n_z, \tag{5}$$

where $\frac{1}{\alpha_{ij}}$ are the entries in the matrix D in Equation 1, v_j are the velocity components in the x, y, and z directions, and Δn_x, Δn_y, and Δn_z are the actual thickness of the porous region in the x, y, and z directions.

This study replaces the explicit model of the LCWT and HAWT with an equivalent momentum sink (EMS) in the through-building openings, the description of which are presented in the following section. Then, the CFD model calculates the pressure and ducted flow velocity in the presence of the relevant momentum sink. Eventually, using the explicit model of the ducted LCWT and ducted HAWT, by simulating the ducted wind turbines subjected to the resulted ducted flow characteristics, their power generation can be calculated accurately. The user-defined function (UDF) codes which apply the relevant EMSs to the CFD simulations are shown in the Appendix.

2.1 | Through-building openings

A building model with a square plan and the dimensions of 96 m × 32 m × 32 m is considered for this study (Figure 3). Two through-building openings are created at a representative height of 3/4H at two ends of building breadth, where "H" refers to the building height. The cross-section area of the through-building openings is 4 × 4 m^2. The 1/80 scaled model of the building is tested at the wind tunnel facility of the University of Sydney (Figure 4A) mainly to validate the CFD results.

Prior to applying the selected velocity profiles to the inlet of the CFD model, a series of experimental tests were undertaken to verify the accuracy of the CFD simulations. A number of velocity measurements were acquired from the incident wind angle of zero to 60° with an interval of 15°, using a Cobra probe with the frequency response of 2 kHz. Cobra probe is a multi-hole pressure probe that resolves the three components of velocity and local static pressure. The setup configuration for Cobra probe measurement is shown in Figure 4A. The tip of the probe would be located at the center of the corridor and facing toward the free-steam wind.

The PIV results have been compared with the Cobra probe measurements in the experimental test and shown that the results have acceptable agreement with error bound of less than 7%.[28] It was also found that Cobra probe showed more accurate result when the flow angle to the tip of the probe was within ±45°. Considering the flow within the through-building opening, the flow angles relative to the cobra probe was far less than ±45°.[28] The data are sampled at a frequency of 4 kHz for the duration of 180 seconds. The average velocity of the measured data at the wind tunnel and computed by the CFD simulations for different wind directions is shown in Figure 4B. As can be seen, although the average velocities predicted by the CFD simulations are slightly greater than the Cobra probe measurements, the discrepancy remains below 10% for all measured wind directions, which is an acceptable range in practice. The main reason of the slight discrepancy between the experimental and CFD results might be the simplification of the CFD model such as ignoring the roughness of the inner walls of the through-building opening and solving the simulation in steady-state condition.

2.2 | EMS for the LCWT

In order to develop the EMS for the selected LCWT (stator-augmented PowerWindow), CFD model of the LCWT developed in a previous study[17] has been scaled up by two times and located in a 4 m × 4 m × 32 m duct. As explained in previous study[16] PowerWindow is a scalable and modular LCWT. Therefore, it would be possible to scale it up, so that it can tightly fit into the through-building opening. In this part of study, the inlet velocity of the duct has been gradually increased from 3 to 15 m/s regardless of the pressure gradient needed along the duct. At each ducted flow velocity, power generation of the LCWT is calculated and the pressure drop it creates along the duct is recorded. The thrust force which the EMS exerts on the ducted flow at each velocity can be calculated by multiplying the duct area by the pressure gradient created along the duct.

The operating λ needs to be known to find the power generation of the LCWT at each ducted flow velocity using the following equation:

$$P = \lambda V F_v, \tag{6}$$

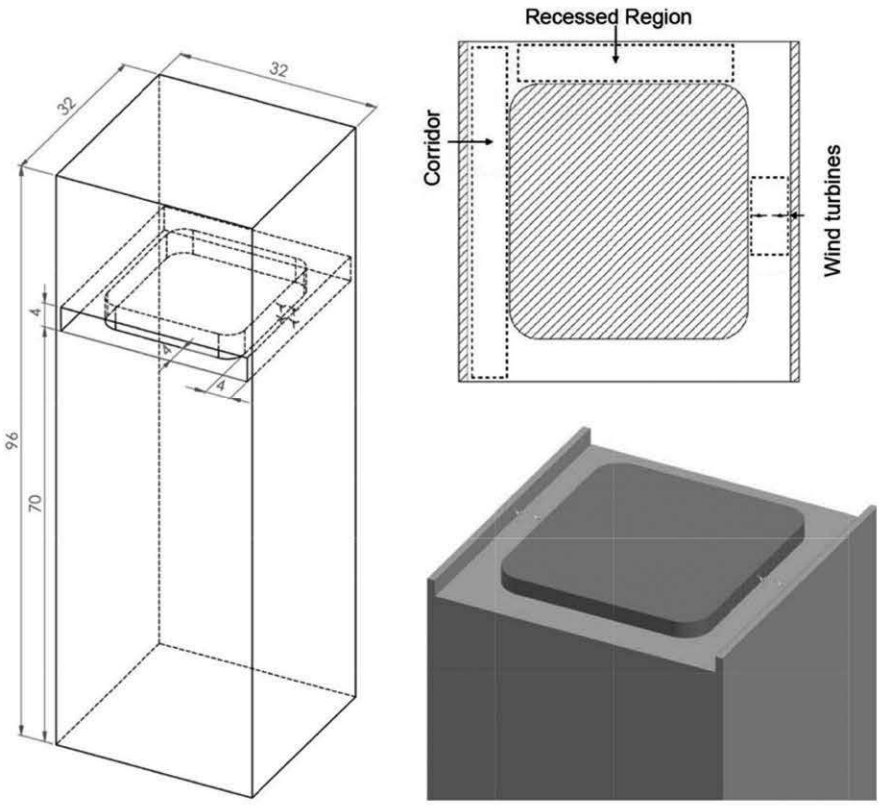

FIGURE 3 Dimensions of the building and schematic view of the wind turbines in the through-building openings[26,27]

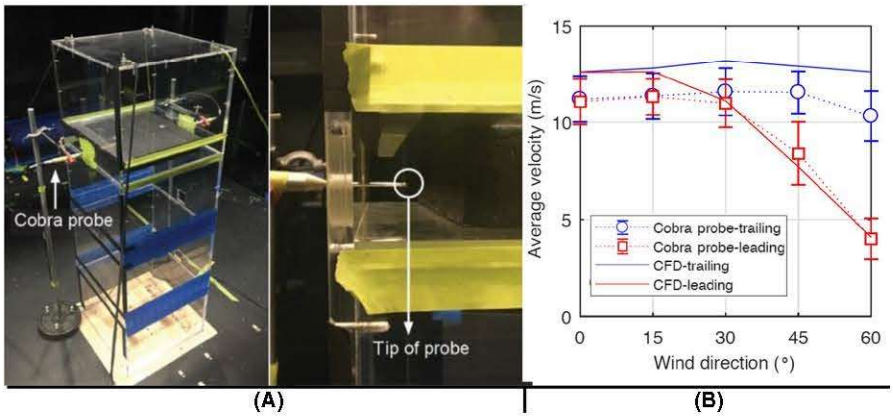

FIGURE 4 A, 1/80 scaled model of the building in the wind tunnel with setup configuration of Cobra probe inside the through-building opening; and B, The average velocity in the through-building opening measured by Cobra probe and computed by CFD simulations[28]

where λ is the ratio of the blade speed to the wind speed and V is the velocity along the duct. Therefore, multiplying λ by V gives the absolute speed of the blades. It should be noted that the blades have only vertical velocity when moving up or down in the LCWT. F_v is the vertical aerodynamic force on the entire LCWT blades. Although the vertical aerodynamic force acting on each individual blade changes when moving from the bottom to the top or vice versa, the total vertical aerodynamic force acting on the entire blade assembly can be assumed to be constant, as each blade is taking the place of another one continuously. Therefore, the total power generation of the ducted LCWT can be calculated by multiplying λV by F_v.

Therefore, a series of CFD simulations have been undertaken at each ducted flow velocity with different λs, and coefficient of performance (C_P) has been calculated at each λ. C_P is the ratio of the power generation by a wind turbine to the total wind power passing through the wind turbine's area:

$$C_P = \frac{P}{\frac{1}{2}\rho V^3 A}, \tag{7}$$

where A is the swept area of the turbine.

Ideally, a wind turbine operates at its maximum C_P which would only be possible at the optimum λ. But in practice, the operating λ is usually higher or lower than the optimum value. Nevertheless, in the previous study,[16] comparison between the experimental test undertaken in the wind tunnel and CFD simulation of the original PowerWindow shows that this device operates at a λ close to the optimum value

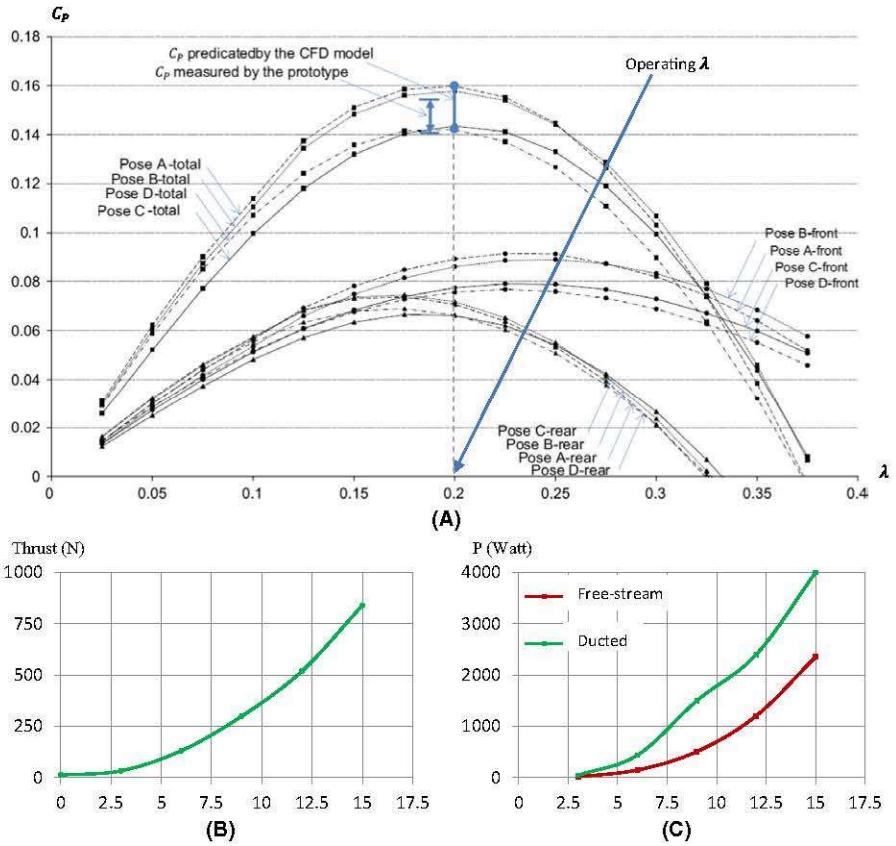

FIGURE 5 A, Operating λ of PowerWindow detected by CFD simulation via calculating the maximum C_P, compared with the operating λ measured in the experimental model;[16] B, The resultant thrust force of the LCWT on the ducted flow; and C, Power generation of the LCWT in the ducted and free-stream conditions

predicted by the CFD simulation. Therefore, this study has used the optimum λ as the operating point in order to calculate the power generation of the LCWT and pressure gradient which it creates along the duct at each ducted flow velocity. However, it should be noted that the efficiency of the generator is not included in the calculation of the power generation. Therefore, the overall C_P would be slightly lower than this.

Figure 5A shows that the operating λ measured in experimental test is very close to the optimum λ predicted by the CFD simulations. Therefore, at every inlet velocity, the optimum (computed) λ is considered as the operational λ. Figure 5B shows the thrust force which the EMS exerts on the ducted flow at each velocity. The process of finding power generation of the stator-augmented PowerWindow has been done once when it is located in the duct and once when it is located in the free-stream condition and the calculated power generations are shown in Figure 5C. As could be expected, power generation of the ducted one is higher than the free-stream one. The reason is further explained in another study.[18]

2.3 | EMS for the HAWT

In order to develop the EMS for the HAWT, CFD model of the device developed in previous study[29] has been located in the same duct. Four HAWTs have been located there to fit the cross-section area. The inlet velocity of the duct has been gradually increased from 4 m/s up to 18 m/s and at each velocity, power generation of the ducted wind turbines are calculated and the pressure gradient they create along the duct is recorded. The thrust force has also been calculated using the similar process as discussed in the previous part.

For finding the power generation of the HAWT at each ducted flow velocity, rotational speed (ω) of the turbine is needed, which is provided by the manufacturer shown in Figure 6A.[30]

$$P = \omega \times \tau, \tag{8}$$

where τ is the resultant torque on the rotor of the HAWT.

Using the operating ω at each wind velocity, CFD simulations have been undertaken at different ducted flow velocities. The power generation of the turbines is calculated and the pressure gradient they create along the duct is recorded. Figure 6B shows the resultant thrust force that all four ducted HAWTs exert on the ducted flow at each velocity. The process of finding power generation of the four HAWTs has been done once when it is located in the duct and once in free-stream condition. Power generations are calculated and shown in Figure 6C. Power generation of four HAWTs using the data provided by the manufacturer is also plotted in Figure 6C to compare with the CFD results, which shows that the CFD results have a good agreement with the manufacturer results.

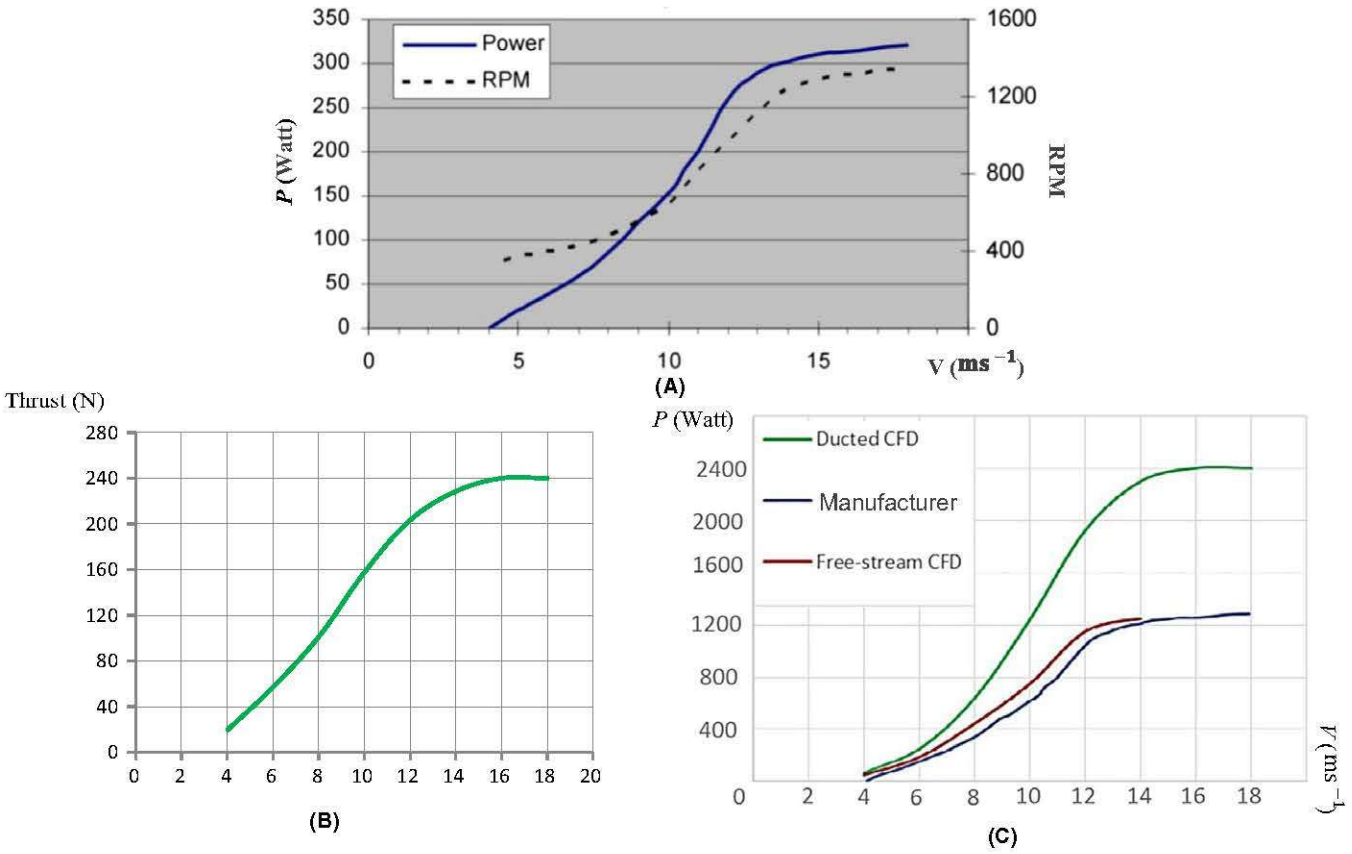

FIGURE 6 A, power generation and rotational speed of Ampair 300 subjected to different approach wind velocities;[30] B, The resultant thrust force that all four HAWTs exert on the ducted flow; and C, Power generation of four ducted and free-stream HAWTs, computed by CFD simulations and using the manufacturer's data

3 | CFD SETUP

As discussed in the methodology section, the ducted flow characteristics need to be investigated in the through-building openings in two phases: (a) when the entire building is subjected to the approach wind and no wind turbine is installed; and (b) when a duct resembling the through-building opening is subjected to the approach wind and the wind turbines are installed. Section 3.1 presents the computational domain enclosing the building with the through-building openings, and Section 3.2 presents computational domain of the through-building opening enclosing the wind turbines.

3.1 | Building computational domain and boundary conditions

The dimensions and boundary conditions of the computational domain enclosing the building are shown in Figure 7A, which are in accordance with the CFD guidelines for flow simulations in urban environment.[31] The building is located in a large domain where it has $3H$ distance from the inlet, $10H$ from the outlet, $1.25H$ from each side and $1.67H$ from the top (to be consistent with the wind tunnel cross-section). The bottom and sides are set to no-slip condition and the top is set to zero shear stress.

At the inlet boundary, a wind profile is imposed in accordance with the mean velocity and turbulent intensity corresponding to an open terrain (TC2) in the Australian Standards AS/NZS 1170.2:2011. As shown in Figure 7B, the velocity is normalized by the velocity magnitude at building height (H) at free-stream (U_{ref}). The outlet is set to outflow condition with zero velocity/turbulent intensity gradient.

The building is located in a cylindrical subdomain, shown in Figure 8A, which can rotate similar to turn table in wind tunnels and enables the inlet flow to approach the building with different incident wind angles (ϕ). As shown in Figure 8B, finer mesh has been generated on and around all the corners and edges of the building especially in those surfaces which are closer to the through-building openings. The EMS is placed at the middle of the through-building openings, instead of the wind turbines. By activating the sink of momentum, the simulations estimate the flow characteristics in the through-building opening in the presence of wind turbine(s) and by deactivating the sink of momentum, the simulations can estimate the flow characteristics of the empty through-building opening. Steady SST $k-\omega$ turbulence model with the SIMPLE scheme for pressure-velocity coupling and second order discretization for

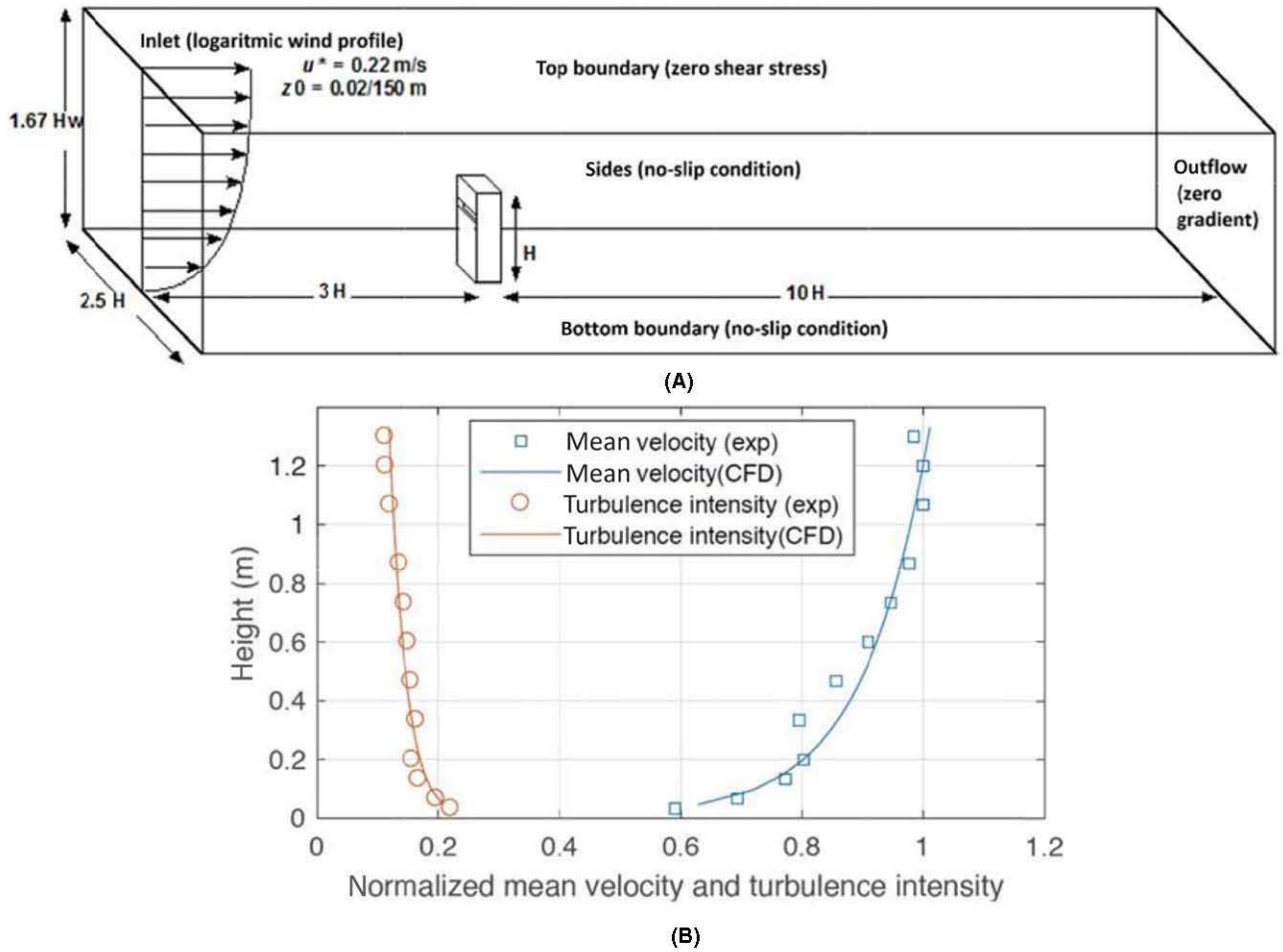

FIGURE 7 A, The CFD domain and boundary conditions; B, Normalized mean velocity and turbulence intensity profiles at the target location in an empty domain[28]

pressure and momentum is considered and the value of y^+ is maintained below 300 on all walls. y^+ is a nondimensional wall distance for a wall-bounded flow which can be calculated by the following equation:

$$y^+ = \frac{u_* y}{\nu}, \tag{9}$$

where u_* is the friction velocity at the nearest wall, y is the distance to the nearest wall, and ν is the local kinematic viscosity of the fluid.

3.2 | Computational domain and boundary conditions of wind turbines

The through-building openings were created at two ends of 3/4*H* of the building's breadth. Each through-building opening is essentially a long duct where the LCWT or the HAWTs are installed in. Dimensions of the duct are 4 m × 4 m × 32 m, and the wind turbine(s) is/are located at the middle as shown in Figure 9A,B. For the HAWTs, using the symmetry boundary condition, one quarter of the corridor housing one single turbine has been built up and extended to the other three quarters. Using Multiple Reference Frame (MRF), the rotor of the HAWTs and front and rear blades of the LCWT are located in a rotating disk and translating frames, respectively. In order to achieve a balance between solution accuracy and calculation time, a combination of structured and unstructured mesh is used in this study. This technique helps to decrease the number of elements while having a high quality mesh around the body.[29] A number of layers with structured rectangular elements are generated around the blades, and this fine mesh region is connected to the outer coarser structured region via unstructured triangular elements. The 3D model of the HAWT and the LCWT contain 1 678 320 and 5 128 740 elements, respectively.

The frame of the hybrid region containing the front and rear blades is selected as moving frames which can move vertically within the domain. The boundaries of the blades are set to moving wall with zero velocity relative to their adjacent cells. As a result, their vertical/rotational velocity would be equal to the MRF-surrounding cells. The inlet boundary condition is changed within the target range. Turbulence intensity of 5% and turbulence viscosity ratio

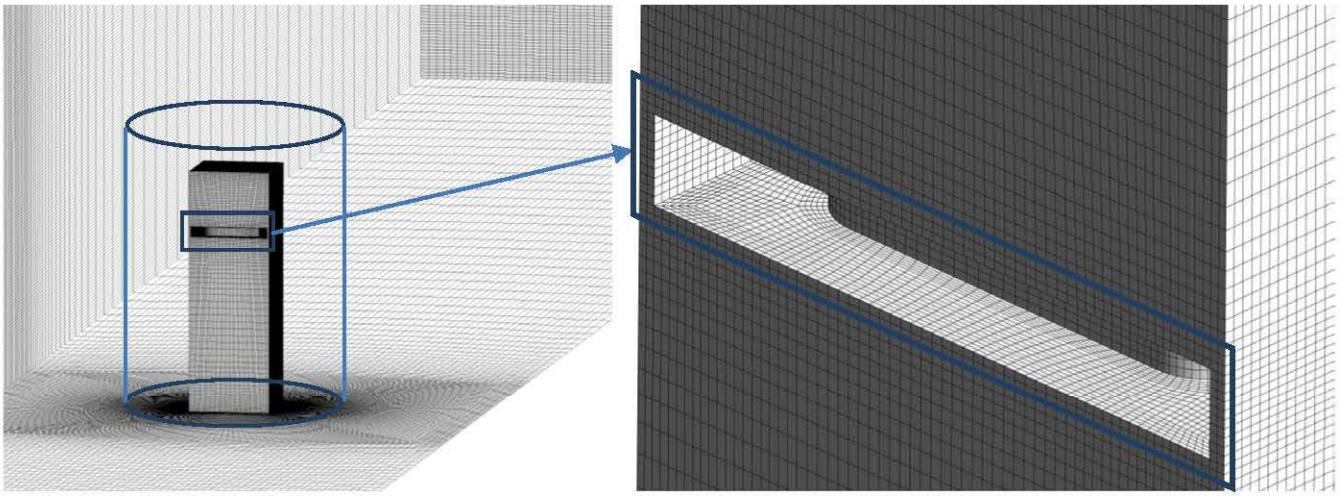

FIGURE 8 A, Cylindrical subdomain containing the building; and B, Fine mesh generated on and the surfaces in and around the through-building openings

(the ratio of turbulent to laminar viscosity) of 10 is set for inlet, and outlet boundary condition is set as outflow. The standard pressure correction method and a first order upwind scheme is used.

The operating λ applied on the rotating disk and the translating frames at each inlet velocity has been identified, as previously discussed in the methodology section. The inlet velocity, the pressure and the turbulent kinetic energy of the through-building opening extracted from the simulations undertaken for the whole building (explained in the previous section) are imposed at the inlet of the duct. Outlet is set as outflow condition. Steady SST $k-\omega$ turbulence model with the SIMPLE scheme for pressure-velocity coupling and second order discretization for pressure and momentum is considered for the simulations. The value of y^+ is maintained below 2 on the blades surfaces of the HAWTs and the LCWT and below 300 on inner duct surfaces.

4 | RESULTS AND DISCUSSION

Using the EMS method and explicit model of the wind turbines in the duct, flow characteristics and power generation have been obtained and presented in the following sections. Section 4.1 presents the effect of the building on the ducted flow in the empty through-building openings. Section 4.2 presents the effect of the LCWT on the ducted flow by installing the synchronized EMS in the through-building openings. And considering the mutual effects of the building and the wind turbines on the ducted flow in the through-building openings, Section 4.3 presents and compares the total power generation of the LCWT and the HAWTs at different approach wind velocities and directions.

4.1 | The effect of the building on the ducted flow

The geometrical parameters of the through-building openings (such as: length, cross-section area, inlet and outlet shape) and the building itself (such as H and ϕ) strongly influence the characteristics of the ducted flow. Therefore, by deactivating the EMS located at the middle of the through-building opening, effect of the mentioned parameters has been investigated on the ducted flow in the absence of HAWTs or LCWT. The velocity contours around the building and inside the through-building openings at $\phi = 0°$ when the free-stream velocity at H is 12 m/s ($U_{ref} = 12$ m/s) and at the 3/4H is 11 m/s ($U_{3/4H} = 11.6$ m/s) and the EMS is deactivated, are shown in Figure 10A,B. These contours indicate that at $\phi = 0°$, the represented through-building opening enhances the velocity. As can be seen in the figures, on the windward side of the building the recessed region has trapped the approach wind which would expect to increase the static pressure there, while the flow detachment at leeward side of the building would expect to decrease the static presser there. The overall effect should result in a high pressure gradient along the through-building openings which has increased the velocity. The pressure contours are presented in Figure 11A. However, the flow characteristics inside and around the building and through-building openings are also strongly dependent on ϕ.

For investigating the effect of ϕ on the ducted flow velocity in the through-building openings, the building model has been rotated by 30° and 60° against the approach wind direction. Figure 11A-C shows the static pressure and resultant velocity contour, in terms of surface pressure coefficient (C_{sp}) and velocity ratio (R_V) in the through-building openings at 0°, 30°, and 60° when $U_{ref} = 12$ m/s and $U_{3/4H} = 11.6$ m/s. C_{sp} shows the ratio of the local static pressure to the free-stream

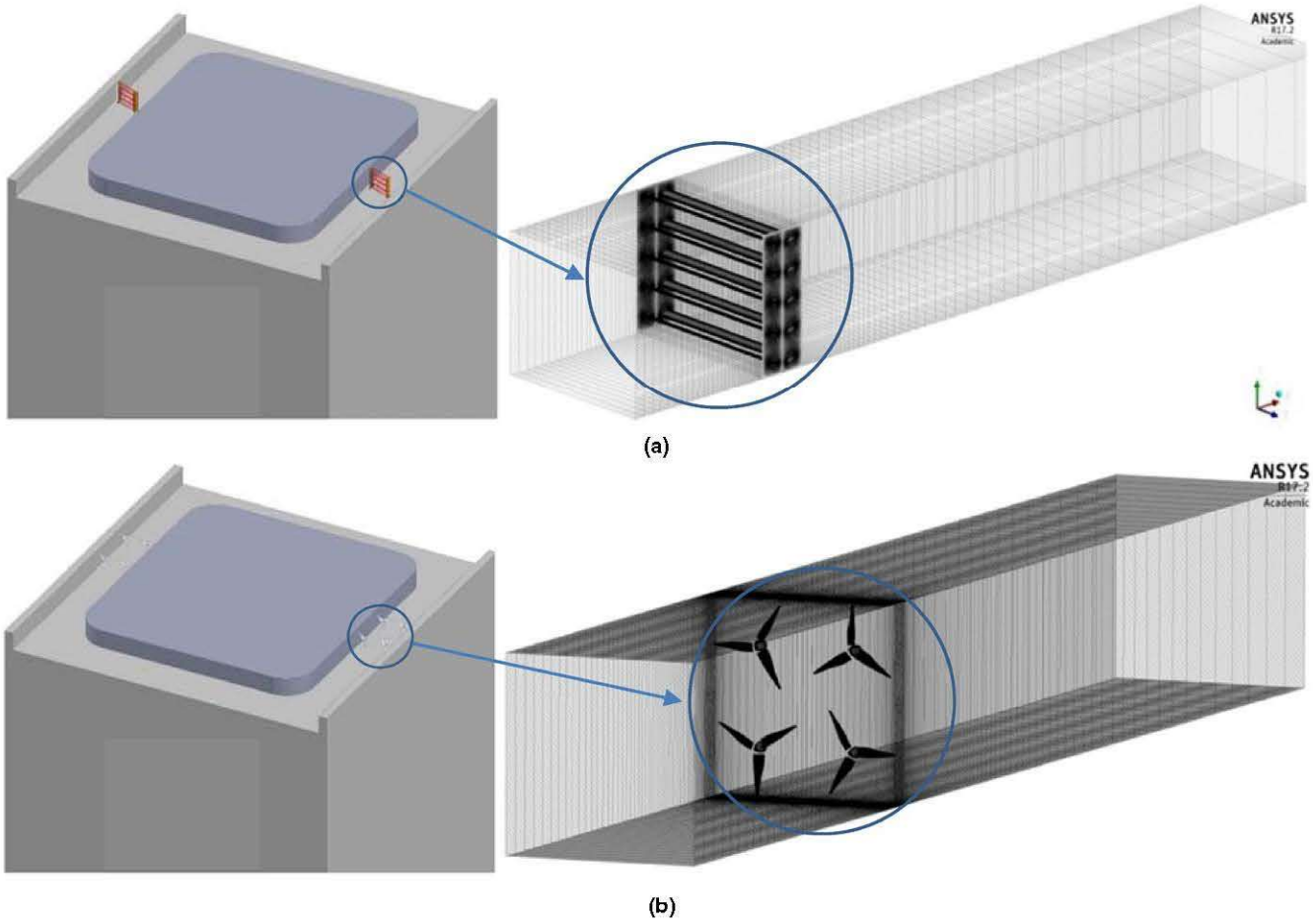

FIGURE 9 Through-building openings replaced by a simple duct containing (A) the LCWT and (B) the HAWTs

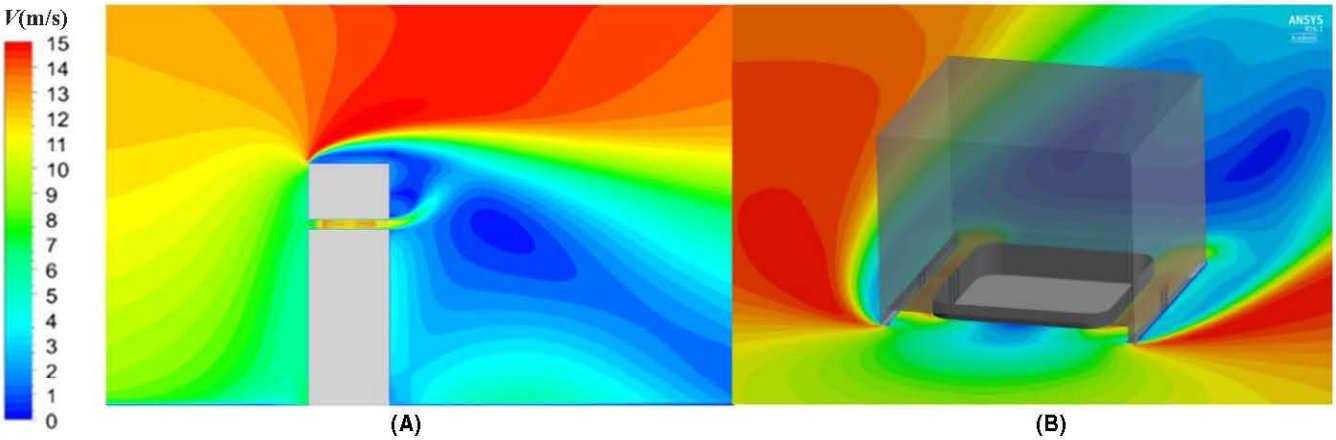

FIGURE 10 (A) Transverse view and (B) isometric close-up view of mean velocity contours around the building and along the through-building openings[27]

dynamic pressure and V_R shows the local velocity to the free-stream velocity:

$$C_{sp} = \frac{P_{local}}{0.5\rho(U_{3/4H})^2} \tag{10}$$

$$V_R = \frac{U_{local}}{U_{3/4H}} \tag{11}$$

Figure 11A shows that as expected at $\phi = 0°$ on the windward side of the building the trapped flow in the recessed

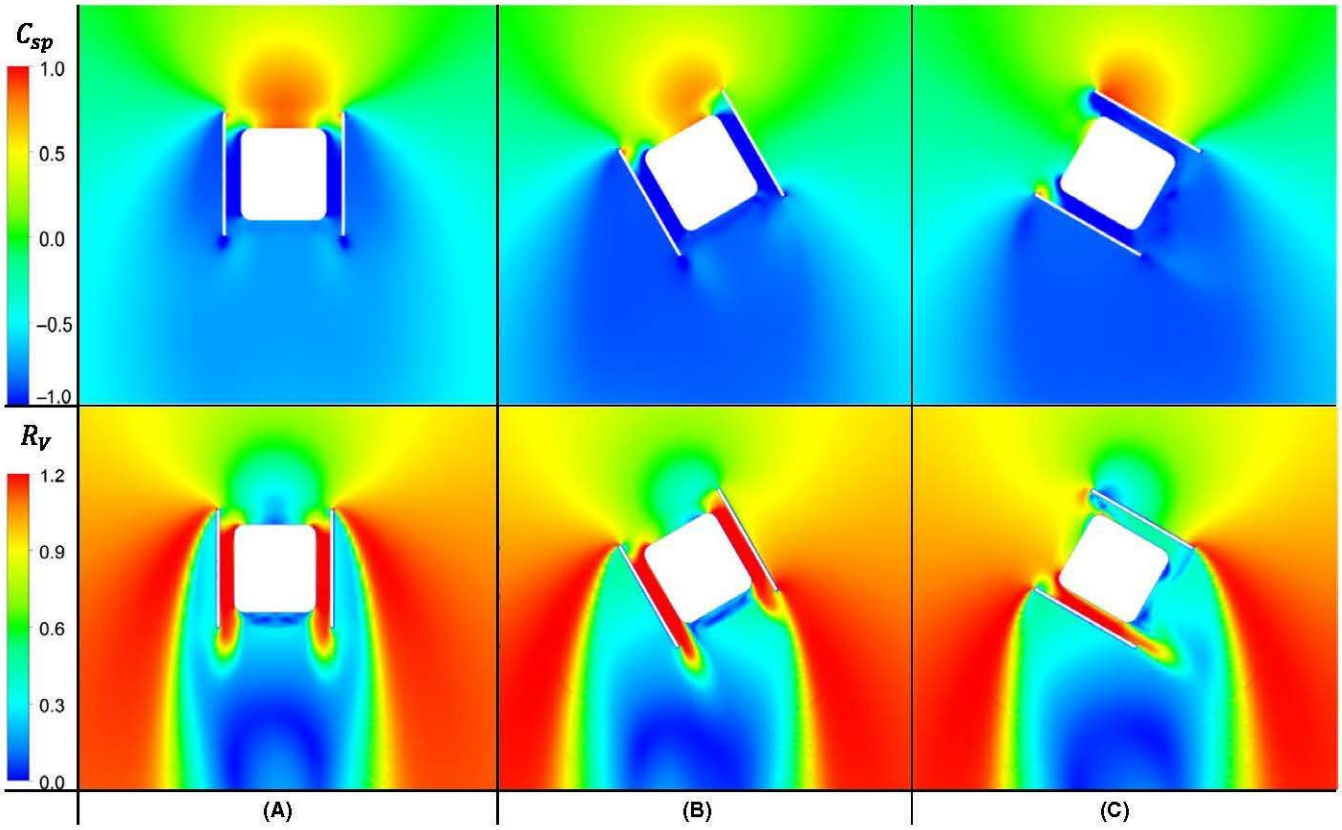

FIGURE 11 C_{sp} and R_V contours of the ducted flow at ϕ = (A) 0°, (B) 30° and (C) 60° when U_{ref} = 12 m/s ($U_{3/4H}$ = 11.6 m/s) and the EMSs for the LCWT are deactivated

region has increased the static pressure there and at the leeward side of the building the flow detachment has created a very low pressure there. Therefore, the high pressure gradient created along the openings at 0° increases the ducted flow velocity in the through-building openings to above $U_{3/4H}$. Comparing Figure 11A,B shows that the velocity of the ducted flow has even slightly increased at $\phi = 30°$ which should be due to the lower negative pressure created at the outlet of the openings. Comparing Figure 11A and C shows that at $\phi = 60°$ the ducted flow velocity has dropped below 6 m/s in the right opening while it is still above 12 m/s in the left one. The reason is that the flow detachment at the inlet of the right through-building opening has strongly decreased the static pressure and consequently the pressure gradient along this opening.

4.2 | The effect of the LCWT on the ducted flow

For investigating the effect of ducted flow on power generation of the LCWT, C_{sp} and R_V contours are plotted at $\phi = 0°$, 30°, and 60° when the free-stream velocity is 12 m/s at the 3/4H of the building, and the EMS of the LCWT is activated. As can be seen in Figure 12A-C, compared with Figure 11A-C, the pressure gradient is focused at the location of the EMS and the velocity has decreased in the through-building openings. According to R_V contours, the ducted flow has lower velocity than $U_{3/4H}$ in the openings at 0° when the LCWT is installed in the through-building openings.

Similar to the empty through-building openings, at 30° the velocity is slightly higher than at 0° which should be due to the similar reason (lower pressure created at the outlet of the openings). Comparing Figure 12A and C shows that at 60° the ducted flow velocity has dropped below 90% of the free-stream velocity in the left through-building opening and below 30% in the right one. On the other hand, according to Figure 4C, power generation of the LCWT in the duct is about 30%-70% higher than in the free-stream condition. Therefore, the overall effect of the through-building opening on the wind turbines at low ϕs may not be decreasing their power generation compared with the free-stream condition. However, the power generation will dramatically drop in one of the through-building openings when the ϕ increases.

Using EMS method, the mean velocity, inlet pressure, and turbulent kinetic energy (TKE) of the ducted flow are estimated and recorded in the presence of the ducted LCWT and shown in Table 1(A-D). U_{ref} is 6, 9, 12, and 15 m/s in Table 1(A-D), respectively. $U_{3/4H}$ at each velocity profile is also presented.

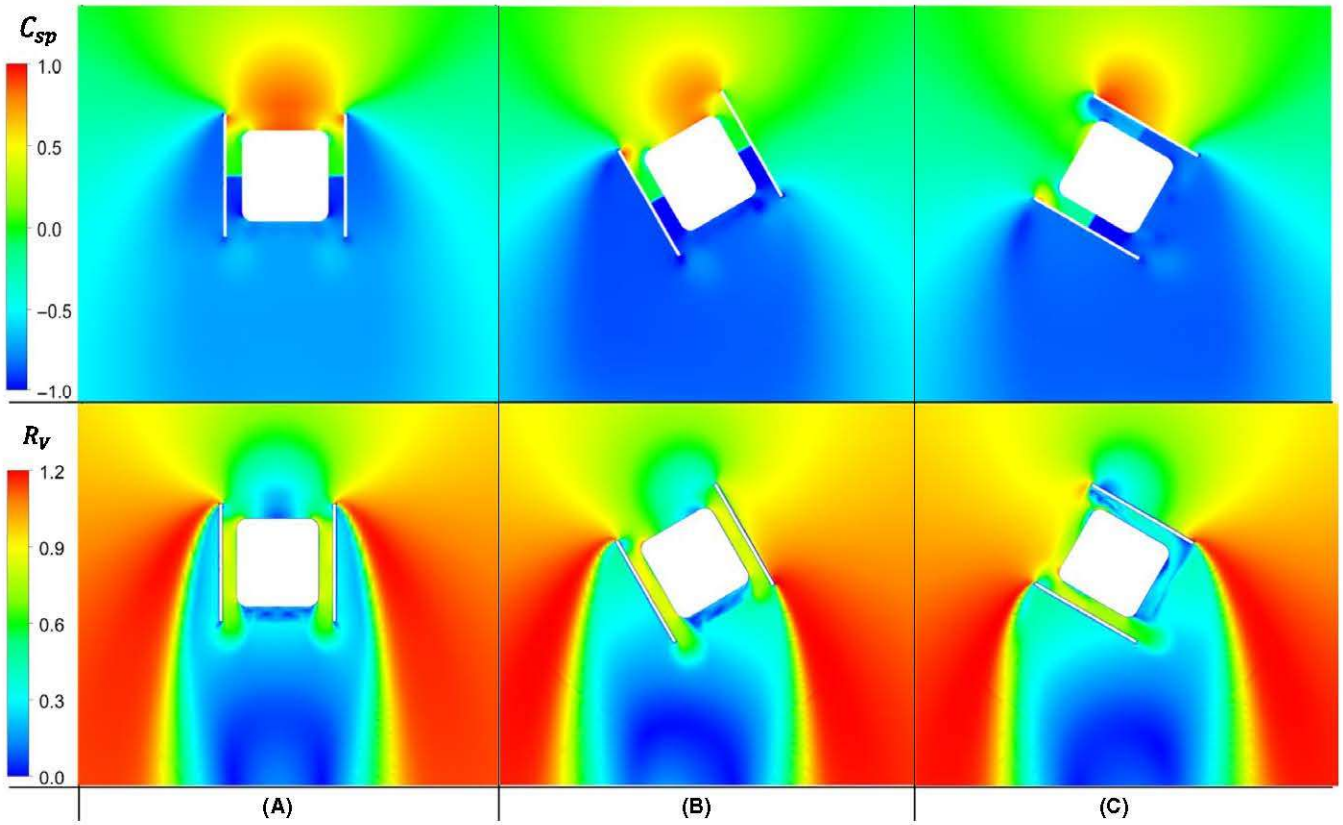

FIGURE 12 C_{sp} and R_V contours of the ducted flow at ϕ = (A) 0°, (B) 30° and (C) 60° when the U_{ref} = 12 m/s ($U_{3/4H}$ = 11.6 m/s) at and the EMSs for the LCWT are activated

4.3 | The effect of the ducted flow on power generation of the LCWT and HAWT

The resultant flow characteristics of the approach wind in the through-building opening in presence of the LCWTs are applied to the inlet of the simple duct which explicitly houses the LCWTs. Power generation of the ducted wind turbines installed in the left and right through-building openings at $\phi = 0°$, 30°, and 60° are computed and compared with each other and their free-stream condition. In Figure 13A-D, the left axis shows the resultant power generation of the LCWT installed in the through-building openings at $\phi = 0°$, 30°, and 60° and the right axis shows the power generation ratio (R_P) of the ducted LCWT to the free-stream one when U_{ref} is 6, 9, 12, and 15 m/s, respectively.

The resultant R_Ps indicate that installing the wind turbines in the selected through-building opening enhances their performance compared with their performance in the free-stream condition, not only at $\phi = 0°$ but also at other angles. As expected from C_{sp} and R_V contours in Figure 12, power generation of the LCWT in $\phi = 30°$ is greater than in $\phi = 0°$ because of the higher pressure difference created across the building. This figure also indicates that the maximum R_P of the LCWT is about 1.8 at U_{ref} = 6 m/s which has decreased to about 1.5 when U_{ref} = 15 m/s. In other words, the enhancement effect of the through-building openings on power generation of the LCWTs is lower at higher velocities. The reason could be that the current configuration (of stator-augmented PowerWindow) is designed for the approach wind velocity of 8 m/s, and needs to be optimized for higher velocities.

Flow characteristics of the approach wind in the through-building opening have also been investigated and recorded in presence of the HAWTs and the resultant flow characteristics are applied to the inlet of the simple duct which explicitly houses the HAWTs. Power generation of the ducted wind turbines installed in the left and right through-building openings at $\phi = 0°$, 30°, and 60° is computed and compared with each other and their free-stream condition. Similar to Figure 13, in Figure 14A-D, the left axis shows the resultant power generation of the HAWTs installed in the through-building openings at $\phi = 0°$, 30°, and 60° and the right axis shows R_P of the ducted HAWTs to the free-stream one when U_{ref} is 6, 9, 12, and 15 m/s, respectively.

The resultant R_Ps of the HAWTs show that similar to the LCWTs, their installation in the selected through-building openings enhances their performance compared with their free-stream condition. However, comparison of Figures 13 and 14 shows that the power generation of the LCWT has not increased as much as the HAWTs. The reason is the higher solidity of the LCWT which demands higher pressure gradient along the through-building opening, and subsequently

TABLE 1 Characteristics of the ducted flow when the EMS of the LCWT is activated in the right and left through-building openings at different ϕ when U_{ref} = (A) 6 m/s, (B) 9 m/s, (C) 12 m/s and (D) 15 m/s

Incident wind angle (°)	Through-building opening	Inlet gauge pressure (Pa)	Mean velocity (m/s)	TKE (m^2/s^2)
(A) $U_{3/4H}$ = 5.8 m/s				
0	Left & right	0.99	4.72	0.65
30	Left	0.08	4.94	0.58
	Right	−1.24	4.90	0.58
60	Left	−3.91	4.35	0.42
	Right	−14.71	1.99	0.26
(B) $U_{3/4H}$ = 8.7 m/s				
0	Left & right	2.25	7.18	1.49
30	Left	0.08	7.40	1.62
	Right	−1.24	7.46	1.33
60	Left	−32.39	6.66	0.96
	Right	−8.29	3.14	0.64
(C) $U_{3/4H}$ = 11.6 m/s				
0	Left & right	3.84	9.61	2.66
30	Left	−0.34	10.00	2.89
	Right	−5.67	9.94	2.37
60	Left	−17.35	8.90	1.69
	Right	−64.32	4.32	1.17
(D) $U_{3/4H}$ = 14.5 m/s				
0	Left & right	5.85	12.03	4.15
30	Left	−1.28	12.54	4.53
	Right	−9.63	12.45	3.72
60	Left	−23.11	11.24	2.68
	Right	−98.43	5.58	1.86

by decreasing the mass flowrate in the opening decreases the ducted velocity.

The sum of the generated power of the right and left LCWTs and HAWTs is calculated when the building is exposed to different velocity profiles and different ϕs and shown in Table 2. As can be seen in the table, at $\phi = 0°$, 30°, and 60° the total power generation of both the ducted wind turbines is relatively close (maximum 20% higher or lower than one another). It should be noted that, the maximum power generation of the selected HAWT (Ampair 300) is not normally above 0.35 KW in free-stream condition but the studies have shown that its capacity increases when it is operating in a ducted configuration.[32] The increase in power generation is due to the increase of τ (in Equation 3). Even though, power generation of each ducted HAWT cannot exceed 0.6 KW. Therefore, at higher approach wind velocity (15 m/s or higher) is a constant 0.6 KW. The other important issue is that, due to the geometrical symmetry of the selected building, the total power generation of the wind turbines is identical at $\phi = 30°$ and $-30°$ or 60° and $-60°$, as the power generation of the right and left wind turbines integrated with the through-building openings would only be swapped with one another at these ϕs. The free-stream velocity at 10 m above sea level (U_{10}) at each U_{ref} is also presented.

The main difference between the power generations of the LCWT and HAWT appears when ϕ exceeds 90°. When the approach wind comes from the other side of the building, regardless of the exact value of ϕ, the ducted flow direction changes by 180° and the passive yaw mechanism of the HAWT is not capable of responding to this change of flow direction. Therefore, the HAWTs cannot operate unless by using active yaw mechanism. However, as shown in the previous study, the LCWT (stator-augmented PowerWindow) is designed and configured to be capable of operating continuously regardless of wind direction. This is a prime advantage for the LCWT. To demonstrate the value of this advantage, the annual operating probability of these two wind turbines can be compared when installed in the selected through-building openings of a building located in Sydney region.

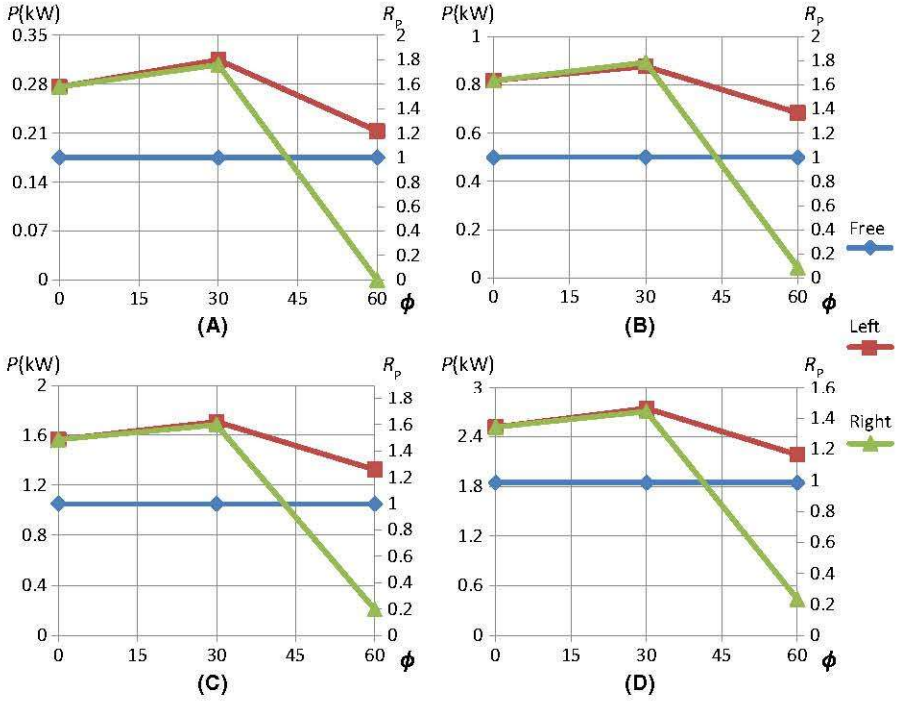

FIGURE 13 Power generation and power generation ratio of the LCWTs installed in the left and right through-building openings at $\phi = 0°$, 30° and 60°, when U_{ref} = (A) 6 m/s, (B) 9 m/s, (C) 12 m/s, and (D) 15 m/s

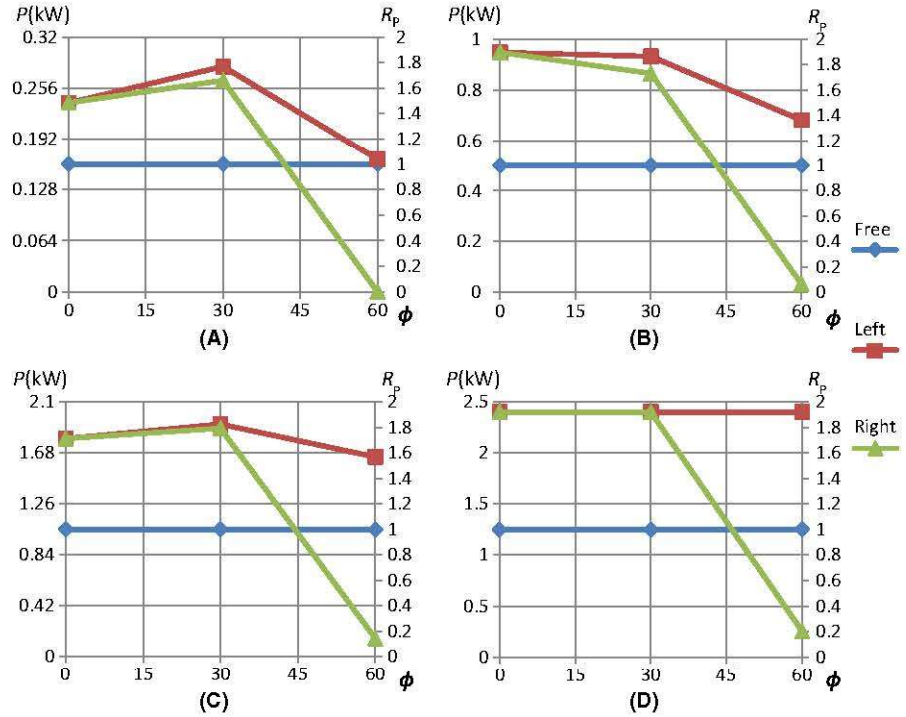

FIGURE 14 Power generation and power generation ratio of the HAWTs installed in the left and right through-building openings at $\phi = 0°$, 30°, and 60°, when U_{ref} = (A) 6 m/s, (B) 9 m/s, (C) 12 m/s, and (D) 15 m/s

Figure 15 shows the probability distributions of hourly mean wind speeds with direction for Sydney Airport at 45° intervals at a height of 10 m over open country. It can be seen that, if the building faces North West, the approach wind has a great probability to channel through the openings. In this case, the HAWT, by collecting the wind energy at $\phi = -45°$, 0, and 45°, excluding the probability of having $U_{10} < 2.8$ m/s (which is below the cut-in speed of both the wind turbines), it has the annual operating probability of about 24%, while the LCWT by collecting the wind energy at $\phi = -135°$, $-45°$, 0, 45°, 135°, and 180°, excluding the probability of having $U_{10} < 2.8$ m/s has the annual operating probability of about 56%. More detailed analysis of the total annual energy production of LCWT in different wind climates and urban terrains needs further investigation which can be considered for future research.

Creating one more pair of the through-building openings (eg, on the next floor of the building), perpendicular to these

U_{ref} (m/s)	U_{10} (m/s)	Incident wind angle (°)	Power generation of the LCWTs (KW)	Power generation of the HAWTs (KW)
6	4.4	0	0.55	0.47
		30	0.62	0.55
		60	0.21	0.17
		90	0	0
		120	0.21	0
		150	0.62	0
		180	0.55	0
9	6.06	0	1.63	1.89
		30	1.77	1.79
		60	0.73	0.71
		90	0	0
		120	0.73	0
		150	1.77	0
		180	1.63	0
12	8.07	0	3.12	3.60
		30	3.38	3.80
		0	1.53	1.80
		90	0	0
		120	1.53	0
		150	3.38	0
		180	3.12	0
15	10.09	0	5.03	4.80
		30	5.45	4.80
		60	2.62	2.65
		90	0	0
		120	2.62	0
		150	5.45	0
		180	5.03	0

TABLE 2 Total power generation of the right and left wind turbines integrated with the through-building opening when the building is exposed to different velocity profiles and ϕs

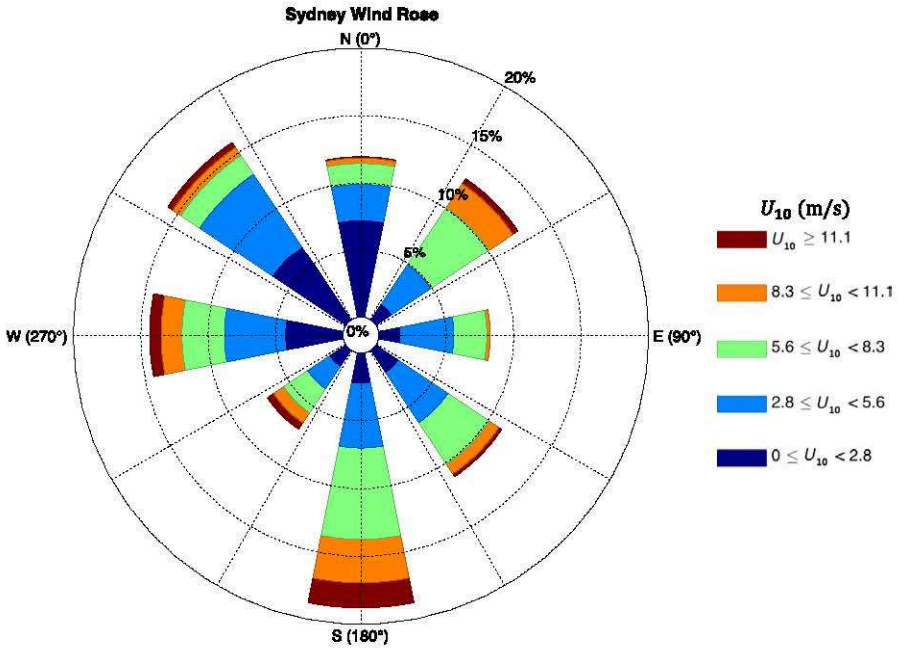

FIGURE 15 Wind rose of Sydney[34]

ones, enables the potential of wind energy harvesting at any direction. In other words, at any given time, at least two of the turbines are operating, provided that the wind speed exceeds the cut-in speed of wind turbines. Based on the wind rose of Sydney (Figure 15), excluding the probability of having $U_{10} < 2.8$ m/s (which is below the cut-in speed of the LCWT), a minimum of (0 + 0.55=) 0.55 KW and maximum of (2.45 + 2.62 =) 8.07 KW power generation can be guaranteed 72% of the times throughout the year, which is sufficient to supply a portion of the electricity consumption of the building facilities.

5 | CONCLUSION

Employing the equivalent momentum sink method, developed in this study, characteristics of the ducted flow is predicted in presence of stator-augmented PowerWindow, a linear cascade wind turbine (LCWT) and power generation capacity of the LCWT is investigated when it is installed in a through-building opening in a tall building. The equivalent momentum sink method enables the estimation of pressure, velocity, and turbulence intensity of the flow in the through-building opening integrated with a wind turbine and subjected to different wind directions. It is shown that the selected through-building openings with a properly designed layout can maintain the velocity of the flow in the openings in a wide range of wind directions ($-60° < \phi < 60°$) and enhances the power generation by 50%-80%. Power generation of the LCWT is also compared with a conventional horizontal axis wind turbine (HAWT), Ampair 300, installed in the same through-building opening. The results show that in certain incident wind angles, velocity of the ducted flow is higher than the free-stream velocity at the same elevation. By installing the LCWT in the through-building opening the ducted flow velocity decreased below the free-stream velocity at the same elevation due to the increase in the pressure gradient demanded along the opening. It is computed and shown that power generation of the ducted LCWT is close to the ducted HAWTs in some incident wind angles, but the LCWT is also able to effectively operate at above 90° where the ducted HAWTs are not. As a result, with 56% annual power generation probability, the LCWT is superior to the HAWT with 24% annual power generation probability for building integration in Sydney. As a case study, it is also shown that in Sydney area by embedding four through-building openings integrated with stator-augmented PowerWindow in the selected building, a minimum of 0.55 KW and maximum of 8.07 KW power generations can be guaranteed 72% of the times throughout the year which is sufficient to supply a portion of the electricity consumptions of the building facilities.

ORCID

Seyed Amir Hosein Jafari
http://orcid.org/0000-0003-0627-0784

NOMENCLATURE:

C_P	Coefficient of performance (dimensionless)
C_{sp}	Surface Pressure Coefficient (dimensionless)
F_V	Vertical aerodynamic force on LAWT blades (N)
H	Building height (m)
P	Power (KW)
p	Pressure (Pa)
R_P	Power generation ratio (dimensionless)
R_V	Velocity ratio (dimensionless)
TKE	Turbulence kinetic energy (m_2/s^2)
U_{10}	Free-stream velocity at 10 m above sea level (m/s)
$U_{3/4H}$	Free-stream velocity at 3/4H (m/s)
U_{ref}	Free-stream velocity at H (m/s)
V	Air velocity along the duct (m/s)
μ	Air viscosity (m^2/s)
ρ	Air density (kg/m^3)
λ	Linear speed ratio (dimensionless)
τ	Aerodynamic torque on HAWT rotor (N.m)
ϕ	Incident wind angle (°)
ω	Rotational speed of HAWT rotor (rad/s)

REFERENCES

1. Ayhan D, Sağlam Ş. A technical review of building-mounted wind power systems and a sample simulation model. *Renew Sustain Energy Rev*. 2012;16(1):1040-1049.
2. Ishugah TF, Li Y, Wang RZ, Kiplagat JK. Advances in wind energy resource exploitation in urban environment: a review. *Renew Sustain Energy Rev*. 2014;37:613-626.
3. Hassanli S, Hu G, Fletcher DF, Kwok KCS. Potential application of double skin façade incorporating aerodynamic modifications for wind energy harvesting. *J Wind Eng Ind Aerodyn*. 2018;174:269-280.
4. Toja-Silva F, Colmenar-Santos A, Castro-Gil M. Urban wind energy exploitation systems: behaviour under multidirectional flow conditions—Opportunities and challenges. *Renew Sustain Energy Rev*. 2013;24:364-378.
5. Duffy MJ. *Small wind turbines mounted to existing structures*. Aerospace Engineering, Georgia Institute of Technology; 2010.
6. Park J, Jung H-J, Lee S-W, Park J. A new building-integrated wind turbine system utilizing the building. *Energies*. 2015;8(10):11846-11870.
7. Abohela I, Hamza N, Dudek S. Effect of roof shape, wind direction, building height and urban configuration on the energy yield and positioning of roof mounted wind turbines. *Renewable Energy*. 2013;50:1106-1118.
8. Hassanli S, Hu G, Kwok KCS, Fletcher DF. Utilizing cavity flow within double skin façade for wind energy harvesting in buildings. *J Wind Eng Ind Aerodyn*. 2017;167:114-127.

9. Hassanli S, Kwok KCS, Zhao M. Performance assessment of a special Double Skin Façade system for wind energy harvesting and a case study. *J Wind Eng Ind Aerodyn*. 2018;175:292-304.
10. Dayan E. Wind energy in buildings: power generation from wind in the urban environment - where it is needed most. *Refocus*. 2006;7(2):33-38.
11. Dannecker RKW, Grant AD. Investigations of a building-integrated ducted wind turbine module. *Wind Energy*. 2002;5(1):53-71.
12. Grant A, Kelly N. A ducted wind turbine model for building simulation. *Build Serv Eng Res Technol*. 2004;25(4):339-349.
13. Grant A, Johnstone C, Kelly N. Urban wind energy conversion: the potential of ducted turbines. *Renewable Energy*. 2008;33(6):1157-1163.
14. Chong WT, Pan KC, Poh SC, et al. Performance investigation of a power augmented vertical axis wind turbine for urban high-rise application. *Renewable Energy*. 2013;51:388-397.
15. Krishnan A, Paraschivoiu M. 3D analysis of building mounted VAWT with diffuser shaped shroud. *Sustain Cities Soc*. 2016;27:160-166.
16. Jafari SAH, Safaei F, Kosasih B, Kwok KCS. Power generation analysis of PowerWindow, a linear wind generator, using computational fluid dynamic simulations. *J Wind Eng Ind Aerodyn*. 2015;147:226-238.
17. Jafari SAH, Kwok KCS, Safaei F, Kosasih B. Aerodynamic analysis of a linear cascade wind turbine. *Wind Energy*. 2018;21(11):1141-1154.
18. Jafari SAH, Kwok KCS, Safaei F, Kosasih B, Zhao M. The effects of installation configuration and solidity on the power generation of a linear cascade wind turbine. *J Wind Eng Ind Aerodyn*. 2018;180:122-135.
19. Bianchini A, Balduzzi F, Gentiluomo D, Ferrara G, Ferrari L. *Comparative analysis of different numerical techniques to analyze the wake of a wind turbine*. Volume 9: Oil and Gas Applications; Supercritical CO2 Power Cycles; Wind Energy Charlotte, North Carolina, USA, June 26–30, 2017
20. Migoya E, Crespo A, García J, et al. Comparative study of the behavior of wind-turbines in a wind farm. *Energy*. 2007;32(10):1871-1885.
21. Barthelmie RJ, Hansen K, Frandsen ST, et al. Modelling and measuring flow and wind turbine wakes in large wind farms offshore. *Wind Energy*. 2009;12(5):431-444.
22. Sanderse B, Pijl SP, Koren B. Review of computational fluid dynamics for wind turbine wake aerodynamics. *Wind Energy*. 2011;14(7):799-819.
23. Jiménez Á, Crespo A, Migoya E. Application of a LES technique to characterize the wake deflection of a wind turbine in yaw. *Wind Energy*. 2010;13(6):559-572.
24. Jimenez A, Crespo A, Migoya E, Garcia J. Advances in large-eddy simulation of a wind turbine wake. *J Phys: Conf Ser*. 2007;75(1):012041.
25. Jimenez A, Crespo A, Migoya E, Garcia J. Large-eddy simulation of spectral coherence in a wind turbine wake. *Environ Res Lett*. 2008;3(1):015004.
26. Jafari S, Hassanli S, Eftekharian E, Kwok K. *Effect of incident wind angle on power generation of building integrated wind turbines*. Paper presented at: 9th Asia-Pacific Conferences on Wind Engineering 2017.
27. Hassanli S, Jafari SA, Eftekharian E, Kwok K. *Performance assessment of cascaded wind turbines inside through-building openings*. Paper presented at: 9th Asia-Pacific Conferences on Wind Engineering 2017.
28. Hassanli S, Chauhan K, Zhao M, Kwok KCS. Application of through-building openings for wind energy harvesting in built environment. *J Wind Eng Ind Aerodyn*. 2019;184:445-455.
29. Jafari SAH, Kosasih B. Flow analysis of shrouded small wind turbine with a simple frustum diffuser with computational fluid dynamics simulations. *J Wind Eng Ind Aerodyn*. 2014;125:102-110.
30. Ampair. Ampair wind turbine. http://www.nfenergies.com/documents/Ampair%20300%20Data%20Sheet.pdf. Published 2016. Accessed January, 2016.
31. Franke J. *Best practice guideline for the CFD simulation of flows in the urban environment*. Meteorological Inst.; 2007.
32. Jafari SAH, Kwok KCS, Hassanli S. *Integration of wind turbines in tall buildings for wind power generation*. 8th International Colloquium on Bluff Body Aerodynamics and Applications; June 7 – 11, 2016; Northeastern University, Boston, Massachusetts, USA.
33. Wind Roses for Selected Locations in Australia. Australia Government – Bureau of Meteorology. http://www.bom.gov.au/climate/averages/wind/selection_map.shtml. 2016. Accessed August, 2018.

How to cite this article: Jafari SAH, Hassanli S, Kwok K, Safaei F, Kosasih B, Zhao M. Building integration of stator-augmented powerwindow, a linear cascade wind turbine. *Energy Sci Eng*. 2019;00:1-18. https://doi.org/10.1002/ese3.300

APPENDIX

The compiled UDF prepared to apply the presence of the LCWT to the CFD solver:

```
#include "udf.h"
#include <math.h>

DEFINE_SOURCE(xmom_source,c,t,dS,eqn)
{

real x[ND_ND];
real source, V;
C_CENTROID(x,c,t);
V=sqrt(pow(C_U(c,t),2)+pow(C_V(c,t),2)+pow(C_W(c,t),2));
source = 4*(0.9841*pow(V,2) - 1.0476*V + 3.3)/(1600*12.8/
(pow(80,3)));
dS[eqn] = 4*(0.9841*2*V - 1.0476)/(1600*12.8/(pow(80,3)));

return source;

}
```

The compiled UDF prepared to apply the presence of the HAWT to the CFD solver:

```
#include "udf.h"
#include <math.h>

DEFINE_SOURCE(xmom_source,c,t,dS,eqn)
{

real x[ND_ND];
real source, V;
C_CENTROID(x,c,t);
V=sqrt(pow(C_U(c,t),2)+pow(C_V(c,t),2)+pow(C_W(c,t),2));
source = 4*(0.0035*pow(V,4)-0.1862*pow(V,3)+3.1501*pow(V,2)-
15.053*V+25.905)/(1600*12.8/(pow(80,3)));
dS[eqn] = 4*(0.0035*4*pow(V,3)-0.1862*3*pow(V,2)+3.1501*2*V-
15.053)/(1600*12.8/(pow(80,3)));

return source;

}
```

Appendix C

The compiled UDF prepared to apply the presence of the LCWT to the CFD solver:

```
#include"udf.h"
#include<math.h>

DEFINE_SOURCE(xmom_source,c,t,dS,eqn)
{

real x[ND_ND];
real source, V;
C_CENTROID(x,c,t);
V=sqrt(pow(C_U(c,t),2)+pow(C_V(c,t),2)+pow(C_W(c,t),2));
source = 4*(0.9841*pow(V,2) - 1.0476*V + 3.3)/(1600*12.8/(pow(80,3)));
dS[eqn] = 4*(0.9841*2*V - 1.0476)/(1600*12.8/(pow(80,3)));

return source;

}
```

The compiled UDF prepared to apply the presence of the HAWT to the CFD solver:

```
#include"udf.h"
#include<math.h>

DEFINE_SOURCE(xmom_source,c,t,dS,eqn)
{

real x[ND_ND];
real source, V;
C_CENTROID(x,c,t);
V=sqrt(pow(C_U(c,t),2)+pow(C_V(c,t),2)+pow(C_W(c,t),2));
source = 4*(0.0035*pow(V,4)-0.1862*pow(V,3)+3.1501*pow(V,2)-
15.053*V+25.905)/(1600*12.8/(pow(80,3)));
dS[eqn] = 4*(0.0035*4*pow(V,3)-0.1862*3*pow(V,2)+3.1501*2*V-
15.053)/(1600*12.8/(pow(80,3)));

return source;

}
```